Indium Sulfide (In₂S₃) Based Nanostructures for Photoelectrochemical Water-Splitting

THESIS

Submitted in partial fulfillment of the requirements for the degree of

Doctor of Philosophy

by

Mamta Devi Sharma

2017PHXF0011P

Under the Supervision of

Dr. Mrinmoyee Basu

&

Dr. Surojit Pande

BIRLA INSTITUTE OF TECHNOLOGY AND SCIENCE PILANI, PILANI CAMPUS (RAJASTHAN), INDIA
2022

BIRLA INSTITUTE OF TECHNOLOGY AND SCIENCE, PILANI

CERTIFICATE

This is to certify that the thesis entitled ''**Indium Sulfide (In_2S_3) Based Nanostructures for Photoelectrochemical Water-Splitting**'' submitted by **Ms. Mamta Devi Sharma** ID No. **2017PHXF0011P** for an award of Ph.D. of the institute embodies original work done by her under our supervision.

Signature of the Supervisor

Dr. Mrinmoyee Basu

Assistant Professor

Department of Chemistry

Birla Institute of Technology and Science

Pilani, Pilani Campus, Rajasthan

Signature of the Co-Supervisor

Dr. Surojit Pande

Associate Professor

Department of Chemistry

Birla Institute of Technology and Science

Pilani, Pilani Campus, Rajasthan

Date: / /2022

Dedicated

To Almighty for showering the grace

To My Parents and Teachers who gave me a luminous path and motivation

To those who believe in hard work and never give-up on their dreams

Acknowledgements

The work presented in this thesis would have been impossible without the guidance and support of certain people to whom I would like to extend my sincere thanks. It is a pleasant opportunity for me to express my gratitude and regard for all of them.

First and foremost, my heartfelt thanks go to my research supervisor Dr. Mrinmoyee Basu and co-supervisor Dr. Surojit Pande for giving me the opportunity to be a part of their research team. They guided and supported me continuously throughout the tenure of my Ph.D. Without their trust, ardent inspiration, guidance, constant feedback, support, and motivation, this thesis work would have remained a dream. I want to extend my regards to Dr. Mrinmoyee Basu, for her encouragement that carried me through difficult times and for her insights, suggestions, and motivation that helped to improve my research skills. Her constant motivation for preparing the presentations for the work done every week really improved my presentation and writing skills. I am indebted to her for all the endless lab sessions, support in lab experiments, energetic presence, knowledgeable and fruitful discussions, and unconditional care that allowed me to progress eventually.

I would like to sincerely thank the Vice-Chancellors, Directors, Deans, and Associate Deans of Birla Institute of Technology and Science (BITS) Pilani and HODs of the Department of Chemistry for providing me all the required facilities and allowing me to pursue my doctoral studies without any problems.

My wholehearted gratitude to all the respected teachers' Department of chemistry for their cooperation and affection. I am obliged to the convener and members of the Doctoral Advisory Committee. I owe my sincere thanks to my Doctoral Advisory Committee members Prof. Inamur Rahman Laskar, and Dr. Arnab Hazra, for their incredible suggestions and cooperation in refining my thesis.

I want to thank the office and lab staff for their all needed help in lab experiments Mr. C. P. Soni, Mrs. Pushpalata, Mr. Suresh Saini, Mr. Nandlal Saini, and Mr. Ashok Sharma. I overwhelmingly acknowledge the office staff of AUGSD, AGSRD, and Library whose secretarial assistance helped me in my Ph.D. tenure. I would like to thanks to central instrument facilities BITS-Pilani and Department of physics for providing the XRD instrument facility.

I was lucky to be in the company of such encouraging and helping seniors during my Ph.D. tenure. I am highly thankful to Dr. Pragati Fageria and Dr. Sunita Kumari for their unflagging love, strong support in distress, hold in difficult times, and immense care all over my Ph.D. I was really

fortunate to have group members Dr. Roshan Nazir, Dr. Chavi Mahala, Ms. Divya Rathore, Mr. Prashant, and Ms. Aastha, I am thankful for their persistent support. I am thankful to friends and batchmates: Dr. Susheela Kumari, Dr. Chavi Mahala, Dr. Jagrity Chaudhary, Mr. Dhritabarta Pal, Mr. Amol, Mr. Santosh, Mr. Bintu, Ms. Prachi, Ms. Aishwarya, Ms. Jyoti, Mr. Pramod, Mr. Ram Prasad, Mr. Bharat who were always with me in my moments of sorrow and joy and were forever ready to help me regardless of time boundaries. I was extremely happy to work with seniors and colleagues in the department of chemistry. My sincere thanks to all my lab mates Dr. Moyna Das, Ms. Vishakha, Mr. Sumit, Ms. Anu, Mr. Ajeet, Mr. Ajeet, Ms. Sakshi, Ms. Sakshi, and Ms. Ritu, and Mr. Mahesh who always motivated me to work tirelessly.

My existence, as a person, as a scholar, was impossible without my great parents. My vision, ethical principles, and teachings about life, which I had inherited from my father (Mr. Niranjan Kumar Sharma). He is a constant source of inspiration and always accompanies me like a shadow. Words cannot define the love and sacrifice of my mother (Mrs. Sushila Sharma) who has unconditionally given me the support and confidence in everything that I strive for. I convey my regards to my father-in-law Mr. Pawan Suroliya and Mother-in-law Mrs. Sudha Sharma for endless support and love. I express my heartfelt thanks to my siblings (Shweta, Awadhesh, Vasu), and cousins for their divine love, and strong support which kept my morale high always. I would like to thank my husband, Mr. Ashutosh Suroliya for the encouragement and strong support, without him I would not have been able to succeed in this endeavor. I thank the almighty for giving me health and strength to face every day with faith and optimism. Finally, my sincere thanks go to BITS Pilani, Rajasthan for all the needed infrastructure, DST-SERB, and BITS Pilani for the research fellowship.

Thanks to All!

Date: /   /2022
Place: Pilani, India   *Mamta Devi Sharma*

Table of Contents

Contents	Page No.

Table of Contents

Table of Contents

Table of Contents

Table of Contents

Table of Contents

Abstract

The thesis entitled "Indium Sulfide (In_2S_3) Based Nanostructures for Efficient Photoelectrochemical Water-Splitting" describes the development of vertically grown nanostructures of the In_2S_3 based semiconductor materials and their application in the photoelectrochemical water-splitting (PEC) reaction for the generation of hydrogen (H_2). The first chapter of the thesis gives an insight into nanoscience and nanotechnology, a brief literature overview about the nanomaterials, their synthetic approaches, and their application in various emerging fields. This chapter provides a detailed discussion of the different pathways for solar water-splitting. This chapter also delivers an overview of semiconductor fundamentals, key features of a photoelectrode, and various strategies for the enhancing efficiency of a photoelectrode. Chapter two illustrates synthesis methodology, calculation methods, chemicals, and instrumentation techniques that are used to carry out thesis work. Chapters three to seven deal with the development of efficient In_2S_3 based nanostructures for photoelectrochemical water-splitting reaction. In_2S_3 is chosen as a model semiconductor and various strategies are undertaken to improve the efficiency of In_2S_3 for PEC water-splitting reaction. Chapter four describes the in-situ development of heterostructuring of the In_2S_3 and In_2O_3 nanopyramid which enhances the PEC activity by improving the charge separation efficacy. In chapter five, In_2S_3 nanosheets are sensitized with 'S' doped C_3N_4-dots to improve the light absorption and charge separation efficiency which leads to enhancement in PEC activity of In_2S_3 in the corrosive environment. Chapter five deals with the development of $ZnIn_xS_y$ nanosheets as photoanode. In this chapter, the band structure and morphology of $ZnIn_xS_y$ are modulated through controlling the calcination time and the indium content for enhancing the PEC activity. In chapter six, the charge carrier density of $ZnIn_{2.2}S_y$ is enhanced via cation exchange method through developing Cd-$ZnIn_{2.2}S_y$. The Cd-$ZnIn_{2.2}S_y$ nanosheets show the improved charge carrier density and widening in the space charge layer compared to $ZnIn_{2.2}S_y$. In chapter seven, vertically grown 2D thin sheets of $CdIn_{2.2}S_y$ are developed. The surface of $CdIn_{2.2}S_y$ is decorated with 'S', 'N' co-doped carbon dots (S, N-CDs) to improve the light absorption and charge transferability which enhances the PEC activity of $CdIn_{2.2}S_y$ nanosheets. Finally, the last chapter summarizes the main results obtained from the study of different photoelectrodes for PEC water-splitting. Additionally, this chapter also provides the directions for future studies using efficient photoelectrodes which may find practical applicability.

Abstract

Keywords: Photoelectrode, nanopyramids, nanosheets, heterostructure, photoelectrochemical water-splitting, carbon dots, corrosive environment.

List of Abbreviations

AM	Air Mass
AU	Arbitrary Unit
atm	Atmosphere
APCE	Absorbed photon-to-current efficiency
ABPE	Applied bias photon-to-current efficiency
BE	Binding energy
CB	Conduction band
CDs	Carbon dots
CIS	Cadmium indium sulfide
CV	Cyclic Voltametry
β-CD	B-cyclodextrin
D_m	Minority diffusion coefficient
D	Dimension
eV	Electron Volt
E_g	Band gap
E_F	Fermi level
ECSA	Electrochemical surface area
EDS	Energy dispersive spectroscopy
EIS	Electrochemical impedance spectra
FTO	Fluorine doped tin coated glass
FTIR	Fourier transform Infrared spectroscopy
FESEM	Field emission scanning electron microscopy
HRTEM	High resolution transmission electron microscopy
HET	Hot electron transfer
HOMO	Highest occupied molecular orbital
h	Hour
HER	Hydrogen evolution reaction
IQE	Internal quantum efficiency
IPCE	Incident photon-to-current efficiency
KJ	Kilo Joule

List of Abbreviations

L_D	Minority diffusion length
LUMO	Lowest unoccupied molecular orbital
L_{SC}	Space charge layer
LSPR	Localized surface plasmon resonance
LSV	Linear sweep voltametry
ms	Milliseconds
mA	Milliampere
µM	Micrometer
MO	Molecular orbital
mW	Milliwatt
τ_m	Minority carrier lifetime
NHE	Normal hydrogen electrode
NP	Nanoparticle
NWs	Nanowires
ns	Nanosecond
nm	Nanometer
NIR	Near Infra-red
OER	Oxygen evolution reaction
PV	Photovoltaic
PEC	Photoelectrochemical
PEIS	Photoelectrochemical impedance spectra
PC	Photocatalytic
PIRET	Plasmon-induced resonance energy transfer
PXRD	Powder X-ray Diffraction
QSE	Quantum size effect
QDs	Quantum dots
Rs	Solution resistance
Rct	Charge transfer resistance
SCE	Saturated calomel electrode
STH	Solar-to-Hydrogen
SCLJ	Semiconductor liquid junction

List of Abbreviations

SPR	Surface plasmon resonance
Sec	Seconds
TW	Terra Watt
UV	Ultraviolet
VB	Valance band
V_{fb}	Flat band potential
W	Depletion layer width
XPS	X-ray photoelectron spectroscopy

List of Symbols

Å	Angstrom
α	Alpha
α^{-1}	absorption coefficient
k	Boltzmann constant
χ	Chi
Δ	Delta
η	Eta
ε_0	Epsilon
°C	Degree Celsius
λ	Lambda
μ	mu
υ	Nu
h	Plank constant
Φ	Phi
π	pi
c	Velocity of light
τ	tau
θ	Theta (diffraction angle)

List of Tables

S. No.	Caption	Page No.

List of Schemes

List of Figures

Chapter 1

Introduction

- The chapter contains an insight of thesis and brief idea about the nanomaterials and their wide application.

- The chapter emphasizes the different ways of solar water-splitting, the fundamentals of semiconductors, and their use in photoelectrochemical water-splitting.

- It contains the factors which are affecting the PEC water-splitting performance and strategies to enhance the performance of photoelectrode in PEC water-splitting.

1.1 Nanoscience and Nanotechnology: Historical Background

The word 'Nano' is a Greek prefix that means tiny or something very small and portrays one billionth (10^{-9} m) of a unit. Hence, the class of materials which have at least one dimension in the nanometer range is called 'Nanomaterials'. The study, manipulation, and engineering of the materials on the nanomaterial scale are related to nanoscience, whereas the use of nanoscience and nanomaterials is allied to nanotechnology.[1] The term 'nanometer' was first used by Richard Adolf Zsigmondy in 1914.[2] On December 29 of 1959, Richard Feynman delivered a talk at the yearly American Physical Society meeting, entitled "There's Plenty of Room at the Bottom: An Invitation to Enter a New Field of Physics". Through the speech, he established the groundwork of Nanoscience and Nanotechnology. In this talk, Feynman explained that the laws of nature do not limit our ability to work at the atomic and molecular levels, but rather it is a lack of appropriate equipment and techniques that limit this.[3] Through this, the concept of modern technology was seeded. Due to this, he is often considered the father of modern nanotechnology. The first person who used the term nanotechnology in 1974, is Norio Taniguchi. Norio Taniguchi stated: ''nano-technology mainly consists of the processing of, separation, consolidation, and deformation of materials by one atom or one molecule.[4]

The applications of nanoscience and nanotechnology are started away before the concept was formally defined. One of the early contributors in this field of nanoscience was James Clerk Maxwell, a Scottish scientist with mathematical physics (1831-1879) background. He studied chemical mixtures made up of ultramicroscopic particles or large molecules of one substance spread consistently throughout another substance, known as colloids, which included gold sols and other nanomaterials. Gold colloids and nanoparticles are the subjects of the most ancient themes of investigation. One of the most popular ancient artifacts created using colloidal gold was the Lycurgus Cup. It is a stunning decorative roman treasure from about 400 AD, made of glass containing gold-silver alloy nanoparticles, distributed such that it makes the glass appear brilliant red in transmitted light and green in reflected light (**Figure 1.1a, b**).

In 1857, Michael Faraday carried out the reduction of aqueous chloroaurate ($AuCl_4^-$) with the help of red phosphorus in carbon disulfide in a two-phase system, leading to the formation of deep red solutions of colloidal gold which is still preserved in the British Museum. The reversible color change was observed from bluish-purple to green in the colloidal gold films prepared by

mechanical compression. Graham coined the term "colloid" (derived from the French word colle) in 1861.[5-8]

Figure 1.1: Uses of the nanomaterials in prehistoric times (a) The Lycurgus Cup, and (b) Michael Faraday's gold colloid preserved in Royal Institution (http://www.thebritishmuseum.ac.uk)

1.2 Nanomaterials: Brief Overview

1.2.1 Uniqueness of Nanomaterials

Nanoscale materials exhibit properties that are distinct from those of their bulk counterparts. This distinct nature of nanomaterials and their physical, optical, chemical, mechanical, magnetic, and electrical properties can be ascribed mostly to two principal factors. First, the confinement effect which causes discrete energy levels a rise in the bandgap and second, the high surface to volume (S/V) ratio. With decreasing in particle size, S/V ratio increases with increase in surface atoms. The details about both the factors are given below.

The nanoscale materials have different electronic configurations than their bulk counterparts and exhibit distinct electrical and optical properties. Nanomaterials link between the bulk materials and the single atom. Hence, the nanomaterials exhibit distinctly different properties than the respective bulk part. The special properties of the nanomaterials are attributed due to two factors; the quantum size effect and surface to volume ratio.[9] Nanoparticles in the range of 1-10 nm length scale, are called quantum size nanoparticles and they show unique and special properties. These nanoscale particles show important quantization effects that arise from the strong

quantum confinement of electrons and holes in the nanocrystals. The term 'quantum confinement' deals with the energy of electrons and holes which are bound due to the columbic interaction or different polarity and named excitons. The strongest quantum confinement occurs when the radius of nanoparticles is less than the Bohr radius of the exciton. When charge carriers are confined by potential barriers to small regions of space where the confinement dimensions are beneath the de Broglie wavelength of these charge carriers, a pronounced quantization effect is observed.[10] Moreover, quantum confinement leads to the discrete energy level of electronic states, while the continuous energy bands succeed in the bulk material.[11, 12] The formation of discrete energy levels can recall such as; when two atoms are bought together, the formation of molecule takes place and the energy level divided into two levels due to the perturbation in the energy level of each atom. In the molecule, the energy levels are termed as the highest occupied molecular orbital and lowest unoccupied molecular orbitals. When the larger numbers (N) of atoms come to close proximity then the number of energy levels increases, and decreasing trend in energy differences occurs between the filled orbitals and empty orbitals. In the bulk, the empty and filled states form a separated continuum i.e. conduction band and valence band. In the case of quantum size particles, the energy levels within the empty and filled states remain discrete. Unlike the continuous energy levels found in bulk materials, the confining nanoscale dimension of the materials makes the energy levels discrete.[13] This effect is defined as a quantum size effect, which is described in **Figure 1.2**.
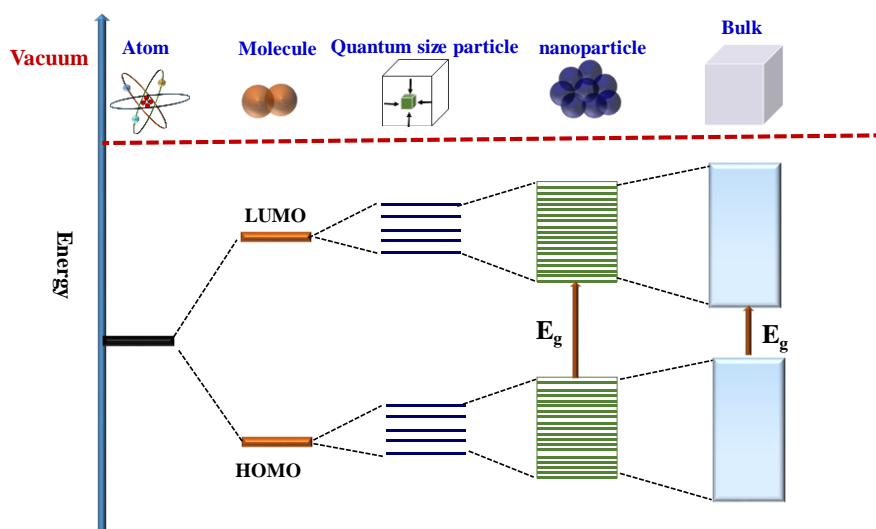
Figure 1.2: Electronic band structure of quantum size particles, nanoparticles, and bulk materials.

From **Figure 1.3,** the reduction in the confining dimension has caused the energy levels to be discrete, which increases the band gap, leading to an increase in the band gap energy.[14] The shift in the energy from the position of bulk can be obtained by the formula $E = n^2h^2/8ma^2$, where a = diameter of the particle, m = effective mass, h = Plank's constant, and n = principal quantum number. The simplest model for that is the quantum dot, which is a particle in a sphere model, assuming that the nanocrystal is a sphere. In quantum dots, electrons are confined at a particular point in space. A quantum dot can be realized when the electronic state of the dot feels the discontinuous nature at the edge of the material. It is evident from this formula that the energy is inversely proportional to the size of the particle, which leads to the striking change in the properties that are dependent on the size and shape of the particles, such as electrical, mechanical, thermal, optical, and magnetic properties.[15]
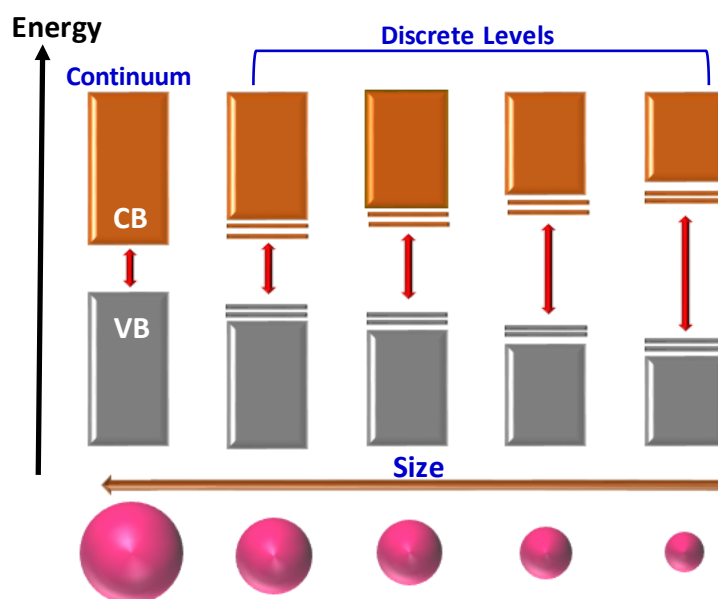
Figure 1.3: Discretization of electronic energy levels (quantum size effect) with the variation in size.

Secondly, the nanomaterials have high surface to volume ratio than the bulk materials. With the increase of the surface to volume ratio, nanomaterials have more active atoms on the surface which leads to more adsorption, more adhesion, storage capacity, and higher catalytic

activity than bulk materials. At the same time, due to more surface-active atoms, the chemical reactions occur fast than in the bulk part. So, it indicates that the inert bulk materials which are present in nature become reactive when they are brought into the nanoscale regime. Therefore, nanomaterials are potentially used for chemical reactions, catalytic reactions, sensing, detection, adsorption, etc.

1.2.2 Dimensionality of Nanomaterials

Depending on the dimension, the nanomaterials are categorized into four type namely zero-dimensional (0D), one-dimensional (1D), two-dimensional (2D), and three-dimensional (3D). In 0D nanomaterials, all dimensions (x, y, z) are in the nanometer regime i.e., not a dimension is greater than 100 nm. In quantum dots, electrons are confined at a particular point in space. Apart from 0D nanomaterials, 1D nanomaterials are formed when electrons are confined in two dimensions and are free to move in only one dimension of the system. Nanowire, nanotubes, nanobelts, nanorods, and nanofibers are categorized in the class of 1D nanomaterials. In 2D nanomaterials, the electrons can move in two directions of the system and be confined in one direction. Nanosheets and nanoplates are in the category of 2D nanomaterials. In 3D nanomaterials, electrons are not confined and are free to move in any direction in the systems. This class of nanomaterials includes hierarchal structures, nanocubes, nanoflowers, truncated cubes, and photonic structures.[16] The schematic presentation and FESEM images of 0D, 1D, 2D, and 3D nanomaterials are given in **Figures 1.4 and 1.5**.
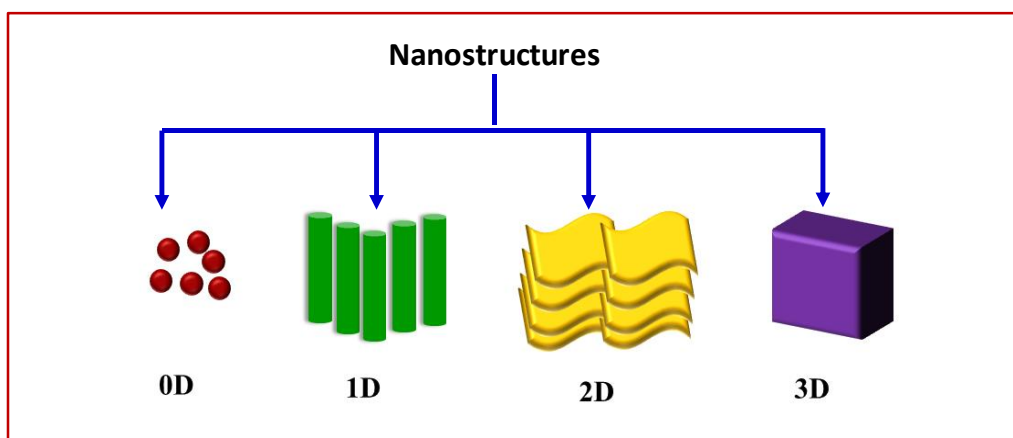
Figure 1.4: Schematic illustration of 0D, 1D, 2D, and 3D nanostructures.
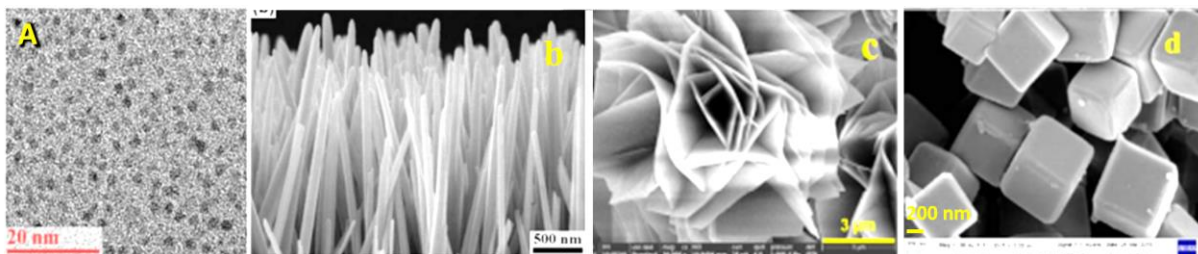
Figure 1.5: FESEM images of (a) C_3N_4-QDs[17] (b) ZnO nanowires[18] (c) Fe doped Ni(OH)$_2$/NiOOH nanosheets[19] (d) Cu_2O nanocubes.[20]

So, due to the uniqueness of the nanomaterials in terms of physical and chemical properties, they are used for various applications in broad and highly interdisciplinary areas (**Figure 1.6**). Nanostructured materials have a significant role to play in wide areas of material science, chemistry, and physics. From the technological aspect, nanostructured materials have been widely used in the construction of microelectronic circuits, which include water-splitting, lithium-air batteries, supercapacitors, hydrogen storage, etc. Li-ion batteries are extensively used in mobiles, laptops, electric vehicles, cameras, etc., as energy storage devices.[21, 22] Now-a-days, researchers are mainly focusing on efficient electrical power capacitors with high energy density because of the excessive requirement for industries and consumers. Supercapacitors or electrochemical capacitors (ECs) made up of nanostructured electrode materials exhibit high energy density storage capacity as compared to conventional batteries. Electrochemical capacitors have high-impact features, including fast charging and an extremely long lifetime. ECs have been extensively studied to complement batteries in the energy storage field when delivery of high power or uptake is requisite.[23, 24] Nanomaterials have drawn considerable attention in the generation and storage of molecular hydrogen. Molecular hydrogen is an alternative energy source that can be produced by both renewable and non-renewable resources. Renewable resources are more acceptable to produce clean hydrogen energy than non-renewable resources. Water-splitting is one of the intriguing ways compared to other renewable resources due to clean hydrogen production and cost-effectiveness.[25, 26] Now-a-days, the main task is to make a cost-effective solar cell device that has an efficient capability for solar energy conversion and can substitute fossil fuel resources. In 1998, Turner and co-workers reported that photovoltaic-photoelectrochemical configuration cells could produce hydrogen with efficiency reaching up to a maximum of 12.4%.[27] In the water-splitting

pathway, the photoelectrochemical (PEC) process is an efficient and greener way to produce H_2 using solar energy. The produced H_2 can be stored directly and it can be used for the hydrogen fuel cells. At present, the available fuel cell-based vehicles use a carbon fiber tank to store hydrogen.
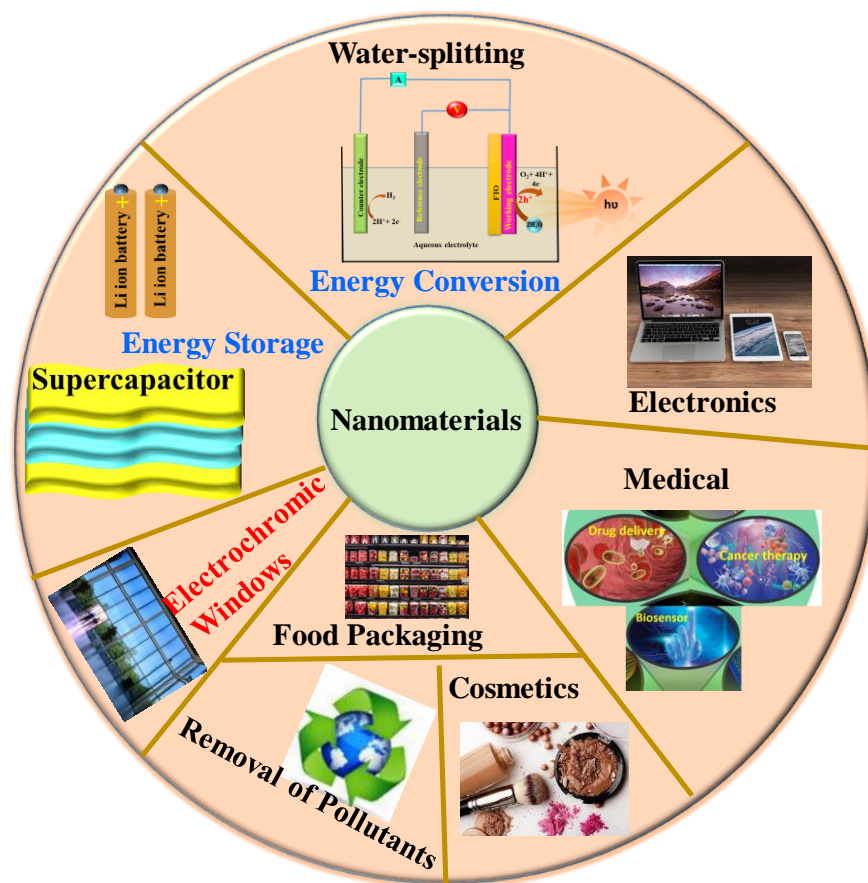
Figure 1.6: Schematic display of the potential application of nanomaterials in various fields.

Recently, nanomaterials are used to make the electrochromic (EC) layer on electrochromic devices. The EC layer generates the reversible or tunable optical properties under the simulation of a suitable voltage. The electrochemical devices have potential applications to construct smart windows for buildings, paper-like electronic devices for eye-friendly, low energy consumption displays, and anti-glare rearview mirrors for automobiles.[28]

Apart from the construction of devices, energy conversion, and storage nanomaterials are immensely used in medical science, biological systems, sensing, environmental remediation, food packaging, cosmetics, etc. Many health diseases and disorders like cancer are typical, asymptomatic, and difficult to detect and diagnose at an early stage due to the lack of effective treatment and cost-effective techniques. In this context, biosensors become a step forward in the development of cost-effective, fast, and sensitive devices for diagnosis. Nanomaterials are used for drug delivery in biological systems.[29, 30] Metal oxides and carbon-based nanomaterials can adsorb toxic materials and heavy metals.[31] The coating of nanomaterials prevents the corrosion of the metals.[32] On the other hand, they are used for chemosensing, electrochemical sensing, and PEC sensing.[33-35] Silver nanoparticles and ZnO-based nanomaterials are used for food packaging due to their antimicrobial properties.[36] Besides these, the ZnO and TiO_2 based nanomaterials are also applied for cosmetic products.

1.2.3 Synthetic Approaches of Nanomaterials

To synthesize the nanomaterials basically, two approaches are used; the top-down (physical) approach and the bottom-up (chemical) approach.

1.2.3.1 Top-down approaches

In this approach, bulk materials are gradually divided to produce nanomaterials. Top-down approaches include many methods such as mechanical or ball milling, laser ablation, arc-discharge, electrospinning, sonication, sputtering, lithography, etc.[37-44] This method is very effective to produce huge quantities of materials. But the main problem with this approach is the considerable variation in the particle size and it is not cost-effective (**Figure 1.7**).

1.2.3.2 Bottom-up approaches

The bottom-up approach denotes to the formation of material from the bottom: atom-by-atom. For the synthesis of the nanomaterials, the atoms are made from the ions followed by reduction and stabilization and accumulated to the nanostructure. Bottom-up approaches contain many methods for the synthesis of nanomaterials like chemical vapor deposition (CVD), solvothermal and hydrothermal methods, sol-gel method, reverse micelle method, electrodeposition method, soft and hard template method, combustion method, chemical reduction, and co-precipitation, etc. (**Figure 1.7**).[45-50]

Both physical and chemical methods have their own benefits. from the perspective of size, shape, composition, mass production, ease of synthesis, and cost-effectiveness, chemical methods are preferably considered better than the physical approaches.
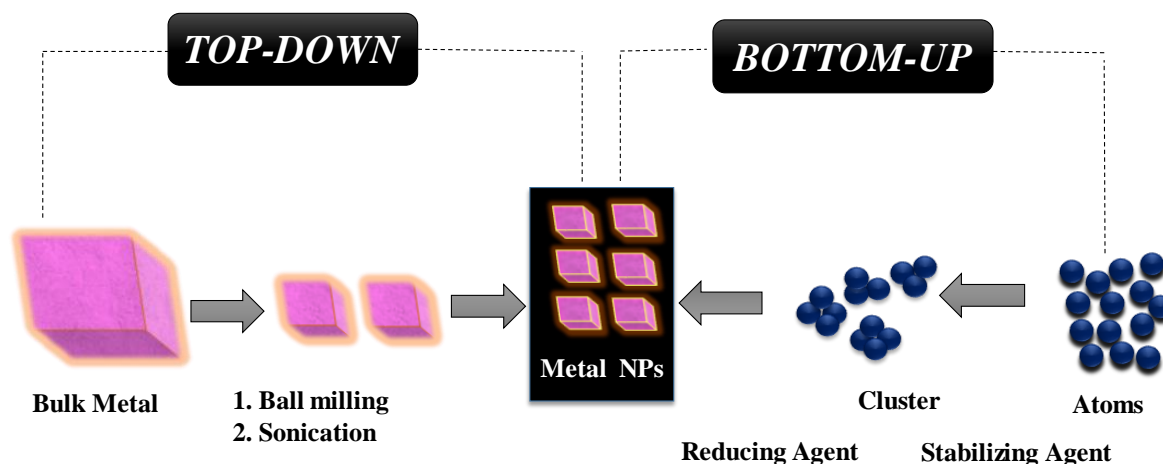
Figure 1.7: Top-down and bottom-up approaches for the synthesis of nanomaterials.

1.3 Application of Nanomaterials in Energy Conversion

Nanomaterials are used widely for energy conversion processes such as water-splitting reactions, CO_2 reduction reactions, nitrogen reduction reactions, and oxygen reduction reactions. In this chapter, energy conversion through a water-splitting reaction is discussed in detail.

1.3.1 Hydrogen Economy

Energy is the most essential prerequisite for human life and is necessary for every kind of service. It is a well-known fact that the fossil fuels such as coal, oil, and natural gas will not last forever and it is also known that their uses severely damage the earth's atmosphere. The use of fossil fuels is contributing to the inequity and disparities in human society: 10% of the population which is living in developed and wealthy countries are using half amount of the primary energy while the poorest 25% of mankind consumes less than 3% of the global energy supply.[51] For all these reasons, fossil fuels should be phased out and renewable energy sources should be involved in humans' life. But sudden stop of their use is unrealistic and the lack of comparable amount of renewable energy sources would cause a ruin of world's economy. In the wait of searching for

alternative energy sources and due to the drastic exploitation of fossil fuels, we have entered an era of energy crisis. Although the energy crisis is a challenge for society we should take it as an opportunity. The energy crisis offers a chance to become more concerned about the world and nature where we are living and the society we have built. Our planet is fragile and it is strongly dependent on the human being how the energy crisis can be tackled, and the fragility can be strongly increased or decreased. In this context, Ludwig Boltzmann states "*The struggle for existence is the struggle for available energy*".[52]

In the past few decades, the hydrogen economy came to the scenario to phase out the energy crisis. At the first glance, the idea of hydrogen economy sounds simple because; (1) hydrogen is the most abundant in the universe and the third most abundant element on the earth's surface, (2) the heat produces from the combustion of molecular hydrogen with oxygen produces, and the combination of molecular hydrogen and oxygen generates electricity and heat in a fuel cell, (3) In fuel cell-powered prototype cars and internal combustion engine hydrogen can be used directly, (4) hydrogen is non-emissive for the environment and human health, whereas after burning of fossil fuels CO_2 is released which is depleting the human health as well as environment.[53, 54] Hydrogen can be produced from water electrolysis and in this context, Jules Verne published his famous novel '**The Mysterious Island**' in 1874 and said "*I believe that water will one day be employed as fuel, that hydrogen and oxygen which constitute it, used singly or together, will furnish an inexhaustible source of heat and light, of an intensity of which coal is not capable…. Water will be the coal of the future*".[55] But unfortunately, on the earth's surface, there is no molecular hydrogen (H_2) and it cannot be generated directly from water; has to be produced by using energy as well. Therefore, hydrogen is not a substitutive source of fossil fuel; it is an energy carrier. Elemental hydrogen can occur in the gas form of molecular hydrogen (H_2); it is an invisible, non-toxic, and light gas. The uncompressed hydrogen occupies 11250 L/kg at room temperature. After applying a high pressure (35.5 MPa or 350 atm) it reduces to 56 L/kg. Hydrogen liquefies at 20 K (-253 °C) and it occupies only 14.1 L/kg. Hydrogen has a higher carrier density (120 MJ/kg) than gasoline (44.4 MJ/kg). So, hydrogen can pack more energy than other commercially available fuels. The predicted cost of green hydrogen is INR 75-150/kg which is comparable with existing fossil fuels.

Currently, India is importing ~40% of energy from other countries at a cost of US$160 billion. India has a very diverse geography and due to this, it can produce 210 million tons per

annum (Mtpa) of hydrogen from wind and solar which meet 32% of Asia-Pacific's (APAC's) hydrogen demand. By moving towards a hydrogen economy, India can export hydrogen to other countries. Energy is produced in different ways such as from biomass, solar, water electrolysis, hydrolytic power, wind, photovoltaic, PEC water-splitting, photocatalytic water-splitting, and nuclear reaction. But hydrogen is a green energy carrier that is mainly produced from solar and water because solar energy is a direct, abundant, and intermittent source of clean energy, and oceans or seawater cover 96.5% of the total water reserves of our planet.[56] So, solar water-splitting is an efficient way to meet the energy demand, and the detailed discussion about solar water-splitting is given below.

1.3.2 Solar Water-Splitting

Nature accomplishes the photosynthesis process in which the water is split in the presence of sunlight and it is a highly desirable and holy grail approach for solving the crisis of energy. Solar energy is the most attractive renewable replacement for depleting fossil fuels because it is abundant, endless, and widely distributed. However, due to the diffuse and intermittent nature of solar irradiation, the generation and collection of solar energy in chemical bonds (H_2) are in demand. In presence of solar light, photoactive materials split water, and the process is named solar water-splitting. The efficient splitting of water into usable green hydrogen can become a new pathway for resolving the energy crisis of the world. To accomplish this new pathway, there could be three possible ways; photovoltaic-electrochemical water-splitting, photocatalytic water-splitting, and PEC water-splitting. A detailed discussion of these three processes is discussed in the below sections.

1.3.2.1 Photovoltaic-Electrochemical Water-Splitting

Photovoltaic-electrochemical (PV-EC) water-splitting is the most important, advanced, and powerful technique for the generation of hydrogen. The PV-EC system is a combination of a photovoltaic cell and an electrocatalyst. The PV cells work as the power source and an electrocatalyst works for water-splitting. In the PV-EC system, the two electrolyzers connect in series with the PV cell. On the other hand, the electrolyzers also connect with H_2 and O_2 gas collector compartment. The PV cell directly converts solar energy into electric energy. The PV cell is also called the solar cell because solar radiation is used to get electric energy. Photovoltaic

cells are made up of semiconductor material and when the PV cell is irradiated with high intensity solar light then the light is absorbed by the semiconductor and it generates electricity by a definite mechanism. After absorbing solar light, the semiconductor gets excited and promotes the electron from the valence band to the conduction band in the crystal system. With the excess energy, the electrons migrate randomly leaving the holes behind. These free electrons and holes play the role of generating electricity in the PV cell. The greater the intensity of the solar light and the area of the semiconductor greater will be the flow of photocurrent. The PV cell transfers the electricity to the electrocatalyst to split water.[57-59] To avoid the loss of incident light the surface of the PV cell is generally coated with an anti-reflective coating. Although the PV-EC water-splitting is greener, more efficient, long-lasting, with zero fuel cost, and doesn't have any fuel supply problem. But it is very expensive and needs a large area of land to produce a more efficient power supply. The schematic presentation of the PV-EC system is shown in **Figure 1.8**.
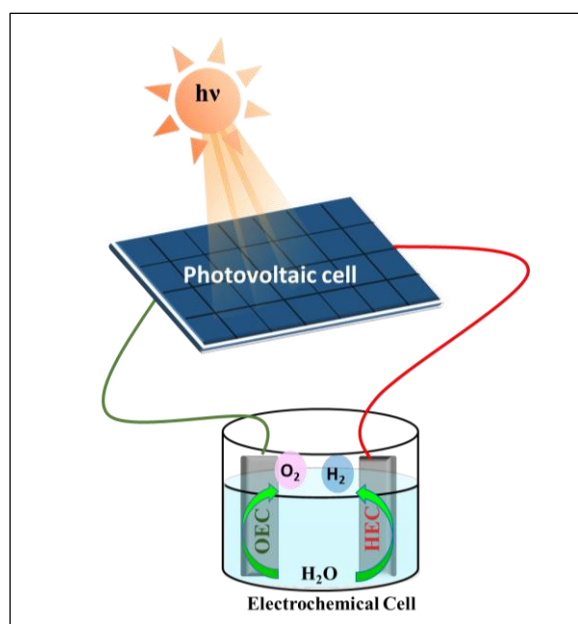
Figure1.8: A schematic presentation of the photovoltaic-electrochemical system.

1.3.2.2 Photocatalytic Water-Splitting

Photocatalytic water-splitting is favorable technology for overall water-splitting in the presence of abundant solar light and water. For overall water-splitting, the photocatalytic system can be divided into two preliminary approaches; In the first approach, a single visible light active semiconductor material or photocatalyst is used to split water into H_2 and O_2 with enough potential

to achieve the overall water-splitting.[60] The main disadvantage of this approach is the fast backward reaction of the produced hydrogen and oxygen instead of the separated liberation. On the other hand, the other approach is a two-step photoexcitation mechanism using two different photocatalysts and the so-called Z-scheme. The Z-scheme photocatalysis is inspired by nature, a more convenient, and useful approach to split water because the Z-scheme photocatalyst can cover the whole range of visible light, and the evolution of H_2 and O_2 remain separate.[61, 62] Furthermore, powdered photocatalyst systems are beneficial for wide applications of solar water-splitting because of their easiness and cost-effectiveness. But the main issue is the low efficiency due to the generation of H_2 and O_2 on the single electrode surface. It requires an external high-cost process to separate them and to avoid back reaction.
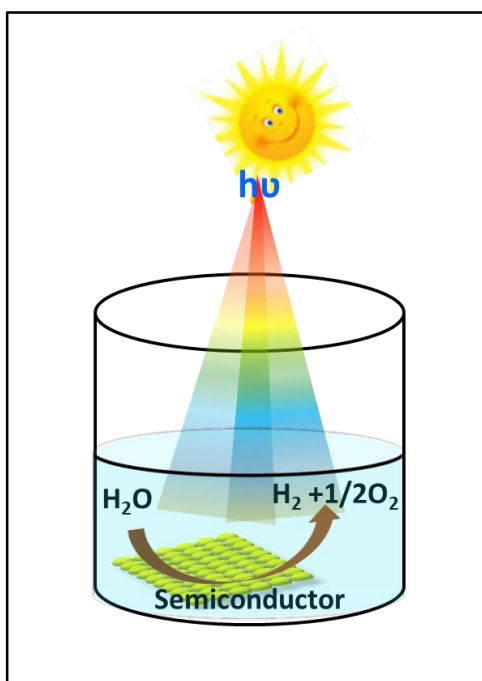
Figure 1.9: A schematic display of the photocatalytic system.

The basic mechanism of photocatalytic water-splitting can be explained in a few steps; initially, the photons fall on the surface of the photocatalyst if the energy of photons is higher than the bandgap of the photocatalyst then the generation of charge-carriers occurs. The generated charge carriers participate in the overall water-splitting reaction.[63, 64] The efficiency of the water-splitting depends on the bandgap and the alignment of the conduction band minima and valence

band maxima with the redox potential of water. Along with this the quick generation and separation of charge carriers is a key factor in choosing an efficient photocatalyst to achieve the successful splitting of water. A schematic display is given in **Figure 1.9**.

1.3.2.3 Photoelectrochemical Water-Splitting

Among the various H_2 production techniques, photoelectrochemical water-splitting (PEC) is an effective and greener method to produce renewable hydrogen energy by converting solar energy to chemical energy. In a PEC water-splitting reaction, the semiconductor material is used that acts as a light absorber and energy converter because the energy by light itself is not sufficient to drive the electrolysis of water. In the PEC cell, the two half-cell reactions take place simultaneously at two different electrodes, and the products; H_2 and O_2 are evolved separately. At the surface of the photoanode, the oxidation of water into O_2, and at the surface of the photocathode, reduction of water into H_2 takes place. The PEC cells are different from conventional electrolytic cells from a structural aspect. In the PEC cell, the photoelectrode is illuminated through an optically transparent window. In the PEC system main component is the photoactive semiconductor which is used as a working electrode either as a photocathode or photoanode. To complete a cell configuration, the counter electrode and reference electrodes are required. The counter electrode may be an inert metal that is attached with an electric wire and both the electrodes should be immersed in the electrolyte. A reference electrode may be an Ag/AgCl or calomel electrode which is also the desired part to exactly determine and controlling the potential of the working electrode, without passing the current. In presence of reference electrode, iR drop (potential drop due to the solution resistance) is negalizable between working electrode and reference electrode. In an ideal case, water- splitting can be carried out under unbiased conditions in presence of the above-mentioned components of a PEC device that are required to transform water and solar energy into H_2 and O_2. However, to proceed water-splitting reaction an extra bias is required. Besides these, a few precautions should be undertaken while constructing the PEC system. Working and counter electrodes must be placed apart from each other to avoid any contamination with the reactants/intermediates of the other electrode and to avoid the backward reaction. Therefore, to prevent the crossover of gaseous products a membrane can be used, which directly allows the evolution of H_2 and O_2 into their separate counterparts. A PEC cell has to fulfill several criteria for the application; (a) arrangement of photoelectrodes, (b) penetration of light to the photoelectrodes

through the cell, (c) resistance to corrosive electrolytes, (d) compulsion of continuously feeding of electrolyte, and (e) a membrane to uphold the evolved gases separated. [65-67]

The main concern about the PEC system is the improvement of efficiency of the photoactive material to attain the 10% of energy conversion. The 10% of energy conversion is the threshold for the commercialization of the PEC cell. In 1972, the pioneered work was executed by Honda and Fujishima using TiO_2 for the PEC water-splitting reaction but the efficiency of this system was very low (<1%).[68] So, to attain the threshold efficiency, an efficient PEC cell is highly required. An efficient cell relies on the inexpensive photoactive material that can fulfill the possible requirement of the ideal photoelectrode; (i) it should have strong light absorption in the entire solar spectrum, (ii) under dark and illuminated conditions, photoactive material should be highly chemically stable in aqueous electrolyte (iii) proper band edges positions for evolutions of H_2 and O_2, (iv) kinetic over-potentials should be low; and finally (v) at the interface of semiconductor/electrolyte the charge transfer must be proper for water-splitting. The PEC technology is an intermediate technique in PV and photocatalysis (PC) technology from the perspective of cost and efficiency. A schematic display is given in **Figure 1.10**.
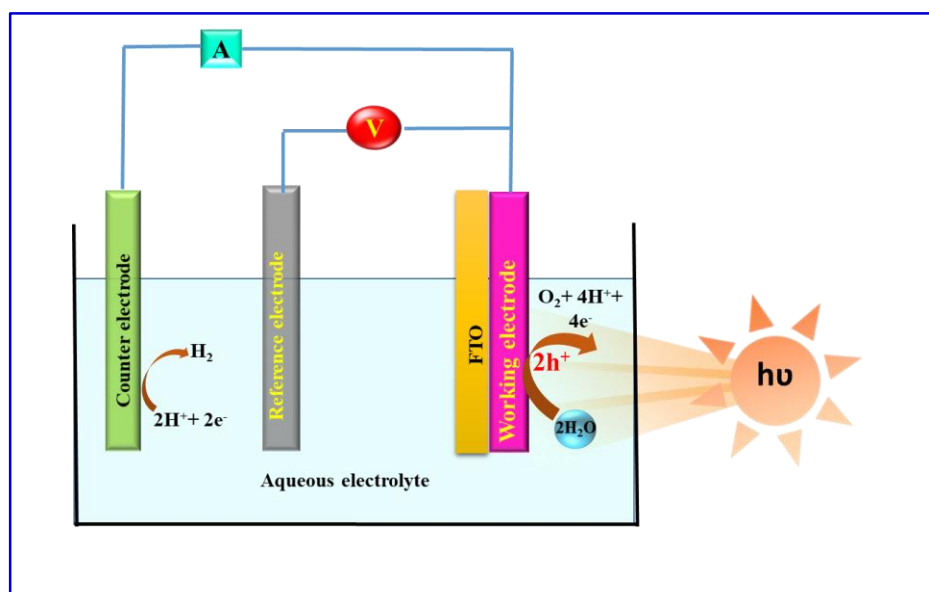
Figure 1.10: A schematic presentation of the PEC cell.

1.4 Semiconductor Fundamentals

According to molecular orbital theory when the molecular orbitals of the various atoms come to close and interact then they split into bonding and antibonding energy levels. The discrete sets of the energy levels form a continuum band called an energy band. Corresponding to bonding and antibonding energy levels the highest occupied (HOMO) and lowest unoccupied molecular orbitals (LUMO) are formed which are named valence band and conduction band, respectively. The difference between these two energy levels is termed bandgap energy and for the semiconductor, the bandgap energy lies in the range of 1-4 eV. According to Pauli's exclusion law, the maximum number of electrons in an energy level is 2N, where N is the energy level in a band. At 0 K, the highest electron occupied level in a semiconductor is the Fermi level. All the orbitals are filled below the Fermi level of semiconductor and above the Fermi level, all orbitals remain vacant. In the intrinsic semiconductor, the Fermi level is located in the forbidden energy state and it shows very poor conductivity. So, to enhance the conductivity of intrinsic semiconductors an intentional chemical impurity can be introduced and termed an extrinsic semiconductor. In an extrinsic semiconductor, 90% of electrons are contributed due to the external impurity and only 10% of electrons are present due to the covalent bond breaking after getting thermal energy.[69-73] In the case of the metal conduction band and valence band get overlap, whereas the bandgap energy lies > 4 eV in the insulator (**Figure 1.11**).
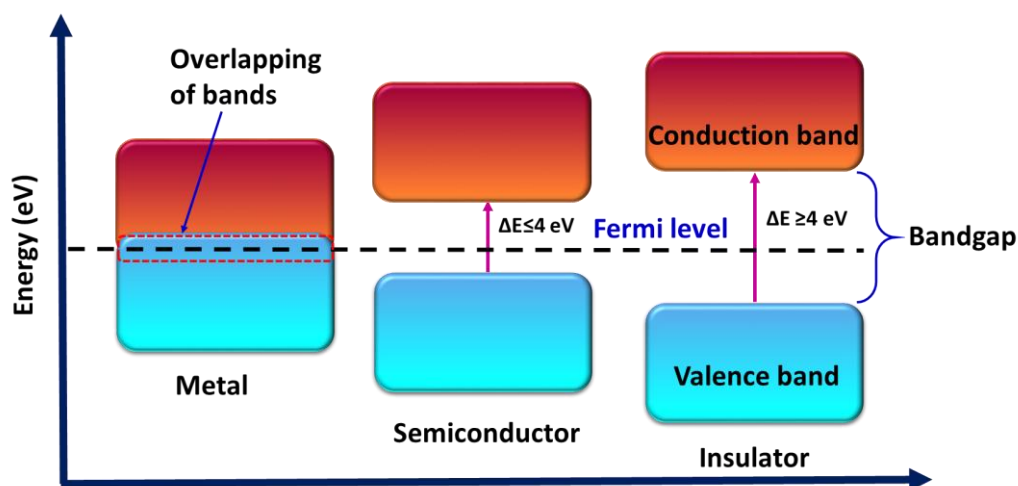
Figure 1.11: Type of materials based on the energy gap between valence and conduction band

According to the type of doping and position of the Fermi level, the extrinsic semiconductor can be divided into two categories: p-type semiconductor and n-type semiconductor. In a p-type semiconductor, the Fermi level positioned near the valence band edge acts as the acceptor level, and electrons are the minority charge carriers. On the other hand, the Fermi level located near the conduction band edge behaves as the donor level, and holes are the minority charge carriers. The schematic view of extrinsic semiconductors and intrinsic semiconductors is given below (**Figure 1.12**):
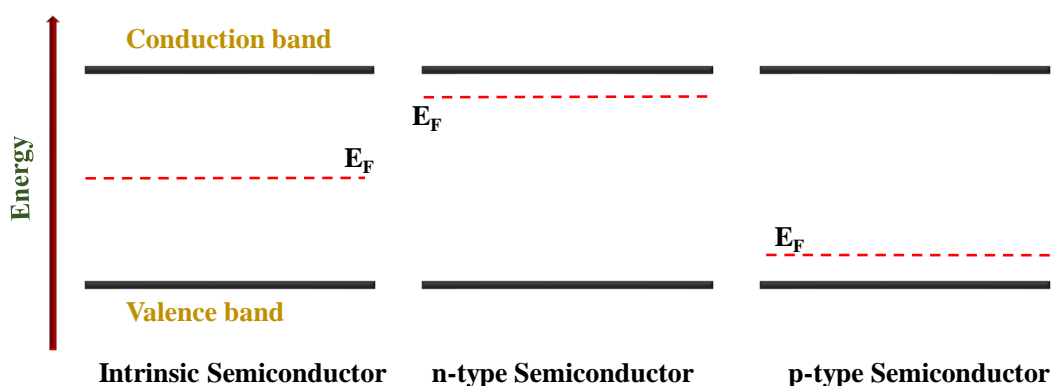
Figure 1.12: The energy levels in intrinsic and extrinsic (n-type and p-type) semiconductors, i.e., valence band (E_{VB}), conduction band (E_{CB}), and Fermi level (E_F). The energy gap between the E_{CB} and E_{VB} is the band gap (E_g) of the semiconductor.

1.5 Key Features of Photoelectrodes

Semiconductor materials are extensively used in solar water-splitting as a photoelectrode and an efficient photoelectrode should have some key features which are discussed in the below sections.

1.5.1 Potential Requirement and Bandgap

Under standard conditions, the conversion of one molecule of water (H_2O) into H_2 and ½O_2 is associated with the 237.2 kJ mol^{-1} of Gibbs free energy change which corresponds to an electrolysis cell voltage of 1.23 eV. To drive the PEC water-splitting reaction, the photoelectrode must absorb enough light to make its electrode potential higher than 1.23 V, so that the water molecule can be split and O_2 and H_2 will be produced. If the photoelectrode is an n-type

semiconductor, then a water oxidation reaction takes place on the surface of the photoanode. The oxidation reaction of water is kinetically sluggish, so other than the threshold electrode potential (1.23 V) other energy losses are taken into account. Especially, the extra potential required for the charge transfer at the interface of electrode/electrolyte, due to the charge separation, and energy loss due to the ionic conductivity of the electrolyte. So, accordingly, the required minimum energy or bandgap of a photoelectrode is given ideally from 1.9-2.4 eV for PEC water-splitting.

$$Eg_{min} = \eta_{trans} + \eta_{sep} + V_{min}$$

So, to generate the charge carriers in the photoelectrode, the energy of light should be greater than the bandgap of the photoelectrode.[74, 75]

Furthermore, the intensity of the solar spectrum falls rapidly below 350 nm, so the upper limit of the required bandgap of a semiconductor should be 3.5 eV. For practical cases, looking at the solar spectrum the total solar photon flux covers the range in wavelength from 680 nm-354nm (1.8 eV-3.5 eV). In this range, based on the semiconductor material, solar spectrum, and various losses the maximum efficiency is investigated 27.5% of total solar photon flux.[60] A photoelectrode can generate 14.5 mA/cm^2 photocurrent density and have 17.8% solar-to-hydrogen (STH) efficiency with a bandgap of 2.0 eV which can exceed the desired STH efficiency (10%) for practical application.[76] The relation of photocurrent density (mA/cm^2) and % STH efficiency with bandgap is shown **in Figure 1.13**.
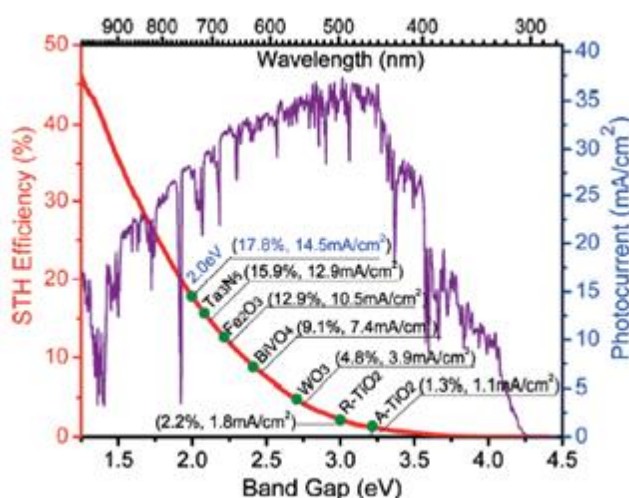
Figure 1.13: Relation between theoretical maximum solar-to-hydrogen (STH) efficiency and the photocurrent density of photoelectrodes with the band gap under AM 1.5 G irradiation (100 mW cm^{-2}).[76]

1.5.2 Band Edge Position and Redox Reaction

Besides the bandgap, another factor which is band alignment has to be considered for the PEC water-splitting. The most fundamental requirement for the band level is that the conduction band should be more negative than the reduction potential of H^+/H_2 and the valence band must be more positive than the water oxidation potential (H_2O/O_2). Hence, the band edge positions must straddle with the redox potential of water (**Figure 1.14**).[77]
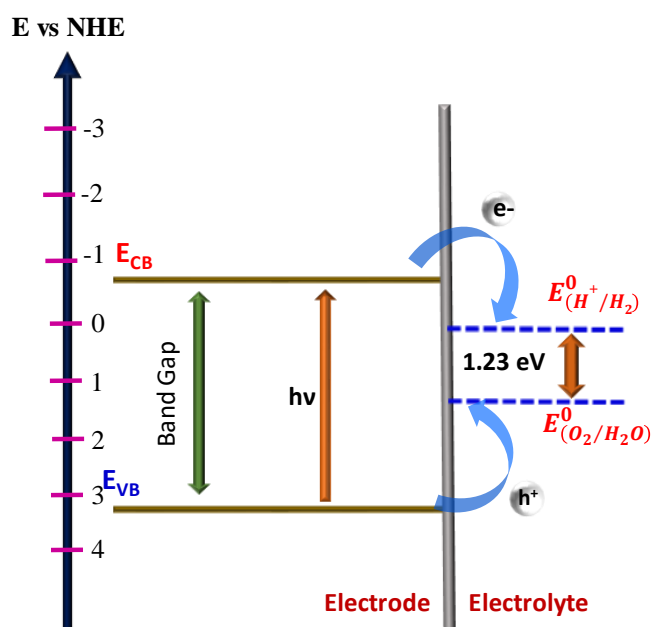
Figure 1.14: Ideal semiconductor for overall water-splitting under irradiation with absolute energy scale and E^0 (O_2/H_2O) and E^0 (H^+/H_2) represents the oxidation and reduction potential for (O_2/H_2O) and (H^+/H_2) redox couple, respectively.

The redox reaction in different media is shown below:

In acidic electrolyte (pH=0), the photo-generated holes oxidize water molecules into oxygen and protons, at the anode surface (oxygen evolution reaction):

$$2H_2O_{(liq)} \rightarrow 4H^+ + O_{2(gas)} + 4e^- \quad E^0 = 1.23\ V\ vs.\ NHE\ldots\ldots.1$$
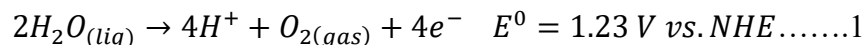
The immigration of electrons and H^+ ions towards the cathode occurs simultaneously through the external circuit and electrolyte, respectively. Hydrogen gas evolved at the surface of cathode due to the reduction of protons by the electrons.[78]

$$4H^+ + 4e^- \rightarrow 2H_{2(gas)} \quad E^0 = 0 \; V \; vs. NHE \ldots\ldots\ldots.2$$
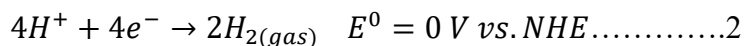
At high pH (pH=14), the redox reaction can be written as:

Oxygen evolution reaction (OER):

$$4OH^-_{(aq.)} \rightarrow 2H_2O_{(liq)} + 4e^- + O_{2(gas)} \; E^0 = -0.401 \; V \; vs. NHE \ldots\ldots.3$$

Hydrogen evolution reaction (HER):

$$2H_2O_{(liq)} + 2e^- \rightarrow H_{2(gas)} + 2OH^- \quad E^0 = -0.828 \; V \; vs. NHE \ldots\ldots.4$$
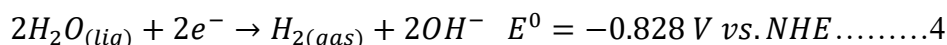
So, the overall water-splitting reaction may be written as follows:

$$2H_2O_{(liq)} + h\vartheta \rightarrow O_{2(gas)} + 2H_{2(gas)} \quad \Delta E^0 = -1.23 \; V \; vs. NHE \ldots.5$$
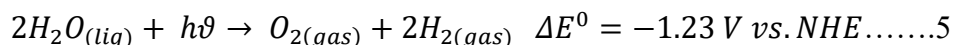
Some semiconductors are capable to reduce water, but not oxidize and vice versa. So, in this condition, extra bias is required to complete the water-splitting reaction and the onset potential of the reaction gets shifted to a higher potential region.[78]

1.5.3 Mechanism at Semiconductor/Electrolyte Interface

It is worth noting that the PEC water-splitting reaction happens on the interface of the semiconductor-electrolyte interface. So, it is necessary to understand the reaction mechanism of the PEC water-splitting at the interface. When a semiconductor is dipped into the electrolyte an interface is formed at the junction of the semiconductor-electrolyte. In semiconductor side, a space charge layer is formed and in electrolyte side, the Helmholtz (inner side) and Gouy Chapman layer (outer layer) are formed. The Helmholtz layer contains the adsorbed ions, trapped electrons in surface states, and oriented water molecule dipoles and it is independent of the nature of the solid photoelectrode. Next to the Helmholtz layer, there is a Gouy-Chapman layer which has the lowest potential among these three layers. It contains few cations and numerous anions. The thickness of the space charge layer and Gouy Chapman layer decreases with the increasing concentration of charge carriers in the semiconductor and electrolyte. The space charge layer for n-type semiconductors is divided into three regions; (1) the accumulation layer, where the majority of charge carriers are accumulated, (2) the depletion layer, in this region the majority of charge carrier are depleted, and (3) inversion layer, where the minority charge carriers move from bulk and accumulated. All these three layers belong to the space charge layer and build up in different bias and electrolyte conditions but they do not develop at a time (**Figure1.15**).[79]
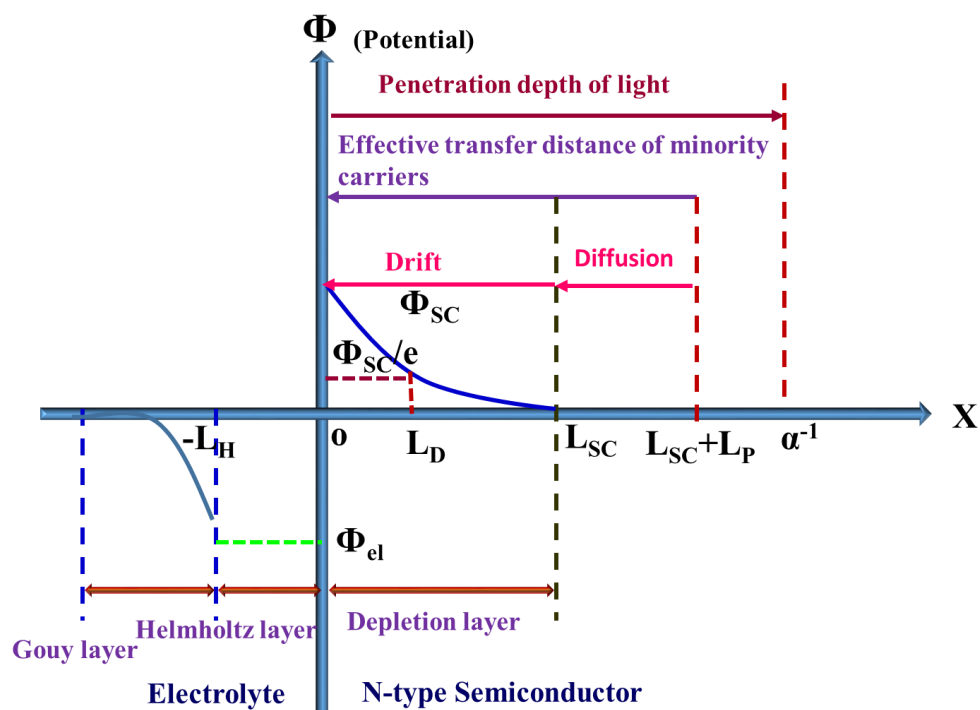
Figure 1.15: Structure of a semiconductor/electrolyte interface. Here, ϕ_{el} depicts the potential drop within the Gouy layer, ϕ_{sc} depicts the potential drop within the depleted layer, α is the optical absorption coefficient of the photoelectrode, L_{SC} is the width of the space charge layer, L_D depicts the Debye length that can be regarded as the characteristic length of potential attenuation (ϕ_{sc}), and L_p illustrates the minority carrier diffusion length.

Initially, the Fermi level (E_F) of the semiconductor and chemical potential/redox potential (E_{redox}) of electrolyte lies at different energy levels and the difference is called barrier height (V_{ph}). When the semiconductor is in contact with the electrolyte, to attain the thermodynamic equilibrium, the redistribution of charge occurs through the interface between the semiconductor and electrolyte until the equilibrium is reached. When the Fermi level of semiconductor and redox potential of electrolyte reaches the same level then the band bending takes place inside the semiconductor. In an n-type semiconductor, the Fermi level is located between the conduction band edge of the semiconductor and the redox potential of water. So, to attain the equilibrium,

electron transfers from the semiconductor to the electrolyte. Hence, there will be the accretion of the positive charge on the side of the semiconductor i.e. in the space charge layer, and the negative charge on the side of the electrolyte. Due to the electron transfer phenomena, the electric field is generated at the interface of semiconductor/electrolyte which results in the formation of band bending. The degree of band bending depends on the potential difference between the Fermi level (E_F) of the semiconductor and the redox potential of the electrolyte (O_2/H_2O). The band bending is a barrier to the recombination of charge carriers.[77, 79-82] The band energetics of the semiconductor/electrolyte interface is shown in **Figure 1.16.**
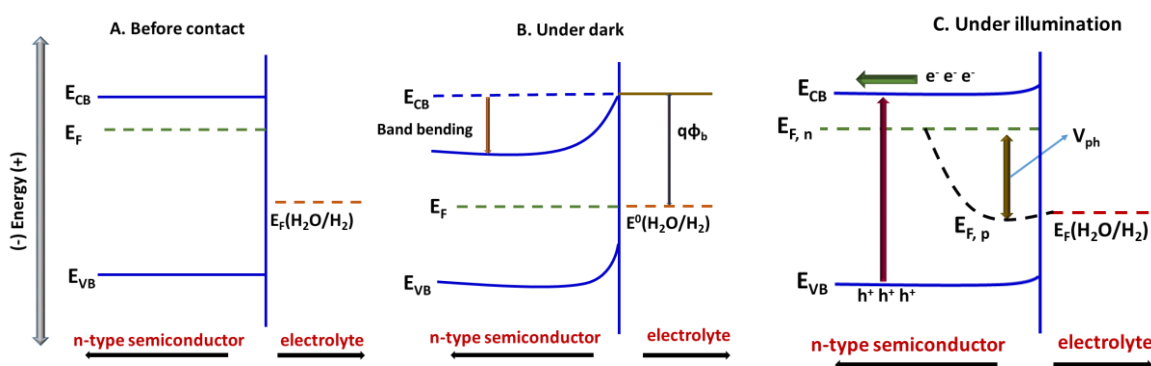
Figure 1.16: A schematic representation of the band energetics of a semiconductor/electrolyte contact is shown in three cases: In the dark; (A) before equilibrium, (B) after equilibrium between the two phases ($q\Phi_b$ = the barrier height), (C) in quasi-static equilibrium under steady-state illumination ($E_{F,n}$ = electron quasi-Fermi level, $E_{F,p}$ = hole quasi-Fermi level. The V_{ph} = photovoltage is determined by the difference between $E_{F,n}$, and $E_0(H_2O/H_2)$).

Now, under steady-state illumination, the Fermi level of the semiconductor is splatted into the quasi-Fermi level of hole and electron. The quasi-Fermi level is basically an account of the electrochemical potential of either electrons or holes at a time under illumination conditions. Under no net current flow, the degree of quasi-Fermi level splitting refers to open circuit potential or photovoltage (V_{oc}) and can be measured for a PEC system. The generated photovoltage at the interface of semiconductor/electrolyte determines the PEC reactions that are governed by the system. PEC water-splitting is not possible unless the developed photovoltage exceeds 1.23 V under unbiased conditions. The rate of hole transfers from semiconductor (n-type) to electrolyte depends on the concentration of holes at the semiconductor surface and the driving force for the

transfer of holes to the electrolyte is depicted by the energy difference between the valence band edge and the redox level of the species presents in the electrolyte (depending on the pH).[83-86]

1.5.4 Stability of Photoelectrode in Electrolyte

The stability of photoelectrode is the main and crucial factor for PEC water-splitting. The material should not corrode, dissolve, and reversibly change during the PEC water-splitting reaction. The main origin of the instability of the photoelectrode in an aqueous solution is that the semiconductor undergoes self-oxidation and reduction by photogenerated charge carriers under illumination rather than taking part in the desired redox reaction i.e. photo corrosion. The stability of the photoelectrodes depends on the rate of the charge transfer for the aimed electrochemical reaction in the semiconductor-electrolyte interface. Mostly the visible light active photoelectrodes undergo photocorrosion in a faster way compared to the UV light active semiconductors. In addition to photocorrosion, certain factors cause the instability of semiconductors in PEC water-splitting which is related to the semiconductor/electrolyte interface, dissolution of semiconductors in the electrolyte, etc. To overcome the issue related to the semiconductor/electrolyte interface, the intrinsic stable semiconductor is required. In this regard, the semiconductor should generate more photovoltage to separate photogenerated charge carriers and facilitate the water-splitting reaction. The problem of semiconductor dissolution in the electrolyte can be resolved by adjusting the pH of the electrolyte, adding the co-ion in the electrolyte, and the in-situ regeneration catalyst process.[87-89]

1.6 Efficiency of PEC cell for Water-Splitting

To measure the PEC efficiency of the PEC system multiple methods are being used which help to gain knowledge about the performance of the material. Mainly the PEC performance is divided into two main categories; (1) Benchmark efficiency (suitable for conventional reporting of stand-alone water-splitting capability) Such as solar-to-hydrogen conversion (STH) efficiency, (2) Diagnostic efficiency (to recognize the material performance) like (a) Applied bias-photon-to-current efficiency (ABPE), (b) Incident photon-to-current efficiency (IPCE), and (c) absorbed photon-to-current efficiency (APCE). All the efficiencies are calculated by the different formulas and have disparate prominence. Hence, they are unique in the PEC research. The detail about all the efficiencies is discussed below.

1.6.1 Solar-to-Hydrogen (STH) Efficiency

Solar-to-hydrogen efficiency is the most vital and useful parameter to determine the ability of PEC water-splitting of a PEC cell. It describes the PEC efficiency under zero bias conditions when the PEC cell is illuminated by broadband sunlight. STH efficiency can be commonly used to act as a reliable reference to rank a PEC device against others. A PEC cell that consists of greater than 10% STH efficiency can be used for practical application. It can be calculated by the below expression:[90-92]

$$STH = \left[\frac{|J_{sc}(mAcm^{-2})| \times 1.23(eV) \times \eta_F}{P_{total}(mWcm^{-2})} \right] \dots \dots \dots 1$$

Where J_{sc} depicts short-circuit photocurrent density, η_F depicts faradaic efficiency for hydrogen evolution, 1.23 (eV) is thermodynamic potential for water-splitting, and P_{total} depicts total power of incident sunlight.

1.6.2 Applied Bias Photon-to-Current Efficiency (ABPE)

To enhance the charge separation efficiency extra bias is needed in PEC water-splitting. ABPE is the particular interest when bias is applied for PEC water-splitting because STH cannot determine a true PEC water-splitting efficiency. It is determined with the help of the following equation:

$$ABPE(\%) = \frac{J_{ph} \times (1.23 - V_{RHE})}{P_{total}} \times 100\% \dots \dots \dots 2$$

Here, J_{ph} depicts the observed photocurrent density, P_{total} depicts the total power of incident sunlight, and V_{RHE} represents the applied potential in RHE.[90, 93]

1.6.3 Incident Photon-to-Current Efficiency (IPCE)

IPCE is the main parameter to estimate the inherent performance of the material. It is also called external quantum efficiency and refers to the photocurrent collected per incident photon as a function of the illumination wavelength. IPCE is independent of the light source which is used in the experiment. Under monochromatic illumination, photocurrent can be measured by using the following expression; [79, 94]

$$IPCE(\%) = \frac{J_{ph} \times 1240}{\lambda \times P_{mono}} \times 100\% \dots\dots\dots 3$$

Here, J_{ph} depicts the observed photocurrent density (mA/cm^2), P_{mono} is the power density achieved at a fixed wavelength (mW/cm^2), λ (nm) represents incident light wavelength, and 1240 is a number obtained when Planck's constant (6.63×10^{-34} Js) is multiplied with the charge of an electron (1.6×10^{-19} J eV^{-1}), and speed of light (3×10^8 ms^{-1}).

1.6.4 Absorbed Photon-to-Current Efficiency (APCE)

APCE is also known as the internal quantum efficiency of photoelectrode. It assesses the efficacy based on the absorbed incident photons and is responsible for the generation of charge carriers in the photoelectrode. APCE can be calculated using the below equation:[95]

$$APCE\ (\%) = \frac{1240 \times J_{ph}}{\lambda \times P_{mono} \times (1 - 10^{-A})} \times 100\% \dots\dots\dots 4$$

Here, J_{ph} depicts the observed photocurrent density, P_{mono} is the power density achieved at a specific wavelength, λ (nm) depicts the incident light wavelength, and 1240 (V $\times$ nm) is the number that is obtained when Planck's constant (6.63×10^{-34} Js) is multiplied with the electron charge (1.6×10^{-19} J eV^{-1}), and speed of light (3×10^8 ms^{-1}), A signifies the absorbance of material.

1.7 Factors affecting the overall PEC efficiency of a photoelectrode

The overall PEC efficiency of the photoelectrodes depends on many factors such as light absorption, charge carrier generation, separation, transportation, and charge carrier collection and reaction efficiency of the photoelectrode. In terms of the overall efficiency of a photoelectrode, it can be defined as:

$$\eta_{total} = \eta_A \times \eta_{CS} \times \eta_{CT} \times \eta_{CR}$$

where η_{total}, η_A, η_{CS}, η_{CT}, and η_{CR} are the overall efficiency, efficiency of light absorption, charge separation, charge transportation, and charge collection and reaction, respectively.

1.7.1 Light Absorption and Charge Carrier Generation Efficiency (η_A)

The efficiency of photon absorption depends on the thickness, morphology, dimensionality, and crystallinity of the semiconductor material. Along with these factors, the semiconductor material should have a proper bandgap to absorb the incident light and for the generation of charge carriers. The absorption of the semiconductor material can be well explained with the Beer-Lambert law (($I = I_0\ e^{-\alpha cl}$). According to this law, the absorbance is dependent on the thickness and light absorptivity (α) of the material. The light absorptivity is an intrinsic property of the material. The inverse of the absorptivity is called penetration depth (α^{-1}) and refers that how deep light can penetrate inside the material or defined as the depth at which the light is absorbed 1/e (37%) of the incident light.[76] For instance, the penetration depth of $BiVO_4$ is 100 nm at 420 nm wavelength,[96] for α-Fe_2O_3 $\alpha^{-1} = 118$ nm at a wavelength of 550 nm,[97, 98] for CdS, the $\alpha^{-1} = 62$ nm at λ=500 nm,[99] for Si, $\alpha^{-1} = 680$ nm at a wavelength of 510 nm.[100] So, to ensure more than 90 % light absorption of incident light the thickness of the semiconductor material should be ~2.7 fold higher than the penetration depth of the material.

The morphology of semiconductor material plays an important role to enhance light absorption. The vertically grown nanostructures such as nanosheets, nanorods, and nanowires help to absorb more light than the thin film. Besides these, vertically grown branched nanostructures can also enhance the light absorption of semiconductor materials. All these vertically grown nanostructured materials help to increase the multiple reflection and scattering of light inside the material which results in enhanced light absorption than planner nanostructure.[101]

Along with morphology, dimensionality is also a responsible factor for the light absorption of semiconductor materials. For instance, vertically grown 2D nanostructures have more exposed surface area to absorb the incident and reflected light than the 1D nanostructures. At the same time, the more crystalline semiconductor materials absorb more light than the amorphous ones.

The bandgap of the semiconductor material is another factor for light absorption and charge carrier generation. Ideally, the optimum range of the semiconductor bandgap should be 1.9-3.5 eV which is within the visible region. In this range, the maximum efficiency is 27.5% of the total solar photon flux.[60] So, the semiconductor having bandgap in this region can absorb more light. After light illumination on the semiconductor, the electrons get excited from the valence band to the conduction band leaving behind the holes thus the electron-hole pair generates. At absolute zero temperature, the energy states are divided into two parts; the lowest energy state is called valence

band maxima (E_{VB}), and the highest energy state is named conduction band minima (E_{CB}). The difference between a higher energy state and a lower energy state is defined as the forbidden energy state or the bandgap (E_g) of the semiconductor material. For the generation of charge carriers in the semiconductor materials, the energy of incident light should be higher than the bandgap of the semiconductor. In the semiconductor, the charge carrier density is higher at the surface than the bulk because after the penetration depth of the material light intensity is reduced ~37% to the intensity of incident radiation. So, to improve the charge carrier generation thickness of the semiconductor material should be ~2.7 fold higher than the penetration depth of the material. On the other hand, the width of the space charge region and thickness of the semiconductor material also should be equal so that charge carriers can easily take part in the redox reaction before recombination.

1.7.2 Charge Separation Efficiency (η_{CS})

After the charge carrier generation, the electrode and holes are located at the conduction band and valence band, respectively. Due to the fast de-excitation process, 90% of photogenerated charge carrier recombination takes place within 10 ns because the recombination time of the charge carrier is in order of 10^{-9} s, whereas, the required time for the chemical interaction with the adsorbed species is about 10^{-8} to 10^{-3} s.[76, 102] The effective charge separation depends on many factors such as the thickness of the semiconductor, minority charge carrier diffusion length, and width of the space charge layer. If the diffusion length of the minority charge carrier is short, then they will recombine with the majority charge carriers before reaching the interface for redox reaction. The diffusion length should be moderate which is determined by the mobility and lifetime of the minority charge carrier. The minority charge carrier comes out through the diffusion process when the width of the space charge layer can be minimized. The width of a part of the space charge layer i.e. depletion layer depends on the concentration of electrolyte. So, by increasing the concentration of electrolyte width of the space charge layer can be minimized and in this condition, charge carriers will transfer via a diffusion process.[103] Thus, charge separation efficiency can be increased by controlling these factors. At the same time, the generation of the suitable internal electric field in the semiconductor also helps to separate the charge carriers.

1.7.3 Charge Transportation Efficiency (η_{CT})

To convert the light into chemical fuel (H_2) efficient charge transfer from semiconductor to electrolyte plays a key role. The energy barrier during the transfer of the charge carrier leads to their recombination and reduces the redox capability. Thus, an applied voltage should be provided to overcome these energy barriers, which brings the additional loss of energy. To avoid the additional loss of energy, some strategies can be undertaken such as tuning of morphology, development of heterostructure, decoration of co-catalyst, adornment of the metal NPs and carbon-based materials on the surface of the semiconductor, formation of the p-n junction, tandem structure, and Z-scheme structure of the semiconductor materials. For instance, the decoration of cobalt phosphate on the surface of semiconductor material enhances the hole transfer kinetics and improves the PEC performance. Metal NPs decorated on the semiconductor materials can act as an electron sink and capture the electron from the semiconductor and can be used for the reduction of the adsorbed species and on the other hand, enhances the lifetime of the holes to oxidize the water molecules.

The minimum distance required for a photogenerated charge/carrier to travel for the effective interfacial reaction is

$$\text{Distance} = L_D + W \text{ -----------1}$$

where L_D = minority diffusion length and W = width of the depletion layer. The minority carrier diffusion length indicates the average distance that a minority carrier can travel from the site of photogeneration before recombination. The expression of L_D is given below:

$$L_D = \sqrt{D\tau} \text{------------------2}$$

where D = minority carrier diffusion coefficient, and τ = minority carrier lifetime. Interestingly, the D is correlated to the minority carrier mobility μ and the expression is shown below:

$$\mu = q\tau/m^* \text{------------------3}$$

here, m^* = effective mass of minority-carrier. From expression (1) it is clear that the charge carriers that generate within a distance (L_D+W) away from the interface, can effectively migrate and participate in the redox reaction without any recombination. Expression (2, and 3) indicates that the decrease in m^* helps to increase the minority carrier diffusion length. There are two main mechanisms which include drift and diffusion. According to equation (1), mobile minority carriers should move under a concentration gradient as well as in an electric field to cover both the diffusion layer (L_D) and drift layer/depletion layer (W).[104, 105]

1.7.4 Charge Collection and Reaction Efficiency (η_{CR})

The STH efficiency of the semiconductor materials depends on the charge collection and reaction efficiency. To increase the charge collection efficiency, the direction of the light absorption and charge carrier collection should be orthogonal or separated in direction to each other. For instance, in the conventional planner semiconductor, the direction of light absorption and minority charge collection is 180 ° or in opposite direction. So, the minority charge carriers are required a longer path to travel to come to the interface of electrode/electrolyte. Hence, the semiconductor must be thick enough to match the penetration depth (α^{-1}).[101] At the same time, the semiconductor must possess sufficient charge mobility, so that the excited minority carriers which are generated deep into the semiconductor can be diffused to the surface and can be utilized for the reaction. In the case of, non-planner geometry or vertically grown nanostructure the direction of incident light and minority charge carriers are in the orthogonal direction. Hence, the vertically grown nanostructures shorten the pathways that minority carriers must travel despite the short minority carrier diffusion length and improve the charge collection efficiency.[106] For example, vertically grown 2D-thin nanosheets, perfectly offer the possibility to facilitate the charge migration with enough light absorption simultaneously.

1.8 Selection of Suitable Photoelectrode for PEC Water-Splitting

The most important aspect of the PEC water-splitting is the selection of a suitable photoelectrode. An efficient photoelectrode should have features that are mentioned in section 1.5. Since 1972, various semiconductors are synthesized and explored for PEC water-splitting reaction which includes transition metal chalcogenides-based semiconductors, metal nitride, carbon nitride, and III-V group-based semiconductors.

1.8.1 III-VI Group Based Semiconductors

Recently, binary and ternary metal chalcogenide-based semiconductors such as Bi_2S_3, CdS, ZnS, In_2S_3, $CuIn_2S_4$. $ZnIn_2S_4$ and $CdIn_2S_4$ have immense potential for efficient PEC water-splitting.[107-113] As a fascinating member of binary metal sulfide, In_2S_3; is a visible light active semiconductor with a bandgap ~2.1-2.3 eV and a superior photo absorption coefficient. Their bandgap can be tuned from visible to NIR region by incorporating second metal, defect engineering, and doping with metal and non-metal. It shows outstanding charge carrier mobility and proper band alignment

with the water redox potential. In_2S_3 exists mainly in three different crystalline structures: α-In_2S_3 (defective cubic), β-In_2S_3 (defective spinel), and γ-In_2S_3 (layered structure), which are dependent on the synthesis temperature. Among them, β-In_2S_3 is stable at room temperature and is an n-type semiconductor with a bandgap 1.9-2.3 eV. At the same time, β-In_2S_3 has a natural defective crystal structure and due to the misvalency in between In and S atoms, an intermediate band or trapping levels form between the bandgap. The formation of the intermediate band helps to absorb the multiple photons due to that β-In_2S_3 shows good photosensitivity and broadband spectral response.[114] Along with these properties, the In_2S_3 is low toxic compared to heavy metal sulfides (PbS and HgS) which reduces the secondary pollution carried out in the photoconversion process using In_2S_3-based nanostructures.[115] To increase the carrier density, regulating the bandgap, structural and electronic properties of ternary metal sulfides such as $ZnIn_2S_4$ and $CdIn_2S_4$ are also recently getting immense interest for PEC water-splitting.

1.8.2 Limitation of Single Photoelectrode for PEC Water-Splitting

The single semiconductors have some strong limitations such as low charge carrier density, mobility of charge carriers, and sluggish surface reaction kinetics. So, for a single semiconductor, it is hard to achieve all the requisite benchmarks for PEC water-splitting. Therefore, to improve the efficiency of the photoelectrode, it is required to have some modifications through different strategies by which it can achieve theoretically estimated efficiency. For the modification of a photoelectrode, strategies can be undertaken such as (i) nanostructuring and morphology-tuning, (ii) heterostructure formation, (iii) sensitization with carbon-based materials, (iv) surface engineering by ion exchange method, (v) co-catalyst decoration, (vi) decoration with the plasmonic nanoparticle, and (vii) surface passivation, etc.

1.8.3 Strategies to Enhance the Efficiency of the Photoelectrode

1.8.3.1 Nanostructuring and Morphology Tuning

Nanostructuring and morphology tuning is a straightforward method for improving the efficiency of the photoelectrode in PEC water-splitting. The nanostructured material is more proficient than the bulk materials due to the more surface area to volume ratio which enhances the active sites for the PEC water-splitting. Another factor for the improvement of the efficiency is the morphology tuning and dimensionality. The capability of light-harvesting, charge separation, charge

transportation, and the recombination of charge carriers somewhat depends on the dimensionality or morphology (0D, 1D, 2D, and 3D) of the nanomaterial photoelectrodes for the PEC water-splitting. The 0D nanomaterials have a large surface area but it suffers from the charge migration problem due to the potentially shortened depletion width, at the same time with grain boundaries which acts as the charge recombination centers.[116] Therefore, 0D materials are not extensively used for PEC water-splitting. 1D and 3D nanomaterials as photoelectrodes are also explored in the PEC water-splitting. The main assistance of the 1D nanomaterial is the light trapping and scattering if they are vertically aligned. The light gets trapped and scattered between vertically aligned 1D nanostructure which increases the photon absorbance and helps to boost the PEC performance. At the same time, the 1D nanostructure in a certain orientation can orthogonalize the direction of the light resulting in the low recombination of charge carriers which provides rapid diffusion of the photogenerated charge carriers to the electrode-electrolyte interface by increasing the charge separation efficiency.[117] But 1D nanomaterials have a smaller active surface area which lowers the charge carrier generation due to less optical absorbance that hampers the efficiency of a photoelectrode for water-splitting. On the other hand, 3D nanomaterials have a larger exposed surface area. But it would also induce the interfacial charge recombination which leads to a decrease in the PEC activity. At the same time, it is hard to ensure which nano-units in 3D nanomaterials selectively expose their highly reactive crystal facet.[118] Hence, 2D nanomaterials, especially vertically grown 2D nanosheets are more advantageous than others and can play an important role in PEC water-splitting. At first, 2D nanosheets can harvest more light through multiple scattering and reflections of light inside the material resulting in more light-matter interaction and enhancing the optical absorbance of a photoelectrode. Secondly, by tuning the thickness of vertically grown 2D nanosheets, the position of band edges of the photocathode can be tuned. With the reduction of the thickness, the valence band edge of the photoelectrode shifts more positive than the water oxidation potential, and the conduction band edge uplifts than the reduction potential of water. From this modification, the favorable band alignment for the PEC water-splitting can be obtained. The third advantage of vertically grown 2D-nanosheets is that they can decouple the direction of light absorption and charge carrier collections at the same time. Finally, the high surface area of 2D nanosheets helps to shorten the path length of the minority charge carriers, hence improving charge collection efficiency. 2D nanosheets offer the possibility to facilitate the charge migration with enough light absorption simultaneously.[101, 119]

1.8.3.2 Heterostucture Formation

To increase the charge carrier separation, the lifetime of the charge carriers, and to improve the optical absorbance of a photoelectrode, heterostructure is the most adopted strategy. Heterostructured photoelectrode requires two or more semiconductor materials with proper band alignments. The heterostructures help to overcome the limitations of the single semiconductor that is used alone in a water-splitting reaction. The synergistic effect of the two semiconductor materials is beneficial for enhancing the PEC activity. Depending on the band offsets or band alignment heterostructure materials can be divided into three categories; straddling alignment (Type-I), staggered alignment (Type-II), and broken alignment (Type-III). The band alignment depends on the electronegativity of the semiconductor (**Figure1.17**).

In the Type-I band alignment, the bandgap of one semiconductor is completely contained in the bandgap of the other one; i.e. E_C (2) > E_V (1) and E_V (2) < E_V (1). So, in this type of heterostructure, the photogenerated charge carriers migrate only at one component resulting in the charge carrier recombination. In the case of Type-III heterostructure, the valence band edge of one semiconductor is higher in energy than the conduction band edge of the second semiconductor i.e. E_V (1) >E_C (2). Type-III heterostructure requires more driving force to charge carrier transfer. Type-II heterostructure is the most suitable and preferable band alignment for photon conversion and in this type of heterostructure, the energy of the conduction band edge and valence band edge of one semiconductor is higher than the second semiconductor i.e. E_C (1) > E_C (2) and E_V (1) >E_V (2). Type-II band alignment favors the movement of photogenerated charge carriers in the opposite direction and enhances the charge separation. The formation of heterostructures has the following advantages (1) to increase the charge separation at the interface of the two semiconductors (2) to minimize the recombination of charge carriers at the surface of the semiconductor (3) to prevent the narrow-band semiconductor from photo corrosion, and (4) to tune the optical activity of the semiconductor or simply to extend the optical band edge to increase the effective light absorption.[119-123]

The formation of heterostructure may take place between (i) a photocathode and a photoanode and (p-n heterojunction) (ii) a narrow bandgap and wide bandgap semiconductor, (iii) similar bandgap semiconductors but having different electronegativity.[124-126] From the heterostructure approach, charge carrier separation, transportation, and light absorption efficiency

of photoanode are increased, as a result, its overall PEC performance can be improved than the bare single photoelectrode system.
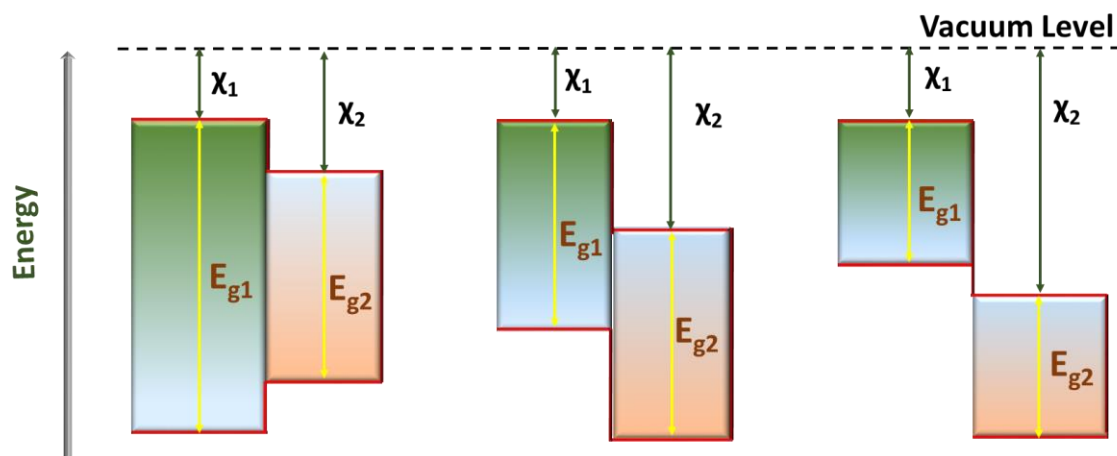
Figure 1.17: Type I, II, and III heterostructures of a semiconductor according to their band alignment design (χ represents the electron affinity and Eg denotes the bandgap energy of the semiconductor).

1.8.3.3 Sensitization with Carbon-Based Materials

Carbon-based nanomaterials such as graphitic carbon nitride (g-C_3N_4) and graphene oxide (GO) have been recognized as a visible light active semiconductor which have bandgap 2.7 eV and 2.2 eV, respectively.[127, 128] g-C_3N_4 and GO have polymeric structure, good thermal and chemical stability, low cost, and it is environmental benign. The suitable band alignment of g-C_3N_4 and GO with water redox potential attracts an interest for PEC water splitting reaction. However, due to the small surface area to volume ratio, the charge carrier transportation efficacy of photogenerated charge carriers hinders in bulk g-C_3N_4 and GO. So, the limitation can be minimized from the alteration of bulk to quantum size carbon based materials.[129-131] Carbon dots (CDs), carbon quantum dots (QDs), graphitic quantum dots (C_3N_4-QDs), and their derivative have attracted immense research interest due to their salient and promising properties which favorably improve the PEC activity of the photoelectrodes. Carbon dots (CDs) are the new class of metal-free photosensitizers, which are extensively used for sensitizing semiconductor materials. The major advantage of such carbon-based dots are as follows: these are chemically stable, earth-abundant,

have broad optical absorption, and have high charge transportation ability. Besides these properties, the additional benefits of carbon dots are: that they have metal-free frameworks, are environmentally benign, and are cost-effective.[132] CDs can be usually refers as a quasi-0D carbon-based material with a size beneath 20 nm, and it entails of two-part: one is the spherical core part which is composed by stacking of various graphene fragments in an ordered or disordered manner, and the other part is the functional group enriched surface. Mainly, the CDs absorb the UV light (200-400 nm) with extending tail in visible light due to the presence of π- π* and n- π* transition of C=C and C=N/C=O, respectively. The absorbance of CDs can be shifted in the red or NIR region, if the CDs contain the conjugated π electrons in the sp^2 skeleton and/or the connected surface functional groups/polymer chains resulting in their absorption in the long-wavelength range 500-800 nm. So, the absorbance of the carbon-based material can be tuned by tuning the synthesis method, reaction conditions, types and content of the surface-functionalized group, size of the π-conjugated domain, and the variation of carbon and nitrogen atom in the core of carbon-based material.[133]

Carbon QDs (C-QDs) are recognized for the absorption of a wide range of the solar spectrum. The absorption and emission behavior of the C-QDs is affected by the surrounding functional groups and carbon core parts. C-QDs which contains the large conjugated π-domains and few surface chemical groups, then the band gap of conjugated π-domains is considered to be the carbon-core states fluorescence center. By altering the size of the conjugated π-domains, the color-emitting of CDs can be adjusted.[134, 135] Due to the effect of Quantum confinement, the bandgap of QDs increases and generates discrete energy bands, which may lead to more favorable band energetics for the photogenerated charge carrier transportation. Functionalization of the QDs on the semiconductor electrodes helps in efficient charge separation and transportation of the charge carriers because of the band edge matching of the semiconductor and QDs.[136]

1.8.3.4 Surface Engineering by Ion Exchange Process

Ion exchange is a versatile and powerful technique to modify the surface of semiconductor materials. In an ion-exchange reaction, the ions are diffused outward from the lattice of the parent semiconductor and become solvated with the solvent. Simultaneously, the substituted ions are incorporate into the lattice of the semiconductor through inward diffusion. The cation exchange reactions are faster than the anion reactions due to the higher mobility and the smaller ionic radii

of the cations. In the cation exchange process mostly the morphology retains because the cation can spread quickly in the parent semiconductor due to the small radii and preserves the anion sublattice from deformation. However, in anion exchange cation diffusion is advanced and the cation sublattice is disordered due to the sluggish exchange of anion. Consequently, the morphology of semiconductors synthesized by anion exchange is converted due to the 'Kirkendall effect' and form hollow structures. The ion exchange reaction is controlled by kinetic and thermodynamic factors such as reaction zone, lattice structure, defects, lattice energy, size of the ion, concentration, acid-base nature of the ion, and activation energy of the ion.[137-139]

1.8.3.5 Co-catalyst Decoration

To make full use of photogenerated charge carriers, effective separation of holes from electrons and rapid charge-carrier transportation from the space charge region to the electrode/electrolyte interface are necessary steps in the PEC reaction. For most semiconductors, even if their conduction/valence band edge is properly straddle with the proton reduction potential or the oxidation potential, HER or the OER kinetics is usually so sluggish on the bare semiconductor surfaces that the reaction efficiency is fairly low for practical applications. So, to accelerate the kinetically rate-limiting step of the multi-step reduction/oxidation reaction a large overpotential is required and to reduce the overpotential. The decoration of the co-catalyst on the surface of the semiconductor is an effective way to reduce the overpotential and speed up the reaction kinetics. Most semiconductors modified with suitable electrocatalysts display higher PEC activity and shift in the onset potential than bare semiconductors. In the case of photoanode, the onset shifts at cathodic potential, and in the case of photocathode the anodic shift in onset occurs. Depending on the nature of the electrocatalyst, the connection between semiconductor and electrocatalyst may form either heterostructure (semiconductor-semiconductor) or Schottky junction (metal cocatalyst).[140] Decoration of the co-catalyst on the surface of the semiconductor must be optimized as it may block the optical absorbance of the semiconductor material if it is a non-transparent material. Sometimes, the thick deposition of the co-catalyst on the surface of the semiconductor material leads to a decrease in the PEC activity of the semiconductor. Mostly co-catalyst can absorb and reflect the light which reduces the light-harvesting efficiency of the semiconductor. So, to avoid parasitic light absorption and reflection of an electrocatalyst it should be optically

transparent, have optimum mass loading on the semiconductor, and have a light absorption spectral range that is synchronized with the semiconductor underneath.[141]

1.8.3.6 Decoration with Plasmonic Nanoparticle

To alter the distribution of electromagnetic energy and design a more efficient semiconductor sensitization with plasmonic NPs a prominent strategy for PEC water-splitting. SPR effect occurs when there is a resonance between the incident photon frequency and the collective oscillation of the conduction electrons. The resonance frequency mostly depends upon the composition of plasmonic metals, size, shape, and dielectric properties, and it can be tuned by changing the properties of nanoparticles. The SPR of metal nanoparticles increases the electric field close to the photoanode, which increases the charge carrier production rate, and improves PEC water-splitting efficiency. The improved light-harvesting ability and the effect on PEC performance of the semiconductor materials can be understood by these four mechanisms; (1) far-field light scattering, (2) near field light concentration, (3) hot electron injection (HEI), and (4) plasmon-induced resonance energy transfer (PIRET).[142]

The near-field light concentration and far-field light scattering are the radiative and light trapping processes that can enhance the light absorption of the semiconductor. In the case of the light concentration mechanism, the NPs behave as optical antennas and concentrate the incident electromagnetic field in the neighboring semiconductor resulting in an increased rate of charge carrier generation in the semiconductor. This electron-hole pair generation occurs in the vicinity of the electrode-electrolyte interface. Due to the presence of the generated electric field in the interface (depletion layer), there will be the immediate separation of the photogenerated charge carriers.[143]

The far-field light scattering mechanism is dominant for relatively larger metal NPs (size >50 nm). When the large size metal nanoparticles are decorated on the semiconductors and irradiated under back illumination, the SPR of metal NPs is convoyed by an efficient scattering of resonant photons. In this case, the incident light is scattered back by the metal nanoparticles and penetrates the semiconductor. This scattering of photons by plasmonic NPs increases the average photon path length in semiconductors resulting in an increased rate of electron-hole pair formation. The scattering effect can boost the light absorption and charge separation in the semiconductor and it is called light trapping.[144-146]

The plasmon-induced resonance energy transfer (PIRET) and hot electron injection (HEI) both are non-radiative processes. The hot electrons have higher energy compared to Schottky barrier at the interface of metal/semiconductor and can be directly injected into the conduction band of the semiconductor. The hot electrons transferred from excited plasmonic metal could have a higher thermodynamic driving force for the PEC reaction. At the same time, lower charge recombination happens as compared to those electrons that are directly photogenerated via interband transitions in the semiconductor.[147]

PIRET process requires the overlapping of surface plasmon resonance of the metal NPs and the optical absorbance of the semiconductor. A strong dipole generates by the excitation of the plasmon in the metal NPs. The plasmonic energy can be transferred from the plasmonic NPs to the semiconductor via dipole-dipole interaction in the near field leading to the generation of charge carriers in the semiconductor and due to dipole-dipole interaction the electric field intensity at the vicinity of the neighboring semiconductor. The efficiency of PIRET strongly depends on two factors: (1) the distance between the semiconductor (energy acceptor) and plasmonic nanoparticles (energy donor), (2) the overlapping of absorption spectra of energy acceptor and SPR band of energy donor.[148, 149]

1.8.3.7 Surface Passivation

Another effective strategy is surface passivation for improving the PEC performance of a semiconductor. Generally, passivation layers are applied to prevent the semiconductor surface from electrolyte corrosion thus bringing photostability to the semiconductor. The environment of the semiconductor surface changes by the decoration of the surface passivation layer and can modulate the performance of the semiconductor including inducing a shift in onset potential. The surface passivation layer can have the ability to reduce the charge carrier recombination or can reduce the catalytic overpotential. Surface passivation layers avoid the formation of the bandgap states which are responsible for the recombination of photogenerated e^- -h^+ pair. By passivation of the semiconductor surface, due to the charge distribution, the shift in band position of the semiconductor relative to the electrolyte occurs which may help to increase the charge separation rate.[150, 151]

1.9 Parameters to calculate the PEC activity of the photoelectrode

1.9.1 Onset Potential

Onset potential is the primary parameter to check the performance of a photoelectrode in PEC water-splitting. It is a point where the photoelectrode starts displaying the photoresponse. The lower onset potential is directly attributed to charge separation, transportation, and better PEC activity.[152, 153]

1.9.2 Photoconversion Efficiency

The quantitative estimation of the photoelectrode is executed by photoconversion efficiency ($\eta\%$), which is determined from the obtained LSV plot. For a photoelectrode, the photoconversion efficiency can be calculated from the following equation:

$$\eta = [J(1.23 - V_{RHE})/P_{in}]\%$$

here, J denotes the photocurrent density, V_{RHE} indicates the applied potential with respect to RHE, and P_{in} displays the intensity of the incident photons. The high photoconversion efficiency of the photoelectrode implies the high performance of the photoelectrode in the PEC water-splitting.[154, 155]

1.9.3 Charge Separation and Injection Efficiencies

To achieve the desired efficiency for the practical application, the efficiency of the charge injection from the electrode to electrolyte interface and charge separation in the bulk of the photoelectrode play a critical role. The PEC activity of a photoelectrode depends on the following factor:

$$J_{PEC} = J_{abs} \times \eta_{sep} \times \eta_{inj}$$

where J_{abs} denotes maximum photocurrent density when photons are completely converted into current (J_{abs}). In the case of photoanode, the addition of hole scavengers as the electrolyte can largely decrease the charge carrier's recombination at the surface without influencing the charge separation in the bulk of the electrode (i.e., η_{trans} could be regarded as 100%). Therefore, η_{sep} and η_{inj} can be determined as follows:

$$\eta_{sep} = J_{hole\ scavanger}/J_{abs} \quad \text{and} \quad \eta_{inj} = J_{H_2O}/J_{hole\ scavanger}$$

where J_{H2O} and $J_{hole\ scavenger}$ is the observed photocurrent density in H_2O and the presence of hole scavenger, respectively. The higher charge separation and injection efficiencies improve the PEC performance of a photoelectrode.[156, 157]

1.9.4 Mott-Schottky Analysis

Mott-Schottky (MS) analysis is generally executed in the dark condition instead of under light. The MS plot defines the specific capacitance (C_S) versus difference in the potential of the semiconductor and the solution for a photoelectrode. From the MS analysis, the charge carrier density (N_d) and flat band potential (V_{fb}) can be calculated. The charge carrier density and flat band potential of a photoelectrode can be deliberated by using the following equation:

$$^1/_{C_s^2} = \left(^2/_{e \varepsilon \varepsilon_0 N_d A^2}\right)\left[\left(V - V_{fb} - \frac{kT}{e}\right)\right]$$

where Cs indicates the specific capacitance, e indicates the electron charge, ε illustrates the dielectric constant of the semiconductor, A denotes the area of the sample, ε_0 illustrates the electric permittivity of vacuum, T denotes the absolute temperature, k indicates the Boltzmann constant, V denotes the applied potential, V_{fb} is the flat band potential. The charge carrier density can be calculated from the slope of the plot and the flat band potential can be calculated from the extrapolation of the plot on the x-axis. At the same time, the obtained slop also dictates the nature of the semiconductor. The obtained positive slop from the MS plot signifies the n-type nature of the semiconductor and the negative slope tells about the p-type semiconductor. In the case of photoanode more negative flat band potential indicates the wider space charge region which helps to increase the charge separation at the interface. Hence, the performance of photoanode material in PEC application can be enriched by increasing the carrier density and lowering the flat band potential.[158-160]

1.9.5 Photostability

The stability of the photoanode is measured by performing the chronoamperometry technique under continuous illumination in the PEC system. The photoanode is considered to be stable if it shows constant photocurrent over time, whereas if it shows degradation in the photocurrent profile, it means that the photoanode has a photocorrosion nature and is unstable. If the photoanode is stable for a long time, it is better for PEC water-splitting.[88, 161]

1.9.6 Transient Decay Time Calculation

The charge-transfer or charge-recombination behavior of the photoelectrode can be investigated by a transient decay time plot which obtains from a chopped illuminated chronoamperometry plot.

It is evident that the photoanodic transient spikes arise due to the accumulation of holes at the electrode/electrolyte interface that are not injected into the electrolyte due to slow reaction kinetics. On the other hand, cathodic spikes are generated at the time of light off that indicates the recombination of the accumulated holes in the interface with the electrons diffused from the external circuit. So, to determine the charge carrier lifetime transient decay time can be calculated by using the below-mentioned equation:

$$D = (I_t - I_s)/(I_{in} - I_s)$$

where I_t denotes current at time t, I_s the steady-state current, and I_{in} demotes the incident current spike. The transient decay time can be defined as the time at which ln D = -1.[96, 162, 163]

1.9.7 Electrochemical Surface Area

It is desirable that the observed current density is normalized by the electrochemically active surface area, not by geometric surface area as the later does not indicate the intrinsic electrochemical property exhibited by the material. The surface area has a direct relation with the active sites; hence it becomes one of the crucial parameters for catalysts to carry out catalytic reactions. It characterizes the surface area because of its sensitivity towards the actual catalyst loading. To determine ECSA, cyclic voltammetry analysis is carried out at variable scan rates in the non-faradic region. Further observed current density is plotted against scan rate, and from the slope of the curve, double-layer capacitance (C_{dl}) is determined. Further ECSA of the solid-liquid interface is estimated by the electrochemical double-layer capacitance.[164, 165]

1.10 Designed Photoelectrodes for PEC Water-Splitting

In our present study, indium-based nanomaterials are explored as a photoanode for the application in PEC water-splitting. Indium-based nanomaterials are more attractive than the extensively used CdS, Bi_2S_3, and CuS due to their stable chemical and physical property, and good photosensitivity. Here, In_2S_3, $ZnIn_2S_4$, and $CdIn_2S_4$ are chosen as a photoanode for the PEC water- splitting. In_2S_3, $ZnIn_2S_4$, and $CdIn_2S_4$ with a bandgap in the range of ~2.0-2.5 eV offer the required conditions for facilitating solar light absorption and conversion. So, with these unique properties, these are extensively explored as an excellent visible-light-active photocatalyst and can be used as a sensitizer for wide bandgap semiconductors in PEC water-splitting. Nevertheless, similar to other narrow bandgaps photoactive semiconductors, the pure indium-based semiconductors suffer from

rapid recombination of photogenerated charge carriers, especially in strong oxidizing conditions. Therefore, in our present work to overcome the problem of charge carrier recombination and to increase the PEC activity of In_2S_3, $ZnIn_2S_4$, and $CdIn_2S_4$, different strategies have been undertaken such as morphology tuning, type-II heterostructure formation, sensitization with carbon-based materials, and ion exchange method.

1. The efficiency of semiconductor depends on the efficiency of light absorption (η_A) and it may increase via morphology tuning. In this context, vertically grown nanostructures of In_2S_3, $ZnIn_2S_4$, and $CdIn_2S_4$ are aimed. Vertically grown nanopyramids and nanosheets may help to increase the light absorption efficiency. Further, η_A may enhance by the sensitization of carbon-based materials on the surface of In_2S_3 and $CdIn_2S_4$.

2. The charge carrier separation (η_A) and transportation efficiency (η_{CS}) may increase through the formation of type-II heterostructure and sensitization with carbon-based materials.

3. The charge carrier density of indium sulfide based nanostructure may enhance via ion exchange technique.

   The details of all these processes are explained in the respective chapters.

1.11 References

1. Manasreh, O., *Introduction to nanomaterials and devices. John Wiley & Sons*: **2011**.

2. Santamaria, A. *Historical overview of nanotechnology and nanotoxicology*. Nanotoxicity **2012**, 1-12.

3. Feynman, R. There's plenty of room at the bottom. *California Institute of Technology, Engineering and Science magazine*, **1960**.

4. Taniguchi, N. On the basic concept of nanotechnology. *Proc. Int. Conf. Prod. Eng. Issue PART II*, **1974**, 18-23..

5. Jellinek, J. Nanoalloys: tuning properties and characteristics through size and composition. *Faraday Discuss.*, **2008**, *138*, 11-35.

6. Thompson, D. Michael Faraday's recognition of ruby gold: the birth of modern nanotechnology. *Gold Bull.*, **2007**, *40*, 267-269.

7. Freestone, I.; Meeks, N.; Sax, M.; Higgitt, C. The Lycurgus cup-a roman nanotechnology. *Gold Bull.*, **2007**, *40*, 270-277.

8. Horikoshi, S.; Serpone, N., *Microwaves in nanoparticle synthesis: fundamentals and applications* **2013**, 1-24.

9. Murty, B. S.; Shankar, P.; Raj, B.; Rath, B.; Murday, J., *Textbook of nanoscience and nanotechnology*. Springer Science & Business Media: **2013**.

10. Mao, J.; Liu, Z. H.; Ren, Z. F., Size effect in thermoelectric materials. *npj Quantum Mater.*, **2016**, 16028.

11. Murray, C. B.; Norris, D. J.; Bawendi, M. G., Synthesis and characterization of nearly monodisperse CdE (E = sulfur, selenium, tellurium) semiconductor nanocrystallites. *J. Am. Chem. Soc.* **1993**, *115*, 8706-8715.

12. Ramalingam, G.; Kathirgamanathan, P.; Ravi, G.; Elangovan, T.; Manivannan, N.; Kasinathan, K., *Quantum confinement effect of 2D nanomaterials. In Quantum Dots-Fundamental and Applications*. IntechOpen: **2020**.

13. Ashrafi, A. *Quantum Confinement: An Ultimate Physics of Nanostructures*. Encyclopedia of Semiconductor Nanotechnology. **2011**, 1-67.

14. Rabouw, F. T.; de Mello Donega, C., Excited-State Dynamics in Colloidal Semiconductor Nanocrystals. *In Photoactive Semiconductor Nanocrystal Quantum Dots: Fundamentals and Applications*. Credi, A., Ed. Springer International Publishing: Cham. **2017**, 1-30.

15. Edvinsson, T. Optical quantum confinement and photocatalytic properties in two-, one-and zero-dimensional nanostructures. *R. Soc. Open Sci*., **2018**, 5, 180387.

16. Kebede, M. A.; Imae, T., *Low-dimensional nanomaterials*. In Advanced Supramolecular Nanoarchitectonics, Elsevier: 2019, 3-16.

17. Fageria, P.; Uppala, S.; Nazir, R.; Gangopadhyay, S.; Chang, C.-H.; Basu, M.; Pande, S., Synthesis of monometallic (Au and Pd) and bimetallic (AuPd) nanoparticles using carbon nitride (C_3N_4) quantum dots via the photochemical route for nitrophenol reduction. *Langmuir* **2016**, *32*, 10054-10064.

18. Liu, L.; Wang, H.; Wang, D.; Li, Y.; He, X.; Zhang, H.; Shen, J., Zno@ TiO_2 core/shell nanowire arrays with different thickness of TiO2 shell for dye-sensitized solar cells. *Crystals* **2020**, *10*, 325.

19. Mahala, C.; Devi Sharma, M.; Basu, M., Fe-Doped Nickel Hydroxide/Nickel Oxyhydroxide Function as an Efficient Catalyst for the Oxygen Evolution Reaction. *ChemElectroChem* **2019**, *6*, 3488-3498.

20. Basu, M.; Sinha, A. K.; Pradhan, M.; Sarkar, S.; Pal, A.; Mondal, C.; Pal, T., Methylene Blue–Cu_2O reaction made easy in acidic medium. *J. Phys. Chem. C* **2012**, *116*, 25741-25747.

21. Su, X.; Wu, Q.; Li, J.; Xiao, X.; Lott, A.; Lu, W.; Sheldon, B. W.; Wu, J., Silicon-based nanomaterials for lithium-ion batteries: a review. *Adv. Energy Mater*., **2014**, 4, 1300882.

22. Jiang, C.; Hosono, E.; Zhou, H., Nanomaterials for lithium ion batteries. *Nano today* **2006**, *1*, 28-33.

23. Abbas, Q.; Raza, R.; Shabbir, I.; Olabi, A., Heteroatom doped high porosity carbon nanomaterials as electrodes for energy storage in electrochemical capacitors: A review. *J. Sci-Adv. Mater. Dev*., **2019**, 4, 341-352.

24. Huang, T.; Jiang, Y.; Shen, G.; Chen, D., Recent Advances of Two-Dimensional Nanomaterials for Electrochemical Capacitors. *ChemSusChem* **2020**, *13*, 1093-1113.

25. Wang, F.; Shifa, T. A.; Zhan, X.; Huang, Y.; Liu, K.; Cheng, Z.; Jiang, C.; He, J., Recent advances in transition-metal dichalcogenide based nanomaterials for water splitting. *Nanoscale* **2015**, *7*, 19764-19788.

26. Li, J.; Zheng, G., One-dimensional earth-abundant nanomaterials for water-splitting electrocatalysts. *Adv. Sci. Lett*., **2017**, *4*, 1600380.

27. Khaselev, O.; Turner, J. A., A monolithic photovoltaic-photoelectrochemical device for hydrogen production via water splitting. *Science* **1998**, 280, 425-427.

28. Yang, G.; Zhang, Y.-M.; Cai, Y.; Yang, B.; Gu, C.; Zhang, S. X.-A., Advances in nanomaterials for electrochromic devices. Chem. Soc. Rev., **2020**, *49*, 8687-8720.

29. Panda, M. K.; Panda, S. K.; Singh, Y. D.; Jit, B. P.; Behara, R. K.; Dhal, N. K., Role of nanoparticles and nanomaterials in drug delivery: an overview. *Biotechnol. Adv*., **2020**, 247-265.

30. Zhang, Q.; Wu, Z.; Li, N.; Pu, Y.; Wang, B.; Zhang, T.; Tao, J., Advanced review of graphene-based nanomaterials in drug delivery systems: Synthesis, modification, toxicity and application. *Mater. Sci. Eng. C* **2017**, *77*, 1363-1375.

31. Ghasemzadeh, G.; Momenpour, M.; Omidi, F.; Hosseini, M. R.; Ahani, M.; Barzegari, A., Applications of nanomaterials in water treatment and environmental remediation. *Front. Environ. Sci. Eng.*, **2014**, 8, 471-482.

32. Sharma, V. P.; Sharma, U.; Chattopadhyay, M.; Shukla, V., Advance applications of nanomaterials: a review. *Mater. Today: Proc*., **2018**, 5, 6376-6380.

33. Shellaiah, M.; Sun, K. W., Review on sensing applications of perovskite nanomaterials. *Chemosensors* **2020**, 8, 55.

34. Chen, A.; Chatterjee, S., Nanomaterials based electrochemical sensors for biomedical applications. *Chem. Soc. Rev*., **2013**, 42, 5425-5438.

35. Zhou, Y.; Yin, H.; Ai, S., Applications of two-dimensional layered nanomaterials in photoelectrochemical sensors: A comprehensive review. *Coord. Chem. Rev*., **2021**, *447*, 214156.

36. Bradley, E. L.; Castle, L.; Chaudhry, Q., Applications of nanomaterials in food packaging with a consideration of opportunities for developing countries. *Trends Food Sci. Technol*., **2011**, *22*, 604-610.

37. Fytianos, G.; Rahdar, A.; Kyzas, G. Z. Nanomaterials in Cosmetics: Recent Updates. *Nanomaterials* **2020**, *979*, 1-9.

38. Zhuang, S.; Lee, E. S.; Lei, L.; Nunna, B. B.; Kuang, L.; Zhang, W., Synthesis of nitrogen-doped graphene catalyst by high-energy wet ball milling for electrochemical systems. *Int. J. Energy Res.*, **2016**, *40*, 2136-2149.

39. Amendola, V.; Meneghetti, M., Laser ablation synthesis in solution and size manipulation of noble metal nanoparticles. *Phys. Chem. Chem. Phys.*, **2009**, 11, 3805-3821.

40. Zhang, J.; Chaker, M.; Ma, D., Pulsed laser ablation based synthesis of colloidal metal nanoparticles for catalytic applications. *J. Colloid Interface Sci.*, **2017**, *489*, 138-149.

41. Zhang, D.; Ye, K.; Yao, Y.; Liang, F.; Qu, T.; Ma, W.; Yang, B.; Dai, Y.; Watanabe, T., Controllable synthesis of carbon nanomaterials by direct current arc discharge from the inner wall of the chamber. *Carbon* **2019**, *142*, 278-284.

42. Kumar, P. S.; Sundaramurthy, J.; Sundarrajan, S.; Babu, V. J.; Singh, G.; Allakhverdiev, S. I.; Ramakrishna, S., Hierarchical electrospun nanofibers for energy harvesting, production and environmental remediation. *Energy Environ. Sci*., **2014**, *7*, 3192-3222.

43. Wender, H.; Migowski, P.; Feil, A. F.; Teixeira, S. R.; Dupont, J., Sputtering deposition of nanoparticles onto liquid substrates: Recent advances and future trends. *Coord. Chem. Rev*., **2013**, *257*, 2468-2483.

44. Pimpin, A.; Srituravanich, W., Review on micro-and nanolithography techniques and their applications. *Eng. J.*, **2012**, 16, 37-56.

45. Jones, A. C.; Hitchman, M. L. Overview of chemical vapour deposition. Chemical Vapour Deposition: Precursors, Processes and Applications **2009**, *1*, 1-36.

46. Wu, X.; Lu, G. Q. M.; Wang, L., Shell-in-shell TiO_2 hollow spheres synthesized by one-pot hydrothermal method for dye-sensitized solar cell application. *Energy Environ. Sci*., **2011**, *4*, 3565-3572.

47. Cao, S.; Zhao, C.; Han, T.; Peng, L., Hydrothermal synthesis, characterization and gas sensing properties of the WO_3 nanofibers. *Mater. Lett.*, **2016**, *169*, 17-20.

48. Danks, A. E.; Hall, S. R.; Schnepp, Z., The evolution of 'sol–gel'chemistry as a technique for materials synthesis. *Mater. Horiz.*, **2016**, *3*, 91-112.

49. Liu, Y.; Goebl, J.; Yin, Y., Templated synthesis of nanostructured materials. *Chem. Soc. Rev*., **2013**, *42*, 2610-2653.

50. Malik, M. A.; Wani, M. Y.; Hashim, M. A., Microemulsion method: A novel route to synthesize organic and inorganic nanomaterials: 1st Nano Update. *Arab. J. Chem.*, **2012**, *5*, 397-417.

51. Balzani, V.; Armaroli, N., *Energy for a sustainable world: from the oil age to a sun-powered future*. John Wiley & Sons: **2010**.

52. Armaroli, N.; Balzani, V., The future of energy supply: challenges and opportunities. *Angew. Chem. Int. Ed.*, **2007**, *46*, 52-66.

53. Rifkin, J., *The hydrogen economy: The creation of the worldwide energy web and the redistribution of power on earth*. Penguin: **2003**.

54. Momirlan, M.; Veziroglu, T. N., The properties of hydrogen as fuel tomorrow in sustainable energy system for a cleaner planet. *Int. J. Hydrog. Energy* **2005**, *30*, 795-802.

55. Armaroli, N.; Balzani, V., The hydrogen issue. ChemSusChem **2011**, *4*, 21-36.

56. Dresp, S. R.; Dionigi, F.; Klingenhof, M.; Strasser, P., Direct electrolytic splitting of seawater: opportunities and challenges.   ACS Energy Lett., **2019**, *4*, 933-942.

57. Jia, J.; Seitz, L. C.; Benck, J. D.; Huo, Y.; Chen, Y.; Ng, J. W. D.; Bilir, T.; Harris, J. S.; Jaramillo, T. F., Solar water splitting by photovoltaic-electrolysis with a solar-to-hydrogen efficiency over 30%. *Nat. Commun*., **2016**, *7*, 1-6.

58. Khalilnejad, A.; Sundararajan, A.; Sarwat, A. I. In Performance evaluation of optimal photovoltaic-electrolyzer system with the purpose of maximum Hydrogen storage, 2016 IEEE/IAS 52nd Industrial and Commercial Power Systems Technical Conference (I&CPS), IEEE: **2016**; 1-9.

59. Lee, M.; Turan, B.; Becker, J. P.; Welter, K.; Klingebiel, B.; Neumann, E.; Sohn, Y. J.; Merdzhanova, T.; Kirchartz, T.; Finger, F., A Bias-Free, Stand-Alone, and Scalable Photovoltaic-Electrochemical Device for Solar Hydrogen Production. *Adv. Sustain. Syst*., **2020**, *4*, 2000070.

60. Kudo, A.; Miseki, Y., Heterogeneous photocatalyst materials for water splitting. *Chem. Soc. Rev*., **2009**, *38*, 253-278.

61. Ng, B. J.; Putri, L. K.; Kong, X. Y.; Teh, Y. W.; Pasbakhsh, P.; Chai, S. P., Z-scheme photocatalytic systems for solar water splitting. *Adv. Sci*., **2020**, *7*, 1903171.

62. Maeda, K., Z-scheme water splitting using two different semiconductor photocatalysts. ACS Catal., 2013, 3, 1486-1503.

63. Maeda, K., Photocatalytic water splitting using semiconductor particles: history and recent developments. *J. Photochem. Photobiol. C: Photochem. Rev.*, **2011**, *12*, 237-268.

64. Ni, M.; Leung, M. K.; Leung, D. Y.; Sumathy, K., A review and recent developments in photocatalytic water-splitting using TiO_2 for hydrogen production. *Renew. Sustain. Energy Rev.*, **2007**, *11*, 401-425.

65. Lopes, T.; Dias, P.; Andrade, L.; Mendes, A., An innovative photoelectrochemical lab device for solar water splitting. *Sol. Energy Mater. Sol. Cells* **2014**, *128*, 399-410.

66. Dias, P.; Mendes, A., *Hydrogen production from photoelectrochemical water splitting. Encyclopedia of Sustainability Science and Technology*; Meyers, RA, Ed.; Springer Science and Business Media LLC: Berlin/Heidelberg, Germany **2017**, 1-52.

67. Grätzel, M., Photoelectrochemical cells. *Mater. Renew. Sustain. Energy* **2011**, 26-32.

68. Fujishima, A.; Honda, K., Electrochemical photolysis of water at a semiconductor electrode. *nature* **1972**, *238*, 37-38.

69. Giménez, S.; Bisquert, J., *Photoelectrochemical solar fuel production. From basic principle to advanced devices*. Cham: Springer **2016**.

70. Sze, S.; Ng, K. K., *Physics and properties of semiconductors-A review*. Physics of semiconductor devices **2006**, 3.

71. Kittel, C., *Introduction to solid state physics* Eighth edition. **2021**.

72. Suresh, S., Semiconductor nanomaterials, methods and applications: a review. *Nanosci. Nanotechnol.*, **2013**, *3*, 62-74.

73. Peter, L. M., Photoelectrochemistry: from basic principles to photocatalysis. **2016**.

74. Hamdani, I.; Bhaskarwar, A., Recent progress in material selection and device designs for photoelectrochemical water-splitting. Renew. Sustain. Energy Rev., **2021**, *138*, 110503.

75. Gupta, M. S.; Baig, H.; Reddy, K.; Mallick, T. K.; Pesala, B.; Tahir, A. A., Photoelectrochemical Water Splitting Using a Concentrated Solar Flux-Assisted LaFeO3 Photocathode. *ACS Appl. Energy Mater.*, **2020**, *3*, 9002-9009.

76. Li, J.; Wu, N., Semiconductor-based photocatalysts and photoelectrochemical cells for solar fuel generation: a review. *Catal. Sci. Technol.*, **2015**, 5, 1360-1384.

77. Walter, M. G.; Warren, E. L.; McKone, J. R.; Boettcher, S. W.; Mi, Q.; Santori, E. A.; Lewis, N. S., Solar water splitting cells. *Chem. Rev.*, **2010**, *110*, 6446-6473.

78. Ros, C.; Andreu, T.; Morante, J. R., Photoelectrochemical water splitting: a road from stable metal oxides to protected thin film solar cells. *J. Mater. Chem. A* **2020**, *8*, 10625-10669.

79. Xu, X. T.; Pan, L.; Zhang, X.; Wang, L.; Zou, J. J., Rational Design and Construction of Cocatalysts for Semiconductor-Based Photo-Electrochemical Oxygen Evolution: A Comprehensive Review. *Adv. Sci.*, **2019**, 6, 1801505.

80. Jiang, C.; Moniz, S. J.; Wang, A.; Zhang, T.; Tang, J., Photoelectrochemical devices for solar water splitting–materials and challenges. *Chem. Soc. Rev.*, **2017**, *46*, 4645-4660.

81. Kim, Y. B.; Kim, J. S.; Baek, S. K.; Yun, Y. D.; Cho, S. W.; Jung, S. H.; Cho, H. K., Electrochemical surface charge-inversion from semi-insulating Sb_2Se_3 photoanodes and abrupt photocurrent generation for water splitting. *Energy Environ. Sci.*, **2018**, 11, 2540-2549.

82. Bessegato, G. G.; Guaraldo, T. T.; Zanoni, M. V. B., *Enhancement of photoelectrocatalysis efficiency by using nanostructured electrodes.* Modern electrochemical methods in nano, surface and corrosion science **2014**, 271-319.

83. Hagfeldt, A.; Graetzel, M., Light-induced redox reactions in nanocrystalline systems. Chemical reviews 1995, 95 (1), 49-68.

84. Malando S.; Fitch A. G.; Lewis N. S.; *Semiconductor/Liquid Junction Photoelectrochemical Solar Cells.* Nanostructured And Photoelectrochemical Systems For Solar Photon Conversion, World Scientific: **2008**, 537-589.

85. Bicelli, L. P., A review of photoelectrochemical methods for the utilization of solar energy. Surf. Coat. Technol., 1983, 20, 357-381.

86. Sharon, M., *The photoelectrochemistry of semiconductor/electrolyte solar cells*. Encyclopedia of Electrochemistry: Online **2007**.

87. Yang, W.; Prabhakar, R. R.; Tan, J.; Tilley, S. D.; Moon, J., Strategies for enhancing the photocurrent, photovoltage, and stability of photoelectrodes for photoelectrochemical water splitting. *Chem. Soc. Rev.*, **2019**, *48*, 4979-5015.

88. Lee, D. K.; Choi, K.-S., Enhancing long-term photostability of $BiVO_4$ photoanodes for solar water splitting by tuning electrolyte composition. *Nat. Energy* **2018**, *3,* 53-60.

89. Kuang, Y.; Jia, Q.; Ma, G.; Hisatomi, T.; Minegishi, T.; Nishiyama, H.; Nakabayashi, M.; Shibata, N.; Yamada, T.; Kudo, A., Ultrastable low-bias water splitting photoanodes via photocorrosion inhibition and in situ catalyst regeneration. *Nat. Energy* 2016, *2*, 1-9.

90. Chen, Z.; Jaramillo, T. F.; Deutsch, T. G.; Kleiman-Shwarsctein, A.; Forman, A. J.; Gaillard, N.; Garland, R.; Takanabe, K.; Heske, C.; Sunkara, M., Accelerating materials development for photoelectrochemical hydrogen production: Standards for methods, definitions, and reporting protocols. *J. Mater. Res.*, **2010**, *25*, 3-16.

91. Shi, X.; Jeong, H.; Oh, S. J.; Ma, M.; Zhang, K.; Kwon, J.; Choi, I. T.; Choi, I. Y.; Kim, H. K.; Kim, J. K., Unassisted photoelectrochemical water splitting exceeding 7% solar-to-hydrogen conversion efficiency using photon recycling. *Nat. Commun.*, **2016**, *7*, 1-6.

92. Döscher, H.; Young, J. L.; Geisz, J. F.; Turner, J. A.; Deutsch, T. G., Solar-to-hydrogen efficiency: shining light on photoelectrochemical device performance. *Energy Environ. Sci.*, **2016**, *9*, 74-80.

93. Huang, D.; Wang, K.; Li, L.; Feng, K.; An, N.; Ikeda, S.; Kuang, Y.; Ng, Y.; Jiang, F., 3.17% efficient Cu_2ZnSnS_4–$BiVO_4$ integrated tandem cell for standalone overall solar water splitting. *Energy Environ. Sci.*, **2021**, *14*, 1480-1489.

94. Kawasaki, S.; Takahashi, R.; Lippmaa, M., Gradient carrier doping as a method for maximizing the photon-to-current efficiency of a $SrTiO_3$ water-splitting photoanode. *J. Phys. Chem. C* **2019**, *123*, 15551-15556.

95. Snaith, H. J.; Ducati, C., SnO_2-based dye-sensitized hybrid solar cells exhibiting near unity absorbed photon-to-electron conversion efficiency. *Nano Lett.*, **2010**, 10, 1259-1265.

96. Zhang, L.; Reisner, E.; Baumberg, J. J., Al-doped ZnO inverse opal networks as efficient electron collectors in $BiVO_4$ photoanodes for solar water oxidation. *Energy Environ. Sci.*, **2014**, *7*, 1402-1408.

97. Jia, L.; Harbauer, K.; Bogdanoff, P.; Herrmann-Geppert, I.; Ramírez, A.; van de Krol, R.; Fiechter, S., α-Fe_2O_3 films for photoelectrochemical water oxidation–insights of key performance parameters. *J. Mater. Chem. A* **2014**, *2*, 20196-20202.

98. Tamirat, A. G.; Rick, J.; Dubale, A. A.; Su, W.-N.; Hwang, B.-J., Using hematite for photoelectrochemical water splitting: a review of current progress and challenges. *Nanoscale Horiz.*, **2016**, 1, 243-267.

99. Bhandari, K. P.; Roland, P. J.; Mahabaduge, H.; Haugen, N. O.; Grice, C. R.; Jeong, S.; Dykstra, T.; Gao, J.; Ellingson, R. J., Thin film solar cells based on the heterojunction of colloidal PbS quantum dots with CdS. *Sol. Energy Mater. Sol. Cells* **2013**, *117*, 476-482.

100. Osterloh, F. E., Inorganic nanostructures for photoelectrochemical and photocatalytic water splitting. *Chem. Soc. Rev.*, **2013**, 42, 2294-2320.

101. Fan, W.; Zhang, Q.; Wang, Y., Semiconductor-based nanocomposites for photocatalytic H_2 production and CO_2 conversion. *Phys. Chem. Chem. Phys.*, **2013**, *15*, 2632-2649.

102. Luo, W.; Zhang, M.; Feng, J.; Zou, Z., Photoelectrochemical cells for solar hydrogen production: current state of promising photoelectrodes, methods to improve their properties, and outlook. *Energy Environ. Sci.*, **2013**, *6*, 347-370.

103. Grundmann, M., *Physics of semiconductors*. Springer: **2010**, 11.

104. Sato, N., *Electrochemistry at metal and semiconductor electrodes*. Elsevier: **1998**.

105. Zhou, M.; Lou, X. W. D.; Xie, Y., Two-dimensional nanosheets for photoelectrochemical water splitting: Possibilities and opportunities. *Nano Today* **2013**, *8*, 598-618.

106. Segev, G.; Dotan, H.; Ellis, D. S.; Piekner, Y.; Klotz, D.; Beeman, J. W.; Cooper, J. K.; Grave, D. A.; Sharp, I. D.; Rothschild, A., The spatial collection efficiency of charge carriers in photovoltaic and photoelectrochemical cells. *Joule* **2018**, *2*, 210-224.

107. Sharma, S.; Kumar, D.; Khare, N. Plasmonic Ag nanoparticles decorated Bi_2S_3 nanorods and nanoflowers: Their comparative assessment for photoelectrochemical water splitting. *Int. J. Hydrog. Energy* **2019**, *44*, 3538-3552.

108. Nasir, J. A.; Rehman, Z. U.; Shah, S. N. A.; Khan, A.; Butler, I. S.; Catlow, C. R. A. Recent developments and perspectives in CdS-based photocatalysts for water splitting. *J. Mater. Chem. A* **2020**, *8*, 20752-20780.

109. Kurnia, F.; Ng, Y. H.; Amal, R.; Valanoor, N.; Hart, J. N. Defect engineering of ZnS thin films for photoelectrochemical water-splitting under visible light. *Sol. Energy Mater. Sol. Cells* **2016**, *153*, 179-185.

110. Wang, L.; Xia, L.; Wu, Y.; Tian, Y. Zr-Doped β-In_2S_3 Ultrathin Nanoflakes as Photoanodes: Enhanced Visible-Light-Driven Photoelectrochemical Water Splitting. *ACS Sustainable Chem. Eng.*, **2016**, *4*, 2606-2614.

111. Matoba, K.; Matsuda, Y.; Takahashi, M.; Sakata, Y.; Zhang, J.; Higashimoto, S. Fabrication of Pt/In_2S_3/$CuInS_2$ thin film as stable photoelectrode for water splitting under solar light irradiation. *Catal. Today* **2021**, *375*, 87-93.

112. Liu, Q.; Lu, H.; Shi, Z.; Wu, F.; Guo, J.; Deng, K.; Li, L. 2D $ZnIn_2S_4$ Nanosheet/1D TiO_2 Nanorod Heterostructure Arrays for Improved Photoelectrochemical Water Splitting. *ACS Appl. Mater. Interfaces* **2014**, *6*, 17200-17207.

113. Song, J-P.; Yin, P-F.; Mao, J.; Qiao, S-Z.; Du, X-W. Catalytically active and chemically inert $CdIn_2S_4$ coating on a CdS photoanode for efficient and stable water splitting. *Nanoscale* **2017**, *9*, 6296-6301

114. Huang, W.; Gan, L.; Yang, H.; Zhou, N.; Wang, R.; Wu, W.; Li, H.; Ma, Y.; Zeng, H.; Zhai, T., Controlled synthesis of ultrathin 2D β-In$_2$S$_3$ with broadband photoresponse by chemical vapor deposition. *Adv. Funct. Mater.*, **2017**, *27*, 1702448.

115. Zhang, J.; Wang, H.; Yuan, X.; Zeng, G.; Tu, W.; Wang, S., Tailored indium sulfide-based materials for solar-energy conversion and utilization. J. *Photochem. Photobiol. C: Photochem. Rev*., **2019**, *38*, 1-26.

116. Joy, J.; Mathew, J.; George, S. C., Nanomaterials for photoelectrochemical water splitting-review. *Int. J. Hydrog. Energy* **2018**, *43*, 4804-4817.

117. Chen, Y.; Zheng, W.; Murcia-Lopez, S.; Lv, F.; Morante, J. R.; Vayssieres, L.; Burda, C., Light management in photoelectrochemical water splitting–from materials to device engineering. J. Mater. Chem. C **2021**, *9*, 3726-3748.

118. Chen, X.; Ye, J.; Ouyang, S.; Kako, T.; Li, Z.; Zou, Z., Enhanced incident photon-to-electron conversion efficiency of tungsten trioxide photoanodes based on 3D-photonic crystal design. *ACS Nano* **2011**, 5, 4310-4318.

119. Low, J.; Cao, S.; Yu, J.; Wageh, S., Two-dimensional layered composite photocatalysts. *ChemComm.*; **2014**, *50*, 10768-10777.

120. Cho, S.; Jang, J.-W.; Lee, K.-H.; Lee, J. S., Research Update: Strategies for efficient photoelectrochemical water splitting using metal oxide photoanodes. APL Mater., **2014**, *2*, 010703.

121. Afroz, K.; Moniruddin, M.; Bakranov, N.; Kudaibergenov, S.; Nuraje, N., A heterojunction strategy to improve the visible light sensitive water splitting performance of photocatalytic materials. *J. Mater. Chem. A* **2018**, *6*, 21696-21718.

122. Yan, J.-H.; Zhu, Y.-R.; Tang, Y.-G.; Zheng, S.-Q., Nitrogen-doped SrTiO3/TiO2 composite photocatalysts for hydrogen production under visible light irradiation. *J. Alloys Compd*., **2009**, *472*, 429-433.

123. Shen, S.; Lindley, S. A.; Chen, X.; Zhang, J. Z., Hematite heterostructures for photoelectrochemical water splitting: rational materials design and charge carrier dynamics. Energy Environ. Sci., **2016,** *9*, 2744-2775.

124. Basu, M.; Garg, N.; Ganguli, A. K., A type-II semiconductor (ZnO/CuS heterostructure) for visible light photocatalysis. *J. Mater. Chem. A* **2014**, 2, 7517-7525.

125. Li, J.; Meng, F.; Suri, S.; Ding, W.; Huang, F.; Wu, N., Photoelectrochemical performance enhanced by a nickel oxide–hematite p–n junction photoanode. ChemComm **2012**, *48*, 8213-8215.

126. D'Amico, N. R.; Cantele, G.; Ninno, D., First principles calculations of the band offset at $SrTiO_3$- TiO_2 interfaces. *Appl. Phys. Lett*., **2012**, *101*, 141606.

127. Jin, Y.; Zheng, Y.; Podkolzin, S. G.; Lee, W. Band gap of reduced graphene oxide tuned by controlling functional groups. *J. Mater. Chem. C* **2020**, *8*, 4885-4894.

128. Siwiec, J.; Sokolowska, A.; Olszyna, A.; Dwilinski, R.;. Kaminska, M.;. Hrabowska, K. Photoluminescence properties of nanocrystalline, wide band gap nitrides (C_3N4, BN, AIN, GaN). *Nanostrcured Mater*., **1998**, *10*, 625-634.

129. Mishra, A.; Basu, S.; Shetti, N. P.; Reddy, K. R.; Aminabhavi, T. M. Photocatalysis of Graphene and Carbon Nitride-Based Functional Carbon Quantum Dots. *Nanoscale Materials in Water Purification*: Elsevier, **2019**; 759-781.

130. Shetti, N. P.; Malode, S. J.; Vernekarg, P. R.; Nayak, D. S.; Shetty, N. S.; Reddy, K. R.; Shukla, S. S.; Aminabhavi, T. M. Electro Sensing Base for Herbicide Aclonifen at Graphitic Carbon Nitride Modified Carbon Eectrode-Water and Soil Sample Analysis. *Microchem. J.* **2019**, *149*, 103976 (8).

131. Wang, L.; Tong, Y.; Feng, J.; Hou, J.; Li, J.; Hou, X.; Liang, J. G-C_3N_4-based films: A Rising Star for Photoelectrochemical Water Splitting, Sustainable Materials and Technologies. **2018**, *17*, e00089 (20).

132. Lim, Y.; Lee, D.-K.; Kim, S. M.; Park, W.; Cho, S. Y.; Sim, U., Low dimensional carbon-based catalysts for efficient photocatalytic and photo/electrochemical water splitting reactions. *Materials* **2019**, *13*, 114.

133. Liu, J.; Li, R.; Yang, B., Carbon dots: A new type of carbon-based nanomaterial with wide applications. *ACS Cent. Sci.*, **2020**, *6*, 2179-2195.

134. Yan, F.; Sun, Z.; Zhang, H.; Sun, X.; Jiang, Y.; Bai, Z., The fluorescence mechanism of carbon dots, and methods for tuning their emission color: a review. *Microchim. Acta* **2019**, *186*, 1-37.

135. Qu, S.; Zhou, D.; Li, D.; Ji, W.; Jing, P.; Han, D.; Liu, L.; Zeng, H.; Shen, D., Toward efficient orange emissive carbon nanodots through conjugated sp^2-domain controlling and surface charges engineering. *Adv. Mater*., **2016**, *28*, 3516-3521.

136. Sahai, S.; Ikram, A.; Rai, S.; Shrivastav, R.; Dass, S.; Satsangi, V. R., Quantum dots sensitization for photoelectrochemical generation of hydrogen: a review. *Renew. Sustain. Energy Rev.*, **2017**, *68*, 19-27.

137. Cho, G.; Park, Y.; Hong, Y.-K.; Ha, D.-H., Ion exchange: an advanced synthetic method for complex nanoparticles. *Nano Converg.*, **2019**, 6, 1-17.

138. Beberwyck, B. J.; Surendranath, Y.; Alivisatos, A. P., Cation exchange: a versatile tool for nanomaterials synthesis. *J. Phys. Chem. C*; **2013**, *117*, 19759-19770.

139. Mahala, C.; Sharma, M. D.; Basu, M., A core@ shell hollow heterostructure of Co_3O_4 and Co_3S_4: An efficient oxygen evolution catalyst. *New J. Chem.*, **2019**, *43*, 15768-15776.

140. Lin, F.; Boettcher, S. W., Adaptive semiconductor/electrocatalyst junctions in water-splitting photoanodes. *Nat. Mater.*, **2014**, *13*, 81-86.

141. Rossi, R. C.; Lewis, N. S., Investigation of the size-scaling behavior of spatially nonuniform barrier height contacts to semiconductor surfaces using ordered nanometer-scale nickel arrays on silicon electrodes. *J. Phys. Chem. B* **2001**, *105*, 12303-12318.

142. Wu, N., Plasmonic metal-semiconductor photocatalysts and photoelectrochemical cells: a review. *Nanoscale* **2018**, 10, 2679-2696.

143. Mascaretti, L.; Dutta, A.; Kment, Š.; Shalaev, V. M.; Boltasseva, A.; Zbořil, R.; Naldoni, A., Plasmon-enhanced photoelectrochemical water splitting for efficient renewable energy storage. *Advanced Materials* **2019**, *31*, 1805513.

144. Zhang, L.; Herrmann, L. O.; Baumberg, J. J., Size dependent plasmonic effect on $BiVO_4$ photoanodes for solar water splitting. Sci. Rep., **2015**, *5*, 1-12.

145. Valenti, M.; Kontoleta, E.; Digdaya, I. A.; Jonsson, M. P.; Biskos, G.; Schmidt-Ott, A.; Smith, W. A., The role of size and dimerization of decorating plasmonic silver nanoparticles on the photoelectrochemical solar water splitting performance of $BiVO_4$ photoanodes. *ChemNanoMat* **2016**, *2*, 739-747.

146. Mahala, C.; Sharma, M. D.; Basu, M., Near-field and far-field plasmonic effects of gold nanoparticles decorated on ZnO nanosheets for enhanced solar water splitting. *ACS Appl. Nano Mater.*, **2020**, *3*, 1153-1165.

147. Kong, X. T.; Wang, Z.; Govorov, A. O., Plasmonic nanostars with hot spots for efficient generation of hot electrons under solar illumination. *Adv. Opt. Mater.*, **2017**, *5*, 1-10.

148. Tian, Y.; Tatsuma, T., Plasmon-induced photoelectrochemistry at metal nanoparticles supported on nanoporous TiO_2. *ChemComm* **2004**, 16, 1810-1811.

149. Kumarasinghe, C. S.; Premaratne, M.; Bao, Q.; Agrawal, G. P., Theoretical analysis of hot electron dynamics in nanorods. *Sci. Rep.*, **2015**, *5*, 1-15.

150. Liu, R.; Zheng, Z.; Spurgeon, J.; Yang, X., Enhanced photoelectrochemical water-splitting performance of semiconductors by surface passivation layers. *Energy Environ. Sci.*, **2014**, 7, 2504-2517.

151. Zhong, D. K.; Gamelin, D. R., Photoelectrochemical water oxidation by cobalt catalyst ("Co-Pi")/α-Fe_2O_3 composite photoanodes: oxygen evolution and resolution of a kinetic bottleneck. *J. Am. Chem. Soc.*, **2010**, *132*, 4202-4207.

152. Peng, G.; Albero, J.; Garcia, H.; Shalom, M., A Water-Splitting Carbon Nitride Photoelectrochemical Cell with Efficient Charge Separation and Remarkably Low Onset Potential. *Angew. Chem. Int. Ed.*, **2018**, *57*, 15807-15811.

153. Guo, M.; Ma, G., Alteration of onset potentials of Rh-doped $SrTiO_3$ electrodes for photoelectrochemical water splitting. *J. Catal.*, **2020**, *391*, 241-246.

154. Jeong, K.; Deshmukh, P. R.; Park, J.; Sohn, Y.; Shin, W. G., ZnO-TiO_2 core-shell nanowires: a sustainable photoanode for enhanced photoelectrochemical water splitting. *ACS Sustain. Chem. Eng.*, **2018**, *6*, 6518-6526.

155. Hisatomi, T.; Kubota, J.; Domen, K., Recent advances in semiconductors for photocatalytic and photoelectrochemical water splitting. *Chem. Soc. Rev.*, **2014**, *43*, 7520-7535.

156. Hisatomi, T.; Dotan, H.; Stefik, M.; Sivula, K.; Rothschild, A.; Graetzel, M.; Mathews, N., Enhancement in the performance of ultrathin hematite photoanode for water splitting by an oxide underlayer. *Adv. Mater.*, **2012**, 24, 2699-2702.

157. Liu, J.; Li, J.; Li, Y.; Guo, J.; Xu, S.-M.; Zhang, R.; Shao, M., Photoelectrochemical water splitting coupled with degradation of organic pollutants enhanced by surface and interface engineering of $BiVO_4$ photoanode. *Appl. Catal. B: Environ.*, **2020**, *278*, 119268.

158. Gelderman, K.; Lee, L.; Donne, S., Flat-band potential of a semiconductor: using the Mott–Schottky equation. *J. Chem. Educ.*, **2007**, *84*, 685.

159. Albery, W. J.; O'Shea, G. J.; Smith, A. L., Interpretation and use of Mott–Schottky plots at the semiconductor/electrolyte interface. J. Chem. Soc. Faraday Trans., **1996**, *92*, 4083-4085.

160. Kennedy, J. H.; Frese, K. W., Flatband Potentials and Donor Densities of Polycrystalline α-Fe_2O_3 Determined from Mott-Schottky Plots. *J. Electrochem. Soc.*, **1978**, 125, 723.

161. Ye, K.-H.; Wang, Z.; Gu, J.; Xiao, S.; Yuan, Y.; Zhu, Y.; Zhang, Y.; Mai, W.; Yang, S., Carbon quantum dots as a visible light sensitizer to significantly increase the solar water splitting performance of bismuth vanadate photoanodes. *Energy Environ. Sci.*, **2017**, *10*, 772-779.

162. Salvador, P., Kinetic approach to the photocurrent transients in water photoelectrolysis at n-titanium dioxide electrodes. 1. Analysis of the ratio of the instantaneous to steady-state photocurrent. *J. Phys. Chem. A* **1985**, *89*, 3863-3869.

163. Gao, L.; Li, F.; Hu, H.; Long, X.; Xu, N.; Hu, Y.; Wei, S.; Wang, C.; Ma, J.; Jin, J., Dual modification of $BiVO_4$ photoanode by constructing heterojunction with $NiMoO_4$ and depositing CoPi co-catalyst for enhanced photoelectrochemical performance. *ChemSusChem* **2018**, *11*, 2502-2509.

164. Anantharaj, S.; Ede, S. R.; Sakthikumar, K.; Karthick, K.; Mishra, S.; Kundu, S., Recent trends and perspectives in electrochemical water splitting with an emphasis on sulfide, selenide, and phosphide catalysts of Fe, Co, and Ni: a review. *ACS Catal.*, **2016**, *6*, 8069-8097.

165. Anantharaj, S.; Ede, S.; Karthick, K.; Sankar, S. S.; Sangeetha, K.; Karthik, P.; Kundu, S., Precision and correctness in the evaluation of electrocatalytic water splitting: revisiting activity parameters with a critical assessment. *Energy Environ. Sci.*, **2018**, *11*, 744-771.

Chapter 2

Materials, Methods, and Instrumentation

- The chapter includes details of chemical and experimental methods used for the synthesis of different types of semiconductors and carbon-based nanomaterials.

- It contains the characterization methods, calculation methods, and instruments used for all the experiments included in the thesis.

This chapter deals with the materials, methodologies used for the synthesis of all the binary and ternary metal sulfides as semiconductor materials. Along with these, the synthesis of carbon-based nanomaterials in the pure form or modified form and their characterization techniques are described. Various techniques were used for the characterization of nanomaterials including powder X-ray diffraction (PXRD), X-ray photoelectron spectroscopy (XPS), Fourier transformation infrared spectroscopy (FTIR), electron microscope; Scanning electron microscope (SEM), Transmission electron microscopy (TEM), and for optical properties solid and solution phase UV-visible spectroscopy (UV-vis), Photoluminescence spectroscopy (PL) were applied. The photoelectrochemical activity was performed with the help of CH-Instrument by using different electrochemical techniques and a Xenon lamp was used for photoelectrode illumination.

2.1 Used Chemicals

The below mentioned chemicals are used for the synthesis of various photoanodes.

Table 2.1 List of the chemicals used in this thesis work with their purchasing company

S. No.	Chemicals	Name of Supplier
1	Indium Chloride [$InCl_3$]	Spectrochem, India
2	Thiourea [CH_4N_2S]	Merk, India
3	Urea, Extra pure	SD fine, India
4	Ethanol	Merck, India
5	β –Cyclodextrine (β–CD)	TCL, India
6	Zinc Chloride anhydrous [$ZnCl_2$]	Merck, India
7	Cadmium Chloride [$CdCl_2. 2H_2O$]	Loba-chemie, India
8	Citric Acid ($C_6H_8O_7$)	MolyChem, India
9	Trisodium Citrate [$Na_3C_6H_5O_7$]	SRL, India
10	L-Cysteine Hydrochloric Acid [$C_3H_7NO_2S.HCl$]	Merck, India
11	Sodium Sulfite [Na_2SO_3]	Merck, India
12	Sodium Sulphate [Na_2SO_4]	SDFCL, India
13	Sodium Chloride [$NaCl$]	SRL, India
14	Acetone [C_3H_6O]	MolyChem, India

| 15 | Methanol [CH$_3$OH] | Merck, India |
| 16 | Ethylenediamine tetra acetic acid [EDTA] | Merck, India |

2.2 Materials Used: All the below mentioned materials are used

2.2.1 Fluorine-Doped Tin Oxide (FTO): Fluorine-doped tin oxide (FTO) coated glass (1×1cm^2, resistivity 10 Ω/sq, thickness 3 mm) was used as a conducting surface for the development of photoelectrode, which was purchased from Sigma-Aldrich. For the cleaning of FTO, initially, small pieces (0.7×4 cm^2) were prepared. Before using the FTO, it was cleaned properly. To remove the adhesive layer present on the surface of FTO, it was sonicated in soap water for 10 h and further with the mixture of ethanol and acetone followed by milli-Q water for a longer period.

2.2.2 Dialysis sack: Dialysis sack (molecular cutoff weight = 10000 kDa) was purchased from Sigma-Aldrich and it was used for the purification of quantum dots (QDs) and carbon dots (CDs).

2.3 Methods

2.3.1 Synthesis Method

2.3.1.1 Ultra-sonication Method: To have a proper dissolution of metal precursor ultra-sonication method is the most useful technique. In this method, high-intensity ultrasound waves (>20 KHz) are passed through the liquid medium and generate acoustic cavitation which drives the micro bubble formation during a very short time and produces the local heating results the break-in metal precursor in its ions and dissolution in the solvent media.[1, 2]

2.3.1.2 Hydrothermal Method

Hydrothermal synthesis is advantageous and emerged technique for the synthesis of various types of nanostructures. This technique is greener, simpler, and cost-effective than the solvothermal method because water is used as a solvent instead of organic solvents. The temperature for the reaction is adopted higher than the boiling point of water so that due to the vapor saturation, self–produced pressure will originate in the closed system. The major advantages of this technique is that through hydrothermal method nanomaterials can be easily synthesized very uniformly. It requires less reaction time than conventional method, produces nanomaterials with phase homogeneity. Several reaction parameters affect the physicochemical properties of the nanostructure in

hydrothermal syntheses such as reaction temperature, pressure, reaction time, pH of the reaction precursor, the concentration of initial metal precursor, and growth directing agents. In this method, the solution of the reaction precursors is kept in the Teflon-lined container at a fixed temperature for the required time of reaction. While the other parameters such as concentration of initial components, solubility, and pH of the solution etc. should be set prior to the reaction.[3]

2.3.1.3 Calcination Method

Calcination refers to the thermal treatment of the solid material at high temperatures in the presence or absence of the air. Mainly, in our present study, this method is explored for incorporation of oxygen as a dopant in the material via air calcination. It is also used to remove the volatile impurity and water or moisture, to enhance the crystallinity of the material, oxidizing a portion of the mass, rendering them friable, and for thermal decomposition of the material. In the calcination process, the temperature is regulated to bring a change in the physical and chemical constitution of the substance. The physicochemical change in the material depends on the operating temperature, that how fast the material is heated, how fast it is cooled, how long the material is kept for calcination etc.

2.3.1.4 Microwave Method

Closed vessel microwave heating technique have been state of art in synthetic chemistry. Microwave rays (2.45 GHz-1.6×10^{-3} eV) are electromagnetic radiations. The microwave heating technique offers a clean, one-pot, fast, and efficient toolkit for chemical transformation. It shows the superheating effect which reduces the reaction time because the microwave radiations interact uniformly with entire solvent molecules leading to the quick and sudden rise in temperature. Irradiation with high-frequency electromagnetic waves can be an efficient method for the preparation of nanomaterials in a short time than the conventional method. The principle of this method is that when a molecule is irradiated with microwave radiation it aligns itself with the applied field. The electric and magnetic components of microwaves change in direction of molecules rapidly thus energy is absorbed. The efficiency of energy conversion from electromagnetic to thermal energy depends on the dielectric constant. The larger the dielectric constant the greater is the coupling with microwave radiations and the solvent will be heated rapidly.

By changing the parameters such as microwave power, pressure, temperature, and solvent nanomaterials can be synthesized in different shapes and sizes.[4]

2.3.1.5 Dialysis Method

The dialysis technique is the best choice to gently purify the nanoparticles and quantum dots. It is based on the concept of diffusion in which the unreacted monomers and solvent residuals come out to the dialysis membrane. At the same time, the small impurities with specific hydrodynamic radius diffuse through a membrane while larger macromolecules are retained by the dialysis membrane. The radius gets standardized to a mass cutoff which is available from 0.5 to 100 kDa. The target molecule has a higher hydrodynamic radius than the selected membrane pores and, thus, stays in the dialysis sac. Dialysis can be performed in the various solvents however dialysis sac membrane should be compatible with the solvent.[5]

2.3.2 Sample Preparation method for Analysis

2.3.2.1 Sample Preparation for TEM

The samples were deposited onto 400-mesh carbon-coated copper grids by placing 3-4 drops of a freshly prepared ethanolic dilute solution of the sample and the grids were dried overnight. Solid powder samples were dispersed in ethanol and liquid samples were used directly for drop casting on the grid.

2.3.2.2 Sample Preparation for XPS

To perform XPS analysis, palates of the desired material was prepared keeping the thickness 8 mm. To compensate for any kind of charging effect, the binding energy of C1s peak at 284.5 eV has been used as a reference.

2.4 Instrumentation

For the detailed characterization and to study the PEC activity of the developed photoelectrodes following instruments and techniques are used.

2.4.1   List of Instruments

1. Quartz cuvettes (ERMA, 1 cm light path, capacity 3.5 ml, Model: MCQ-4/104).

2. Magnetic stirrer, IKA RCT basic.

3. Centrifuge Machine, Tarsons (SPINWIN-MC03).

4. Sonicator, Leelasonic.

5. Balance, Denver Instrument, Japan.

6. Teflon lined container (autoclave) and Oven, Genetix (GX-A5030A).

7. Muffle Furnance, MAC (MSW-251).

8. Hot Air Ovan, MAC (MSW-211).

9. UV-visible Spectrophotometer: UV-vis absorption spectra for liquid samples were obtained using a Shimadzu (UV-1800) and Jasco V-650 spectrophotometer. UV-vis diffuse reflection spectra for solid samples were recorded on the Shimadzu Spectrophotometer (model no. UV-2450).

10. PXRD analysis: For PXRD, Rigaku Mini Flex II diffractometer with Cu-Kα radiation was used. The PXRD analysis was carried out with 2θ values ranging from 10°- 80° and scanning rate of 2° per minute and 0.5° per minute at 25 °C.

11. XPS Analysis: For XPS measurements a commercial Omicron EA 125 spectrometer equipped with a seven-channel detection system was used. Monochromatic light of Al-Kα radiation with 1486.7 eV energy was used as an X-ray source. The emission current was set to 15 mA and chamber base pressure was maintained below $<10^{-9}$ mbar during the measurement.

12. FESEM analysis: To determine the morphology of the synthesized samples FESEM FEI microscope (Model- "APREO S") was used. To carry out EDS analysis, X-MaxN, Aztec (software), NS: 77887 (Detector) was used which was attached to the FESEM. Before FESEM and EDS analysis, the synthesized materials were coated with gold or chromium by sputtering.

13. TEM analysis: TEM and HRTEM analysis were carried out using a Bruker microscope and FEI Technai G2 instrument operated with an electron beam with energy of 200 kV.

14. Fourier Transform Infrared Spectroscopy (FTIR): To acquire FTIR spectra Shimadzu IR Affinity-1S spectrometer was used.

15. Raman Analysis: HORIBASCI Raman instrument (Model: LabRAM HR EVO) was used to carry out Raman analysis. The detector was a thermoelectrically cooled charged coupled device (CCD) detector of 576×384 pixels.

16. Room temperature Photoluminescence measurements were performed using a Horiba Jobin Yvon Fluoromax-4 spectrofluorimeter. The excitation and emission slit widths were fixed to 5 nm each and according to absorbance spectra the excitation wavelength (λ_{ex}) was fixed.

17. All the photoelectrochemical data was recorded in CH Instrument (CHI604E) at 25°C.

18. A PEC Cell (Quartz beaker-80 mL) and electrodes Ag/AgCl (reference electrode), Pt wire (counter electrode), and sample decorated FTO were used to perform the PEC reaction.

19. A power meter (Model: 843-R) was used to check the intensity of light.

20. Xenon Lamp was used as a light source during PEC water splitting.

The details of the characterization techniques are as follows:

2.4.2 Spectroscopy Tools

2.4.2.1 UV-visible Spectroscopy

Absorption and emission spectroscopy are the most vitally used to investigate the optical properties of the semiconductors and nanomaterials. It deals with the interaction of the electromagnetic radiations with the material in the range of ultraviolet region to the visible region. The sample is irradiated with UV-visible radiation for the investigation and the absorption of radiation is recorded as a function of wavelength. The absorption peaks of semiconductors or nanomaterials shift towards the smaller and higher wavelengths depending on their size. Electronic transitions and energy band gap of a material can be obtained with the help of UV-visible spectra. Energies related with the UV-visible radiations are enough to excite molecular electrons from ground to higher energy states. The absorbance (A) of an absorber (concentration, C) having a molar extinction coefficient ε_λ at wavelength λ is given by the equation.

$$A = \log (I_o/I_t) = \varepsilon_\lambda \, cl$$

where A is absorbance (optical density), I_0 and I_t represent the intensity of the incident and transmitted light, respectively, C is the concentration of the light-absorbing species and 'l' is the path length of the light-absorbing medium.[6, 7]

2.4.2.1.1 Calculation of Band Gap

The bandgap generally denotes the energy difference (in electron volts) between the bottom of the conduction band (E_{CB}) and top of the valence band (E_{VB}) in semiconductors. To calculate the

bandgap of the sample, UV-vis absorption spectra is used. The following equation is used to relate the absorption coefficient to incident photon energy.

$$\alpha(v)hv = B(hv - E_g)^{1/2}$$

where α = absorption coefficient, E_g = optical gap, B = constant that depends on the transition probability, h is the Plank constant and v is the frequency.

Known function:

$$hv = h\frac{c}{\lambda} = \frac{1240}{\lambda}$$

$$(\alpha\frac{1240}{\lambda})^2 = B(\frac{1240}{\lambda} - E_g)$$

$$\alpha Ep = B(Ep - E_g)^{1/2}$$

A classical Tauc approach is further employed to estimate the bandgap (E_g) value of semiconductors using a plot of $(\alpha E_p)^2$ vs. E_p for direct band gap semiconductors.[8]

2.4.3 Photoluminescence Spectroscopy

Photoluminescence (PL) spectroscopy works in a non-contact mode and it is a non-destructive and simple technique to examine the electronic transitions of the materials. It belongs to the emission process in which firstly the material absorbs the light and electrons get excited from the ground state to the excited state. The excited electrons have excess energy and it loses before coming to the resting stage in the form of the luminescent photon which is emitted by the material. So, the process of photoexcitation followed by photoemission is called photoluminescence. The output of the PL spectroscopy is a relation between the wavelength and counts of the intensity of the emitted photons which are represented on the x-axis and y-axis, respectively. The PL spectroscopy is useful to identify the level of impurity and defects present in the semiconductor material, recombination phenomena, and excited state of the semiconductor material.[9,10]

2.4.3 Powder X-ray Diffraction

In 1912 German Physicist, Max Von Laue first demonstrated X-ray diffraction (XRD) which is a non-destructive, versatile, and well-established analytical technique. X-ray diffraction technique is the most extensively used for the analysis of crystallinity, phase, purity, determination of particle size, crystal structure and lattice parameters, etc.

X-rays are short-wavelength electromagnetic radiations (10^{-7} to about 10^{-15} m) and are generated when the high energy accelerated electrons (30 KV) hit the core electrons to out of the metal, and electrons drop downs from the outer orbitals to fill the vacancies. The energy difference between these two shells comes out as an electromagnetic wave which is called an X-ray. Cathode ray tube acts as the source of the X-rays and before directed to the sample these rays filtered to produce monochromatic radiation. The X-ray is reflected by the lattice planes of the sample only when it satisfies the Bragg diffraction condition:

$$2d_{hkl} \sin \theta = n\lambda$$

where λ denotes the wavelength of the X-ray, θ represents the scattering angle, d_{hkl} presents the spacing between the crystal planes with Miller indices hkl, and n is an integer. These energetic X-rays provide information about the structural arrangement of atoms and molecules by penetrating into the deep of the material. Crystal diffract X-rays in a unique characteristic pattern because each crystalline material has a characteristic atomic structure.[11]

2.4.3.1 Determination of Particle Size

To determine the particle size the diffraction method is used which is based on the upshot of diffraction peak broadening. It is associated with the particle size. The incident X-ray beam must meet the reflection plane at one of the specified angles for the diffraction maxima by a crystal. The crystallite size can be deliberate using the width of the peak in the XRD analysis. The crystallite size or the particle size can be determined using the following Scherer's equation:

$$d = 0.9 \, \lambda \, / \, B \cos \theta$$

Where d represents the particle size, λ is the wavelength of the incidence X-ray, and B represents the intensity of full width at half maximum (FWHM) in terms of 2θ. From the given equation it is clear that decrease in crystallite size leads to peak broadening. The Scherer's equation is only applicable for spherical particles.[12, 13]

2.4.4 X-ray Photoelectron Spectroscopy (XPS)

This technique related to the photoemission spectroscopy in which a material is irradiated with the X-rays and core electrons are ejected. The spectra deal with intensity of photo ejected electrons of the material. The XPS is a quantitative and surface-sensitive technique. It is based on the photoelectric effect. In this technique, an atom, molecule, or solid surface absorbs the light and

ejected an electron from the core. Al Kα (1486.6 eV) or Mg Kα (1253.6 eV) photons are generally used for the XPS. The core electron binding energies are characteristic of oxidation state of each element. They are under the peak can be used to determine the composition. XPS can provide chemical bonding information as the binding energy and peak shape are sensitive to the oxidation and chemical state of the emitting atom.[14, 15]

2.4.5 Electron Microscopy

Electron microscopy is an imaging technique that uses energetic electrons beam to examine objects on a very fine scale. There are many electron microscopes but most widely field emission scanning and transmission electron microscope are used.

2.4.5.1 Field Emission Scanning Electron Microscope (FESEM)

This technique is largely used electron microscopic technique due to its versatility, different modes of imaging, simple sample preparation including easy interpretation of images. In the FESEM, a cathode is a source for the electron beam; it may be tungsten filament or LaB_6. When an electron beam interacts with the specimen, it loses energy by various mechanisms. The energy lost is transformed into alternative forms such as emission of low-energy secondary electrons, heat, high-energy backscattered electrons, Auger electron, light emission (cathode luminescence), or X-ray emission. All of which deliver signals carrying information about topography and composition of a specimen sample. In a general FESEM image, only secondary electrons are detected. The detected electrons transfer to the processor in the form of signals and are processed to obtain an image of the specimen.[16, 17]

2.4.5.2 Transmission Electron Microscope (TEM)

TEM has nearly similar components to the SEM. In this technique transmitted electrons uses to create the images of the sample. In TEM, the electron beam is passed through a thin layer of the sample. The beam interacts with this layer and the transmitted beam is then focused onto an imaging device. Such devices include fluorescent screens and photographic films. Since SEM works on the beam scattering principle it only provides information on the surface morphology of the sample. In the case of TEM, imaging is done from the transmitted electrons, it can also provide information on magnetic domains, stresses, size, lattice plane, crystal structure, and selected area

electron diffraction (SAED). It also has a higher resolution than SEM. TEM is categorized into two parts; low-resolution TEM and high-resolution transmission electron microscopy (HRTEM). From HRTEM images lattice spacing (d) can be calculated which corresponds to the particular crystal plane (hkl).[16, 17]

2.4.5.3 Energy-Dispersive X-ray (EDX) Spectroscopy

EDX also known as energy dispersive spectroscopy (EDS). This analytical technique is generally added with SEM and TEM. An electron beam (typically 10-20 keV) strikes the conducting sample surface, causing X-rays to be emitted, whose energies depend on the material under examination. The X-rays are produced in a region about 2 µM in depth. By scanning the electron beam across the material, an image of each element in the sample can be obtained which shows the chemical composition of the individual material. [18] In EDS, all photons emitted by the samples are collected and measured simultaneously by a solid-state X-ray detector. Each element has a unique atomic structure allowing a unique set of peaks on its electromagnetic emission spectrum during characterization.[16, 17]

2.4.6 Fourier Transform Infrared (FTIR) Spectroscopy

Infrared (IR) spectroscopy deals with the interaction of the IR region of the electromagnetic spectrum with the matter. In this region associated photon energies (1 to 15 kcal/mole) are not adequate to excite the electrons; however, they may induce vibrational excitation in covalently bonded atoms. In this spectroscopy, 4000 to 400 cm^{-1} spectrum region is used because the inorganic and organic functional groups can absorb radiations within this region. According to the gross selection rule of IR spectroscopy, an 'IR active' vibrational mode must be associated with changes in the electric dipole moment. The molecule need not have 'i' permanent dipole however, requires only a change in dipole moment during the vibration. This spectroscopy helps to identify the functional group that is present on the surface of the material.[18, 19]

2.4.7 Raman Spectroscopy

Raman spectroscopy is an analytical technique to measure vibrational energy modes of a sample scattered light is used. According to the sample, lasers [354 nm, 532 nm, 785 nm] are used that are focused by the microscope to a very small spot of the sample. The frequency difference between

incident monochromatic light frequency and scattered light frequency (re-emitted photons) is called the Raman effect or Raman shift. The obtained plot between Raman shift and detected photons provides the Raman spectrum. The Raman spectrum gives details about vibrational, rotational, and other low-frequency modes existing in the sample. Raman spectroscopy can provide both chemical and structural information, as well as the identification of substances through their characteristic Raman 'fingerprint'. This spectroscopy is also used for the identification of symmetry, crystalline nature, disorders, and defects in the sample.[20]

2.5 Techniques for Photoelectrochemical Application and Calculations

2.5.1 Voltammetry

It is an electroanalytical technique in which upon application of potential (V) the current (i) flowing through a cell is measured. It is usually carried out with a three-electrode system comprising a working electrode, a counter electrode, and a reference electrode. The working electrode is the one on which the oxidation or reduction reaction occurs depending on the applied potential. The counter or auxiliary electrode simply serves to complete the analogous circuit, i.e., if the working electrode behaves as a cathode, the counter behaves as an anode and vice versa. The reference electrode on the other hand is an electrode that has a known electrode potential. The potential of the working electrode is measured against the potential of the reference electrode.

There are many voltammetry techniques in which cyclic voltammetry, Linear Sweep Voltammetry (LSV), chronoamperometry, and chronocoulometry are most commonly used.

2.5.1.1 Cyclic voltammetry

In cyclic voltammetry (CV), the potential of the electrode ramps linearly with the time in the cyclic phase. After reaching the set potential in CV analysis, the potential of the working electrode is ramped in the opposite direction to return to the initial potential. The plot between current (i) at the working electrode and applied potential (V) is called a voltammogram. Cyclic voltammetry is generally used to know the electrochemical properties of the analyte in solution and adsorbed species on the electrode surface. The analyte and adsorbed species should be redox-active within the potential window to be scanned.[21-23] On the other hand, the CV technique is also useful to calculate the bandgap of the semiconductor nanomaterials.

2.5.1.1.1 Calculation of Band Gap from Cyclic Voltammetry Analysis

The valence band and conduction band positions are determined from the onset potential of oxidation peak (E_{ox}) and reduction peak (E_{red}), respectively of the cyclic voltammogram.[24, 25] The relationship between the band energy levels and the redox potentials can be described by the following equations:

$$E_{VB} = - (4.71 + E_{ox})\ eV$$
$$E_{CB} = - (4.71 + E_{red})\ eV$$
$$E_g = E_{VB} - E_{CB}$$

2.5.1.2.1 Linear Sweep Voltammetry (LSV)

LSV is a technique in which current is measured at the working electrode and the potential sweeps linearly with time between the working electrode and reference electrode. The current is a direct measure of the rate at which electrons are being exchanged through the interface of electrode and electrolyte. The scanning of the curve starts where no electrochemical reaction happens and current can be perceived at the potential where charge transportation begins and rises with an increase in potential. However, after reaching a maximum value (peak current plateau) it begins to drop due to the depletion of reacting species at the interface. The results of interest from this technique are the onset potential and the current which is produced due to reacting species.[26]

2.5.2 Amperometry

2.5.2.1 Chronoamperomtery

Chronoamperometry is an electrochemical technique where the potential of the working electrode is stepped and the resulting current (i) occurring at the electrode surface due to the faradaic process is monitored as a function of time (t). The current and time correlation is measured after applying the single or double steeped potential to the working electrode in the electrochemical system. The current is integrated over relatively long time intervals. Chrornoamperometry gives a better signal-to-noise ratio than the other amperometry techniques. This technique is used to study the photostability of the photoelectrode.[27]

2.5.2.2 Chronocoulomtery

Chronocoulometry is also an electrochemical method that has a similar principle to chronoamperometry, but it gives the relationship between charge (Q) and time (t) instead of current

and time.

2.5.3 Photoelectrochemical Impedance Spectroscopy

Photoelectrochemical impedance spectroscopy (PEIS) is a powerful technique and is used to know the electron transfer kinetics taking place at the electrode/electrolyte interface during the PEC water-splitting reaction. The Nyquist plot obtained from PEIS analysis is the plot of the imaginary part of impedance against the real part of the impedance. From the Nyquist plot two types of information can be extracted for the electrode/electrolyte interface; first, the solution resistance, when the semicircle shifts from the starting point to the high frequency and the difference between the endpoint (low frequency) and starting point of the semicircle (high frequency) is calculated for the charge transfer resistance of the photoelectrode. The solution resistance is independent of the intensity of light and the applied bias. To calculate the resistance of a single electrode/electrolyte interface Randles model is used in which the polarization resistor (R1 or R_{CT}) is connected parallel with the constant phase element (CPE) and in series with the bulk resistor (R2 or R_S). The CPE is used for the non-ideal behavior of the electric double layer due to the porosity, roughness, poly-crystallinity, and dynamic disorders which are associated with diffusion.[28, 29]

2.6 Photoelectrochemical Cell to Perform the Photoelectrochemical Water-Splitting

To examine the behavior of photoanodes, PEC water-splitting was performed in various electrolytes (Na_2SO_4, Na_2SO_3, NaCl) using three electrode configurations. The used photoelectrochemical cell is made of quartz. In the cell, the sample deposited FTO acts as a working electrode, Ag/AgCl as a reference electrode, and Pt wire as a counter electrode. The scan rate was 50 mV/s during the LSV experiment. The intensity of illuminated light on the PEC cell was fixed at 100 mW/cm^2 using a power meter. We have used In_2S_3 and In_2S_3 based as a photoanode to perform the PEC water-splitting reaction. Considering the case of photoanode in PEC water splitting, the photoanode was illuminated from the back side. Under back illumination, electrons need to travel a lesser path compare to front illumination.

2.7 References

1. Okoli, C. U.; Kuttiyiel, K. A.; Cole, J.; McCutchen, J.; Tawfik, H.; Adzic, R. R.; Mahajan, D., Solvent effect in sonochemical synthesis of metal-alloy nanoparticles for use as electrocatalysts. *Ultrason Sonochem.*, **2018**, *41*, 427-434.

2. Kaboorani, A.; Riedl, B.; Blanchet, P., Ultrasonication technique: a method for dispersing nanoclay in wood adhesives. *J. Nanomater.,* **2013,** *2013*.

3. Malwal, D.; Packirisamy, G., Recent advances in the synthesis of metal oxide (MO) nanostructures. *Synthesis of Inorganic Nanomaterials* **2018**, 255-281.

4. Saleh, T. A.; Majeed, S.; Nayak, A.; Bhushan, B., Principles and advantages of microwave-assisted methods for the synthesis of nanomaterials for water purification. In *Advanced nanomaterials for water engineering, treatment, and hydraulics*, IGI Global: 2017; 40-57.

5. Schuett, T.; Geitner, R.; Zechel, S.; Schubert, U. S., Dialysis Diffusion Kinetics in Polymer Purification. *Macromolecules* **2021,** *54*, 9410-9417.

6. Weckhuysen, B. M., Ultraviolet-visible spectroscopy. **2004**.

7. Rocha, F. S.; Gomes, A. J.; Lunardi, C. N.; Kaliaguine, S.; Patience, G. S., Experimental methods in chemical engineering: Ultraviolet visible spectroscopy-UV-Vis. *Can. J. Chem. Eng.*, **2018,** *96*, 2512-2517.

8. Ghobadi, N., Band gap determination using absorption spectrum fitting procedure. *Int. Nano Lett.*, **2013**, *3*, 1-4.

9. Perkowitz, S., Optical characterization of semiconductors: infrared, Raman, and photoluminescence spectroscopy. Elsevier: **2012**.

10. Gilliland, G., Photoluminescence spectroscopy of crystalline semiconductors. *Mater. Sci. Eng. R Rep.*, **1997**, *18*, 99-399.

11. Holder, C. F.; Schaak, R. E., Tutorial on powder X-ray diffraction for characterizing nanoscale materials. *ACS Nano* **2019**, *13*, 7359-7365.

12. Weibel, A.; Bouchet, R.; Boulc', F.; Knauth, P., The big problem of small particles: a comparison of methods for determination of particle size in nanocrystalline anatase powders. *Chem. Mater.*, 2005, 17, 2378-2385.

13. He, K.; Chen, N.; Wang, C.; Wei, L.; Chen, J., Method for determining crystal grain size by x-ray diffraction. *Cryst. Res. Technol.*, **2018**, *53*, 1700157 (1-6).

14. Singh, B.; Diwan, A.; Jain, V.; Herrera-Gomez, A.; Terry, J.; Linford, M. R., Uniqueness plots: A simple graphical tool for identifying poor peak fits in X-ray photoelectron spectroscopy. *Appl. Surf. Sci.*, **2016**, *387*, 155-162.

15. Fadley, C. S., X-ray photoelectron spectroscopy: Progress and perspectives. J. Electron Spectrosc. Relat. Phenom., **2010**, *178*, 2-32.

16. arghese, P.; Pradeep, T., *A textbook of nanoscience and nanotechnology*. Tata McGraw-Hill Education: **2003**.

17. Amelinckx, S.; Van Dyck, D.; Van Landuyt, J.; van Tendeloo, G., *Electron microscopy: principles and fundamentals*. John Wiley & Sons: **2008**.

18. Khan, S. A.; Khan, S. B.; Khan, L. U.; Farooq, A.; Akhtar, K.; Asiri, A. M., Fourier transform infrared spectroscopy: fundamentals and application in functional groups and nanomaterials characterization. *In Handbook of materials characterization*, Springer: 2018; 317-344.

19. Ng, L. M.; Simmons, R., Infrared spectroscopy. *J. Anal. Chem.*, **1999**, *71*, 343-350.

20. Bumbrah, G. S.; Sharma, R. M., Raman Spectroscopy-Basic principle, instrumentation and selected applications for the characterization of drugs of abuse. *Egypt. J. Forensic Sci.*, **2016**, *6*, 209-215.

21. Heinze, J., Cyclic voltammetry- "electrochemical spectroscopy". New analytical methods (25). *Angew. Chem., Int. Ed. Engl.*, **1984**, *23*, 831-847.

22. Elgrishi, N.; Rountree, K. J.; McCarthy, B. D.; Rountree, E. S.; Eisenhart, T. T.; Dempsey, J. L., A practical beginner's guide to cyclic voltammetry. *J. Chem. Educ.*, **2018**, *95*, 197-206.

23. Nicholson, R. S.; Shain, I., Theory of stationary electrode polarography. Single scan and cyclic methods applied to reversible, irreversible, and kinetic systems. *Anal. Chem.*, **1964**, *36*, 706-723.

24. Bera, R.; Jana, B.; Mondal, B.; Patra, A., Design of CdTeSe–Porphyrin–Graphene Composite for Photoinduced Electron Transfer and Photocurrent Generation. *ACS Sustain. Chem. Eng.*, **2017**, *5*, 3002-3010.

25. Liu, J.; Yang, W.; Li, Y.; Fan, L.; Li, Y., Electrochemical studies of the effects of the size, ligand and composition on the band structures of CdSe, CdTe and their alloy nanocrystals. *Phys. Chem. Chem. Phys.*, **2014**, *16*, 4778-4788.

26. Nahir, T. M.; Clark, R. A.; Bowden, E. F., Linear-sweep voltammetry of irreversible electron transfer in surface-confined species using the Marcus theory. *Anal. Chem*., **1994**, *66*, 2595-2598.

27. Saveant, J.; Vianello, E., Potential-sweep chronoamperometry: Kinetic currents for first-order chemical reaction parallel to electron-transfer process (catalytic currents). Electrochim. Acta **1965**, *10*, 905-920.

28. Klotz, D.; Grave, D. A.; Dotan, H.; Rothschild, A., Empirical analysis of the photoelectrochemical impedance response of hematite photoanodes for water photo-oxidation. *J. Phys. Chem. Lett*., **2018**, *9*, 1466-1472.

29. Lim, S. Y.; Han, D.; Kim, Y.-R.; Chung, T. D., Photoelectrochemical and impedance spectroscopic analysis of amorphous Si for light-guided electrodeposition and hydrogen evolution reaction. *ACS Appl. Mater. Interfaces* **2017**, *9*, 23698-23706.

Photoelectrochemical Water Splitting by In₂S₃/In₂O₃ Composite Nanopyramids
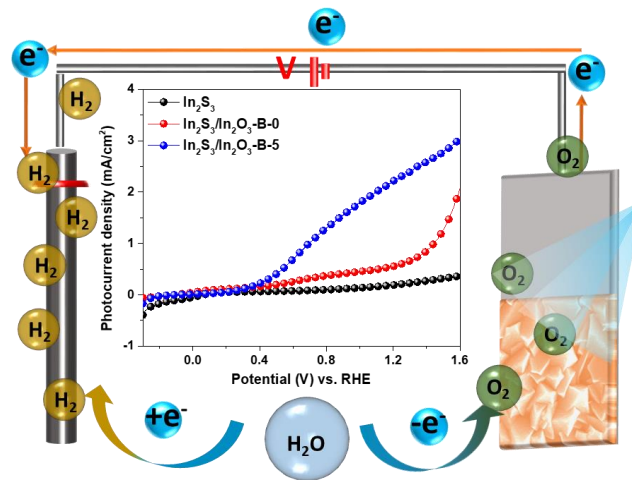
- In this chapter heterostructure of In₂S₃/In₂O₃ is developed via a simple hydrothermal technique.

- The developed heterostructure of In₂S₃/In₂O₃ is applied as photoanode for photoelectrochemical water splitting and it shows enhanced photoelectrochemical activity compared to bare In₂S₃ and In₂O₃.

Abstract

Photoelectrochemical (PEC) water-splitting reaction becomes an important path for the requirement of the fulfillment of global energy demand. For PEC water-splitting reaction, here In_2O_3 is grown in-situ in the nanopyramidal structure of In_2S_3 via a simple hydrothermal technique. The limited supply of S^{2-} in the reaction medium plays an important role in the development of In_2O_3 along with In_2S_3 leading to In_2S_3/In_2O_3 nanocomposite. In_2S_3/In_2O_3 nanocomposite shows enriched carrier density compared to bare In_2S_3. The optimum amount of In_2O_3 in the composite helps to achieve efficient photoactivity. In addition, the observed negative shift of the flat band potential of the nanocomposite, demonstrates the assistance of early onset potential. Moreover, In_2S_3/In_2O_3 nanocomposite shows improved visible light absorbance due to having the pyramidal nanostructure. It can generate high photoconversion efficiency ~ 0.55% at 0.77 V vs. RHE in 0.5 M Na_2SO_4. The stability of the In_2S_3/In_2O_3 nanopyramid is determined under chopped illumination condition for 1000 seconds, which shows decay in stability in Na_2SO_4 medium. Importantly, to widen the applicability of In_2S_3/In_2O_3 composite, PEC water-splitting performance is determined in 3.5 wt% saline water. Under such corrosive environment, In_2S_3/In_2O_3 can show efficient photoactivity as well as outstanding stability. It can generate photocurrent density of 0.83 mA/cm^2 under an applied potential of 1.18 V vs. RHE. The present research suggests the development of In_2S_3/In_2O_3 nanopyramid composite as a chloride environment withstanding and high corrosion resistance photoanode. The advantage of the faceted nanopyramidal structure and the composite is focused here. It paves an avenue for developing and engineering highly persistent seawater-splitting photoelectrodes which offers an opportunity to use the vast seawater on earth as an energy carrier.

3.1 Introduction

Hydrogen fuel generation via PEC water-splitting can be a greener, alternative and chemical pathway for the development of renewable energy sources.[1-3] To determine the PEC performance, photoelectrode plays a crucial role because the optical properties, charge carrier generation, transportation, and successful collection and reaction often.[4] Various metal sulfide semiconductors also have drawn fascinating attention for PEC water-splitting due to the narrower band gap. Therefore, with great passion, researchers have devoted themselves to the exploration of visible light active metal sulfides like CdS, In_2S_3, SnS_2, Bi_2S_3, $CdIn_2S_4$, $CuIn_2S_4$, and $ZnIn_2S_4$.[5-11]

Among these, In_2S_3 has drawn significant interest due to its merits such as moderate band gap, superior photogenerated charge-carriers mobility, as well as outstanding absorption coefficient.[12-15] In_2S_3 exists in five phases: α-In_2S_3 (phase defect cubic structure), β-In_2S_3 (phase defect spinel structure), γ-In_2S_3 (phase layered hexagonal structure), ϵ-In_2S_3 (phase rhombohedra structure), Th_3P_4-type In_2S_3 (phase cubic defect structure).[16] From literature reports, it is evident that β-In_2S_3 is a stable phase at room temperature and it can exist either a cubic or tetragonal form.[17] In the tetragonal form Indium (In) atoms will occupy 2/3 of the tetrahedral sites and 1/3 sites are vacant to maintain the stoichiometry of In_2S_3. Thus, a large no. of indium vacancies is present. The tetragonal and cubic phase differs from each other based on the arrangement of the vacancies in the crystal structure.[18] In the case of the tetragonal phase, vacancies are in an ordered manner whereas, in the cubic form vacancies are located at octahedral sites in a disordered manner. In In_2S_3, these vacancies act as an electron trap center which boosts in efficient charge-carrier separation.[19, 16]

β-In_2S_3 is well explored due to having such interesting properties. Rengaraj *et* al. reported that the hierarchal tetragonal In_2S_3 microspheres are more photoactive than the cubic form.[20] A highly crystallized tetragonal β-In_2S_3 has been synthesized by Ma *et.* al. They have reported that the tetragonal β-In_2S_3 exhibited better intrinsic visible light photoactivity in both water and nitro reduction than the cubic crystal of β-In_2S_3.[21] Besides the phase, morphology of In_2S_3 also plays an important role for PEC water-splitting. Li *et* al. synthesized vertically grown cubic β-In_2S_3 nanosheets array via a hydrothermal process which shows 35.7 $\mu A/cm^2$ photocurrent density.[22] Morphology not only influences the light-harvesting efficiency but also affects the mobility of photogenerated charge carriers. The various morphologies from zero-dimensional to three-dimensional of In_2S_3 are correlated with the PEC water-splitting performance. Tian *et al*. have

synthesized different morphologies of β-In$_2$S$_3$ such as nanoparticle, nanobelt, and nanoflakes and observed that nanoflakes show superior PEC water-splitting activity. β-In$_2$S$_3$ nanoflakes can generate 18.5 and 3.08-fold higher photocurrent density compared to nanoparticles and nanobelts, respectively.[23] Recently, Chen *et al*. reported the various phases as well as a different type of morphologies of β-In$_2$S$_3$ for PEC water-splitting. The PEC test shows the cubic phase β-In$_2$S$_3$ nanocubes with cuneiform like morphology can generate a higher photocurrent density than the tetragonal nanoflakes. They emphasized that cuneiform special type morphology is responsible for efficient charge separation and charge transfer for PEC water-splitting.[24] People have also tried to develop the heterostructure of In$_2$S$_3$/In$_2$O$_3$ to enhance the PEC water-splitting activity. Recently, Xu *et al*. reported that the type-II In$_2$S$_3$/In$_2$O$_3$ heterostructure can show enhanced photocurrent density in PEC water-splitting.[25] Hou and co-workers have synthesized atomically thin mesoporous heterostructure of In$_2$O$_{3-x}$/In$_2$S$_3$ to get the interface bonding at atomic level. The developed In$_2$O$_{3-x}$/In$_2$S$_3$ layers generate a photocurrent of 1.28 mA cm^{-2} at 1.23 V vs. RHE, which is ~21 times higher than In$_2$S$_3$ atomic layers.[26] In another report, Xu *et al*. have reported In$_2$S$_3$/In$_2$O$_3$ heterostructure can generate the highest photocurrent density of 2.5 μA/cm^2, which is ~ 25-fold and 2.5-fold higher than bare In$_2$O$_3$ and bare In$_2$S$_3$, respectively.[27]

In this chapter, nanopyramid of In$_2$S$_3$/In$_2$O$_3$ composite are developed and the photoanodic activity in PEC water-splitting reaction is studied using 0.5M Na$_2$SO$_4$ and 3.5 wt% NaCl. Nanopyramid type structure of In$_2$S$_3$/In$_2$O$_3$ is synthesized on fluorine-doped tin oxide coated glass (FTO) via a hydrothermal technique followed by air calcination. Further to understand the importance of in-situ grown In$_2$O$_3$, the PEC water-splitting activity of bare In$_2$S$_3$ and In$_2$O$_3$ is determined. Nano-bricks of In$_2$S$_3$ is synthesized on FTO via a hydrothermal technique followed by air calcination. It is observed that nanopyramid structure helps in enhanced light absorbance through light trapping by multiple reflection and scattering inside the material. At the same time, efficient photoinduced charge carriers (e$^-$-h$^+$) separation and transportation takes place through in-situ composite formation in the nanopyramidal structure. So, it is assumed that all the above mentioned factors are contributing together to maximize the PEC performance. From the point of practical applicability of the photoelectrode, the PEC performance as well as stability is also determined in 3.5 wt% saline water. Literature indicates that the electrodes which can withstand the corrosive environment of Cl$^-$, may find itself suitable to address the huge energy crisis using plenty of sea water and sunlight.[28] Nanopyramids of In$_2$S$_3$/In$_2$O$_3$ can show efficient photoactivity

as well as outstanding stability. Photocurrent density of 0.83 mA/cm^2 is produced under an applied 1.18 V vs. RHE in 3.5 wt% saline water. The In$_2$S$_3$/In$_2$O$_3$ nanocomposite can generate maximum photocurrent density of 3.02 mA/cm^2 at potential 1.6 V vs. RHE in 0.5 M Na$_2$SO$_4$ which is 8.23-fold higher than nanobrick type bare In$_2$S$_3$. The calculated carrier density (N$_d$) and flat band potential (V$_{FB}$) of In$_2$S$_3$/In$_2$O$_3$ nanocomposite is 7.390×10^{20} cm^{-3} and -0.32 V vs. RHE, respectively. Finally, the nanopyramid shows the maximum photoconversion efficiency (η%) 0.55 at potential 0.77 V vs. RHE, which is 3.64 and 12.79-folds higher than In$_2$S$_3$/In$_2$O$_3$-less crystalline one and bare In$_2$S$_3$, respectively.

3.2 Experimental Section

3.2.1 Synthesis of In$_2$S$_3$/In$_2$O$_3$ Nanopyramide: In$_2$S$_3$/In$_2$O$_3$ nanopyramide was synthesized on FTO via hydrothermal technique using InCl$_3$ and thiourea as the sources of indium and sulfur. Initially, FTO was cleaned with soapy water, a mixture of ethanol and acetone, and Milli-Q water, respectively. Then, 0.397 mmol of InCl$_3$ and 0.599 mmol of thiourea were dissolved in 15 mL of Milli-Q water and stirred to have a homogeneous solution. The cleaned FTO was immersed in a Teflon container and the prepared solution was poured into it. The hydrothermal reaction was followed out at 160 ºC for 6 hours. Sample deposited FTO was rinsed with Milli-Q water and ethanol for 2-3 times and dried well. After the hydrothermal reaction, the sample was calcined at 200 ºC for 5 hours and named as In$_2$S$_3$/In$_2$O$_3$-B-5. To optimize the reaction time and calcination temperature, different conditions were followed. The hydrothermal reaction time was varied as 4, 6 and 8 hours and the samples are named as In$_2$S$_3$/In$_2$O$_3$-A-5, In$_2$S$_3$/In$_2$O$_3$-B-5, and In$_2$S$_3$/In$_2$O$_3$-C-5, respectively. Along with this, the calcination temperature was also varied from 0-12 hours and named as In$_2$S$_3$/In$_2$O$_3$-B-n (n = 0, 3, 5, and 12). The synthesis procedure is shown in **Scheme 3.1**.

3.2.2 Synthesis of In$_2$S$_3$ Nanobricks: Hydrothermal reaction was followed for the synthesis of pure In$_2$S$_3$ nanostructure on the surface of FTO. The similar reaction procedure mentioned above was followed. Here, 0.599 mmol of thioacetamide was used instead of thiourea.

3.2.3 Synthesis of In$_2$O$_3$ Nanocubes: To synthesize In$_2$O$_3$ on the surface of FTO, the similar hydrothermal reaction procedure mentioned above was followed by using urea (0.599 mmol) as a

hydrolyzing agent instead of thioacetamide. After the hydrothermal reaction, calcination process is carried out for 2 hours at 350 ℃.
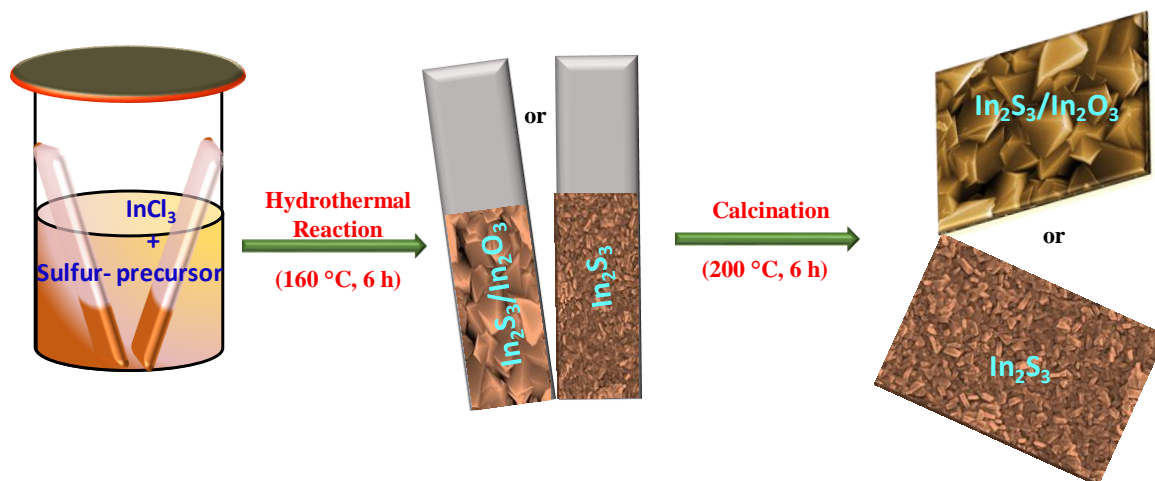
Scheme 3.1: Schematic presentation for the development of In_2S_3/In_2O_3 nanopyramids and nanobricks of In_2S_3.

3.3 Results and Discussions

The characterization and application of developed In_2S_3, In_2O_3, and In_2S_3/In_2O_3 heterostructure are discussed in the below mentioned sections.

3.3.1 Characterization

3.3.1.1 XRD and Raman Analysis

The crystal structure, crystallinity, and phase purity of the synthesized materials are determined with the help of X-Ray diffraction (XRD) analysis. XRD pattern of In_2S_3/In_2O_3-B-0, In_2S_3/In_2O_3-B-3, In_2S_3/In_2O_3-B-5, and In_2S_3/In_2O_3-B-12 are well indexed to the nanocomposite of In_2S_3/In_2O_3 crystal structure. The comparative XRD pattern of In_2S_3/In_2O_3-B-0, In_2S_3/In_2O_3-B-5, and bare In_2S_3 is shown in (**Figure 3.1a**). The diffraction peaks at 14.37 (103), 23.34 (116), 27.52 (109), 28.88 (206), 33.28 (0012), 43.67 (1015), 47.84 (2212), and 56.20 (419) are associated with tetragonal phase (JCPDS no:00-025-0390), and well-matched with the reported literature, [29,30] and the XRD peaks of In_2O_3 are observed at 22.43 (211), 31.66 (222), 41.06 (420), 45.42 (431), 50.11

(521), 51.11(440), 56.43 (611), and 59.47 (541),[31] which confirm the nanocomposite formation of In_2S_3/In_2O_3.
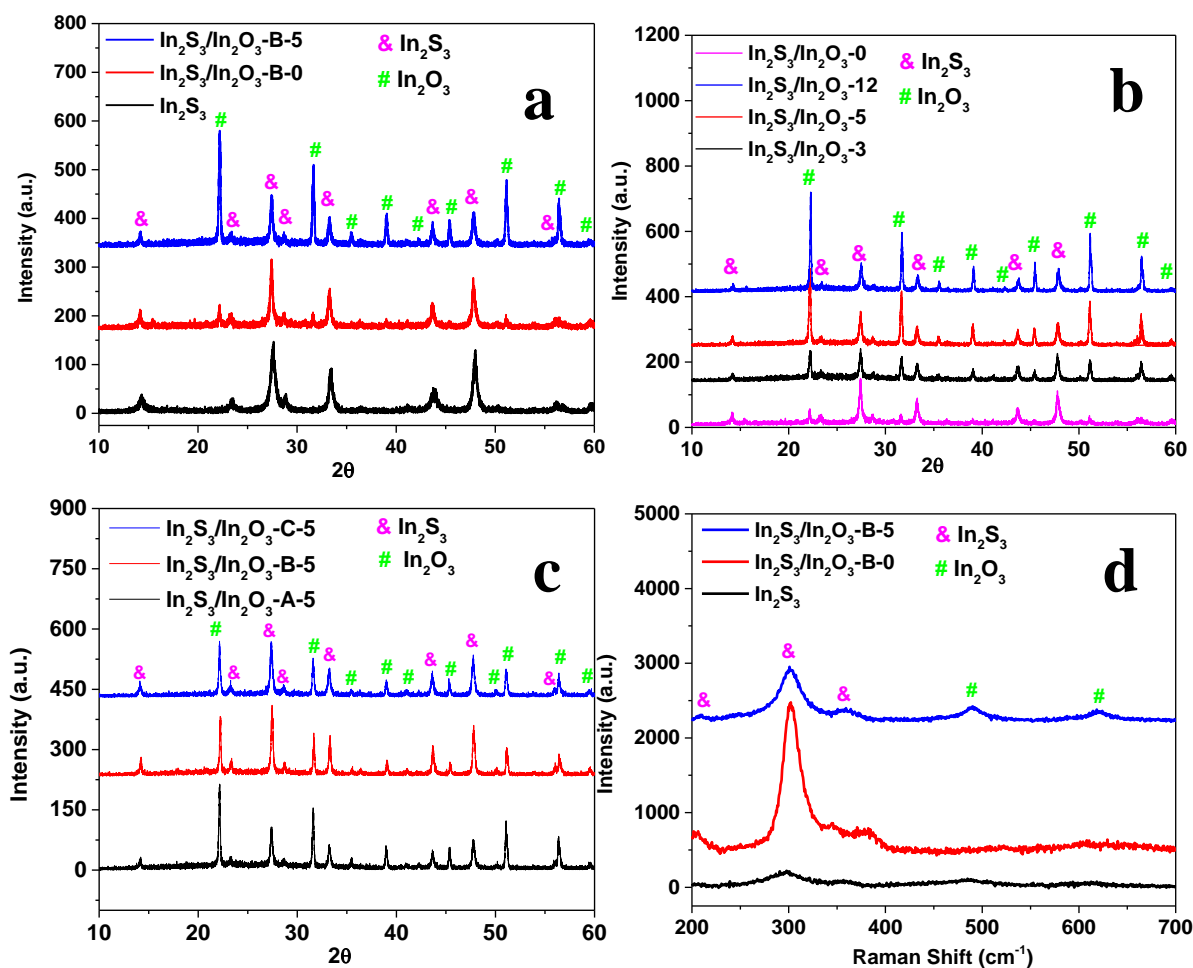
Figure 3.1: Comparative XRD pattern of (a) In_2S_3/In_2O_3-B-5, In_2S_3/In_2O_3-B-0, and In_2S_3, (b) In_2S_3/In_2O_3-B-12, In_2S_3/In_2O_3-B-5, In_2S_3/In_2O_3-B-3, In_2S_3/In_2O_3-B-0, and In_2S_3, (c) In_2S_3/In_2O_3-A-5, In_2S_3/In_2O_3-B-5, and In_2S_3/In_2O_3-C-5, and (d) Raman spectra of In_2S_3/In_2O_3-B-5, In_2S_3/In_2O_3-B-0 and In_2S_3.

The observed ratios of In_2S_3:In_2O_3 in In_2S_3/In_2O_3-B-0, In_2S_3/In_2O_3-B-3, In_2S_3/In_2O_3-B-5 are 3.56:1, 0.9:1, and 0.39:1, respectively. After calcination from 0-5 hours, the peak intensities of all the crystal planes are enhanced, which indicate the improved crystallinity of the In_2S_3/In_2O_3 nanocomposite. For further calcination to 12 hours, it is observed that the peak of In_2O_3 further

enhances more compared to In_2S_3 which indicates the partial conversion of In_2S_3 to In_2O_3 after prolong calcination (ratio of In_2S_3: In_2O_3 is 0.24:1) and comparative PXRD data are shown in **Figure 3.1b**. PXRD pattern of bare In_2S_3 is well-matched with the pure phase tetragonal structure without any side product. So, from PXRD analysis confirms the tetragonal phase In_2S_3/In_2O_3 composite when thiourea was used as hydrolyzing agent in the synthesis. The comparative PXRD pattern of In_2S_3/In_2O_3-A-5, In_2S_3/In_2O_3-B-5, and In_2S_3/In_2O_3-C-5 confirm the composite formation (**Figure 3.1c**).

The crystallinity and the formation of In_2S_3/In_2O_3 composite are further investigated with the help of the Raman analysis and the data is shown in **Figure 3.1d**. In_2S_3/In_2O_3-B-5 shows prominent Raman peaks at 208, 302, and 308 cm^{-1} which are due to the tetragonal phase of In_2S_3.[32,33] The peak at 302 cm^{-1} is associated to the symmetric stretching vibrating mode of InS_4 tetrahedra.[34] Peaks located at 489 and 620 cm^{-1} are depicting the formation of In_2O_3.[35] The observed data certifies the formation of In_2S_3/In_2O_3 nanocomposite. Raman spectra of In_2S_3 indicates the formation of a pure tetragonal phase. Comparative Raman spectra of In_2S_3 and In_2S_3/In_2O_3-B-0 indicates the red shift of peaks which can be attributed due to the composite formation. On the other hand, In_2S_3/In_2O_3-B-5 shows clear peak due to In_2O_3 as well as decrease in peak intensity of In_2S_3. Such decrease in peak intensity of In_2S_3 indicates the partial conversion to In_2O_3 and optimum condition is achieved in the case of In_2S_3/In_2O_3-B-5. The observed blue shift in the peak is due to the incorporation of 'O' in the nanocomposite.[36]

3.3.1.2 XPS Analysis of In_2S_3/In_2O_3

Using X-ray photoelectron (XPS) analysis, the surface composition, oxidation states of the elements are determined. The survey spectrum confirms the presence of 'In', 'S', and 'O' as elements in the nanopyramid composite of In_2S_3/In_2O_3-B-5 (**Figure 3.2a**). The high-resolution XPS spectrum of 'In' indicates the presence of two peaks at 444.6 and 452.1 eV which are due to the presence of $3d_{5/2}$ and $3d_{3/2}$ of In^{3+} (**Figure 3.2b**). The observed result is well-matched with the reported literature.[41] The deconvoluted spectra of 'S^{2-}' assure the presence of S $2p_{1/2}$ and $2p_{3/2}$ peaks at 161.1 eV and 159.9 eV, respectively (**Figure 3.2c**). The observed peaks of 'S' appear at lower binding energy than the reported literature of In_2S_3. The lowering binding energy of 'S^{2-}' in the composite than pure In_2S_3 indicates that the change in the chemical environment of 'S' after formation of the composite. The observed shift towards lower binding energy indicates the

presence of In-O bond where 'O' is more electronegative than 'S'. So, the successful composite formation affects the chemical environment of In_2S_3, can be well understood from the XPS analysis.[27,37] The high-resolution XPS spectra of 'O' 1s is shown in **Figure 3.2d** and spectrum reflect peak at 529.5 eV due to the metal-oxygen (M-O) bond, peak at 530.1 eV due to the presence of defects/under coordinated lattice oxygen on the surface, and the peak at 531.4 eV is due to the adsorbed oxygen on the surface of In_2S_3 /In_2O_3-B-5. So, from the XPS analysis, synthesis of In_2S_3 /In_2O_3 composite is confirmed.
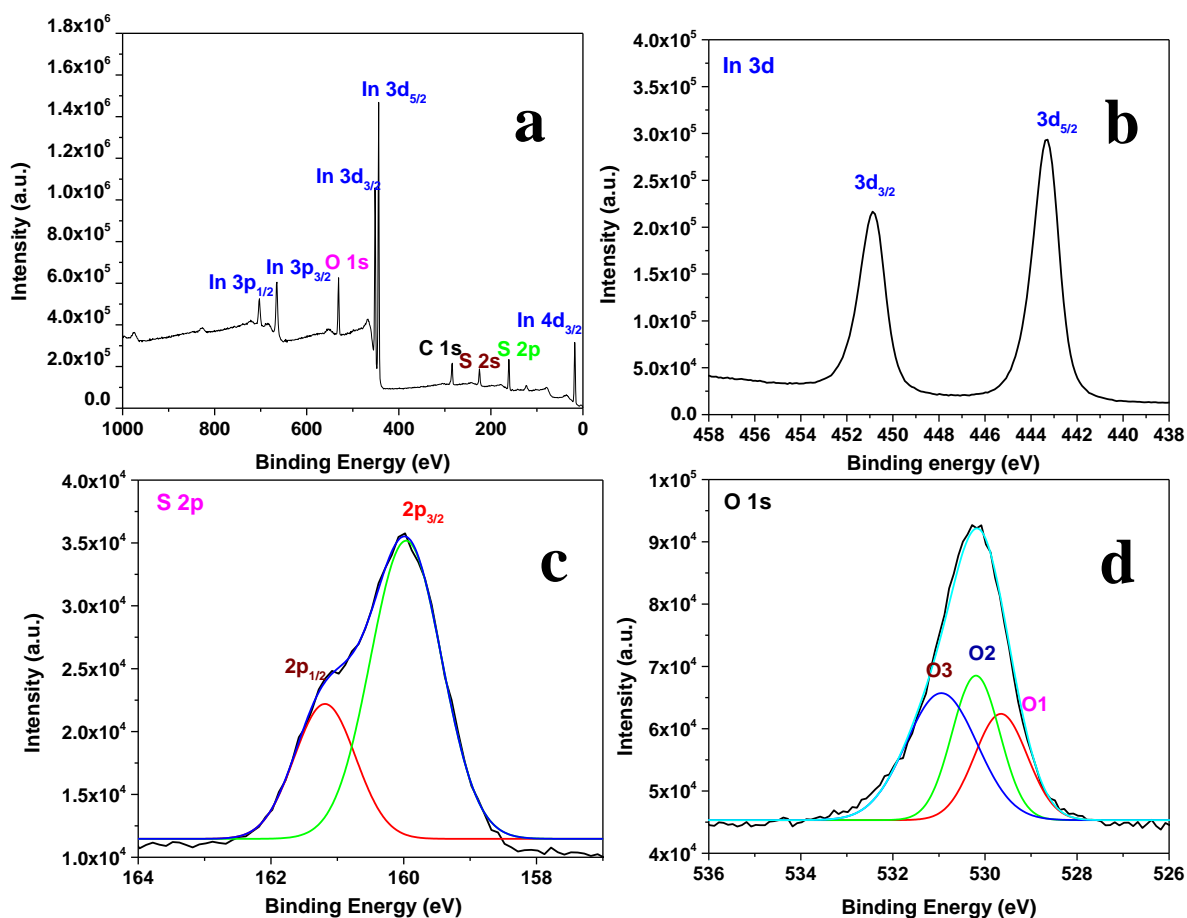
Figure 3.2: (a) XPS survey spectrum of In_2S_3/In_2O_3-B-5, high resolution XPS spectrum of (b) In 3d, (c) S 2p, (d) O 1s, respectively.

3.3.1.3 FESEM and EDS Analysis

To know the morphology of synthesized materials, Field Emission Scanning Electron Microscopy (FESEM) analysis is carried out. FESEM images of the In_2S_3/In_2O_3-B-0 observed in different magnifications are shown in **Figure 3.3a, b**, which indicate the initiation of the growth of non-uniform nanopyramid like structure with blunt edges. Further, the FESEM images of the In_2S_3/In_2O_3-B-5 show the uniform nanopyramid like structure, which is compact and uniformly grown on the FTO surface (**Figure 3.3c**).
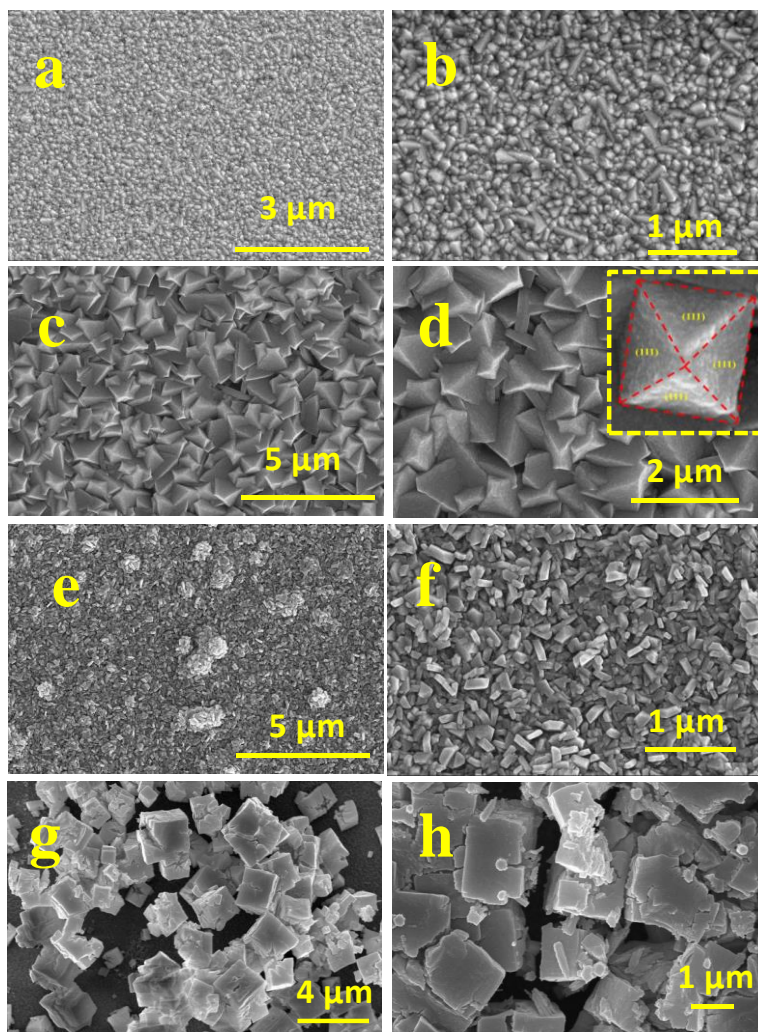
Figure 3.3: FESEM images of (a, b) In_2S_3/In_2O_3-B-0, (c,d) In_2S_3/In_2O_3-B-5 nanopyramid (inset image shows the facets of nanopyramid), (e, f) In_2S_3, and (g, h) In_2O_3, at low and high magnifications, respectively.

High magnification FESEM image is shown in **Figure 3.3d**, which reveals that the bottom of nanopyramid In_2S_3/In_2O_3-B-5 are interlaced with each other.Nanopyramid structures are developed with four triangular faces [(111) crystal plane], oriented in upward direction and with eight edges and five vertices (**Figure 3.3d inset**). Low and high magnification images of In_2S_3 and In_2O_3 shows the nanobrick and nanocube structure, respectively (**Figure 3.3e, f, and 3.3g, h**).

To confirm the elements, present in the synthesized materials EDS mapping and EDS line scanning are carried out. In In_2S_3/In_2O_3-B-5, it is observed that the 'In', 'S, and 'O' are distributed uniformly. The observed result indicates the in-situ formation of nanocomposite in the hydrothermal reaction condition. In the case of In_2S_3 and In_2O_3 'In' and 'S', 'In' and 'O' are present as elements, respectively (**Figure 3.4-3.7**).
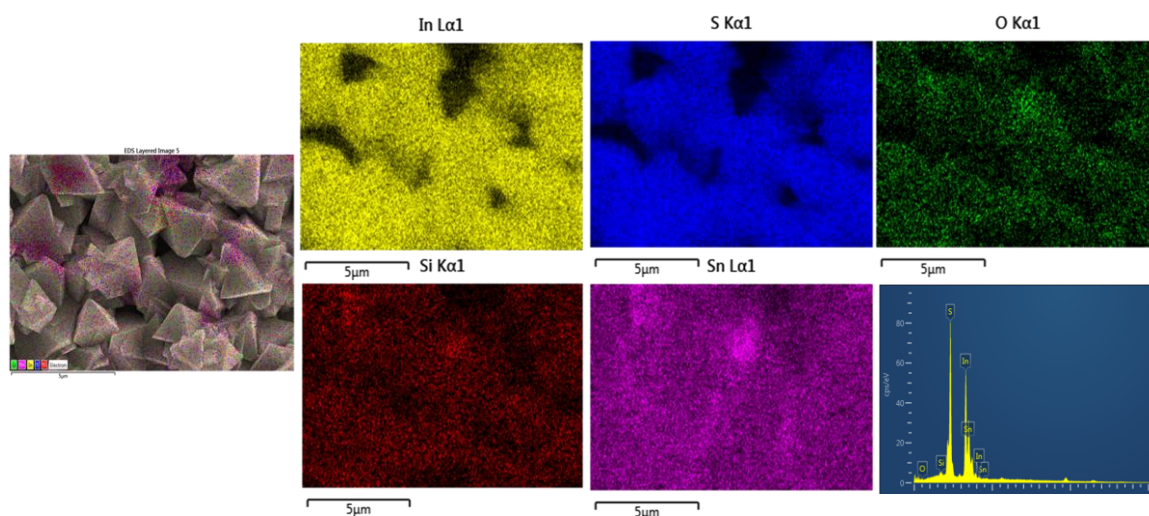
Figure 3.4: EDS analysis of In_2S_3/In_2O_3-B-5 nanocomposite on FTO which shows the uniform distribution of 'In' 'S' and 'O'.
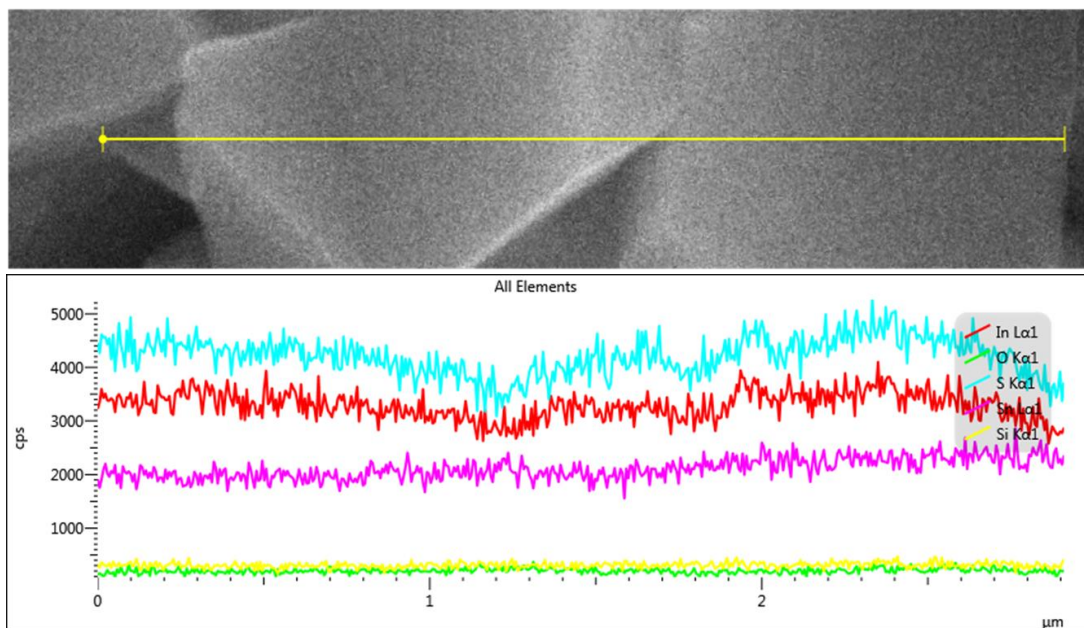
Figure 3.5: EDS line scanning of In$_2$S$_3$/In$_2$O$_3$-B-5 nanocomposite on FTO which shows the uniform distribution of 'In' 'S' and 'O'.
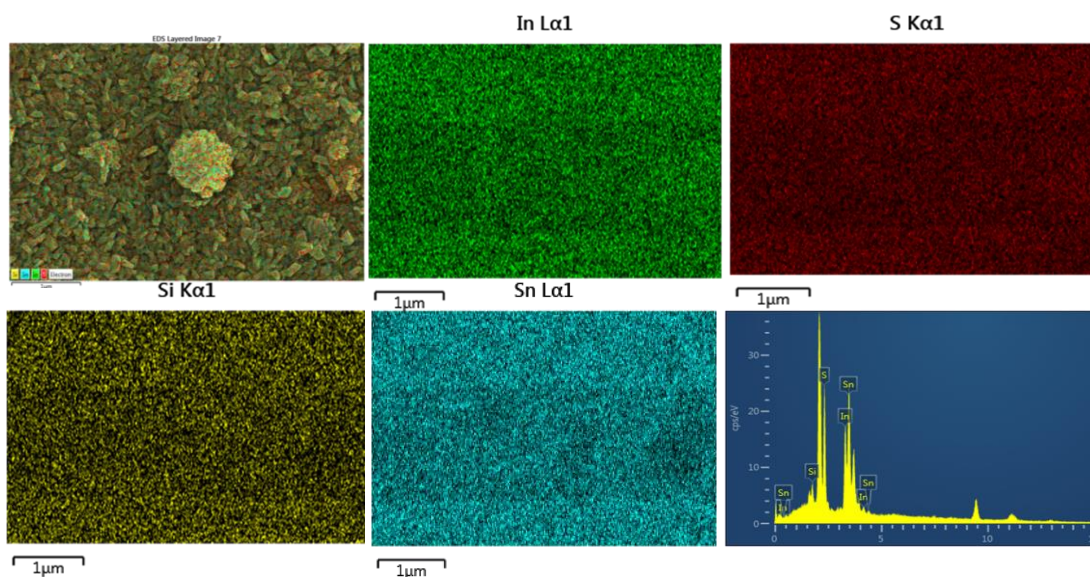
Figure 3.6 : EDS analysis of In$_2$S$_3$ nanobricks on FTO which shows the uniform distribution of 'In'and 'S'.
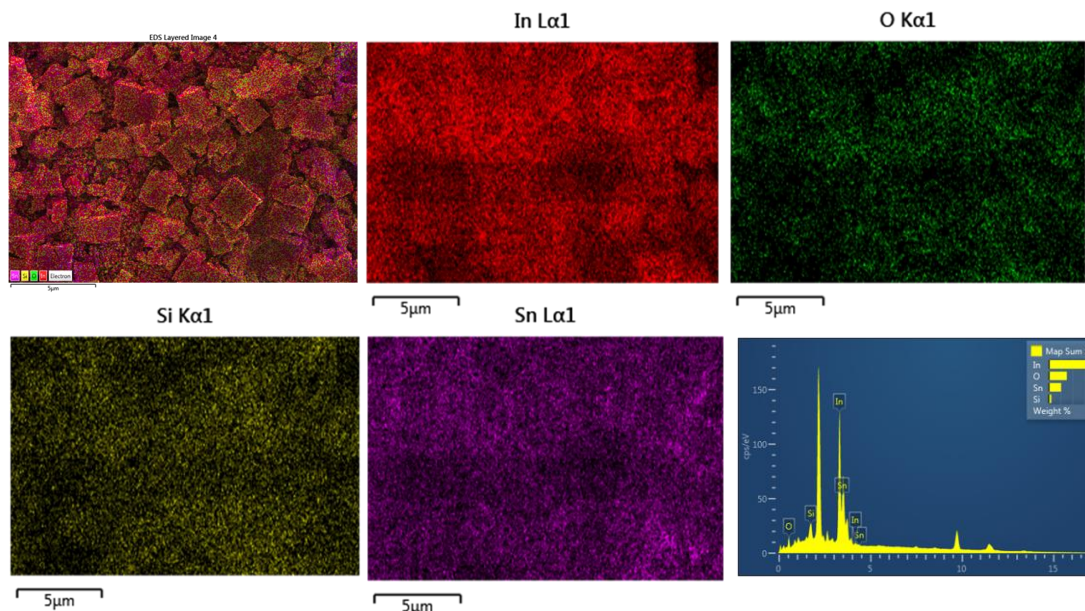
Figure 3.7: EDS analysis of In_2O_3 on FTO which shows the uniform distribution of 'In' and 'O'.

3.3.1.4 Optical Activity

With the help of UV-Visible absorbance spectroscopy, the optical properties of the synthesized materials are determined (**Figure 3.8a**). The developed nanopyramid of In_2S_3/In_2O_3-B-5 shows enhanced visible light absorbance with a band edge at ~600 nm compare to bare In_2S_3, where the band edge is located at ~500 nm. The red shift in the absorbance band edge reflects the higher capability of visible light absorbance by the nanopyramid structure of In_2S_3/In_2O_3-B-5 than the nanobrick of In_2S_3. So, the successive increase in optical absorbance as well as widen the absorbance band indicate the effectiveness of the nanopyramidal structure and composite formation. The faceted nanopyramidal structure helps in multiple reflection and scattering of light inside the material which increase the matter and light interaction. The UV-visible spectra of bare In_2O_3 is shown in **Figure 3.8b**.
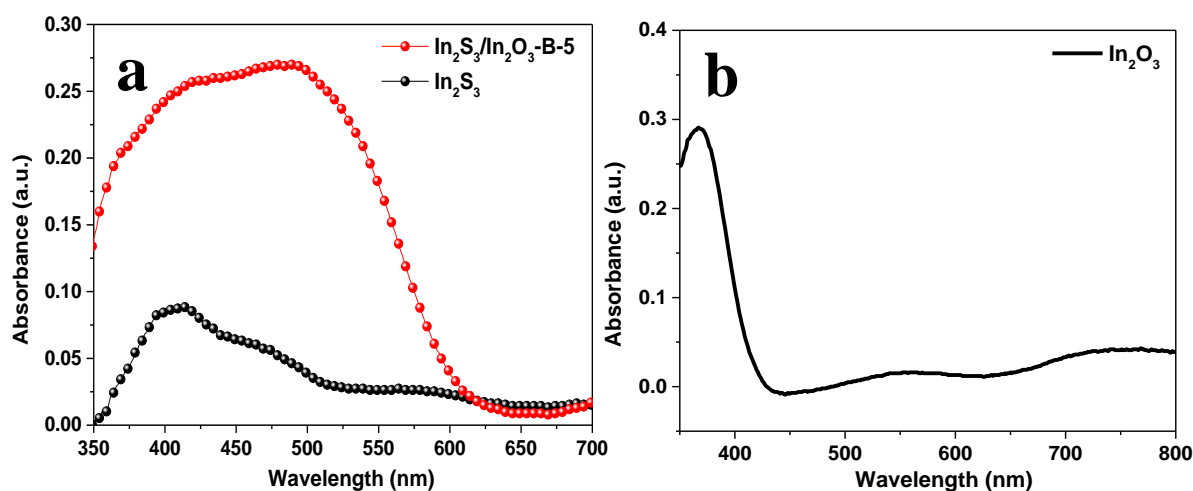
Figure 3.8 : UV-visible spectra of (a) In_2S_3/In_2O_3-B-5, and In_2S_3, (b) In_2O_3.

The band gap of bare In_2S_3 and In_2O_3 are calculated with the help of cyclic voltammetry technique (**Figure 3.9a, b**).[38-39] The results indicate that the bare In_2S_3 and In_2O_3 have band gap 2.4 eV and 2.7 eV, respectively. The conduction band and valence band edges for the In_2S_3 are -3.50 and -5.90 eV vs. vacuum. On the other hand, the conduction band and valence band edges for the In_2O_3 are -3.93 and -6.65 eV vs. vacuum.
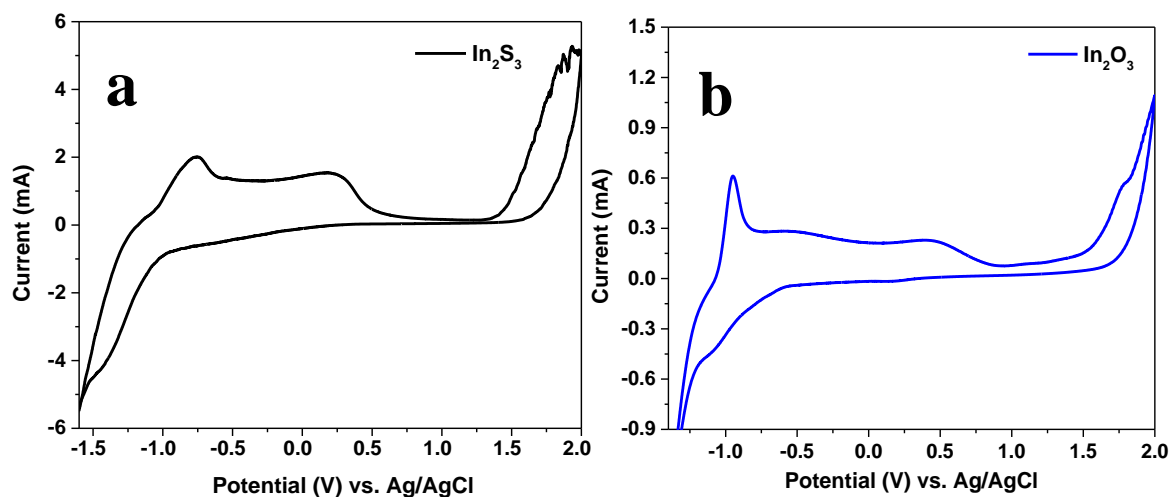
Figure 3.9: CV plot of (a) bare In_2S_3, (b) bare In_2O_3.

3.3.2 Mechanism for the development of the nanocomposite

For the synthesis of In_2S_3/In_2O_3 nanocomposite, thiourea has played an important role. When TAA (Thioacetamide) is used as a sulfur source for the synthesis of metal sulfide nanostructure, it is observed that pure phase metal sulfide is developed. Whereas, when Tu (Thiourea) is used as a hydrolyzing agent, the nanocomposite of In_2S_3/In_2O_3 is developed. The reason behind this is the limited supply of S^{2-} by Tu compared to TAA. To determine comparatively the released amount of S^{2-} from the hydrolysis of Tu and TAA, the blank hydrothermal reaction is carried out using equal mole of Tu and TAA following the same condition separately. Further released S^{2-} is determined with the help of a UV-visible spectrophotometer using sodium nitroprusside as the model reactant. From the comparative UV-visible absorbance spectra of sodium thio nitroprusside from Tu and TAA, it can be concluded that the released amount of S^{2-} is higher in TAA compared to Tu. As, Tu supply comparatively less amount of S^{2-}, there is a high probability for the formation of In_2O_3 along with In_2S_3 in the reaction condition where water is used as solvent (**Figure 3.10a, b**).
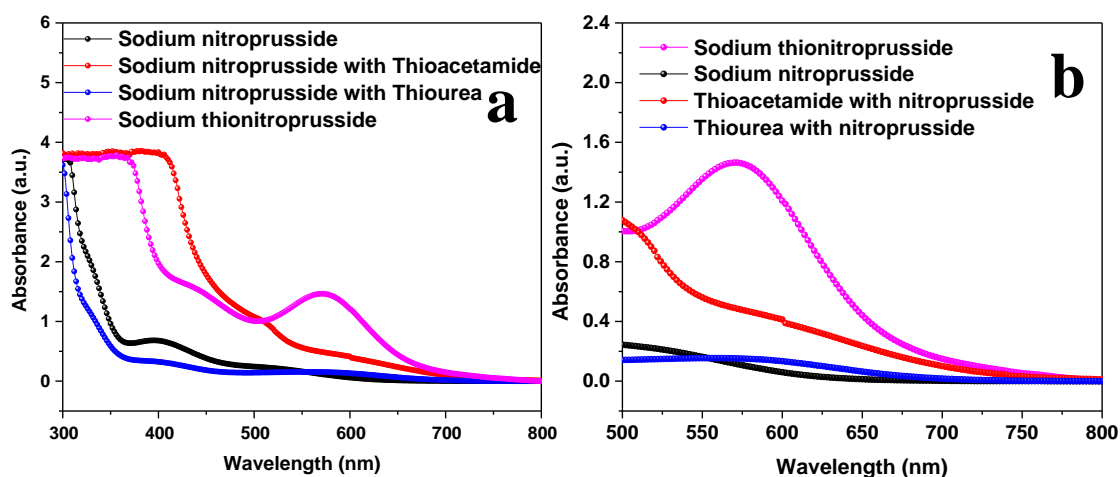
Figure 3.10: Comparative UV-visible spectra of (a, b) thiourea and thioacetamide with sodium nitroprusside.

3.3.3 Photoelectrochemical Activity

3.3.3.1 Linear Sweep Voltametry

The PEC performance of the synthesized photoanodes are determined with the help of linear sweep voltammetry (LSV) under back irradiation of light ($100 \ mW/cm^2$) using the Ag/AgCl, Pt wire, and

the sample decorated FTO as the reference, counter and the working electrode, respectively. Aqueous solution of 0.5 M Na_2SO_4, and 3.5 wt% saline water are used as electrolyte for the PEC water-splitting reaction. Upon continuous application of potential, photocurrent density increases under the irradiation of light. The stability of the materials is determined with the help of the chronoamperometry technique. All the electrochemical measurement data are obtained with respect to Ag/AgCl (reference) and converted to RHE applying the Nernst equation. The nanocomposite of In_2S_3/In_2O_3-B-5 shows efficient activity towards PEC water-splitting reaction where it can produce a photocurrent density of 2.24 mA/cm^2 at 1.23 V vs. RHE.
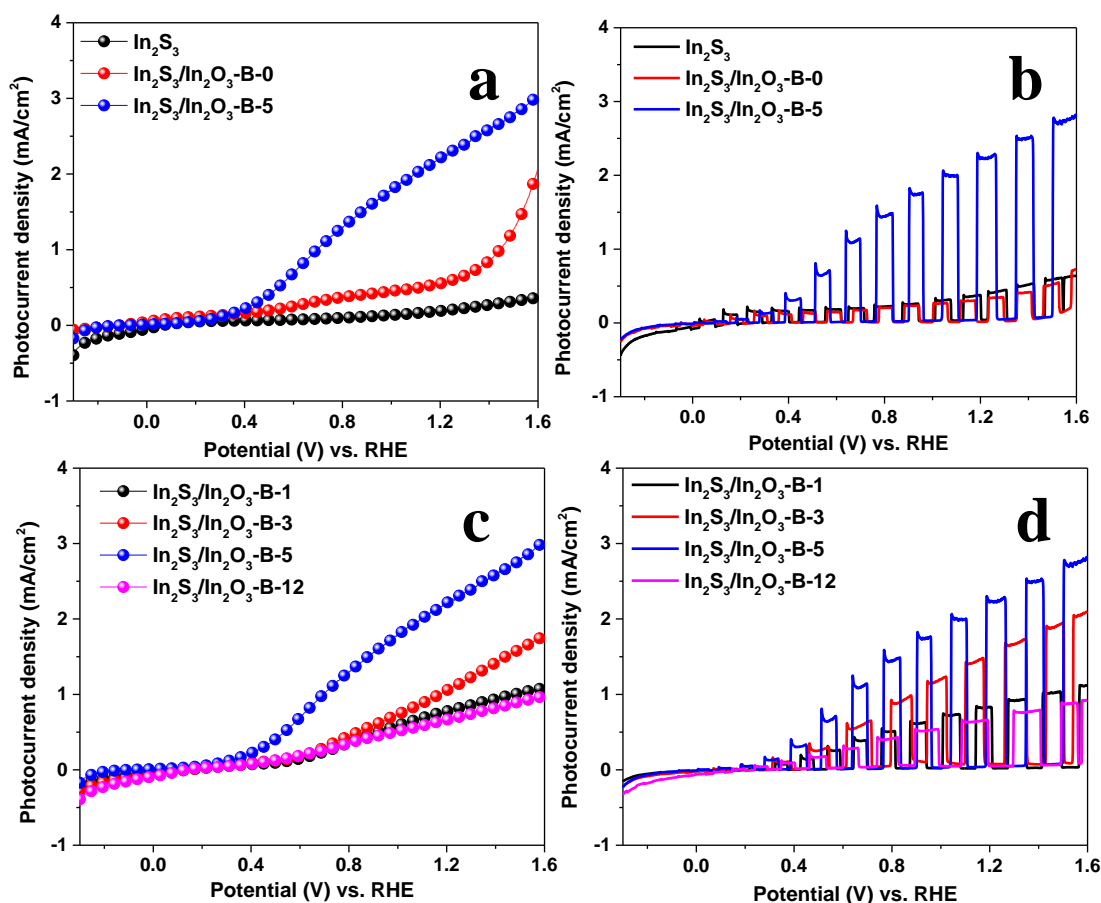
Figure 3.11: LSV plots of In_2S_3/In_2O_3-B-5, In_2S_3/In_2O_3-B-0, and In_2S_3 under (a) continuous illumination and (b) chopped illumination, (c, d) continuous and chopped illumination of In_2S_3/In_2O_3-B-1, In_2S_3/In_2O_3-B-3, In_2S_3/In_2O_3-B-5, In_2S_3/In_2O_3-B-12 in 0.5 M Na_2SO_4.

Whereas, In_2S_3/In_2O_3-B-0 can generate a photocurrent density of 0.58 mA/cm^2 at the same potential. It is important to note that with the increase in the amount of In_2O_3 in In_2S_3 as well as the enhanced crystallinity of the nanocomposite successively help to increase the photocurrent density, which is ~ 3.86-fold. In_2S_3/In_2O_3-B-5 can generate maximum photocurrent density of 3.02 mA/cm^2 at an applied potential of 1.6 V vs. RHE which is 1.45-fold higher than that of In_2S_3/In_2O_3-B-0, and the comparative LSV plot is shown in **Figure 3.11a**. The chopped illumination data of In_2S_3, In_2S_3/In_2O_3-B-0, and In_2S_3/In_2O_3-B-5 are shown in **Figure 3.11b** and it shows negligible dark current under the applied potential window. The enhancement in photocurrent density is observed due to the formation of In_2S_3/In_2O_3 nanocomposite with enhanced crystallinity and enhanced light absorbance efficiency of the faceted nanopyramidal structure. Further it is verified with the help of In_2S_3/In_2O_3-B-1, 3 and 12 electrodes. In_2S_3/In_2O_3-B-1, and 3 can generate maximum photocurrent densities of 0.80, and 1.11 mA/cm^2 at 1.23 V vs. RHE, respectively which are higher compared to In_2S_3/In_2O_3-B-0. It indicates that with the increase in the amount of In_2O_3 in In_2S_3, the PEC activity enhances, and the optimum condition is obtained in the case of In_2S_3/In_2O_3-B-5. With a further increase in calcination time to 12 hours, photocurrent density (0.68 mA/cm^2) dramatically decreases (**Figure 3.11c**). It may be presumed that excess amount of In_2O_3 in the nanocomposite of In_2S_3/In_2O_3 leads to decreased PEC activity. The chopped illumination data of In_2S_3/In_2O_3-B-0, 1, 3, 5 and 12 are shown in **Figure 3.11d**, which indicates that all the developed materials show negligible dark current under the used potential window.
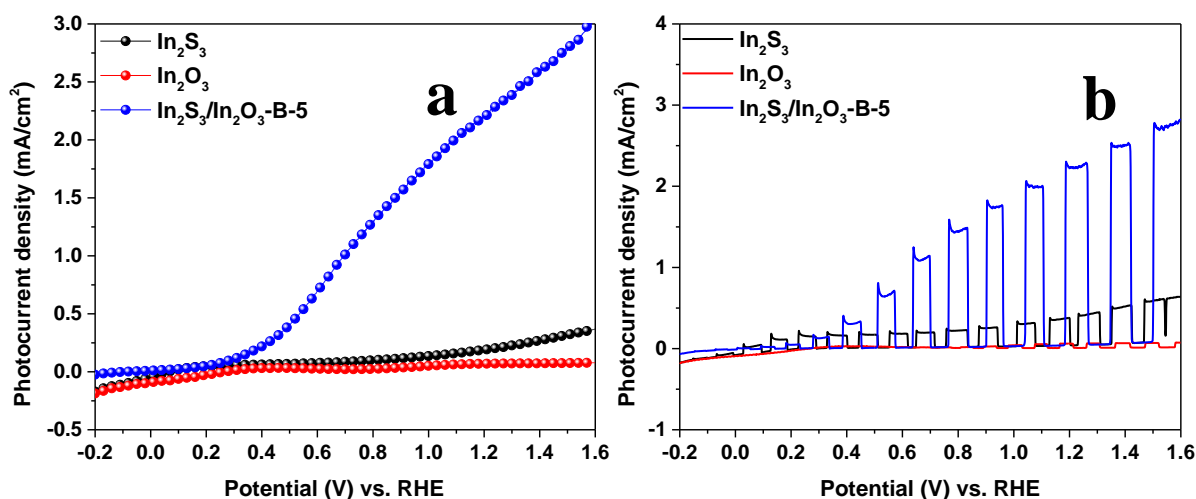
Figure 3.12: Comparative LSV plot of bare In_2S_3, bare In_2O_3, and In_2S_3/In_2O_3-B-5 in 0.5 M Na_2SO_4 under (a) continuous illumination and (b) chopped illumination condition, respectively.

To ensure the role of In_2O_3 in the nanocomposite, the photoactivity of In_2S_3 is determined. Bare In_2S_3 can generate photocurrent density of 0.20 mA/cm^2 at potential 1.23 V vs. RHE, that is ~2.90-fold and ~11.2-fold lower than In_2S_3/In_2O_3-B-0, and In_2S_3/In_2O_3-B-5, respectively. In_2S_3/In_2O_3-B-5 can generate maximum photocurrent density 3.02 mA/cm^2 at potential 1.6 V vs. RHE which is 8.22 and 1.45-fold is higher than In_2S_3 and In_2S_3/In_2O_3-B-0, respectively and comparative LSV data are shown in **Figure 3.11a**. Bare In_2O_3 shows weak PEC response and the observed LSV under continuous and chopped illumination are shown in **Figure 3.12a, b**. The observed enhanced photocurrent density is due to the formation of the nanocomposite of In_2S_3/In_2O_3 and the faceted nanopyramidal structure. In the nanocomposite of In_2S_3/In_2O_3 the induced synergistic effect will help to achieve the maximum PEC activity.

Here, morphology plays a significant role for the enhancement in PEC performance. In_2S_3/In_2O_3 has a close-packed faceted nanopyramidal structure, while the bare In_2S_3 has a nanobrick like structure. Nanopyramid structure helps in the effective light trapping through multiple reflection and scattering of light inside the material, which further increases the light and matter interaction. So, as a result it can absorb more visible light than the nanobrick like structure (**Scheme 3.2a**). The close packing of In_2S_3/In_2O_3-B-5 covers the large volume of the material. It results in enhanced light-matter interaction leading to enhanced light absorbance. Nanopyramids can decouple the direction of light absorbance and charge carrier collection.[40] Due to having such nanopyramid like structure charge transportation will be faster because the minority charge carriers need to travel lesser path to react with the electrolyte.
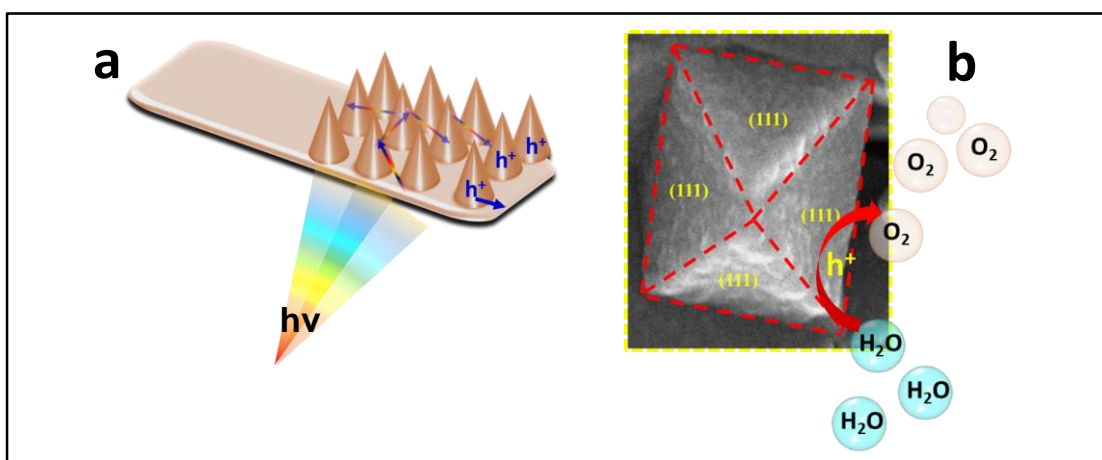
Scheme 3.2: (a) Light traping in vertically grown In_2S_3/In_2O_3 nanopyramids, (b) Water oxidation reaction at exposed (111) facets of In_2S_3/In_2O_3 nanopyramids.

On the other hand, nanopyramid has the four exposed (111) facets which have high surface energy, attributed to the higher mobility of holes and the high abundance of dangling bonds as oxidation sites. It plays an important role to increase the water oxidation activity.[41-42] So, the cumulative effect of nanopyramid morphology with exposed (111) facets, and in situ formation of composite are responsible to better performance in PEC water-splitting than nanobrick and nanocube structure (**Scheme 3.2b**).

To determine the optimum condition of hydrothermal duration, PEC activity of In_2S_3/In_2O_3-A-5, In_2S_3/In_2O_3-B-5, and In_2S_3/In_2O_3-C-5 are determined and the comparative LSV data are shown in **Figure 3.13a**. In_2S_3/In_2O_3-B-5 can generate 2.24 mA/cm^2 photocurrent density at 1.23 V vs. RHE, whereas In_2S_3/In_2O_3-A-5 and In_2S_3/In_2O_3-C-5 can generate photocurrent density 0.74, and 1.10 mA/cm^2 photocurrent density at the same potential (1.23 V vs. RHE), respectively.
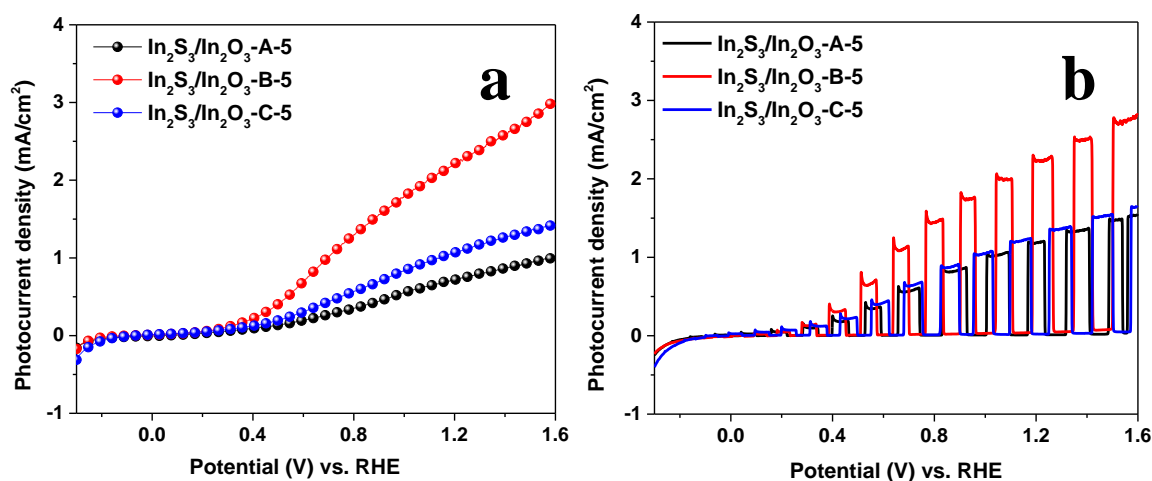
Figure 3.13: LSV plots of In_2S_3/In_2O_3-A-5, In_2S_3/In_2O_3-B-5, and In_2S_3/In_2O_3-C-5 in 0.5 M Na_2SO_4 under (a) continuous illumination and (b) chopped illumination condition, respectively.

The photocurrent densities of In_2S_3/In_2O_3-A-5 and In_2S_3/In_2O_3-C-5 are ~ 3.01 and 2.03-fold lower than In_2S_3/In_2O_3-B-5. The chopped illumination data of In_2S_3/In_2O_3-A-5, In_2S_3/In_2O_3-B-5, and In_2S_3/In_2O_3-C-5 are shown in **Figure 3.13b** and it shows negligible dark current. The limiting photocurrent density of In_2S_3/In_2O_3-B-5 is ~2.99 and 2.11-fold higher than In_2S_3/In_2O_3-A-5 and In_2S_3/In_2O_3-C-5, respectively. In_2S_3/In_2O_3-B-5 is observed as the best photoelectrode in PEC water-splitting. Along with the enhancement in photocurrent density, a cathodic shift in onset

potential for the nanocomposite is observed. Onset potential of In_2S_3/In_2O_3-B-0 is -0.213 V vs. RHE. Whereas onset potential for bare In_2S_3 and nanocomposite of In_2S_3/In_2O_3-B-5 are -0.151 V and -0.145 V vs. RHE. The negative shift in the onset potential reveals uplifting of the fermi level, which facilitate the charge carrier separation as well as transportation in the developed material.

From the point of practical application, the PEC activity of In_2S_3/In_2O_3-B-5 is determined in 3.5 wt% saline water (sea-water). Interestingly, the developed nanocomposite can generate photocurrent density of 0.61 and 0.83 mA/cm^2 at applied potentials of 0.98 and 1.18 V vs. RHE (**Figure 3.14a**). It shows very negligible dark current and switch off-on behavior under chopped illumination (**Figure 3.14b**).
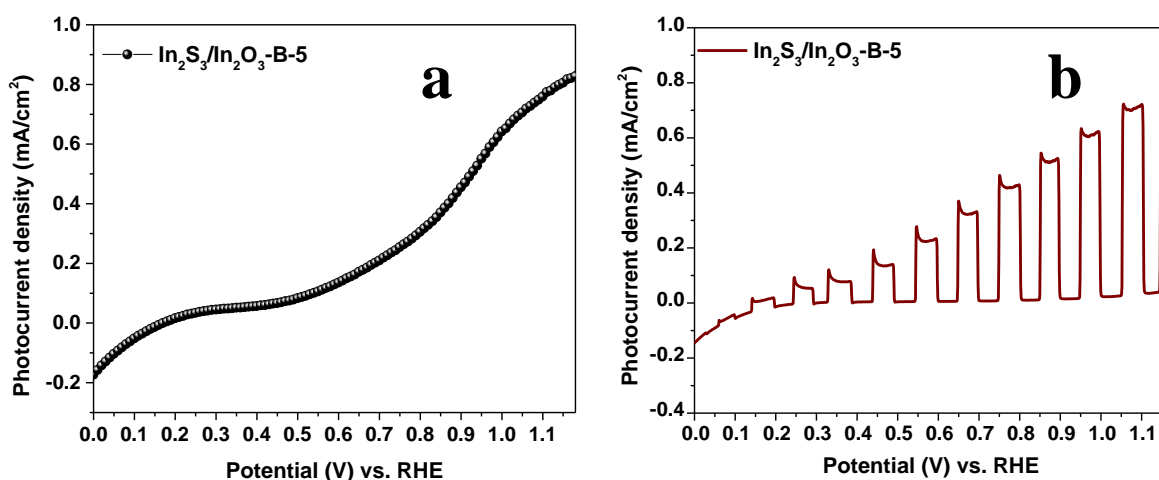
Figure 3.14: LSV plot of In_2S_3/In_2O_3-B-5 (a) under continuous, and (b) chopped illumination condition in 3.5 wt% saline water.

3.3.3.2 Photostability and stability of Photoanodes

The photostability of the nanocomposite is determined at 0.6 V vs. RHE up to 90 seconds and shown in **Figure 3.15a**. The observed anodic spikes originate due to the accumulation of holes at the electrode/electrolyte interface. These holes are not injected in the electrolyte due to the sluggish kinetics. Instead, they have the ability to oxidize trap states in the bulk and on the surface. The long-term stability of the nanocomposite is determined for 1000 seconds in 0.5 M Na_2SO_4 which shows a little decay in photocurrent density (**Figure 3.15b**). Whereas, the developed

nanocomposite is very stable in 3.5 wt% saline water. It can generate unaltered photocurrent density upto 1 h which indicates the superior corrosion resistance nature (**Figure 3.15c-e**).
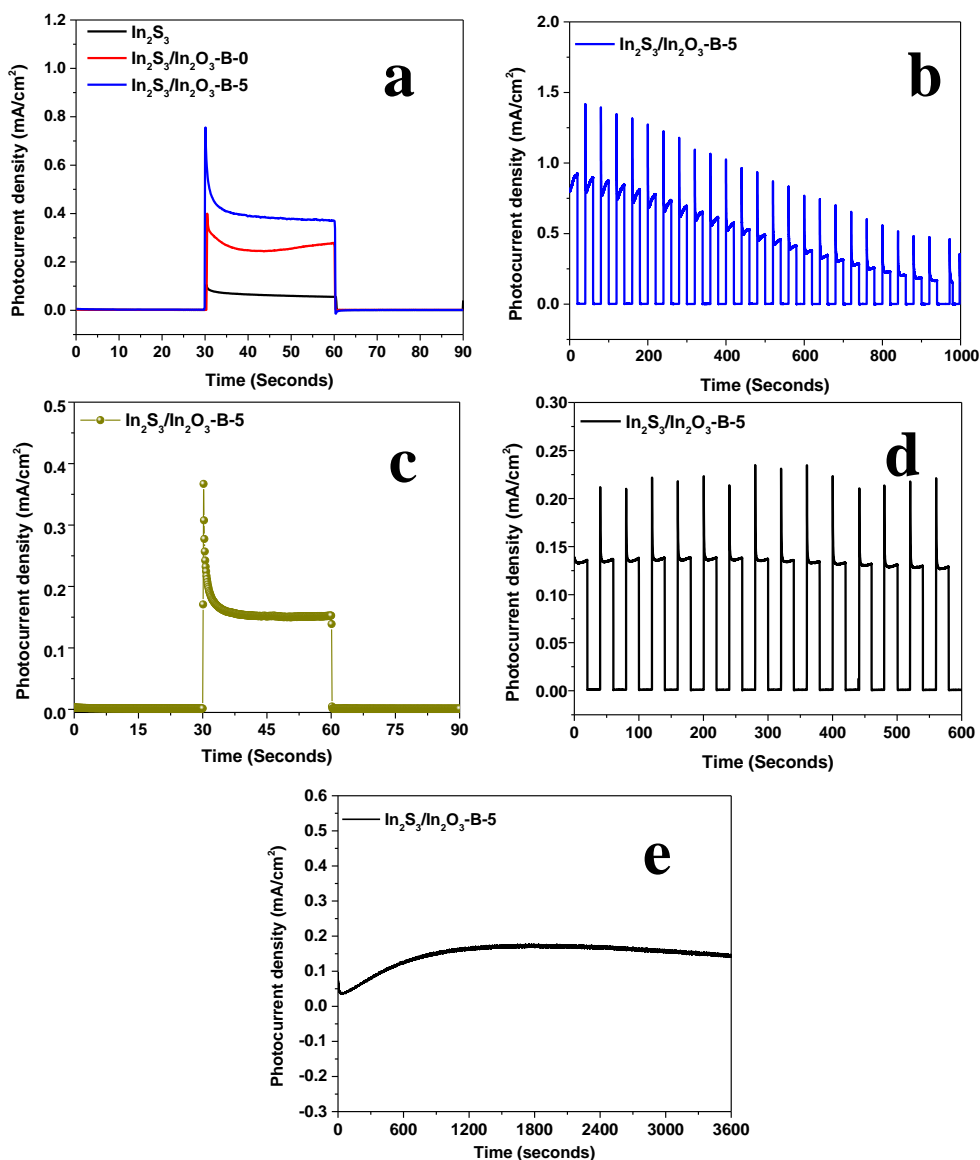
Figure 3.15: (a) i-t plot of In$_2$S$_3$/In$_2$O$_3$-B-5, In$_2$S$_3$/In$_2$O$_3$-B-0, and In$_2$S$_3$ at potential of '0.6' V vs. RHE for 90 seconds in chronoamperometry study, (b) plot of photostability of In$_2$S$_3$/In$_2$O$_3$-B-5 at potential of '0.6' V vs. RHE for 1000 seconds under chopped illumination in 0.5 M Na$_2$SO$_4$, respectively. Chronoamperometry (i-t) plot of In$_2$S$_3$/In$_2$O$_3$-B-5, at potential of '0.98' V vs. RHE for (c) 90 seconds, (d) 600 seconds, and (e) 1h in 3.5 wt% NaCl, respectively.

The morphological robustness of In$_2$S$_3$/In$_2$O$_3$-B-5 nanopyramid is checked after PEC water-splitting with the help of FESEM analysis and it is observed that the In$_2$S$_3$/In$_2$O$_3$-B-5 can retain its morphology (**Figure 3.16a, b**).
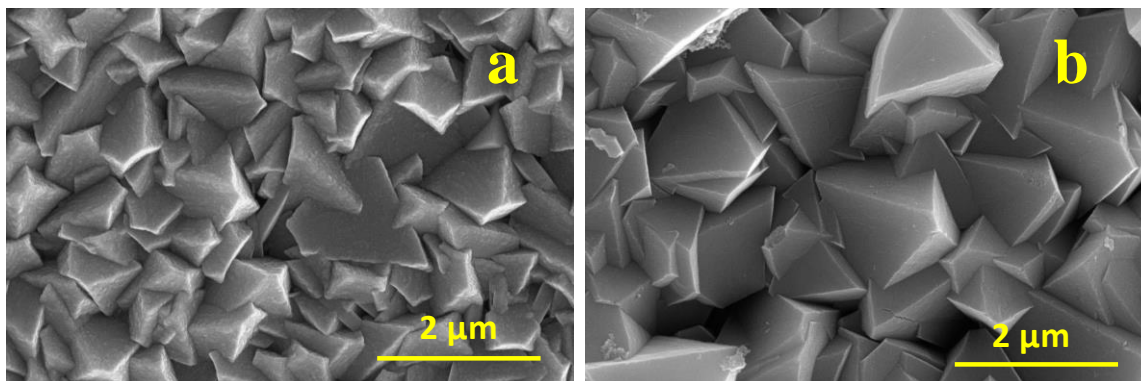
Figure 3.16: FESEM images of In$_2$S$_3$/In$_2$O$_3$-B-5 after PEC in 0.5 M Na$_2$SO$_4$ at (a, b) low and high magnifications, respectively.

3.3.3.3 Determination of Carrier Density through Mott-Schottky Measurements, Impedance Spectra, and Photoconversion Efficiencies

Further to strengthen the observation on the superior activity of In$_2$S$_3$/In$_2$O$_3$-B-5, electronic properties, and carrier concentration are quantitatively elucidated with the help of Mott-Schottky analysis. It is presumed that the superiority is originated due to the presence of an optimum amount of In$_2$O$_3$ as well as due to the faceted nanopyramid structure. **Figure 3.17a** shows the comparative MS plot indicating the flat band potential values of In$_2$S$_3$, and In$_2$S$_3$/In$_2$O$_3$-B-5 nanocomposite. The carrier density and flat band potentials are calculated with the help of the following equation.[43,44]

$$1/Cs^2 = (2/e\varepsilon\varepsilon_0N_dA^2) \, [(V-V_{FB}-kT/e)]$$

Where C, N$_d$, e, ε_0, ε, V$_{FB}$, A, T, and k are specific capacitance, carrier density, electron charge, electric permittivity of vacuum, dielectric constant of the semiconductor, flat band potential, area of the sample, temperature, and Boltzmann constant, respectively. The positive slopes of the synthesized materials indicate the n-type nature of the semiconductor. Flat band potential (V$_{FB}$) is one of the most important physical parameters to study the semiconductor materials and can be calculated by the extrapolation of the Mott-Schottky plot. The calculated flat band potential of the In$_2$S$_3$/In$_2$O$_3$-B-5 is -0.32 V vs. RHE, which is more negative compared to In$_2$S$_3$ nanobricks (-0.15 V vs. RHE). The negative shift in the flat band potential shows the faster charge transportation of

the carrier species for the water oxidation reaction. The slope of In_2S_3/In_2O_3-B-5 nanocomposite is 1.470×10^{10} F^{-2} cm^4 V^{-1} and carrier density is 7.390×10^{20} cm^{-3}, which is 3.25-fold is higher than In_2S_3 (slope = 4.775×10^{10} F^{-2} cm^4 V^{-1}, N_d = 2.27×10^{20} cm^{-3}). The higher carrier density of the nanocomposite of In_2S_3/In_2O_3-B-5 dictates the higher PEC activity of the material.
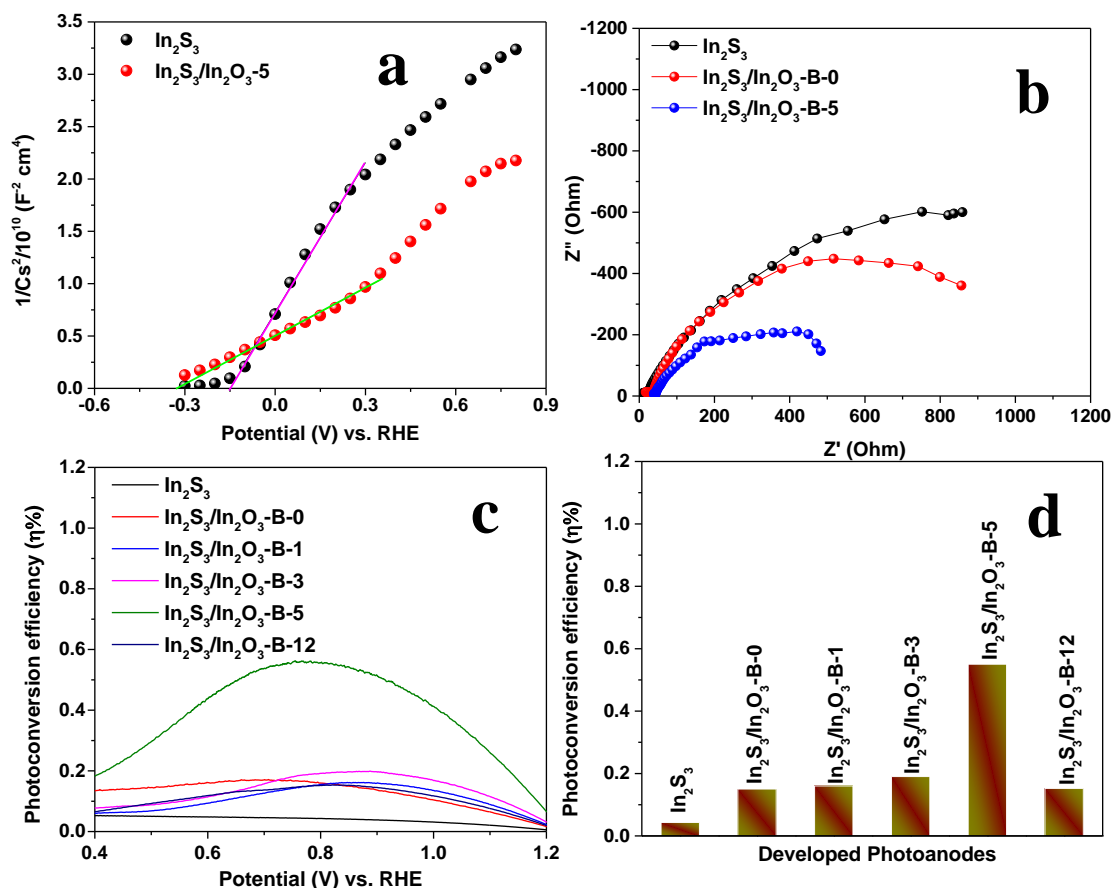
Figure 3.17: (a) Mott-Schottky plot of In_2S_3/In_2O_3-B-5, and In_2S_3, (b) EIS plot of In_2S_3/In_2O_3-B-5, In_2S_3/In_2O_3-B-0, and In_2S_3, (c, d) photoconversion efficiency of In_2S_3/In_2O_3-B-1, -3, -5, -12, -0, and In_2S_3.

To further investigate the ease of charge transportation of In_2S_3/In_2O_3 nanocomposite, electrochemical impedance analysis is carried out under the irradiation of light upon applying the potential of 0.6 V vs. RHE (**Figure 3.17b**). The radius of the obtained arc of In_2S_3/In_2O_3-B-5 nanocomposite is significantly smaller than that of In_2S_3/In_2O_3-B-0, and In_2S_3. It reflects the lower charge transfer resistance, higher charge transportation, and further effective charge separation of

photoinduced electron-hole pair in the In_2S_3/In_2O_3 nanocomposite. The lower R_{CT} further assists to acquire higher photocurrent density in PEC water-splitting. The formation of nanocomposite and the nanopyramidal structure show the cumulative effect for the enhancement of PEC water-splitting performance.

Further, to quantify the efficacy of the nanopyramidal structure, photoconversion efficiency (η %) is determined. The photoconversion efficiency is calculated with the help of the J-V curve and the following equation is used:[45,46]

$$\eta = [J (1.23-V_{RHE})/P_{in}] \%$$

where J = photocurrent density, V_{RHE} = applied potential with respect to RHE, and P_{in} = incident light intensity. The maximum photoconversion efficiency is observed in the case of In_2S_3/In_2O_3-B-5 nanopyramid structure, that is 0.55% at 0.770 V vs. RHE. Whereas, In_2S_3/In_2O_3-B-0 and bare In_2S_3 show 0.151% and 0.043% at 0.710 V and 0.815 V vs. RHE, respectively (**Figure 3.17c, d**). The maximum photoconversion efficiency signifies the maximum photon trapping by the nanopyramids. Nanopyramids have more exposed (111) facets which have high surface energy and play a role to increase the water oxidation activity. At the same time, there is maximum charge separation and transportation in the case of the nanopyramid structure.

3.3.3.4 Determination of Charge Injection and Charge Separation Efficiencies

To estimate the role of composite material in the PEC activity enhancement, the charge separation (η_{sep}%) and charge injection efficiencies (η_{inj}) are determined. To measure the charge injection efficiency photocurrent density is measured in 0.5 M Na_2SO_4 along with EDTA and methanol as hole scavenger. The photocurrent density arising from PEC water-splitting depends on the following factors:

$$J_{PEC}= J_{abs} \times \eta_{sep} \times \eta_{inj}$$

where J_{abs} is the maximum photocurrent density when photons are completely converting into current (J_{abs}). The addition of hole scavengers as the electrolyte can largely suppress the surface recombination of charge carriers without influencing the charge separation in the electrode bulk (i.e., η_{trans} could be regarded as 100%). Therefore, η_{sep} and η_{inj} can be determined as following:[30]

$$\eta_{sep} = J_{hole\ scavanger}/J_{abs,}\ and\ \eta_{inj} = J_{H2O}/ J_{hole\ scavenger}$$

where J_{H2O} and $J_{hole\ scavenger}$ is the observed photocurrent density in H_2O and in the presence of hole scavenger, respectively. The charge injection efficiencies of the nanopyramid composite are

84.52% and 67.26% at the potential of 1.23 V vs. RHE in the presence of EDTA and methanol, respectively. These are ~5.67 and ~ 4.24-fold higher than bare In_2S_3 nanobricks.
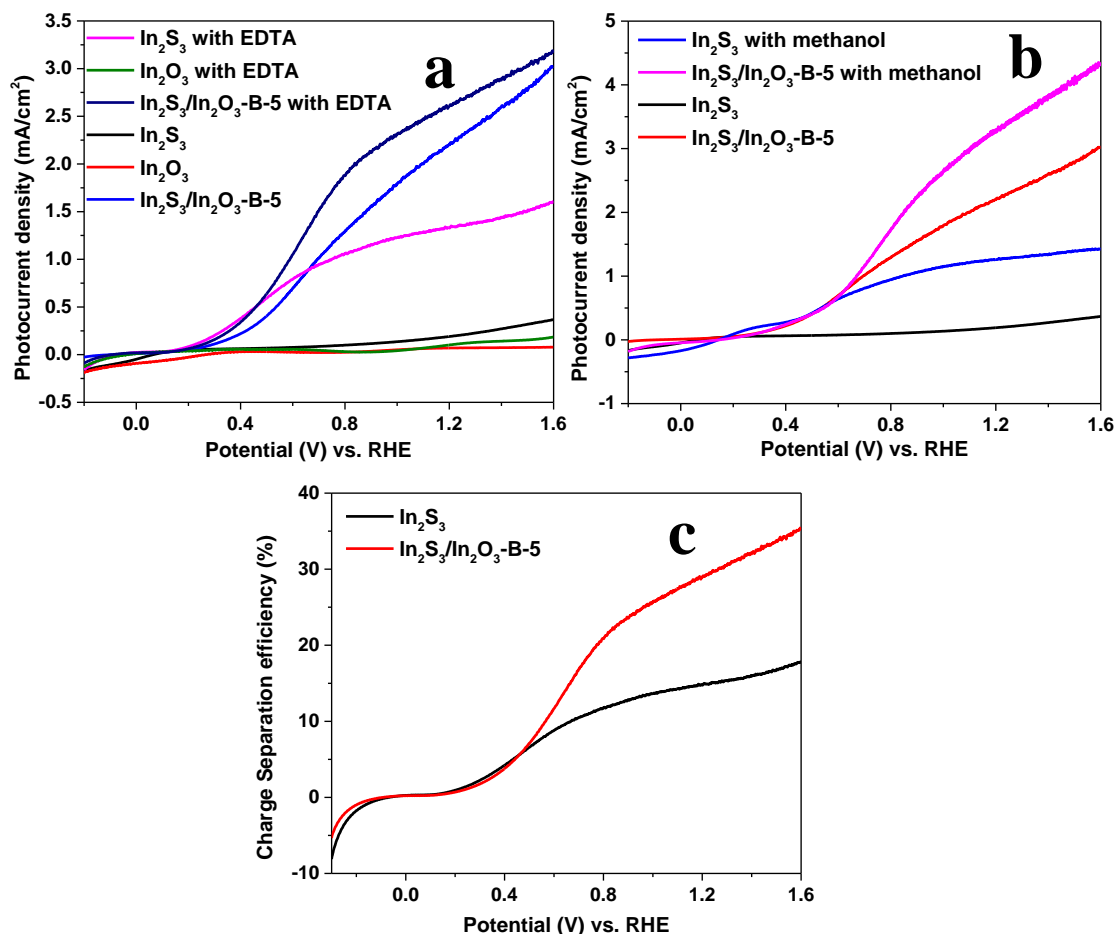
Figure 3.18: Comparative LSV plots of bare In_2S_3, bare In_2O_3, and In_2S_3/In_2O_3-B-5 in 0.5 M Na_2SO_4 and applying different hole scavanger (a) with EDTA, (b) in methanol, and (c) charge separation efficiency of bare In_2S_3, and In_2S_3/In_2O_3-B-5.

Similarly, the charge separation efficiency of nanopyramid is 2-fold higher than bare In_2S_3(**Figure 3.18a-c**). The high charge separation efficiencies show the high carrier separation rate beyond the depletion layer region and the high charge injection efficiency reflects the better charge transportation from electrode surface to electrolyte in the nanopyramid In_2S_3/In_2O_3 composite than In_2S_3 nanobricks.

3.3.3.5 Mechanism of Charge Carrier Separation through Type-II Heterostructure Formation of In_2S_3 and In_2O_3

To understand the mechanism of charge transportation in the In_2S_3/In_2O_3 nanocomposite, the band alignments of In_2S_3, and In_2O_3 are unveiled. The position of valence band and conduction band of pure In_2S_3, and pure In_2O_3 are calculated with the help of following formula: $E_{CB} = -X + ½ E_g$; $E_{VB} = E_{CB} - E_g$, where, X = electronegativity of the semiconductor, E_g = band gap, E_{VB}, and E_{CB} are the valence band and conduction band edge potentials. The electronegativity values of In_2S_3, and In_2O_3 are 4.70 and 5.28 eV, respectively.[51] The calculated valence band of bare In_2O_3 (-6.65 eV vs. vacuum) is more negative than bare In_2S_3 (-5.90 eV vs. vacuum). Whereas, the conduction band position of In_2O_3, and In_2S_3 is -3.93 and -3.50 eV vs. vacuum, respectively. The band alignment of In_2S_3/In_2O_3 supports the type-II heterostructure formation (**Scheme 3.2**).
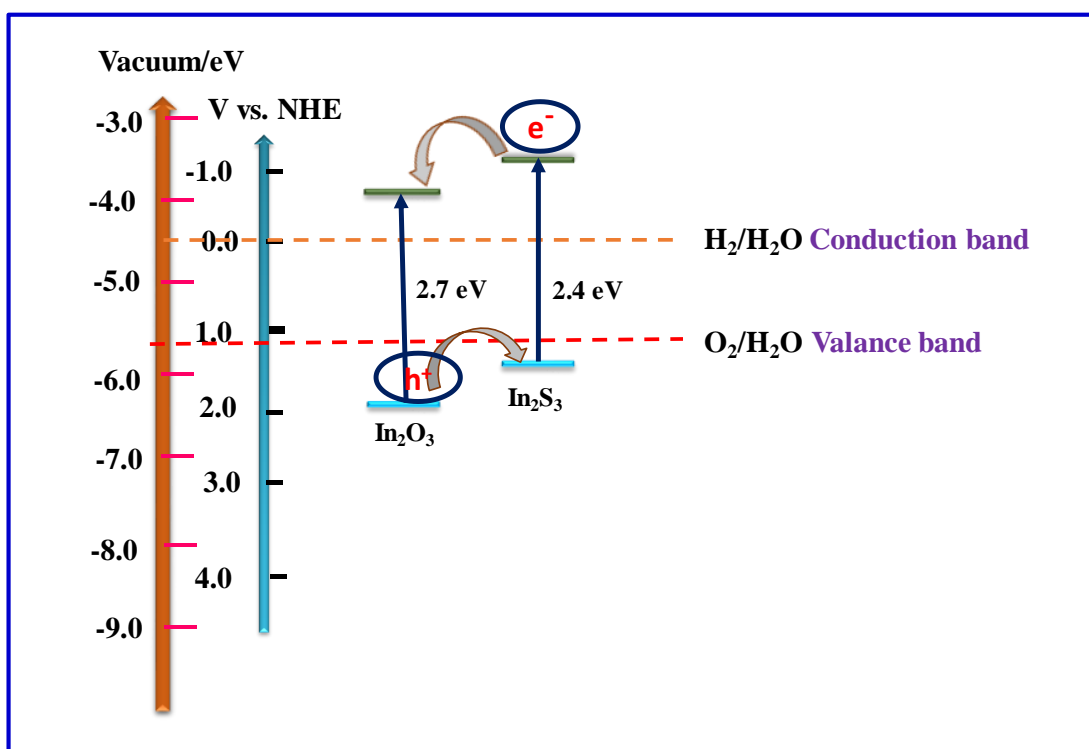
Scheme 3.3: Schematic representation of the band alignment of In_2S_3, In_2O_3 in the composite and the charge transportation mechanism.

Scheme 3.3 illustrates the charge separation and ease of charge transportation which further delay the recombination process. Under the irradiation of light, electrons and holes are

generated and electrons will lift up to the conduction band of In_2S_3. Further, due to having favorable band alignment, electrons will easily move from the conduction band of In_2S_3 to the conduction band of In_2O_3. Consequently, electrons and holes will be separated and holes left in the VB oxidize H_2O into O_2. So, type-II heterostructure formation provides an efficient lifetime to the photogenerated charge carriers. As a result, the nanocomposite of In_2S_3/In_2O_3 function as an efficient photoanode in PEC water-splitting than the bare counterpart In_2S_3 and In_2O_3.

3.4 Comparative Study

The observed PEC activity of the developed In_2S_3/In_2O_3 indicates that heterostructure shows the higher photocurrent density than the bare counterparts. A comparative study for the heterostrucure of In_2S_3/In_2O_3 is shown in **Table 3.1**. In this present study, the photocurrent density is comparable with the existing literature reports.

Table 3.1 Comparative PEC performance data of In_2S_3/In_2O_3 heterostructure with the existing literature.

S. N.	Photoanodes	Photocurrent Density	Electrolyte	References
1.	In_2S_3/In_2O_3 Nanocubes	4.47 mA/cm^2 at 0.244 V vs. RHE	0.5 M Na_2SO_3 and 0.43 M Na_2S	28
2.	In_2O_{3-x}/In_2S_3	1.28 mA/cm^2 at 1.23 V vs. RHE	1 M KOH	30
3.	In_2S_3/In_2O_3	2.5 µA/cm^2 at 1.23 V vs. RHE	0.5 M Na_2SO_4	31
4.	Porous In_2S_3/In_2O_3 heterostructure	8.2 mA/cm^2 at 1.23 V vs. RHE	0.25 M Na_2S and 0.35 M Na_2SO_3	52
5.	In_2S_3/In_2O_3 nanopyramid	2.24 mA/cm^2 at 1.23 V vs. RHE	0.5 M Na_2SO_4	**In this Study**
		0.83 mA/cm^2 at 1.18 V vs. RHE	3.5 wt% NaCl	

3.5 Conclusion

In this study, an easy, green and cost-effective method is developed to synthesize in-situ nanopyramid structure of In_2S_3/In_2O_3, bare In_2S_3, and In_2O_3 via a hydrothermal technique followed by calcination in air. The maximum carrier density and photoconversion efficiency are observed in the case of nanocomposite of In_2O_3 and In_2S_3. It signifies the maximum photon trapping capability of the nanopyramidal structure with exposed (111) facets. The facile charge separation

and transportation in the In_2S_3/In_2O_3 originate due to the close-packing of nanopyramidal structure. The developed nanopyramid structure also helps in decoupling the direction of light absorbance and the charge carrier migration. Nanopyramid with exposed (111) facets which have high surface energy, which play an important role to increase the water oxidation activity. The developed nanocomposite can generate photocurrent density of 3.02 mA/cm^2 under application of 1.6 V vs. RHE whereas, bare In_2S_3 nanobricks can generate 0.36 mA/cm^2 in 0.5 M Na_2SO_4. From the point of practical applicability of PEC water-splitting, here the PEC water-splitting performance is also determined in 3.5 wt% saline water. In saline water, In_2S_3/In_2O_3 nanocomposite shows exceptional stability as well as high efficiency indicating the superior corrosion resistance nature. The present study opens a new avenue to all for developing efficient photoanodes for PEC water-splitting, which may have practical applicability in near future using plenty of sea-water and sunlight.

3.6 References

1. Grätzel, M. Photoelectrochemical Cells. *Nature* **2001**, *414*, 338-344.

2. Hisatomi, T.; Kubota, J.; Domen, K. Recent Advances in Semiconductors for Photocatalytic and Photoelectrochemical water splitting. *Chem. Soc. Rev.*, **2014**, *43*, 7520-7535.

3. Basu, M.; Zhang, Z-W.; Chen, C-J.; Chen, P-T.; Yang, K-C.; Ma, C-G.; Lin, C. C.; Hu, S-F.; Liu, R-S. Heterostructure of Si and CoSe$_2$: A Promising Photocathode Based on a Non-Noble Metal Catalyst for Photoelectrochemical Hydrogen Evolution. *Angew. Chem.*, **2015**, *54*, 6211-6216.

4. Lee, D. K.; Lee, D.; Lumley, M. A. Progress on Ternary oxide-based Photoanodes for use in Photoelectrochemical Cells for Solar Water Splitting. *Chem. Soc. Rev.,* **2019**, *48*, 2126-2157.

5. Natarajan, K.; Saraf, M.; Mobin, S. M. Visible-Light-Induced Water Splitting Based on a Novel α-Fe$_2$O$_3$/CdS Heterostructure. *ACS Omega* **2017**, *2*, 3447-3456.

6. Wang, L.; Xia, L.; Wu, Y.; Tian, Y. Zr-Doped β-In$_2$S$_3$ Ultrathin Nanoflakes as Photoanodes: Enhanced Visible-Light-Driven Photoelectrochemical Water Splitting. *ACS Sustainable Chem. Eng.*, **2016**, *5*, 2606-2614.

7. Liu, G.; Li, Z.; Hasan, T.; Chen, X.; Zheng, W.; Feng, W.; Jia, D.; Zhou, Y.; PingAn, H. Vertically Aligned Two-dimensional SnS$_2$ Nanosheets with a Strong Photon Capturing Capability for Efficient Photoelectrochemical Water Splitting. *J. Mater. Chem. A* **2017**, *5*, 1989-1995.

8. Wang, Y.; Tian, W.; Chen, L.; Cao, F.; Guo, J.; Li, L. Three-Dimensional WO$_3$ Nanoplate/Bi$_2$S$_3$ Nanorod Heterojunction as a Highly Efficient Photoanode for Improved Photoelectrochemical Water Splitting. *ACS Appl. Mater. Interfaces* **2017**, *9*, 40235-40243.

9. Song, J-P.; Yin, P-F.; Mao, J.; Qiao, S-Z.; Du, X-W. Catalytically Active and Chemically Inert CdIn$_2$S$_4$ coating on a CdS Photoanode for Efficient and Stable Water Splitting. *Nanoscale* **2017**, *9*, 6296-6301.

10. Liu, Z.; Lu, Z.; Chen, D. Photoelectrochemical Water Splitting of CuInS$_2$ Photocathode Collaborative Modified with Separated Catalysts Based on Efficient Photogenerated Electron-Hole Separation. *ACS Sustainable Chem. Eng.*, **2018**, *6*, 10289-10294.

11. Zhou, M.; Liu, Z.; Song, Q.; Li, X.; Chen, B.; Liu, Z.; Hybrid 0D/2D edamame shaped ZnIn$_2$S$_4$ photoanode modified by Co-Pi and Pt for charge management towards efficient photoelectrochemical water splitting. *Appl. Catal. B: Environ.*, **2019**, *244*, 188-196.

12. Basu, S. S.; Rahut, S.; Chinthala, C.; Basu. J. K. Tuning of the morphological and electronic properties of In_2S_3 nanosheets by cerium ion intercalation for optimizing photocatalytic activity. *CrystEngComm*, **2020**, *22*, 4758-4767.

13. Li, J.; Ma, Y.; Ye, Z.; Zhou, M.; Wang, H.; Ma, C.; Wang, D.; Huo, P.; Yan, Y. Fast Electron Transfer and Enhanced Visible Light Photocatalytic Activity using Multi-Dimensional Components of Carbon Quantum Dots@3D Daisy-like In_2S_3/single-wall carbon nanotubes. *Appl. Catal. B-Enviorn.;* **2017**, *204*, 224-238.

14. Huang, W.; Gan, L.; Yang, H.; Zhou, N.; Wang, R.; Wu, W.; Li, H.; Ma, Y.; Zeng, H.; Zhai, T. Controlled Synthesis of Ultrathin 2D β-In_2S_3 with Broad Band Photoresponse by Chemical Vapor Deposition. *Adv. Funct. Mater.*, **2017**, *27*, 1702448-1702456.

15. Wang, S.; Guan, B. Y.; Lu, Y.; Lou, X. W. D. Formation of Hierarchical In_2S_3-$CdIn_2S_4$ Heterostructured Nanotubes for Efficient and Stable Visible Light CO_2 Reduction, *J. Am. Chem. Soc.*, **2017**, *139*, 17305-17308.

16. Zhanga, J.; Wanga, H.; Yuana, X.; Zenga, G.; Tuc, W.; Wang, S. Tailored Indium Sulfide-based Materials for Solar-Energy Conversion and Utilization. *J. Photochem. Photobiol. C: Photochem. Rev*., **2019**, *38*, 1-26.

17. Liu, Y.; Xu, H.; Qian, Y. Double-Source Approach to In_2S_3 Single Crystallites and Their Electrochemical Properties. *Cryst. Growth Des.*, **2006**, *6*, 1304-1307.

18. Ma, B.; Yue, M.; Zhang, P.; Li, S.; Cong, R.; Gao, W.; Yang, T. Tetragonal β-In_2S_3: Partial ordering of In^{3+} Vacancy and Visible-light Photocatalytic Activities in both Water and Nitrate Reduction. *Catal. Commun*., **2017**, *88*,18-21.

19. Gao, W.; Liu, W.; Leng, Y.; Wang, X.; Wang, X.; Hu, B.; Yu, D.; Sang, Y.; Liu, H. In_2S_3 Nanomaterial as a Broadband Spectrum Photocatalyst to Display Significant Activity. *Appl. Catal. B-Enviorn*., **2015**, *176*, 83-90.

20. Rengaraj, S.; Venkataraj, S.; Tai, C.; Kim, Y.; Repo, E.; Sillanpää, M. Self-assembled Mesoporous Hierarchical-like In_2S_3 Hollow Microspheres Composed of Nanofibers and Nanosheets and Their Photocatalytic Activity. *Langmuir* **2011**, *27*, 5534-5541.

21. Li, M.; Tu, X.; Su, Y.; Lu, J.; Hu, J.; Cai, B.; Zhou, Z.; Yang, Z.; Zhang, Y. Controlled Growth of Vertically Aligned Ultrathin In_2S_3 Nanosheet Arrays for Photoelectrochemical Water Splitting. *Nanoscale* **2018**, *10*, 1153-1161.

22. Tian, Y.; Wang, L.; Tang, H. Zhou, W.; Ultrathin Two-dimensional β-In$_2$S$_3$ Nanocrystals: Oriented-Attachment Growth Controlled by Metal Ions and Photoelectrochemical Properties. *J. Mater. Chem. A* **2015**, *3*, 11294-11301.

23. Chen, D.; Liu, Z. Efficient Indium Sulfide Photoelectrode with Crystal Phase and Morphology Control for High-Performance Photoelectrochemical Water Splitting. *ACS Sustainable Chem. Eng*., **2018**, *6*, 12328-12336.

24. Xu, R.; Li, H.; Zhang, W.; Yang, Z.; Liu, G.; Xu, Z.; Shao, H.; Qiao, G. The Fabrication of In$_2$O$_3$/In$_2$S$_3$/Ag nanocubes for Efficient Photoelectrochemical Water Splitting. *Phys. Chem. Chem. Phys*., **2016**, *18*, 2710-2717.

25. Hou, J.; Cao, S.; Sun, Y.; Wu, Y.; Liang, F.; Lin, Z.; Sun, L. Atomically Thin Mesoporous In$_2$O$_{3-x}$/In$_2$S$_3$ Lateral Heterostructures Enabling Robust Broadband-Light Photo-Electrochemical Water Splitting. *Adv. Energy Mater*., **2017**, *8*, 1701114-1701122.

26. Xu, H.; Wang, Y.; Dong, X.; Zheng, N.; Ma, H.; Zhang, X. Fabrication of In$_2$O$_3$/In$_2$S$_3$ microsphere heterostructures for efficient and stable photocatalytic nitrogen fixation. *Appl. Catal. B: Environ*., **2019**, *257*, 117932-117939.

27. Kuang, Y.; Kenney, M. J.; Meng, Y.; Hung, W-H.; Liu, Y.; Huang, J. E.; Prasanna, R.; Li, P.; Li, Y.; Wang, L.; Lin, M-C.; McGehee, M. D.; Sun, X.; Dai, H. Solar-driven, Highly Sustained Splitting of Seawater into Hydrogen and Oxygen Fuels. *PNAS* **2019**, *116*, 6624-6629.

28. Hua, E.; Jin, S.; Wang, X.; Ni, S.; Liu, G.; Xu, X.; Ultrathin 2D Type-II p-n Heterojunctions La$_2$Ti$_2$O$_7$/In$_2$S$_3$ with Efficient Charge Separations and Photocatalytic Hydrogen Evolution under Visible Light Illumination. *Appl. Catal. B-Enviorn*., **2019**, *245*, 733-742.

29. Nayak, A. K.; Lee, S.; Sohn, Y.; Pradhan, D. Synthesis of In$_2$S$_3$ Microspheres using a Template Free and Surfactant-less Hydrothermal Process and Their Visible Light Photocatalysis. *CrystEngComm*., **2014**, *16*, 8064-8072.

30. Khan, M. A.; Khan, W.; Ahamed, M.; Alhoshan, M. Structural and Optical Properties of In$_2$O$_3$ Nanostructured Thin Film. *Mater Lett*., **2012**, *79*, 119-121.

31. Izadneshana, H.; Gremenok, V. F. Micro Structural Analysis of In$_2$S$_3$ Thin Films by Raman Spectroscopy. *J. Appl. Spectrosc*., **2014**, *81*, 765-770.

32. Yang, M-Q.; Weng, B.; Xu, Y-J. Synthesis of In$_2$S$_3$-CNT Nanocomposites for Selective Reduction under Visible Light. *J. Mater. Chem. A* **2014**, *2*, 1710-1720.

33. Alqahtani, T.; Cernik, R. J.; O'Brien, P.; Lewis, D. J. Solid Solutions of $M_{2-2x}In_{2x}S_3$ (M = Bi or Sb) by Solvent Less Thermolysis. *J. Mater. Chem. C* **2019**, *7*, 5112-5121.

34. Gan, J.; Lu, X.; Wu, J.; Xie, S.; Zhai, T.; Yu, M.; Zhang, Z.; Mao, Y.; Wang, S. C. I.; Shen, Y.; Tong, Y. Oxygen Vacancies Promoting Photoelectrochemical Performance of In_2O_3 Nanocubes. *Sci. Rep.*, **2013**, *3*, 1021-1028.

35. Sharma, M. D.; Mahala, C.; Basu, M. Band gap tuning to improve the photoanodic activity of $ZnIn_xS_y$ for photoelectrochemical water oxidation. *Catal. Sci. Technol.*, **2019**, *9*, 6769-6781.

36. Tien, L. C.; Shih, J. L. Type-II a-In_2S_3/In_2O_3 Nanowire Heterostructures: Evidence of Enhanced Photo-Induced Charge Separation Efficiency. *RSC Adv.*, **2016**, *6*, 12561-12570.

37. Zhang, F.; Li, X.; Zhao, Q.; Chen, A. Facile and Controllable Modification of 3D In_2O_3 Microflowers with In_2S_3 Nanoflakes for Efficient Photocatalytic Degradation of Gaseous ortho-Dichlorobenzene. *J. Phys. Chem. C* **2016**, *120,* 19113-19123.

38. Challagulla, S.; Dr. Tarafder, K.; Ganesan, R.; Roy, S. All That Glitters Is Not Gold: A Probe into Photocatalytic Nitrate Reduction Mechanism Over Noble Metal Doped and Undoped TiO_2. *J. Phys. Chem. C* **2017**, *121*, 27406-27416.

39. Challagulla, S.; Payra, S.; Chakraborty, C.; Roy, S. Determination of band edges and their influences on photocatalytic reduction of nitrobenzene by bulk and exfoliated g-C_3N_4. *Phys. Chem. Chem. Phys.*, **2019**, 21, 3174-3183.

40. Yang, M.-Q.; Weng, B.; Xu, Y.-J. Improving the Visible Light Photoactivity of In_2S_3-Graphene Nanocomposite via a Simple Surface Charge Modification Approach. *Langmuir* **2013**, *29*, 10549-10558.

41. Yang, M-Q.; Weng, B.; Xu, Y-J. Improving the Visible Light Photoactivity of In_2S_3-Graphene Nanocomposite via a Simple Surface Charge Modification Approach. *Langmuir* **2013**, *29*, 10549-10558.

42. Li, B.; Li, X.; Shao, C.; Li, X.; Liu, H.; Yang, S.; Tao, R.; Liu, Y. Hierarchically Porous In_2O_3/In_2S_3 Heterostructures as Micronano Photocatalytic Reactors Prepared by a Novel Polymer-Assisted Sol-Gel Freeze-Drying Method. *Ind. Eng. Chem. Res.*, **2019**, *58*, 14106-14114.

43. Panneerdoss, I. J.; Jeyakumar, S. J.; Ramalingam, S.; Jothibas, M. Characterization of prepared In_2O_3 thin films: The FT-IR, FT-Raman, UV-Visible investigation and optical analysis. *Spectrochim. Acta A Mol. Biomol. Spectrosc.*, **2015**, *147*, 1-13.

44. Wang, K. X.; Yu, Z.; Liu, V.; Brongersma, M. L.; Jaramillo, T. F.; Fan, S. Nearly Total Solar Absorption in Ultrathin Nanostructured Iron Oxide for Efficient Photoelectrochemical Water Splitting. *ACS Photonics* **2014**, *1*, 235-240.

45. Martin, D. J.; Liu, G.; Moniz, S. J. A.; Bi, Y.; Beale, A. M.; Ye, J.; Tang, J. Efficient visible driven photocatalyst, silver phosphate: performance, understanding and perspective. *Chem. Soc. Rev.*, **2015**, *44*, 7808-7828.

46. Zheng, B.; Wang, X.; Liu, C.; Tan, K.; Xie, Z.; Zheng. L. High-efficiently visible light-responsive photocatalysts: Ag_3PO_4 tetrahedral microcrystals with exposed {111} facets of high surface energy. *J. Mater. Chem. A* **2013**, *1*, 12635-12640.

47. Xu, D.; Xia, T.; Xu, H.; Fan, W.; Shi, W. Synthesis of ternary spinel MCo_2O_4 (M = Mn, Zn)/$BiVO_4$ photoelectrodes for photolectrochemical water splitting. *Chem. Eng. J.*, **2020**, *392*, 124838-124846.

48. Naghavia, N.; Henriquez, R.; Laptev, V.; Lincot, D. Growth studies and Characterisation of In_2S_3 Thin Films Deposited by Atomic Layer Deposition (ALD). *Appl. Surf. Sci.*, **2004,** *222*, 65-73.

49. Tian, W.; Chen, C.; Meng, L.; Xu, W.; Cao, F.; Li, L. PVP Treatment Induced Gradient Oxygen Doping in In_2S_3 Nanosheet to Boost Solar Water Oxidation of WO_3 Nanoarray Photoanode. *Adv. Energy Mater.*, **2020**, *10*, 1903951-1903958.

50. Sun, M.; Fang, Y.; Kong, Y.; Yuan, X.; Shi, J.; Umar, A. Direct in situ synthesis of Fe_2O_3-codoped N-doped TiO_2 nanoparticles with enhanced photocatalytic and photo-properties. *J. Alloys Compd.*, **2017**, *705*, 89-97.

51. Xu, Y.; Schoonen, M. A. A. The Absolute Energy Positions of Conduction and Valence Bands of Selected Semiconducting Minerals. *Am. Mineral.*, **2000**, *85*, 843-856.

52. Cao, S.; Wu, Y.; Hou, J.; Zhang, B.; Li, Z.; Nie, X.; Sun, L. 3D Porous Pyramid Heterostructure Array Realizing Efficient Photo-Electrochemical Performance. *Adv. Energy Mater.*, **2019**, 10, 1902935-1902943.

S-C$_3$N$_4$-Dots Decorated In$_2$S$_3$ Nanosheets Function as an Efficient Photoanode for Photoelectrochemical Water-Splitting in Saline Water
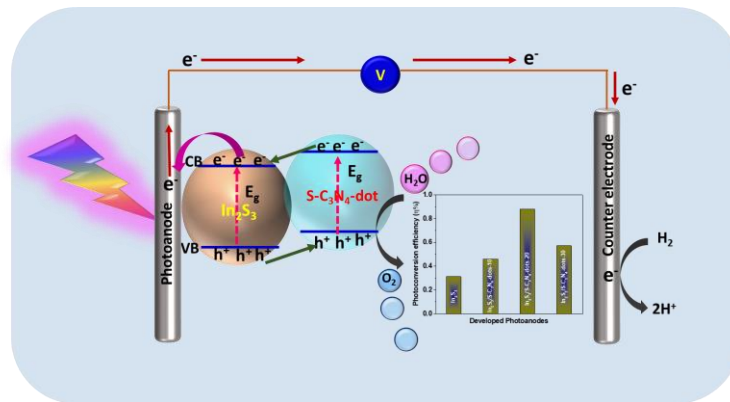
- *In this chapter In$_2$S$_3$ nanosheets are sensitized with S-C$_3$N$_4$-dots to develop heterostructure.*
- *The developed heterostructure of In$_2$S$_3$/S-C$_3$N$_4$-dots is able to enhance the charge separation efficiency than bare In$_2$S$_3$ nanosheets which boosts the PEC activity.*

Abstract

In search of finding an efficient and stable photoelectrode for PEC water-splitting reaction, here In_2S_3 is explored as it is a visible light active semiconductor with proper band alignment with the oxidation and reduction potential of water. In_2S_3 nanosheets are developed via hydrothermal technique followed by calcination in air. The nanosheets of In_2S_3 absorb high visible light due to the multiple reflection and scattering of light inside the material. High light absorbance results in enhanced PEC activity. But the severe problem of In_2S_3 is the observed photocorrosion: self-oxidation by the minority charge carriers, especially in corrosive saline water. To improve the efficacy of the In_2S_3 nanosheets in saline water, the charge-carrier transportation ability of In_2S_3 is increased by decorating $S-C_3N_4$-dots on In_2S_3. Here, $S-C_3N_4$-dots act as an optical antenna and increase the range of visible light absorbance of In_2S_3. Sensitization of $S-C_3N_4$-dots on In_2S_3 results in the type-II heterostructure, which increases both the charge-carrier transportation and separation. In the heterostructure, the transient decay time (τ) enhances which indicates the decrease of photogenerated charge-carrier recombination. The developed In_2S_3 nanosheets can generate a maximum photocurrent density of 2.07 mA/cm^2 at an applied potential of 1.18 V vs. RHE in the 3.5 wt% NaCl. Whereas, the heterostructure can generate ~2.38-fold higher photocurrent density at the same applied potential. The photoconversion efficiency of the heterostructure is 0.88% at 0.95 V vs. RHE. The nanosheets of In_2S_3 and $In_2S_3/S-C_3N_4$-dots are stable and photocurrent density is measured up to 2700 seconds under continuous back illumination condition.

4.1 Introduction

Solar energy can play an important role by providing the most promising alternative energy source to imitate the world's energy crisis due to its universality, sustainability, abundance, and environmental benignity. Although, solar energy has been widely used in photothermal and photoelectrical approaches, but the practical application is still remaining a great challenge.[1,2] These problems could be solved by storing the sunlight into the chemical energy as hydrogen (H_2). Therefore, the direct transformation of solar energy to chemical energy through water-splitting, which is suitable for storage, transportation, and utilization has received prodigious interest in research.[3,4] Photocatalytic and photoelectrochemical (PEC) water-splitting both strategies are developed based on the conversion of sunlight into chemical energy; H_2. The landmark work reported by Honda and Fujishima used TiO_2 as a photoanode.[5] But the main problem is that TiO_2 can be excited only by irradiating with ultraviolet light. A sequence of physicochemical processes occurs in the photoelectrodes of PEC cells during the solar water-splitting reaction, which includes light-harvesting, charge-carrier generation, separation, transportation, and injection at the interface for redox reactions. On the other hand, the competitive charge recombination process happens on the photoelectrode, which reduces the number of active charge carriers.[6] The capability of light-harvesting, charge separation, charge transportation, and the recombination of charge carriers depend on the dimensionality or morphology (0D, 1D, 2D, and 3D) of the nanomaterial photoelectrodes for the PEC water-splitting.[7] 2D nanomaterials, especially vertically grown 2D nanosheets are advantageous than others and can play an important role in PEC water-splitting. 2D nanosheets can harvest more light through multiple scattering and reflections of light inside the material resulting in more light-matter interaction. Another advantage of vertically grown 2D nanosheets is that they can decouple the direction of light absorption and the carrier's migration path and at the same time, the thin 2D nanosheets help to shorten the diffusion length of the minority carriers, hence improving the charge collection efficiency. Further, it offers the possibility to facilitate the charge migration with enough light absorption simultaneously.[8,9]

Various semiconductors with 2D nanosheets like morphology have drawn potential interest in PEC water-splitting due to having excellent visible light absorption.[10-13] Among them, In_2S_3 is one of the active visible light-responsive semiconductors with a higher absorption coefficient, photoelectric sensitivity, superior carrier mobility, and moderate bandgap (~2.0-2.3 eV).[14] Suitable bandgap provides the prerequisite condition for facilitating solar light absorption. In_2S_3 has five

different crystalline forms: α-In_2S_3, β-In_2S_3, γ-In_2S_3, Ɛ-In_2S_3, Th_3P_4-type In_2S_3.[15] The β-In_2S_3 is the most stable one, which is extensively explored as an excellent visible-light-active photocatalyst and can be used as a sensitizer for wide bandgap semiconductors. β-In_2S_3 has a defective spinel structure due to sulfur vacancy, indium vacancy, and oxygen vacancy. Such an interesting defect structure of β-In_2S_3 is especially helpful to realize a transition of absorption range from visible to NIR because of the formation of a transitionally defect band above the VB of In_2S_3. At the same time, these vacancies display electron affinity and can act as electron traps.[16]

Tian *et al.* have developed ultrathin 2D nanoflakes of β-In_2S_3 and reported the superior activity of it compared to nanoparticles and nanobelts. The 2D nanoflakes can generate 370 μA/cm^2 at 0.7 V vs. Ag/AgCl in 0.5 M NaOH, which is ~3-fold and ~18-fold higher than nanobelts and nanoparticles, respectively.[17] Li *et al*. developed vertically grown 2D ultrathin nanosheets of β-In_2S_3 for PEC water-splitting. β-In_2S_3 can generate only 35.7 μA/cm^2 photocurrent density at a potential 1.2 V vs. RHE in 1.0 M KCl.[11] From the reported literature, it is clear that although β-In_2S_3 has the ability to achieve high photocurrent density but till now the obtained PEC performance is not satisfactory. The major obstacle is the charge-carrier recombination. The successful water-splitting reaction requires efficient charge-carrier separation. In this regard, carbon-based nanomaterials are taken care of as these materials have high charge transportation capability. Graphitic carbon nitride (g-C_3N_4) is a visible light active semiconductor, which is recognized as metal-free, high thermal, and chemical stable, non-toxic with layer structure. It is a low-cost material at the same time it has an easy synthetic route. Importantly, the g-C_3N_4 is suitable for the PEC water-splitting reaction due to the appropriate band alignment with the redox potential of water. The g-C_3N_4 speeds up the rate of charge transportation rate due to the layer structure. The high conductivity of the g-C_3N_4 enables it to capture photogenerated charge carriers (e$^-$ or h$^+$) from semiconductors and rapidly transfer them through the surface to the oxidized or reduced species. To increase the surface-to-volume ratio and the efficiency of charge transportation over bulk g-C_3N_4, dots of g-C_3N_4 can be synthesized.[18] At the same time, doping of heteroatom could be helpful to tune the optical property, and the electronic structure, and increasing the density of states in the C_3N_4 framework. Generally, doping of non-metals (S, O, B, P, F) have a great impact on the electronic structure of g-C_3N_4, which is beneficial for separation and transportation of the charge carriers, retaining the non-metallic properties of g-C_3N_4.[19, 20] Recently, our group has developed a type-II heterostructure of ZnO/g-C_3N_4 quantum dot to increase the visible light

absorbance and to improve the migration of photogenerated charge carriers.[21] Liu *et al.* doped a series of non-metals (S, P, F, and Br) in the g-C_3N_4 to modulate the molecular and electronic properties. After doping of non-metals in the g-C_3N_4 framework, the photocatalytic activity enhances due to broadening the range of visible light absorbance and increase in photoinduced charge-carrier separation and migration.[22] In the literature there are many reports for the S-doped g-C_3N_4 in photocatalytic H_2 generation.[23, 24] But in PEC water-splitting, the sensitization effect of S-C_3N_4-dots is yet to explore extensively. Recently, He *et al.* decorated S-C_3N_4 QDs on the ZnO nanorods to improve the light-harvesting efficiency and enhance the charge-carrier transportation ability in PEC water-splitting. [25]

In this chapter, 2D nanosheets of In_2S_3 are grown vertically on a conducting substrate (fluorine-doped tin oxide; FTO) via a simple hydrothermal technique followed by air calcination. Here, calcination in the air is carried out to increase the active sites in In_2S_3 nanosheets. Further, the heterostructure of In_2S_3 nanosheets and S-C_3N_4-dots is developed to increase the charge transportation ability of In_2S_3. Various techniques are used to characterize bare In_2S_3 and the heterostructure. The optical property of bare In_2S_3 and the heterostructure is resolute with the help of UV-visible spectroscopy. The PEC performance of the synthesized materials is investigated in 3.5 wt% saline water, assuming the seawater. The PEC activity of the developed heterostructure of In_2S_3/S-C_3N_4-dots is ~2.38 fold higher than the bare In_2S_3 nanosheets. The heterostructure shows enhanced photoelectrochemical activity. An in-depth study is carried out to understand improved charge separation and transportation. The developed In_2S_3 and In_2S_3/S-C_3N_4-dots are stable up to 2700 seconds of continuous back illumination in the corrosive environment.

4.2 Experimental Section

4.2.1 Synthesis of In₂S₃ Nanosheets: The In_2S_3 nanosheets were synthesized on the FTO via hydrothermal technique followed by air calcination. Firstly, FTO was cleaned with soap water, a mixture of ethanol and acetone, and Milli-Q water, respectively. For the synthesis of In_2S_3 on the FTO surface, 0.397 mmol of $InCl_3$ and 0.599 mmol of L-Cysteine were dissolved into 15 mL of DI water and sonicated to prepare a homogenous solution. Then the FTO was aligned vertically in the Teflon container and the whole solution was poured into it. The hydrothermal reaction was carried out at 160 ℃ for 6 h. After natural cooling, the sample decorated FTO was rinsed with DI

water and ethanol 2-3 times to remove the impurity and dried well. It was stored for further characterization and decoration of S-C$_3$N$_4$-dots.

4.2.2 Synthesis of S-C₃N₄-dots: To synthesize the S-C$_3$N$_4$-dots, first trisodium citrate (0.180 g) and thiourea (0.101 g) was ground in a mortar pestle to make a fine mixture powder. The prepared powder was transferred to the crucible and heated at 180 ℃ for 1 h in a muffle furnace. Ethanol was used to remove the impurity of synthesized powder and dried well in the oven. Afterward, the whole powder was dispersed into 10 mL of Milli-Q water and dialyzed for 24 h. After synthesis, the S-C$_3$N$_4$-dot was immediately kept under the UV light (λ-365 nm) and it shows cyan emission which is shown in **Scheme 4.1**.

4.2.3 Decoration of S-C₃N₄-dots on the surface of In₂S₃-Nanosheets: The adornment of the S-C$_3$N$_4$-dots on the In$_2$S$_3$ nanosheets was done via the dip-coating method. A dilute solution was prepared by using 1 mL of S-C$_3$N$_4$-dots and 9 mL DI water for the decoration of S-C$_3$N$_4$-dots. The sample coated FTO was dipped into the dilute solution of S-C$_3$N$_4$-dots for different time intervals like 10, 20, and 30 minutes and named In$_2$S$_3$/ S-C$_3$N$_4$-dots-10, -20, and -30 to have optimum decoration of S-C$_3$N$_4$ on In$_2$S$_3$ nanosheets (**Scheme 4.1**).
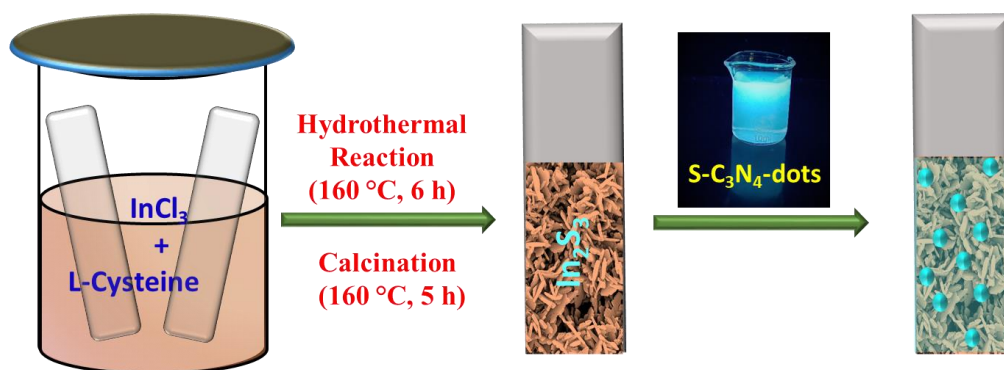
Scheme 4.1: Schematic presentation for the synthesis of In$_2$S$_3$ nanosheets and In$_2$S$_3$/S-C$_3$N$_4$-dots.

4.3 Result and Discussion

The characterization and application of developed In$_2$S$_3$ nanosheets and In$_2$S$_3$/S-C$_3$N$_4$-dots heterostructure are discussed in the below mentioned sections.

4.3.1 Characterization

4.3.1.1 XRD and Raman Analysis

The X-ray diffraction (XRD) analysis is carried out to know the crystallinity, phase, purity, and crystal structure of synthesized materials. **Figure 4.1a** demonstrates the XRD pattern of In_2S_3 and In_2S_3/S-C_3N_4-dots. The peaks of In_2S_3 are well-matched with the JCPDS no.00-25-0390, which confirms the pure tetragonal phase of In_2S_3.[26] After the decoration of S-C_3N_4-dots on the surface of In_2S_3 nanosheets, the XRD peaks remain intact and no other significant peak is observed due to the S-C_3N_4-dots.
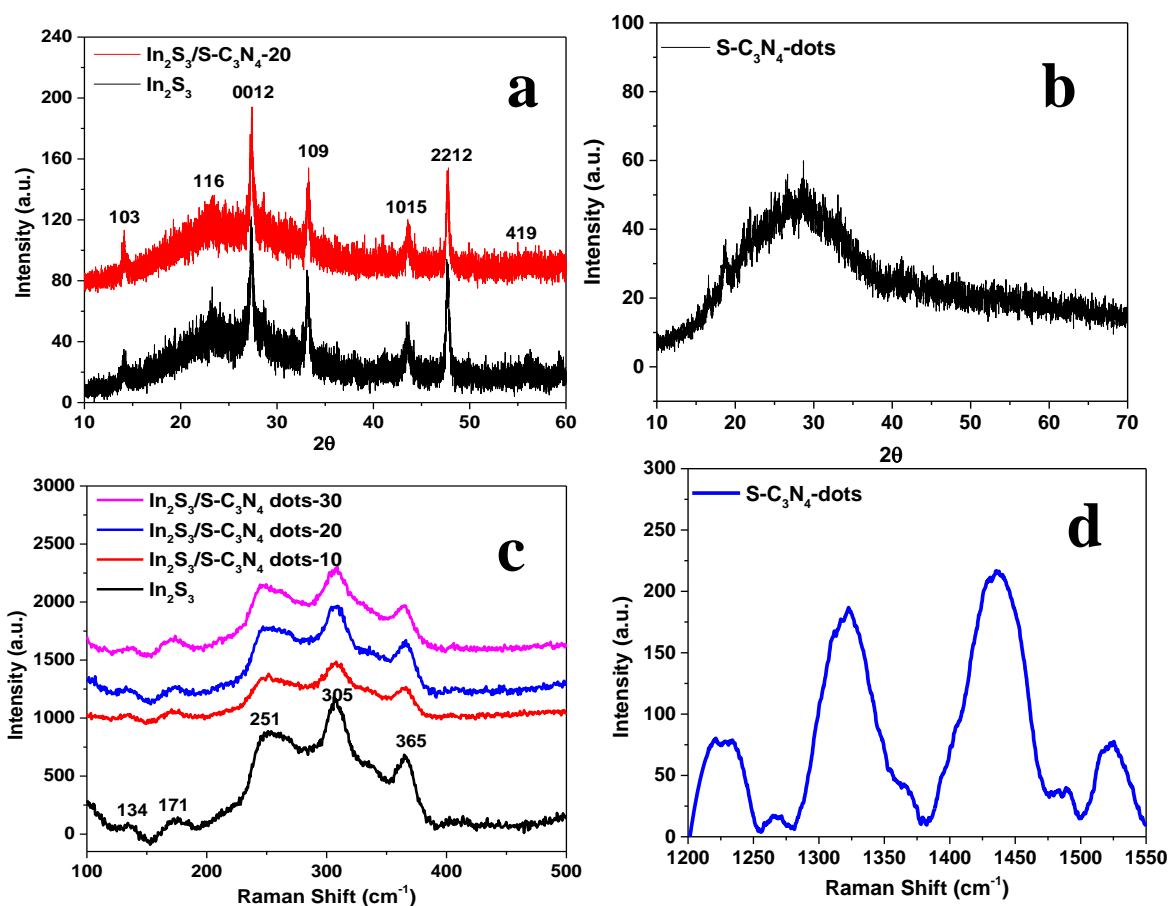
Figure 4.1: XRD pattern of (a) In_2S_3 nanosheets and In_2S_3/S-C_3N_4-dots-20, (b) bare S-C_3N_4-dots. Raman spectra of (c) In_2S_3 nanosheets and In_2S_3/S-C_3N_4-dots-10, -20, and -30, and (d) S-C_3N_4-dots.

The absence of the peak for the S-C_3N_4-dots may be due to the low loading on the surface or it may be due to the amorphous nature. From the existing literature, it is clear that the bare C_3N_4-

dots contain the XRD peak at 27.8° corresponding to the (002) plane.[27, 28] Here, the observed XRD pattern of S-C_3N_4-dots displays the peak at 26.9° corresponding to the (002) plane. The detected shift in (002) plane indicates the incorporation of strain in C_3N_4-dots which is due to the successful doping of 'S' in the C_3N_4-dots matrix (**Figure 4.1b**). So, from XRD analysis, it is clear that C_3N_4-dots are doped with 'S' and crystalline in nature.

Further, Raman analysis confirms the phase purity, the crystallinity of bare In_2S_3, and the developed heterostructure. The peaks at 134, 171, 251, 305, and 365 cm^{-1} confirm the synthesis of tetragonal β-In_2S_3 which is well-matched with the literature.[29] After the decoration of S-C_3N_4-dots on the surface of In_2S_3 nanosheets, the intensity of all peaks is decreased. This observation is the indication of the successful decoration of S-C_3N_4-dots on In_2S_3 and the interaction between In_2S_3 and S-C_3N_4-dots (**Figure 4.1c**). The S-C_3N_4-dots show four Raman peaks at 1225, 1322, 1436, and 1524 cm^{-1}, which are due to the vibration in the β-C_3N_4 lattice (**Figure 4.1d**).[30]

4.3.1.2 FTIR Analysis

To know the surface functional groups of S-C_3N_4-dots, FTIR analysis is carried out (**Figure 4.2**). Broadband observed at 3100-3300 cm^{-1} indicates the presence of O-H/N-H stretching vibrations. A sharp peak at 1652 cm^{-1} confirms that the amino groups are attached to the surface of C_3N_4-dots. The peaks present in the range of 1000-1500 cm^{-1} show the presence of the C-N group and indicate the formation of a heterocycle ring in the C_3N_4-dot's skeleton. The deformed mode at 872 cm^{-1} signifies the presence of the triazine ring in the C_3N_4 framework.
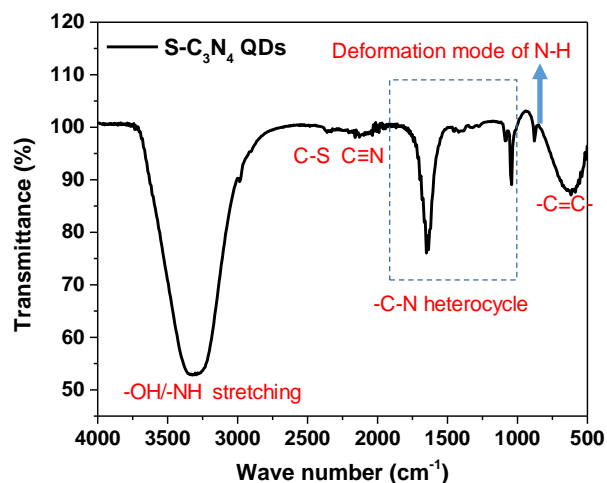
Figure 4.2: FTIR spectra of S-C_3N_4-dots.

The very less intense peak at 2100 cm^{-1} and 2358 cm^{-1} signifies the presence of C≡N and C-S groups in the C$_3$N$_4$-dots and confirms successful 'S' doping in the C$_3$N$_4$-dots.[31,32] The less intense peak corresponding to the functional group of C-S signifies that the low amount of 'S' is introduced in the framework of C$_3$N$_4$-dots.

4.3.1.3 Optical Property

The optical property of the synthesized materials is checked with the help of UV-visible absorption spectroscopy. The bare In$_2$S$_3$-nanosheets show the absorbance peak at 495 nm with an absorption edge in the visible region ~550-600 nm (**Figure 4.3a**). The S-C$_3$N$_4$-dots show the absorption maxima at 330 nm with a shoulder peak at 451 nm which is corresponding to the n-π* transition of the conjugate structure of the carboxylic group and π-π* transition of the triazine framework of C$_3$N$_4$ dots,[32] respectively (**Figure 4.3b**).
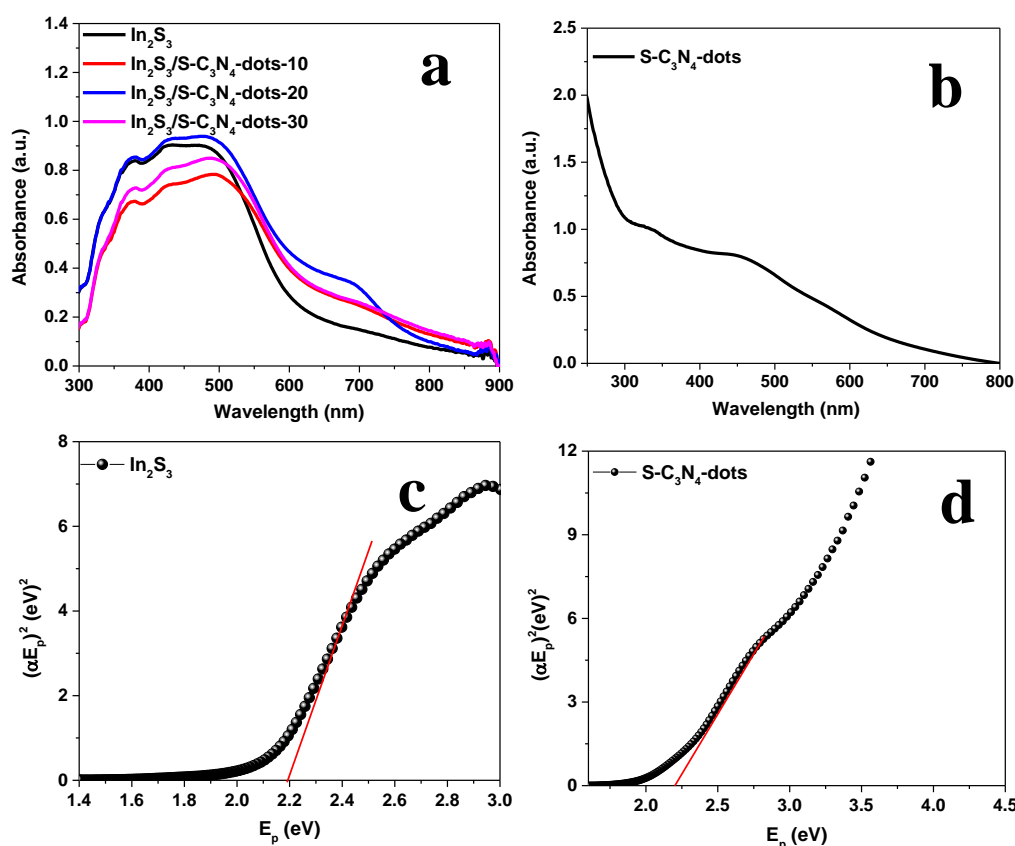
Figure 4.3: UV-visible spectra of (a) In$_2$S$_3$ nanosheets and In$_2$S$_3$/S-C$_3$N$_4$-dots-10, -20, and -30, respectively, and (b) bare S-C$_3$N$_4$-dots. Tauc plot of (c) In$_2$S$_3$ nanosheets, and (d) S-C$_3$N$_4$-dots.

The 'S' doping effectively decreases the bandgap resulting in a shift in the absorbance edge which is well-matched with the existing literature report.[33] The absorbance edge of S-C$_3$N$_4$-dots is located near the NIR region. After the decoration of S-C$_3$N$_4$-dots on the surface of In$_2$S$_3$-nanosheets, the absorption edge of In$_2$S$_3$ is shifted to a higher wavelength. The redshift in the absorption edge of In$_2$S$_3$ signifies the widening of the absorption of solar light. The Tauc plots for In$_2$S$_3$ and S-C$_3$N$_4$-dots are shown in **Figure 4.3c, d** and the calculated bandgaps are 2.20 eV and 2.22 eV for In$_2$S$_3$ nanosheets and S-C$_3$N$_4$-dots, respectively.

4.3.1.4 FESEM and EDS Analysis

The FESEM (field emission scanning electron microscope) analysis is executed to determine the morphology of the developed materials. **Figure 4.4a-d** shows the morphology of In$_2$S$_3$ and S-C$_3$N$_4$-dots decorated In$_2$S$_3$. Interconnected vertically grown nanosheets of In$_2$S$_3$ are observed through the FESEM imaging. From the FESEM analysis, it is hard to detect the decoration of S-C$_3$N$_4$-dots on the surface of In$_2$S$_3$ which presumably due to the very small size of S-C$_3$N$_4$-dots.
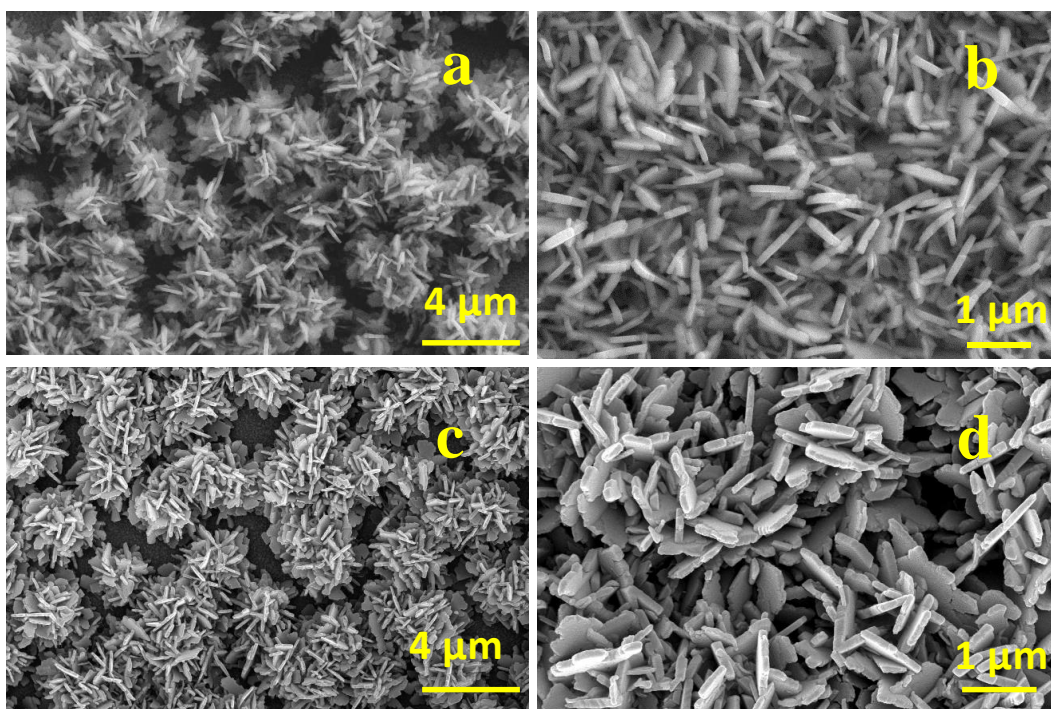
Figure 4.4: FESEM images of (a, b) In$_2$S$_3$ nanosheets, and (c, d) heterostructure of In$_2$S$_3$/S-C$_3$N$_4$-dots-20 at low and high magnifications, respectively.

To confirm the elemental composition, EDS (energy-dispersive X-ray spectroscopy) analysis is carried out and the mapping spectra are recorded for In_2S_3 nanosheets and decorated In_2S_3/S-C_3N_4-dots. It confirms the presence of 'In', 'S', 'C', and 'N' as elements in the synthesized heterostructure and it depicts the presence of S-C_3N_4-dots on In_2S_3 nanosheets (**Figures 4.5 and 4.6**).
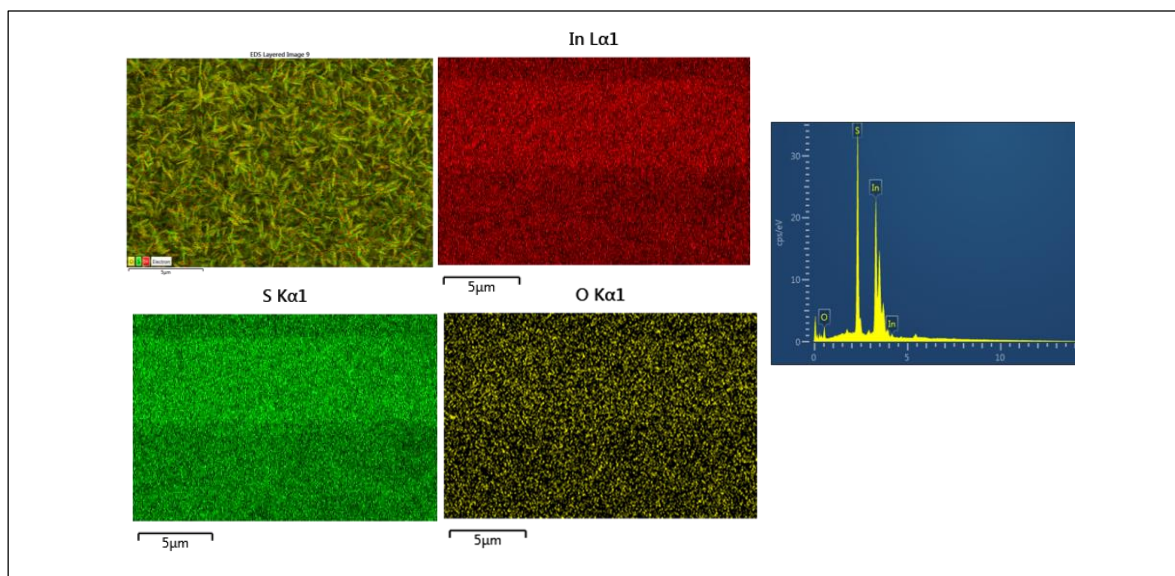
Figure 4.5: EDS analysis of In_2S_3 nanosheets on FTO which shows the uniform distribution of 'In' and 'S', and 'O' as an element.
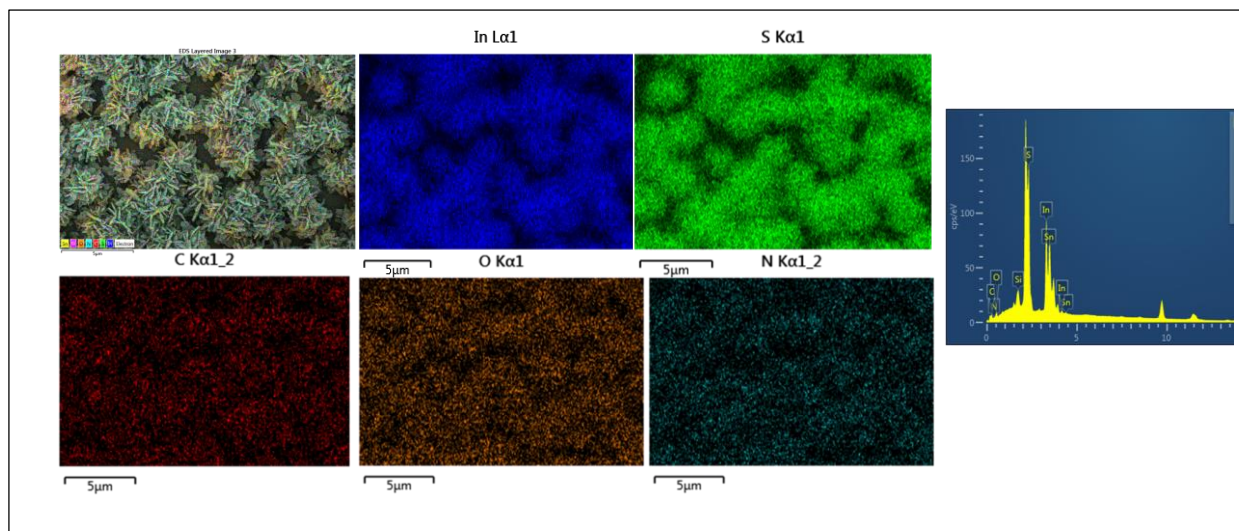
Figure 4.6: EDS analysis of In_2S_3/S-C_3N_4-dots-20 nanosheets on FTO which shows the uniform distribution of 'In', 'S', 'O', 'N' and 'C' as an element.

4.3.1.5 HRTEM and SAED Analysis

The size and crystallinity of the synthesized S-C_3N_4-dots are determined with the TEM and HRTEM analysis. **Figure 4.7a** shows that the size of the synthesized S-C_3N_4-dots is ~10-15 nm. The observed HRTEM image is shown in **Figure 4.7b**. The calculated lattice spacing of S-C_3N_4-dots is 0.33 nm, which corresponds to the (002) crystal plane. Whereas, the lattice spacing for C_3N_4-QDs is 0.32 nm corresponding to the same plane which is reported in the literature.[34] The increase in lattice spacing indicates the successful doping of 'S' in the C_3N_4 framework. The crystalline nature of S-C_3N_4-dots is further confirmed with the help of the SAED pattern (**Figure 4.7c**).
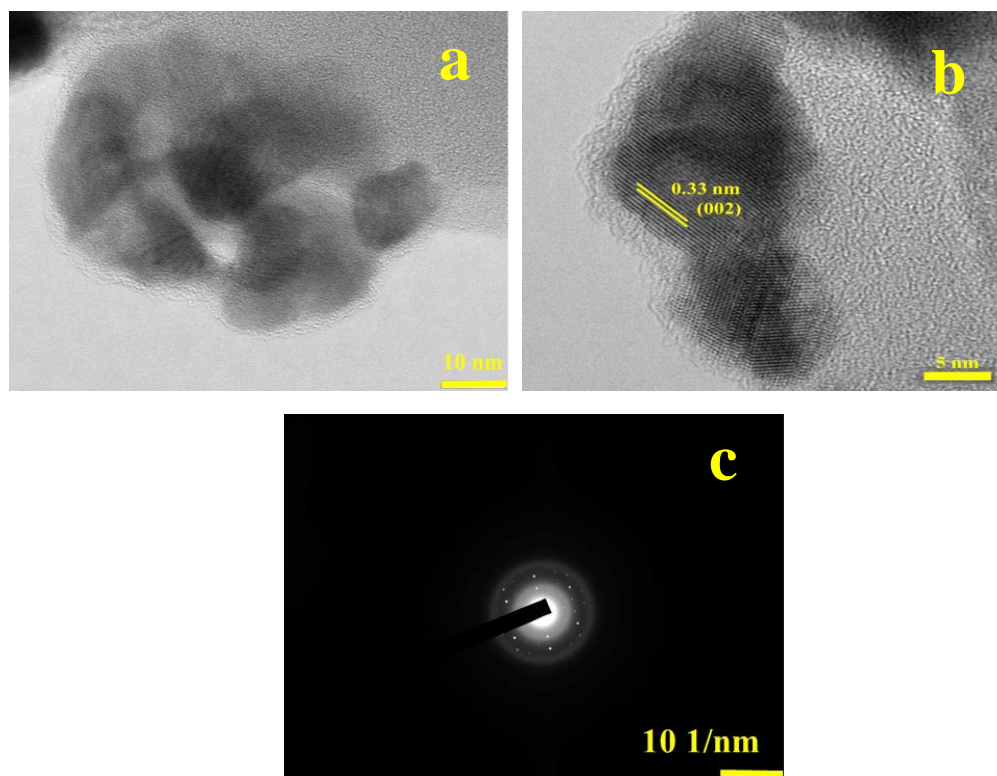
Figure 4.7: (a) TEM, (b) HRTEM images, and (c) SAED pattern of S-C_3N_4-dot, respectively.

4.3.1.6 Zeta Potential Measurement

The mode of attachment of S-C_3N_4-dots on the surface of In_2S_3 nanosheets is determined with the help of zeta potential measurement. The In_2S_3 nanosheets has positive surface charge and S-C_3N_4-dots have negative surface charge. The presence of opposite charge on the surface of In_2S_3

nanosheets and S-C$_3$N$_4$-dots indicates the electrostatic interaction between In$_2$S$_3$ nanosheets and S-C$_3$N$_4$-dots (**Figure 4.8**).
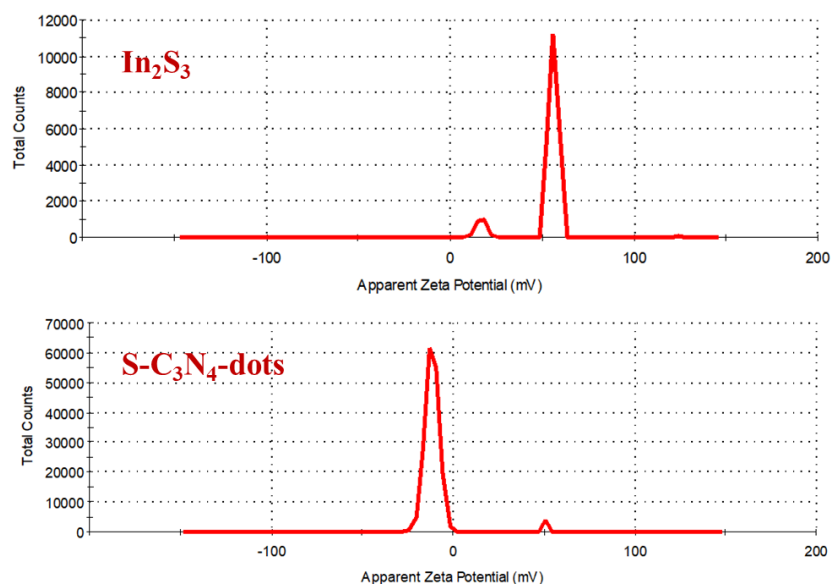
Figure 4.8: Zeta potential plots of In$_2$S$_3$ nanosheets and S-C$_3$N$_4$-dots.

4.3.2 Photoelectrochemical Activity

4.3.2.1 Linear Sweep Voltammetry

The PEC activities of all synthesized photoanodes such as In$_2$S$_3$, In$_2$S$_3$/ S-C$_3$N$_4$-dots-10, -20, and -30 are determined by using a three-electrode configuration under back illumination condition where Ag/AgCl is used as a reference electrode, Pt wire as a counter electrode, and the sample decorated FTO is used as a working electrode, respectively. 3.5 wt% NaCl solution (assuming seawater) and Na$_2$SO$_4$ are used as electrolytes. **Figure 4.9a** represents the comparative LSV curves under continuous illumination (100 mW/cm^2) condition, which show the dependence of the photocurrent with the applied potential for all the developed photoanodes. The developed bare In$_2$S$_3$ nanosheets can generate efficiently 0.22 mA/cm^2 photocurrent density at an applied potential of 0.58 V vs. RHE and 2.07 mA/cm^2 at 1.18 V vs. RHE. Further, to enhance the PEC activity, synthesized photoanode of In$_2$S$_3$ nanosheets is dipped into the S-C$_3$N$_4$-dots solution for different time intervals. Initially, for the decoration of S-C$_3$N$_4$-dots, In$_2$S$_3$ photoanode is dipped for 10 min (In$_2$S$_3$/S-C$_3$N$_4$-dots-10). The developed In$_2$S$_3$/S-C$_3$N$_4$-dots-10 nanosheets can generate 0.44 mA/cm^2 at an applied potential of 0.58 V vs. RHE which is ~2-fold higher than bare In$_2$S$_3$-

nanosheets. At the same time, it can generate a maximum photocurrent density of ~2.99 mA/cm^2 at an applied potential of 1.18 V vs. RHE. Further, an increase in the amount of 'S-C$_3$N$_4$-dots' on In$_2$S$_3$ by increasing the dipping time from 10 min to 20 min leads to the enhancement in the PEC activity of In$_2$S$_3$. In this condition, synthesized In$_2$S$_3$/S-C$_3$N$_4$-dots-20 photoanode can produce 0.77 mA/cm^2 and 4.93 mA/cm^2 photocurrent density at applied potentials of 0.58 and 1.18 V vs. RHE, respectively. The obtained maximum photocurrent density is ~2.38-fold higher compared to bare In$_2$S$_3$ nanosheets. Further, an increase in S-C$_3$N$_4$-dots on the surface of In$_2$S$_3$ does not lead to any enhancement in photocurrent density, however photocurrent density decreases in the case of In$_2$S$_3$/S-C$_3$N$_4$-dots-30. The In$_2$S$_3$/ S-C$_3$N$_4$-dots-30 can attain only 0.53 mA/cm^2 and 3.32 mA/cm^2 photocurrent density at potential of 0.58 and 1.18 V vs. RHE.
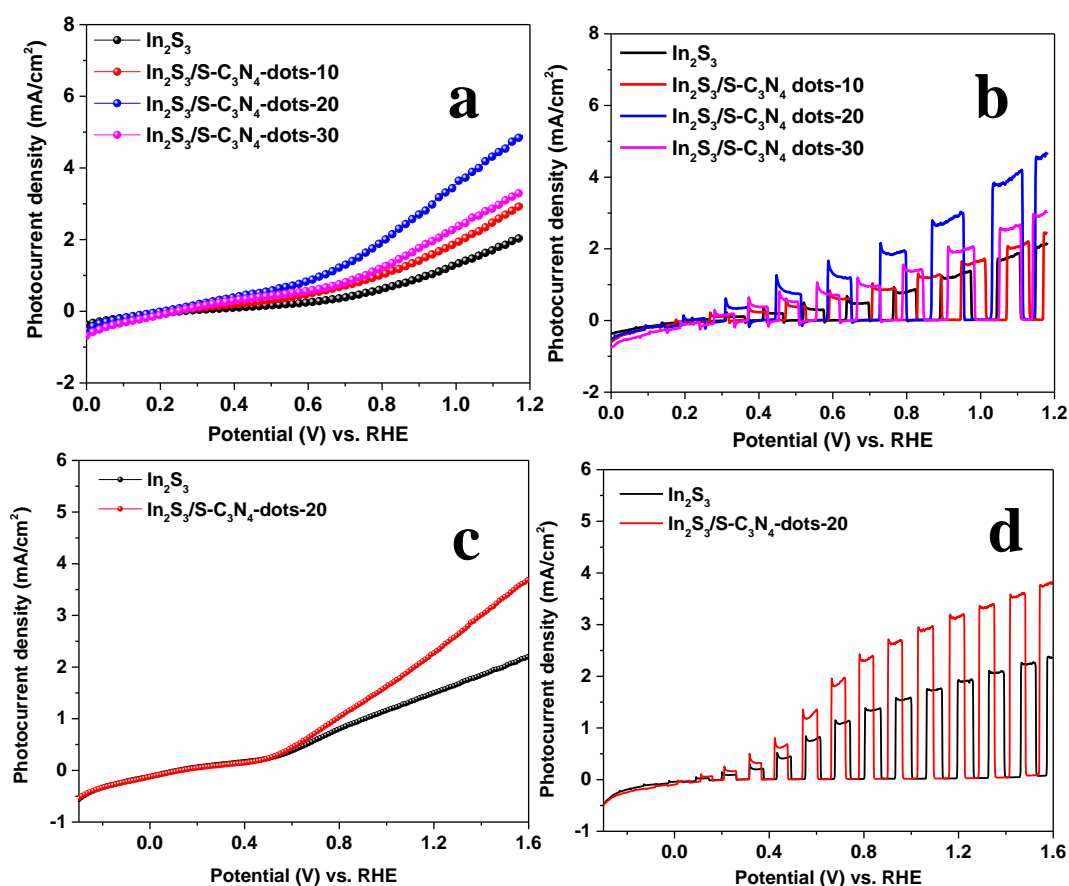
Figure 4.9: LSV plots of In$_2$S$_3$, and In$_2$S$_3$/S-C$_3$N$_4$-dots-10, 20, and -30 under (a) continuous, (b) chopped illumination in 3.5 wt% NaCl. LSV plot of In$_2$S$_3$, and In$_2$S$_3$/S-C$_3$N$_4$-dots-20 under (c) continuous, (d) chopped illumination in 0.5 M Na$_2$SO$_4$, respectively.

Figure 4.9b shows the LSV curves under chopped illumination, which indicates the switch 'on' and 'off' behavior of the photoelectrodes with negligible dark currents. The PEC activity of the developed electrodes is also determined in 0.5 M Na_2SO_4. **Figure 4.9c, d** shows the behavior of photoelectrodes under continuous and chopped illumination in 0.5 M Na_2SO_4. From the observed PEC activity, it is clear that In_2S_3/S-C_3N_4-dots-20 is achieved higher PEC activity than the In_2S_3 nanosheets. It is presumed that the more deposition of S-C_3N_4 on In_2S_3 blocks the In_2S_3-electrolyte interface which leads to hindrance in the photogenerated charge-carrier transportation. The optimum amount of 'S-C_3N_4-dots' enhances the optical absorbance of In_2S_3 which further helps to enhance the PEC activity.

4.3.2.2 Photostability and Transient Decay Time (τ)

The chronoamperometry study is carried out for 90 seconds at an applied potential of 0.7 V vs. RHE to investigate the transient decay time (**Figure 4.10a**). The photostabilities of all the developed photoanodes are checked for 2700 seconds under continuous illumination at 0.7 V vs. RHE (**Figure 4.10b**). While studying the switch 'on' and 'off' behavior, anodic spikes are observed due to the accumulation of holes at the interface of the electrode/electrolyte, which is not injected into the electrolyte due to slow reaction kinetics. [35] The behavior of charge carrier transport is investigated from the transient photocurrent curve (**Figure 4.10c**). The transient decay time is calculated by using the following equation:[36, 37]

$$D = (I_t - I_s)/(I_{in} - I_s)\ldots\ldots 1$$

where I_t is the photocurrent at time t, I_s is the current at steady state, and I_{in} is the current of the anodic spike. The transient decay time (τ) is defined as the time at which ln D = -1. **Figure 4.10d** shows that after the decoration of S-C_3N_4 on In_2S_3 nanosheets transient decay time becomes longer than that of bare In_2S_3 nanosheets. The result reveals that heterostructure suppresses the recombination at the interface by transporting holes to the electrolyte.
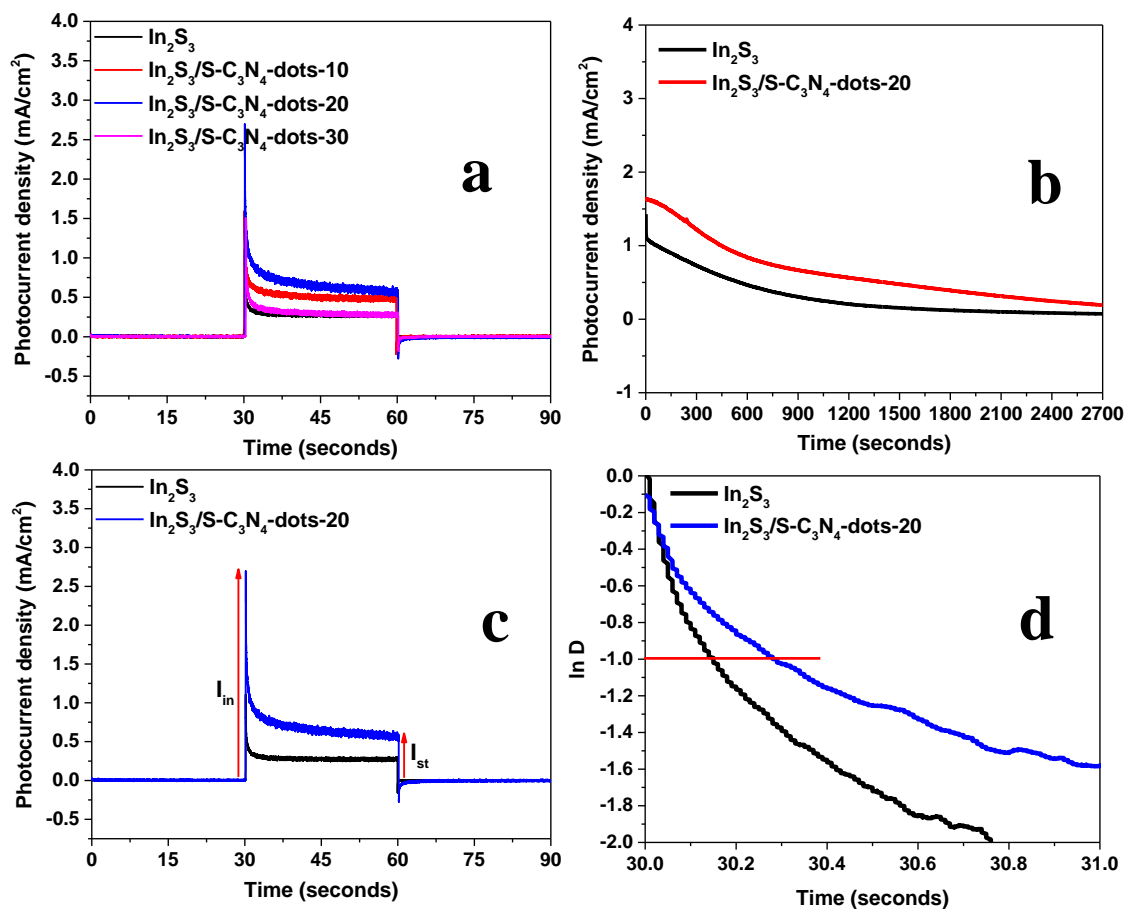
Figure 4.10: (a) i-t plot of In_2S_3 nanosheets, In_2S_3/S-C_3N_4-dots-10, -20, and -30 in chronoamperometry study, (b) plot of photostability of In_2S_3, In_2S_3/S-C_3N_4-dots-20 for 1h under continuous illumination, (c) plot of transient photocurrent density under chopped illumination condition, and (d) plot of transient decay time (τ) of In_2S_3 and In_2S_3/S-C_3N_4-dots-20 and, respectively.

4.3.2.3 Determination of Photoconversion Efficiency

The improved photoactivity after the decoration of 'S-C_3N_4-dots' on In_2S_3 nanosheets is quantitatively estimated with the help of applied-bias-to-photon conversion (ABPE) efficiency ($\eta\%$). It is calculated with the help of the J-V plot and the following equation is used:[38]

$$\eta = [J\ (1.23\text{-}V_{RHE})/P_{in}]\ \%..........2$$

where J is the photocurrent density, V_{RHE} is the applied potential with respect to RHE, and P_{in} is the incident light intensity. The photoconversion efficiency values are plotted and shown in **Figure**

4.11a, b and it indicates the enhancement in efficiency after the decoration of 'S-C$_3$N$_4$-dots'. The η% of bare In$_2$S$_3$ is 0.31% at a potential of 0.95 V vs. RHE. The In$_2$S$_3$/S-C$_3$N$_4$-dots-20 can attain the maximum photoconversion efficiency (η)%: 0.88% at 0.95 V vs. RHE, which is ~2.83 fold higher than the bare In$_2$S$_3$ nanosheets. The observed η% for In$_2$S$_3$/ S-C$_3$N$_4$-dots-10 and In$_2$S$_3$/S-C$_3$N$_4$-dots-30 are 0.46 and 0.57, respectively at a potential of 0.95 V vs. RHE. From the observed ABPE%, it is confirmed that the best-obtained photoanode is In$_2$S$_3$/S-C$_3$N$_4$-dots-20.
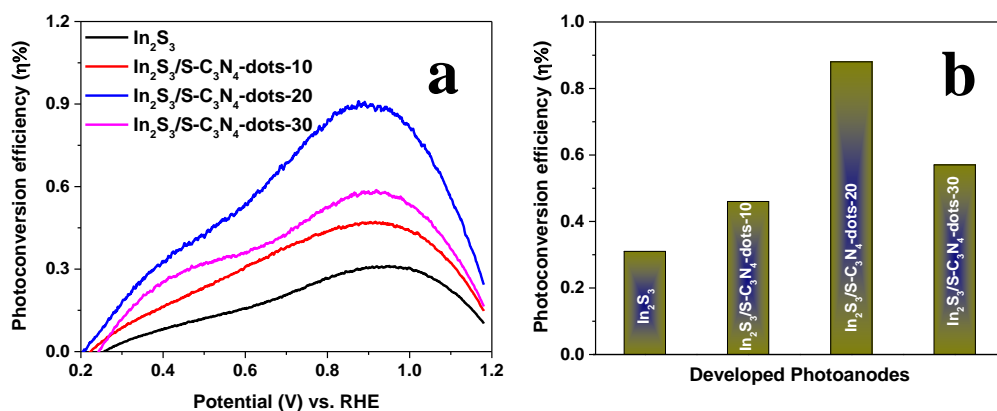
Figure 4.11: (a, b) Plot of photoconversion efficiency of In$_2$S$_3$ nanosheets and heterostructure of In$_2$S$_3$/S-C$_3$N$_4$-dots-10, -20, and-30.

4.3.2.4 Determination of Charge Transfer Resistance through Impedance Spectroscopy

PEC enhancement of the heterostructure was initially thought of due to the enhancement in optical absorbance. Whether the PEC enhancement is only due to the contribution of enhancement in optical absorbance or there are some other effects that are also contributing simultaneously, needs to be investigated. First, to know the role of 'S' doping in the C$_3$N$_4$ framework the electrochemical impedance spectra (EIS) measurement is carried out for C$_3$N$_4$-dots and S-C$_3$N$_4$-dots. It is observed that the radius of the semicircle arc of S-C$_3$N$_4$-dots is smaller than the C$_3$N$_4$-dots which shows the higher charge transfer ability after doping of 'S' in the C$_3$N$_4$ framework (**Figure 4.12a**). On the other hand, the ease of charge transfer feasibility in bare In$_2$S$_3$ and the heterostructure is determined with help of the photoelectrochemical impedance measurement under continuous illumination at an applied potential of 0.58 V vs. RHE. The radius of the semicircle arc of the Nyquist plot indicates the charge transfer achievability. For In$_2$S$_3$/S-C$_3$N$_4$-dots-20, the radius of the arc of the

semicircle is the smallest. It indicates that the In_2S_3/S-C_3N_4-dots-20 show low charge transfer resistance which means high charge transferability at the electrode-electrolyte interface. The comparative EIS plot is shown in **Figure 4.12b** and the observed order of charge transferability of all the developed photoanodes is as follows: In_2S_3/S-C_3N_4-dots-20> In_2S_3/S-C_3N_4-dots-10> In_2S_3/S-C_3N_4-dots-30> In_2S_3. The increase in charge transportation after the decoration of S-C_3N_4-dots on the surface of In_2S_3 nanosheets indicates the favorable charge-carrier separation in the heterostructure. Further investigation has also been carried out to know the reason for the improved charge-carrier separation in the heterostructure.
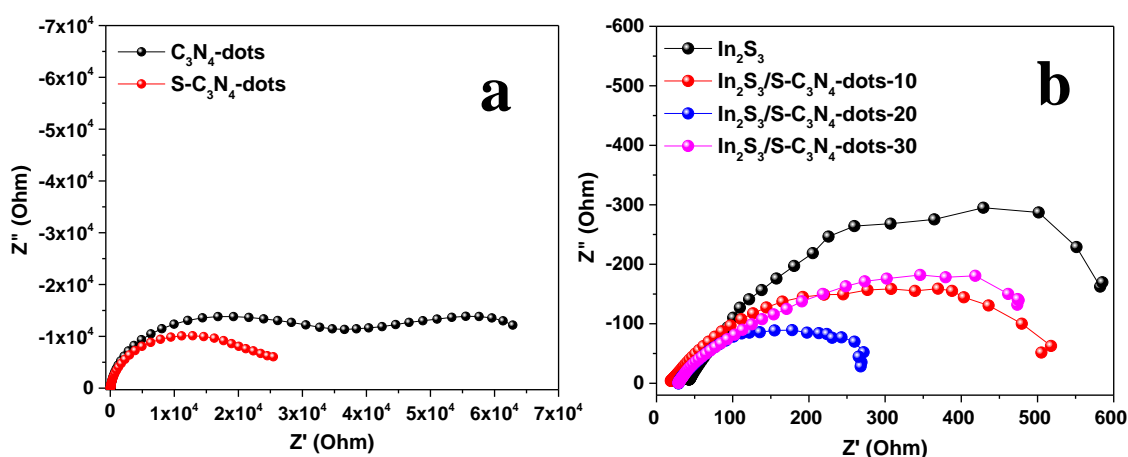
Figure 4.12: (a) EIS spectra of C_3N_4-dots and S-C_3N_4-dots, (b) EIS spectra of In_2S_3 nanosheets and heterostructure of In_2S_3/S-C_3N_4-dots-10, -20, and -30, respectively.

4.3.2.5 Calculation of Carrier Density through Mott-Schottky Analysis

In this context, the electronic property and the carrier density of the developed photoanodes are determined with the help of Mott-Schottky (M-S) analysis (**Figure 4.13a**). The observed positive slope in the M-S plot confirms the n-type nature of developed photoanodes. Carrier density and the flat band potentials are calculated by using the following equation:[39,40]

$$1/C_s^2 = (2/e\varepsilon\varepsilon_0 N_d A^2) \ [(V-V_{FB}-kT/e)]\ldots\ldots\ldots3$$

where C_s, e, ε_0, ε, N_d, V_{FB}, A, T, and k are specific capacitance, electron's charge, the electric permittivity of vacuum, the dielectric constant of the semiconductor, carrier density, flat band potential, area of the sample, temperature, and Boltzmann constant, respectively. The slopes of all the S-C_3N_4-dots decorated In_2S_3 nanosheets are lower compared to the bare In_2S_3 which signifies

the higher carrier density. The carrier density of In_2S_3 nanosheets is 3.2×10^{18} cm^{-3} which is nearly 1.77 fold lower than the In_2S_3/S-C_3N_4-dots-20 photoanode. The negative flat band potential signifies the widening of the space charge region. The flat band potential of In_2S_3/S-C_3N_4-dots-20 is 0.07 V vs. RHE, which indicates increased band bending than the bare In_2S_3 nanosheets (0.27 V vs. RHE). Further, the enhanced band bending signifies the higher charge-carrier separation as well as transportation after the decoration of 'S-C_3N_4-dots' on In_2S_3 nanosheets.
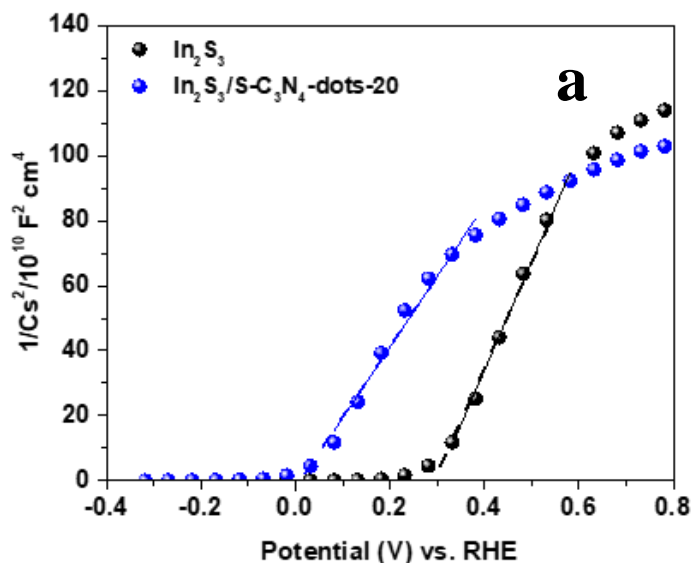
Figure 4.13: (a) Mott-Schottky plot of In_2S_3 nanosheets and In_2S_3/S-C_3N_4-dots-20 heterostructure.

4.3.2.6 Determination of Electrochemical Surface Active Area through Cyclic Voltammetry

To know the importance of air calcination of In_2S_3 nanosheets, the electrochemical surface area before and after calcination of In_2S_3 is calculated from the cyclic voltammetry (CV) analysis. After calcination of In_2S_3 nanosheets the electrochemical active surface area is enhanced ~1.3-fold. It confirms that calcination in the air increases the active sites (**Figure 4.14a-c**).
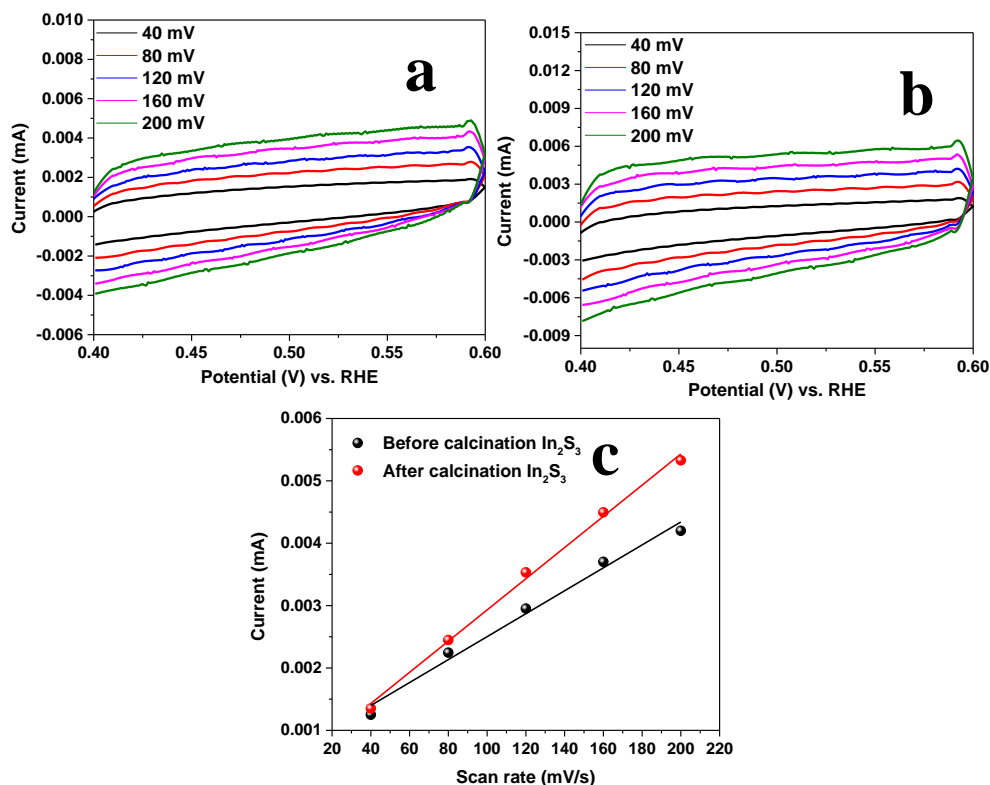
Figure 4.14: CV plot from (a, b) 0.40 V to 0.60 V vs. RHE, (c) plot of double-layer capacitance (C_{dl}) for before and after calcination of In_2S_3 nanosheets, respectively.

4.3.2.7 Mechanism of Charge Carrier Separation through Type-II band Alignment

From the experimental data it is clear that after the formation of the heterostructure, optical absorbance enhances, which is due to the presence of 'S-C_3N_4-dots' on the surface of In_2S_3. Similarly, carrier density also enhances in the heterostructure. From the EIS analysis, it is also observed that the charge transportation enhances at the interface of the heterostructure. The reason behind enhanced charge separation needs to be investigated. For that the band alignment of S-C_3N_4-dots and In_2S_3 are determined.

It is assumed that S-C_3N_4-dots and In_2S_3 form type-II heterostructure which may enhance the charge-carrier separation and transportation depending on the band alignment. To ensure the formation of the type-II heterostructure, the band alignment of both materials needs to be determined. The position of the energy band can be calculated with the help of the given equation:

E_{CB} = -X + ½ E_g; E_{VB} = E_{CB}-E_g, where X = electronegativity of the semiconductor, E_g = bandgap, E_{VB} and E_{CB} = band edge position of valance band and conduction band, respectively. The electronegativity values of C_3N_4 and In_2S_3 are given in the literature, which is 4.64 eV and 4.7 eV, respectively.[41, 42] The calculated band gap values from UV-visible spectra are 2.20 eV and 2.22 eV for In_2S_3 and S-C_3N_4-dots, respectively. From the calculated bandgap and known electronegativity values, the conduction band (CB) edge positions are determined and the values are -3.60 eV and -3.54 eV for In_2S_3 and S-C_3N_4-dots, respectively. Further, the valance band (VB) edge positions are determined as -5.80 eV and -5.76 eV for both of them. The band edge positions indicate the type-II heterostructure formation. Such band alignment facilitates charge carrier separation and restricts the charge-carrier recombination process. Under the illumination of light, the charge-carrier is generated in both the materials where electrons are injected from the CB of S-C_3N_4-dots to CB of In_2S_3. Whereas, holes migrate in the opposite direction, i.e., from VB of In_2S_3 to VB of S-C_3N_4-dots. The migration of charge carriers in opposite direction in the heterostructure leads to improved charge-carrier separation, less recombination, and enriched minority carrier injection in the semiconductor-electrolyte interface. Therefore, the process of charge-carrier separation and decrease in recombination is well understood from the above-mentioned band alignment of In_2S_3 and S-C_3N_4-dots (**Scheme 4.2**).
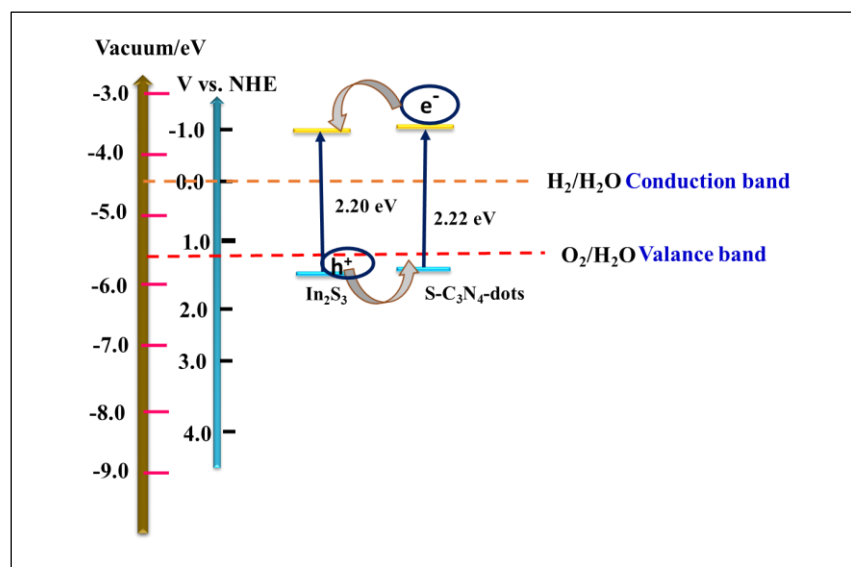
Scheme 4.2: Schematic presentation of band alignments of In_2S_3 nanosheets and S-C_3N_4-dots.

4.4 Comparative Study

The heterostructure (In_2S_3/S-C_3N_4-dots) and In_2S_3 nanosheets show efficient PEC activity compared to the existing literature in both the electrolytes (3.5 wt% NaCl and 0.5 M Na_2SO_4) (**Table 4.1**).

Table 4.1: Comparative data of PEC activity of In_2S_3/S-C_3N_4-dots heterostructure with the reported data in the literature.

S.N.	Photoanodes	Electrolyte	Photocurrent density	References
1.	β-In_2S_3 nanosheets	1 M NaOH	0.15 mA/cm^2 at 1.23 V vs. RHE	43
2.	β-In_2S_3 nanoplates	1 M NaOH	1.26 mA/cm^2 at 1.23 V vs. RHE	44
3.	β-In_2S_3 2D ultrathin nanosheets	1.0 M KCl	35.7 μA/cm^2 at 1.2 V vs. RHE	11
4.	β-In_2S_3 nanoflakes	0.5 M NaOH	370 μA/cm^2 at 0.7 V vs. Ag/AgCl	17
5.	$BiVO_4$/GCN photoanode	0.1 M K_2HPO_4	7.4 mA/cm^2 at 2.2 V vs. RHE	45
6.	α-Fe_2O_3/ g-C_3N_4	0.5 M Na_2SO_4	1.17 mA/cm^2 at 1.2 V vs. Ag/AgCl	46
7.	CNQDs@TiO_2	0.5 M Na_2SO_4	0.3 mA/cm^2 at 1.23 V vs. RHE	47
8.	$BiVO_4$/g-C_3N_4-NS	0.1 M Na_2SO_4	3.12 mA/cm^2 at 1.23 V vs. RHE	48
9.	g-C_3N_4/TiO_2	0.1 M Na_2SO_4	0.86 mA/cm^2 at 1.23 V vs. RHE	49
10.	$NiFeO_x$/B-C_3N_4/Mo-$BiVO_4$	PBS	5.93 mA/cm^2 at 1.23 V vs. RHE	50
11.	ZnO/S-C_3N_4 QDs	0.2 M Na_2SO_4	100 μA/cm^2 at 1.0 V vs. RHE	26
12.	In_2S_3	0.5 M Na_2SO_4	1.42 mA/cm^2 at 1.23 V vs. RHE	In this study
	In_2S_3/S-C_3N_4-dots		2.16 mA/cm^2 at 1.23 V vs. RHE	
13.	In_2S_3	3.5 wt% NaCl	2.07 mA/cm^2 at 1.18 V vs. RHE	In this study
	In_2S_3/S-C_3N_4-dots		4.93 mA/cm^2 at 1.18 V vs. RHE	

4.5 Conclusion

In this study, an efficient photoanode is developed through the sensitization of In_2S_3 nanosheets by S-C_3N_4-dots. Initially, In_2S_3 nanosheets are developed on FTO through the hydrothermal method. The synthesized In_2S_3 nanosheets can harvest visible light and can produce a maximum photocurrent density of 2.07 mA/cm^2 at an applied potential of 1.18 V vs. RHE in a corrosive environment (3.5wt% NaCl). Further, the PEC activity is improved after the adornment of S-C_3N_4-dots on In_2S_3 nanosheets, which is executed through the dip-coating method. The developed heterostructure: In_2S_3/S-C_3N_4-dots can generate ~2.38-fold higher photocurrent density than the bare In_2S_3 nanosheets. The increase in PEC activity is due to the enhancement in the optical absorbance and the development of the type-II heterostructure. The formation of type-II heterostructure leads to enhanced carrier density, increased charge carrier separation at the space charge layer, and transportation. The transient decay time of the heterostructure indicates a delay in charge-carrier recombination compared to bare In_2S_3. Besides, the determined more negative flat band potential signifies the broadening in the space charge layer and more band bending in the heterostructure. The large band bending of the heterostructure further confirms the higher charge-carrier transportation than the bare In_2S_3 nanosheets. The developed heterostructure can work efficiently in a corrosive environment for up to 2700 seconds. This study paves a new avenue to increase the efficiency of a photoanode for solar-driven water-splitting.

4.6 References

1. Lewis, N. S.; Nocera, D. G. Powering the planet: Chemical challenges in solar energy utilization. *PNAS* **2006**, *103*, 15729-15735.

2. Armaroli, N.; Balzani, V. The Future of Energy Supply: Challenges and Opportunities. *Angew. Chem. Int. Ed.*, **2007**, *46*, 52-66.

3. Walter, E. L.; McKone, W. J. R.; Boettcher, S. W.; Mi, Q.; Santori, E. A.; Lewis, N. S. Solar Water Splitting Cells. *Chem. Rev.*, 2010, **110**, 6446-6473.

4. Zhang, P.; Wang, T.; Chang, X.; Gong, J. Effective Charge Carrier Utilization in Photocatalytic Conversions. *Acc. Chem. Res*., **2016**, *49*, 911-921.

5. Fujishima, A.; Honda, K. Photolysis-decomposition of Water at the Surface of an Irradiated Semiconductor. *Nature* **1972**, *238*, 37-38.

6. Yang, J-S.; Wu, J-J. Toward Eco-Friendly and Highly Efficient Solar Water Splitting Using In_2S_3/Anatase/Rutile TiO_2 Dual-Staggered-Heterojunction Nanodendrite Array Photoanode. *ACS Appl. Mater. Interfaces* **2018**, *10*, 3714-3722.

7. Chen, Y.; Zheng, W.; Murcia-Lopez, S.; Lv, F.; Morante, J. R.; Vayssieres, L.; Burda, C. Light management in photoelectrochemical water splitting-from materials to device engineering. *J. Mater. Chem. C* **2021**, *9*, 3726-3748.

8. Zhou, M.; Lou, X. W. D.; Xie, Y. Two-dimensional nanosheets for photoelectrochemical water splitting: Possibilities and opportunities. *Nano Today* **2013**, *8*, 598-618.

9. Sharma, M. D.; Mahala, C.; Basu, M. Band gap tuning to improve the photoanodic activity of $ZnIn_xS_y$ for photoelectrochemical water oxidation. *Catal. Sci. Technol*., **2019**, *9*, 6769-6781.

10. Liu, Q.; Lu, H.; Shi, Z.; Wu, F.; Guo, J.; Deng, K.; Li, L. 2D $ZnIn_2S_4$ Nanosheet/1D TiO_2 Nanorod Heterostructure Arrays for Improved Photoelectrochemical Water Splitting. *ACS Appl. Mater. Interfaces* **2014**, *6*, 17200-17207.

11. Li, M.; Tu, X.; Su, Y.; Lu, J.; Hu, J.; Cai, B.; Zhou, Z.; Yang, Z.; Zhang, Y. Controlled growth of vertically aligned ultrathin In_2S_3 nanosheet arrays for photoelectrochemical water splitting. *Nanoscale* **2018**, *10*, 1153-1161.

12. Hou, Y.; Qiu, M.; Zhang, T.; Zhuang, X.; Kim, C-S.; Yuan, C.; Feng, X. Ternary Porous Cobalt Phosphoselenide Nanosheets: An Efficient Electrocatalyst for Electrocatalytic and Photoelectrochemical Water Splitting. *Adv. Mater.*, **2017**, *29*, 1701589 (1-8).

13. Wang, L.; Xia, L.; Wu, Y.; Tian, Y. Zr-Doped β-In$_2$S$_3$ Ultrathin Nanoflakes as Photoanodes: Enhanced Visible-Light-Driven Photoelectrochemical Water Splitting. *ACS Sustainable Chem. Eng.*, **2016**, *4*, 2606-2614.

14. Kim, W-T.; Kim, C-D. Optical energy gaps of β-ln$_2$S$_3$ thin films grown by spray pyrolysis. *J. Appl. Phys.*, **1986**, *60*, 2631-2632.

15. Zhang, J.; Wang, H.; Yuan, X.; Zeng, G.; Tu, W.; Wang, S. Tailored Indium Sulfide-based Materials for Solar-Energy Conversion and Utilization. *J. Photochem. Photobiol. C: Photochem. Rev*., **2019**, *38*, 1-26.

16. Gao, W.; Liu, W.; Leng, Y.; Wang, X.; Wang, X.; Hu, B.; Yu, D.; Sang, Y.; Liu, H. In$_2$S$_3$ nanomaterial as a broadband spectrum photocatalyst to display significant activity. *Appl. Catal. B: Environ*., **2015**, *176*, 83-90.

17. Tian, Y.; Wang, L.; Tang, H.; Zhou, W. Ultrathin two-dimensional β-In$_2$S$_3$ nanocrystals: oriented-attachment growth controlled by metal ions and photoelectrochemical properties. *J. Mater. Chem. A* **2015**, *3*, 11294-11301.

18. Ke, J.; He, F.; Wu, H.; Lyu, S.; Liu, J.; Yang, B.; Li, Z.; Zhang, Q.; Chen, J.; Lei, L.; Hou, Y.; Ostrikov, K. Nanocarbon-Enhanced 2D Photoelectrodes: A New Paradigm in Photoelectrochemical Water Splitting. *Nano-Micro Lett.*, **2021**, *24*, 1-29.

19. Xu, X. J.; Liu, Y.; Zhang, R.; Zhu, Y. A Strategy of Enhancing the Photoactivity of g-C$_3$N$_4$ via Doping of Nonmetal Elements: A First-Principles Study. *J. Phys. Chem. C* **2012**, *116*, 23485-23493.

20. Arumugam, M.; Tahir, M.; Praserthdam, P. Effect of nonmetals (B, O, P, and S) doped with porous g-C$_3$N$_4$ for improved electron transfer towards photocatalytic CO$_2$ reduction with water into CH$_4$. *Chemosphere* **2022**, *286*, 131765 (11).

21. Mahala, C.; Sharma, M. D.; Basu, M. ZnO Nanosheets Decorated with Graphite-Like Carbon Nitride Quantum Dots as Photoanodes in Photoelectrochemical Water Splitting. *ACS Appl. Nano Mater*., **2020**, *3*, 1999-2007.

22. Liu, M.; Jiao, Y.; Qin, J.; Li, Z.; Wang, J. Boron doped C$_3$N$_4$ nanodots/nonmetal element (S, P, F, Br) doped C$_3$N$_4$ nanosheets heterojunction with synergistic effect to boost the photocatalytic hydrogen production performance. *Appl. Surf. Sci.*, **2021**, *541*, 148558 (11).

23. Guo, H.; Shu, Z.; Chen, D.; Tana, Y.; Zhou, J.; Meng, F.; Li, T. One-step synthesis of S-doped g-C$_3$N$_4$ nanosheets for improved visible-light photocatalytic hydrogen evolution. *Chem. Phys.*, **2020**, *533*, 110714 (1-7).

24. Long, D.; Chen, Z.; Rao, X.; Zhang, Y. Sulfur-Doped g-C$_3$N$_4$ and BiPO$_4$ Nanorod Hybrid Architectures for Enhanced Photocatalytic Hydrogen Evolution under Visible Light Irradiation. *ACS Appl. Energy Mater.*, **2020**, *3*, 5024-5030.

25. He, H.; Li, J.; Liu, Y.; Liu, Q.; Zhan, F.; Li, Y.; Li, W.; Wen, J. S-C$_3$N$_4$ Quantum Dot Decorated ZnO Nanorods to Improve Their Photoelectrochemical Performance. *Nano: Brief Reports and Reviews* **2017**, *12*, 1750064 (1-11).

26. Hashemi, M.; Minbashi, M.; Mohammad, S.; Ghorashi, B.; Ghobadi, A. A modeling study on utilizing low temperature sprayed In$_2$S$_3$ as the buffer layer of CuBaSn(S, Se) solar cells. *Sci. Rep.*, **2021**, *11*, 20038 (1-11).

27. Zhan, Y.; Liu, Z.; Liu, Q.; Huang, D.; Wei, Y.; Hu, Y.; Liana, X.; Hu, C. A facile and one-pot synthesis of fluorescent graphitic carbon nitride quantum dots for bio-imaging applications. *New J. Chem.*, **2017**, *41*, 3930-3938.

28. Dang, X.; Zhao, H.; Wang, X.; Sailijiang, T.; Chen, S.; Quan, X. Photoelectrochemical aptasensor for sulfadimethoxine using g-C$_3$N$_4$ quantum dots modified with reduced graphene oxide. *Microchimica Acta* **2018**, *185*, 345 (1-8).

29. Kambas, K.; Spyridelis, J.; Balkani, M.; Far Infrared and Raman Optical Study of α-and β-In$_2$S$_3$ compounds. *Phys. stat. sol.*, **1981**, *105*, 291-296.

30. Sciortino, L.; Sciortino, A.; Popescu, R.; Schneider, R.; Gerthsen, D.; Agnello, S.; Cannas, M.; Messina, F. Tailoring the Emission Color of Carbon Dots through Nitrogen-Induced Changes of Their Crystalline Structure. *J. Phys. Chem. C* **2018**, *122*, 19897-19903.

31. Kalisamy, P.; Lallimathi, M.; Suryamathi, M.; Palanivel, B.; Venkatachalam, M. ZnO-embedded S-doped g-C$_3$N$_4$ heterojunction: mediator-free Z-scheme mechanism for enhanced charge separation and photocatalytic degradation. *RSC Adv.*, **2020**, *10*, 28365-28375.

32. Wang, K.; Li, Q.; Liu, B.; Cheng, B.; Ho, W.; Yu, J. Sulfur-doped g-C$_3$N$_4$ with enhanced photocatalytic CO$_2$-reduction performance. *Appl. Catal. B: Environ*, **2015**, *176-177*, 44-52.

33. Stolbov, S.; Zuluaga, S. Sulfur doping effects on the electronic and geometric structures of graphitic carbon nitride photocatalyst: insights from first principles. *J. Phys.: Condens. Matter* **2013**, *25*, 085507 (11).

34. Wu, X.; Yang, L.; Luo, L.; Shi, G.; Wei, X.; Wang, F. Engineered g-C_3N_4 Quantum Dots for Tunable Two-Photon Imaging and Photodynamic Therapy. *ACS Appl. Bio Mater*., **2019**, *2*, 1998-2005.

35. Sivula, K. Metal Oxide Photoelectrodes for Solar Fuel Production, Surface Traps, and Catalysis. *J. Phys. Chem. Lett.*, **2013**, *4*, 1624-1633.

36. Gao, L.; Li, F.; Hu, H.; Long, X.; Xu, N.; Hu, Y.; Wei, S.; Wang, C.; Ma, J.; Jin, J. Dual Modification of a $BiVO_4$ Photoanode for Enhanced Photoelectrochemical Performance. *ChemSusChem*, **2018**, *11*, 2502-2509.

37. Tafalla, D.; Salvador, P.; Benito, R. M. Kinetic Approach to the Photocurrent Transients in Water Photoelectrolysis at n-TiO_2 Electrodes II. Analysis of the Photocurrent-Time Dependence. *J. Electrochem. Soc*., **1990**, *137*, 1810-1815.

38. Xu, X-T.; Pan, L.; Zhang, X.; Wang, L.; Zou, J-J. Rational Design and Construction of Cocatalysts for Semiconductor-Based Photo-Electrochemical Oxygen Evolution: A Comprehensive Review. *Adv. Sci.*, **2018**, *6*, 1801505 (35).

39. Basu, M. Porous Cupric Oxide: Efficient Photocathode for Photoelectrochemical water splitting. *ChemPhotoChem* **2019**, *3*, 1254-1262.

40. Masudy-Panah, S.; Moakhar, R. S.; Chua, C. S.; Kushwaha, A.; Wong, T. I.; Dalapati, G. K. Rapid thermal annealing assisted stability and efficiency enhancement in a sputter deposited CuO photocathode. *RSC Adv*., **2016**, *6*, 29383-29390.

41. Che, Y.; Liu, Q.; Lu, B.; Zhai, J.; Wang, K.; Liu, Z. Plasmonic ternary hybrid photocatalyst based on polymeric g-C_3N_4 towards visible light hydrogen generation. *Sci. Rep.*, **2020**, *10*, 721(1-12).

42. Xu, Y.; Schoonen, M. A. A. The Absolute Energy Positions of Conduction and Valence Bands of Selected Semiconducting Minerals. *Am. Mineral* **2000**, *85*, 543-556.

43. Gao, Y.; Zhang, S.; Wu, Y.; Tian, Y.; Fu, H.; Zhan, S.; P-doped In_2S_3 nanosheets coupled with $InPO_x$ overlayer: Charge-transfer pathways and highly enhanced photoelectrochemical water splitting. J. Catal., **2019**, *375*, 389-398.

44. Gao, Y.; Zhang, S.; Bu, X.; Tian, Y. Surface Defect Engineering via Acid Treatment Improving Photoelectrocatalysis of β-In_2S_3 Nanoplates for Water Splitting. *Catal. Today* **2019**, *327*, 271-278

45. Prakash, J.; Prasad, U.; Alexander, R.; Bahadur, J.; Dasgupta, K.; Kannan, A. N. M. Photoelectrochemical Solar Water Splitting: The Role of the Carbon Nanomaterials in Bismuth Vanadate Composite Photoanodes toward Efficient Charge Separation and Transport. *Langmuir* **2019**, *35*, 14492-14504.

46. Arzaee, N. A.; Firdaus, M.; Noh, M.; Suraya, N.; Ita, H. M.; Mohamed, N. A.; Farhana, S. N.; Nasir, M.; Nawas, I.; Mumthas, N.; Ismail, A. F.; Teridi, M. A. M. Nanostructure-assisted charge transfer in α-Fe_2O_3/g-C_3N_4 heterojunctions for efficient and highly stable photoelectrochemical water splitting. *Dalton Trans*., **2020**, *49*, 11317-11328.

47. Huang, L.; Meng, Q.; Shang, C.; Jin, M.; Shui, L.; Zhang, Y.; Zhang, Z.; Chen, Z.; Yuan, M.; Wang, X.; Kempa, K.; Zhou, G. Modified Nanopillar Arrays for Highly Stable and Efficient Photoelectrochemical Water Splitting. *Global Challenges* **2019**, *3*, 1800027 (5).

48. Feng, C.; Wang, Z.; Ma, Y.; Zhang, Y.; Wang, L.; Bi, Y. Ultrathin graphitic C_3N_4 nanosheets as highly efficient metal-free cocatalyst for water oxidation. *Appl. Catal. B: Environ*., **2017**, *205*, 19-23.

49. C. Liu, F. Wang, J. Zhang, K. Wang, Y, Qiu, Q, Liang, and Z, Chen, Efficient Photoelectrochemical Water Splitting by g-C_3N_4/TiO_2 Nanotube Array Heterostructures. *Nano-Micro Lett*., **2018**, *10*, 37 (13)

50. K-H. Ye, H. Li, D. Huang, S. Xiao, W. Qiu, M. Li, Y. Hu, W. Mai, H. Ji, and S. Yang, Enhancing photoelectrochemical water splitting by combining work function tuning and heterojunction engineering. *Nat. Commun*., **2019**, *10*, 3687 (9).

Band Gap Tuning to Improve the Photoanodic Activity of ZnIn$_x$S$_y$ for Photoelectrochemical Water Oxidation
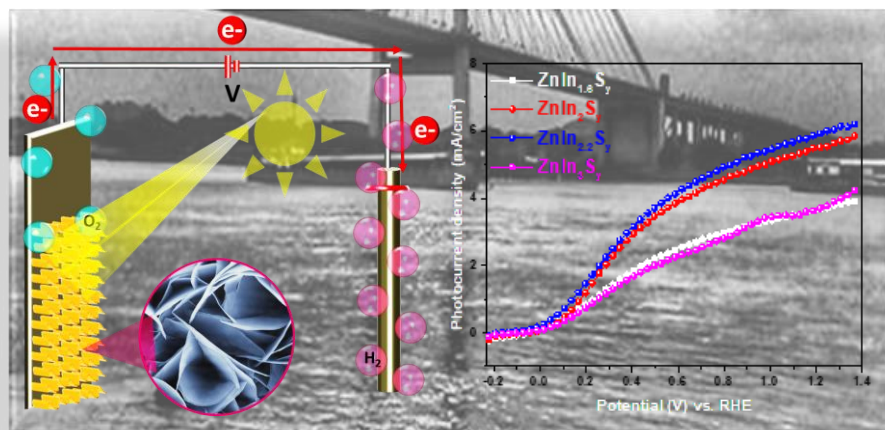
- In this chapter Zn:In ratio is varied for tuning the bandgap of ZnIn$_x$S$_y$ (x =1.6, 2, 2.2, and 3) nanosheets.

- The developed nanosheets of ZnIn$_x$S$_y$ is used as photoanode for photoelectrochemical water splitting and ZnIn$_{2.2}$S$_y$ shows optimum band gap which enhances PEC activity.

Abstract

Ternary metal chalcogenide $ZnIn_xS_y$ (x = 1.6, 2, 2.2, and 3) is synthesized as an efficient photoanode for PEC water-splitting reaction. Tuning of morphology helps to improve the PEC performance through enhanced light absorbance and charge carrier transportation. Similarly, elemental doping is a very fruitful strategy to modulate the band structure. Here, a facile hydrothermal approach is developed to synthesize thin nanosheets of $ZnIn_xS_y$ (x = 1.6, 2, 2.2, and 3) followed by calcination. Through controlling the calcination time and the indium content, the band structure and morphology of $ZnIn_xS_y$ are modulated. The observed results indicate that $ZnIn_{2.2}S_y$ has the optimum and appropriate amount of indium content and oxygen doping. $ZnIn_{2.2}S_y$ can generate maximum photocurrent density of 4.83 mA/cm^2 at '0.7767' V vs. RHE. Furthermore, with the help of Mott-Schottky analysis, carrier density is calculated. The calculated carrier density of $ZnIn_{2.2}S_y$ is 8.82×10^{21} cm^{-3}, which is 3.8, 1.37, and 3.4-fold higher compared to $ZnIn_{1.6}S_y$, $ZnIn_2S_y$, $ZnIn_3S_y$, respectively. Photoconversion efficiency (η) is direct evidence to legitimize the superiority of $ZnIn_{2.2}S_y$; it shows the maximum efficiency 2.744% at potential 0.507 V vs. RHE. $ZnIn_{2.2}S_y$ shows high photostability. It can generate nearly unaltered photocurrent density for 1000 seconds. Band alignment of $ZnIn_{2.2}S_y$ indicates the more negative shift of valence band energy compared to others phases, which promotes easy oxidation of H_2O to O_2.

5.1 Introduction

Now-a-days; a wide range of visible light active materials have been investigated to optimize for the PEC performance. The optimization of visible light active materials based on these-consideration: photoactive material should be a narrow band gap (1.9-3 eV) material with wide spectrum response, a proper band alignment that is conduction band/valence band satisfying the water oxidation and reduction potential, faster charge separation and transportation, photostability and so on.[1] Various semiconductor materials such as $BiVO_4$, Fe_2O_3, WO_3, TiO_2, and ZnO have been explored for PEC water-splitting.[2-14] But the insufficient charge separation and high charge recombination impede the photoactivity and stability of these semiconductors. Recently, vertically grown thin 2D sheets are receiving more attention for PEC water-splitting because of multifold advancement of 2D sheets. 2D thin sheets have larger surface-active atoms which help to increase the electrolyte/semiconductor contact. Vertically grown 2D sheets decouple the directions of light absorption and charge collection lowering down the carrier diffusion length; increase the light absorbance by increasing light-matter interactions via multiple reflections and scattering.[15] But, in-depth study on vertically grown 2D sheets for PEC water-splitting is yet to explore. Further research is needed for the development of such a type of photoanode/cathode that can fulfill all the requirements for PEC water-splitting.

As an important ternary metal sulfide, $ZnIn_2S_4$ with 2D thin sheet structure has drawn great attention due to its multiple advantages in various field such as photoconduction, charge storage, photocatalytic water-splitting, and CO_2 photoreduction etc.[16-18] Since, Li *et al*. reported for the first time that $ZnIn_2S_4$ as a visible-light-driven photocatalyst to produce H_2 production through water-splitting.[19] But its hydrogen production efficiency is not at per. So, people are putting strong efforts to improve the production of H_2 by using $ZnIn_2S_4$. Elemental doping and introduction of vacancies are two effective routes to regulate the electronic structure and reduce the recombination of the photogenerated charge-carriers.[20,21] Doping can narrow the band gap of semiconductor materials, making it suitable for visible light active, and can promote charge separation or create a doped over layer for catalyzing water oxidation reaction.[22] Tian *et al*. synthesized a series of La-doped $ZnIn_2S_4$ for hydrogen generation under visible light. They have studied that La present in the form of La_2O_3, which is decorated on $ZnIn_2S_4$ surface and claim that the higher amount of La decreases the crystallinity of $ZnIn_2S_4$ and inhibits the grain growth of $ZnIn_2S_4$. So, the dopant amount plays a great role in photocatalytic performance.[23] Recently, Xie *et al*. synthesized oxygen doped

$ZnIn_2S_4$ for enhancing the carrier charge separation, carrier density, and remarkably enhancement in photocatalytic activity.[24]

In this chapter, we have tuned the band gap of $ZnIn_2S_4$ by varying the ratio of Zn:In Following a simple hydrothermal technique and calcination process, here, we have grown vertically $ZnIn_xS_y$ thin sheets via a hydrothermal process which are interconnected to each other. The low-temperature heat treatment (calcination) in the air is enabled to the incorporation or doping of oxygen. Here, we have calcined the $ZnIn_xS_y$ (x = 1.6, 2, 2.2, and 3) at 200 °C for different time intervals such as 3, 4, 5, 8, and 10 hours to optimize the appropriate O doping in $ZnIn_xS_y$. It is assumed the appropriate amount of O is doped in $ZnIn_{2.2}S_y$-5, which favors the PEC performance. The $ZnIn_{2.2}S_y$-5 can generate the maximum photocurrent density 4.83 mA/cm^2, 6.23 mA/cm^2 at '0.7767' as well as '1.378' V vs. RHE respectively, which is much higher than others. The calculated carrier density of $ZnIn_{2.2}S_y$-5 is 7.886×10^{21} cm^{-3}. At the same time, it shows the maximum photoconversion efficiency of 2.744% at applied potential 0.507 V vs. RHE. The electrochemical impedance spectra (EIS) also stands in support of the superiority of the $ZnIn_{2.2}S_y$-5 photoanode in PEC water-splitting. $ZnIn_{2.2}S_y$ can generate unaltered photocurrent up to 1000 seconds.

5.2 Experimental Section

5.2.1 Synthesis of $ZnIn_xS_y$: $ZnIn_xS_y$ nanosheets were synthesized via a simple hydrothermal method on FTO. Initially, FTO was cleaned by using soap water 2-3 times followed by ethanol and acetone to remove the thin layer of adhesive. Typically, 0.179 mmol of $ZnCl_2$, 0.599 mmol of thiourea and 0.286, 0.358, 0.397 and 0.537 mmol of $InCl_3$ (separately) were dissolved in 15 mL DI water and stirred properly. The precursor solutions of Zn, In and S were kept in a Teflon container and FTO was immersed in the solution. The hydrothermal reaction was carried out for 6 hours at 160 °C. Sample deposited FTO was washed with DI water and ethanol for 2-4 times. A series of $ZnIn_xS_y$ (x = 1.6, 2, 2.2, and 3) were synthesized. The synthesized $ZnIn_{2.2}S_y$@FTO was calcined for a different time interval like 3, 4, 5, 8 and 10 hours at 200 °C. These $ZnIn_{2.2}S_y$ are named as $ZnIn_{2.2}S_y$-3, 4, 5, 8, and 10 and the pre-calcined $ZnIn_{2.2}S_y$ is named as $ZnIn._{2.2}S_y$-0 throughout the MS. Synthesized $ZnIn_xS_y$@FTO were further used for characterization and PEC water-splitting (**Scheme 5.1**).
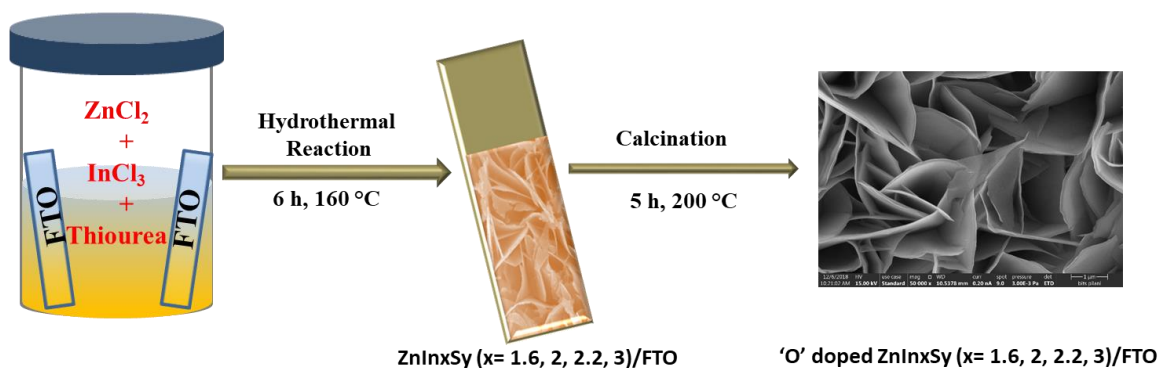
Scheme 5.1: Schematic representation for the development of vertically grown thin nanosheets of $ZnIn_xS_y$ (x= 1.6, 2, 2.2, and 3).

5.3 Result and Discussion

The characterization and application of developed $ZnIn_xS_y$ photoanodes are discussed in the below mentioned sections.

5.3.1 Characterization

5.3.1.1 XRD and Raman Analysis

To investigate the crystal structure, phase, and purity of as-synthesized $ZnIn_xS_y$ (x= 1.6, 2, 2.2, and 3) X-Ray diffraction (XRD) analysis is carried out and shown in Figure 5.1a. It is found that $ZnIn_xS_y$ have hexagonal crystal phase with (006), (102), (008), (104), (105), (0010), (108), (0010), (0012), (203), (0012), (0017), and (211) planes that is well matched with JCPDS no. 72-0773.[25] $ZnIn_{2.2}S_y$-0 shows the presence of all the crystal planes with less intensity which denotes the less crystalline nature of the $ZnIn_{2.2}S_y$-0 at the same time formation of an insignificant amount of cubic phase In_2S_3 is detected at 2θ value of 15.6º.[26] $ZnIn_xS_y$ (x = 1.6, 2, 2.2, and 3) after calcination show very intense peak which indicates the enhanced crystallinity. Comparative PXRD pattern of $ZnIn_{2.2}S_y$-0, $ZnIn_{2.2}S_y$-5, $ZnIn_2S_y$-5, $ZnIn_{1.6}S_y$-5, and $ZnIn_3S_y$-5 are shown in **Figure 5.1b** which indicates the clear blue shift of (006) plane. The blue shifting occurs in $ZnIn_xS_y$ (x=1.6, 2, 2.2, and 3) after calcination is the indication of relaxation of the crystal due to the 'O' doping. It is worth noting that, compared to reflections of undoped sample, small shifts in all reflections of doped sample are observed in **Figure 5.1b**. These changes are due to the smaller ionic radius of O^{2-} anions

toward S^{2-} anions. No impurity peak of In_2S_3, and ZnS are detected, which indicates the pure phase crystallization of the developed materials. The peak intensity increases with increasing indium content in $ZnIn_xS_y$. XRD pattern confirm the phase purity, crystallinity of as-prepared $ZnIn_xS_y$ (x= 1.6, 2, 2.2, and 3). XRD pattern of $ZnIn_{2.2}S_y$-10 indicates an intense peak due to In_2O_3 along with $ZnIn_{2.2}S_y$ (**Figure 5.1c**). So, calcination in air at 200 °C for longer period leads to oxidation of $ZnIn_xS_y$.
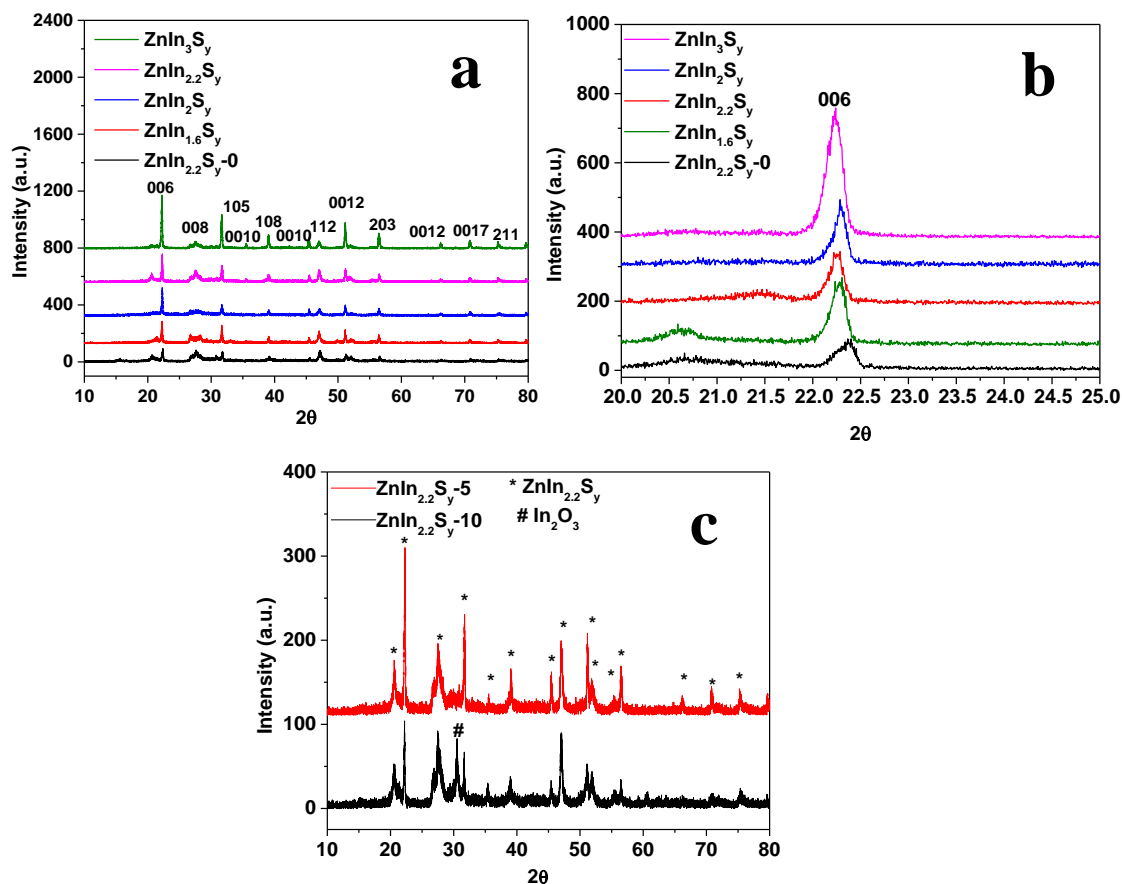
Figure 5.1: Comparative XRD pattern of $ZnIn_xS_y$ (x=1.6, 2, 2.2, and 3) and $ZnIn_{2.2}S_y$-0 obtained (a) from 10° to 80° at 2θ/min, (b) from 20° to 25° at 2θ/min. (c) XRD pattern of $ZnIn_{2.2}S_y$-5 and $ZnIn_{2.2}S_y$-10.

To investigate the crystallinity of the developed $ZnIn_xS_y$, Raman analysis is carried out, and the obtained data is shown in **Figure 5.2a, b**. To figure out the incorporation of 'O' dopant in $ZnIn_xS_y$, Raman analysis of $ZnIn_xS_y$-0 is carried out and the spectra are shown in Figure 5.2a, which indicates a strong peak at 131 cm^{-1} which depicts formation of an insignificant amount of

In_2S_3, and two weak signals at 302 and 358 cm^{-1} are assigned to the transverse optical mode (TO_2) and second harmonic longitudinal mode (LO_2) of $ZnIn_xS_y$, respectively. The observed Raman peaks are well matched with the reported literature.[27,28] After calcination $ZnIn_xS_y$, the clear blue shift in the Raman peaks of 302 and 358 cm^{-1} are observed. Blue-shifting in Raman peak is due to the incorporation of 'O' dopant in the matrix and peak at 131 cm^{-1} is disappeared, which signifies the complete conversion of In_2S_3 into $ZnIn_xS_y$. Along with the peaks at 302 and 358 cm^{-1}, three peaks at 123, 217, and 245 cm^{-1} are observed. Raman peak at 123 cm^{-1} is due to the layered structure of hexagonal $ZnIn_xS_y$. Raman peaks at 217 and 245 cm^{-1} are assigned the F_{1u} (TO_1) and LO_1 (longitudinal optical mode) mode of $ZnIn_xS_y$.[29] After incorporation of 'O' dopant in the $ZnIn_xS_y$ crystallinity increases. Raman analysis indicates that $ZnIn_{2.2}S_y$-5 is the most crystalline one compared to others. The comparative Raman spectra of $ZnIn_{2.2}S_y$-0, 3, 4, and 8 are shown in **Figure 5.2b.**
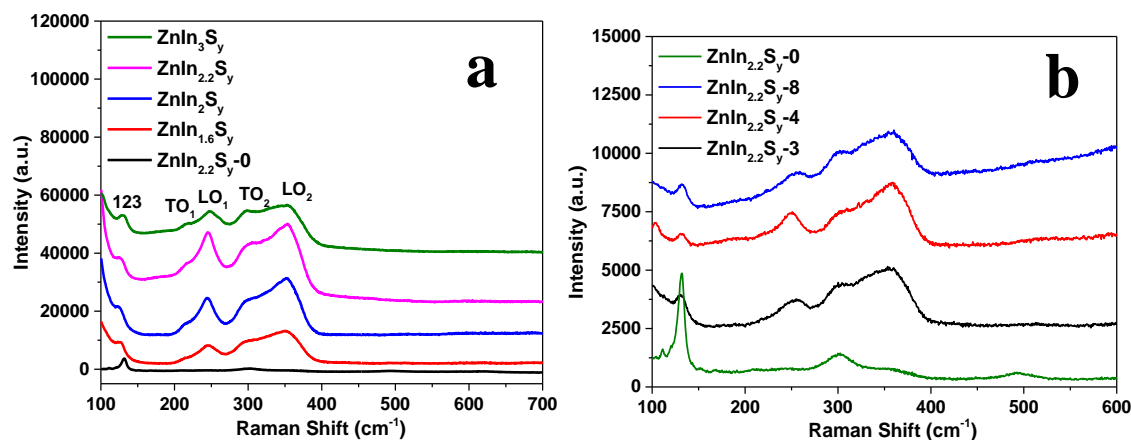
Figure 5.2: Raman spectra of (a) $ZnIn_xS_y$ (x=1.6, 2, 2.2, and 3) and $ZnIn_{2.2}S_y$-0, and (b) $ZnIn_{2.2}S_y$-0, 3, 4, and 8.

5.3.1.2 XPS Analysis

X-ray photoelectron spectroscopy (XPS) analysis is carried out for both $ZnIn_{2.2}S_y$-0 and $ZnIn_{2.2}S_y$-5 to know the surface composition, oxidation states of the elements present and to ensure the incorporation of 'O' dopant after calcination in air. The survey spectrum of $ZnIn_{2.2}S_y$-0 is shown in **Figure 5.3a** and it signifies the presence of 'Zn', 'In', 'S' and a very small amount of 'O' compared to others. The high resolution XPS spectrum of Zn 2p shows the presence of two peaks due to $2p_{1/2}$ and $2p_{3/2}$ at 1045.38 and 1022.46 eV indicating the presence of Zn(II) in the system

(**Figure 5.3b**). Similarly, the high resolution XPS spectrum of 'In' indicated presence of two peaks at 444.7 and 452.3 eV which are of $3d_{5/2}$ and $3d_{3/2}$ of In^{3+} (**Figure 5.3c**).
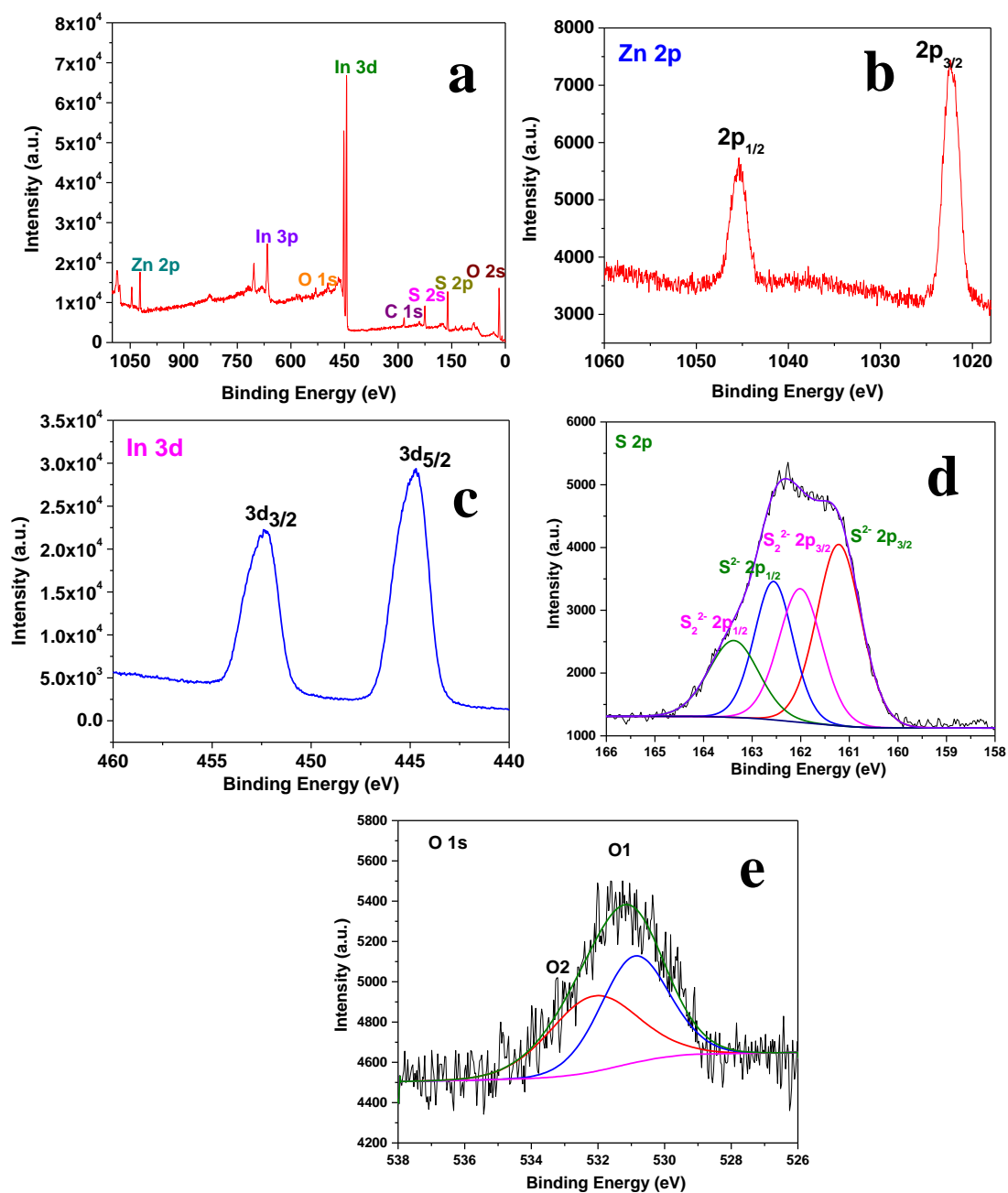
Figure 5.3: XPS spectra of $ZnIn_{2.2}S_y$-0 (a) survey spectrum, high resolution XPS spectrum of (b) Zn 2p, (c) In 3d, (d) S 2p (e) O 1s, respectively.

Deconvoluted XPS spectrum of S 2p is shown in **Figure 5.3d** which indicates the presence of both S^{2-} and S_2^{2-}. High resolution XPS spectrum of O 1s indicates the presence of two peaks at 530.9 and 531.1 eV which are indicated as O1 and O2 in the spectrum (**Figure 5.3e**). From the spectrum it is clear that the ratio of O1:O2 is ~1:1. The observed peaks are due to the presence of defects/under-coordinated lattice oxygen on the surface and physisorbed/chemisorbed water at or near the surface $ZnIn_{2.2}S_y$, respectively. The Observed result is in well accordance with the existing literature.[30,31] The survey spectrum of $ZnIn_{2.2}S_y$-5 is shown in **Figure 5.4a** which indicates the presence of 'Zn', 'In', 'S', and 'O' as elements. Figure 5.4b shows the high-resolution XPS spectrum of Zn 2p and peaks are located at 1045.13 eV and 1021.89 eV which are corresponding to Zn $2p_{3/2}$ and Zn $2p_{1/2}$, respectively. XPS analysis of Zn 2p indicates the presence of Zn^{2+} in the system.
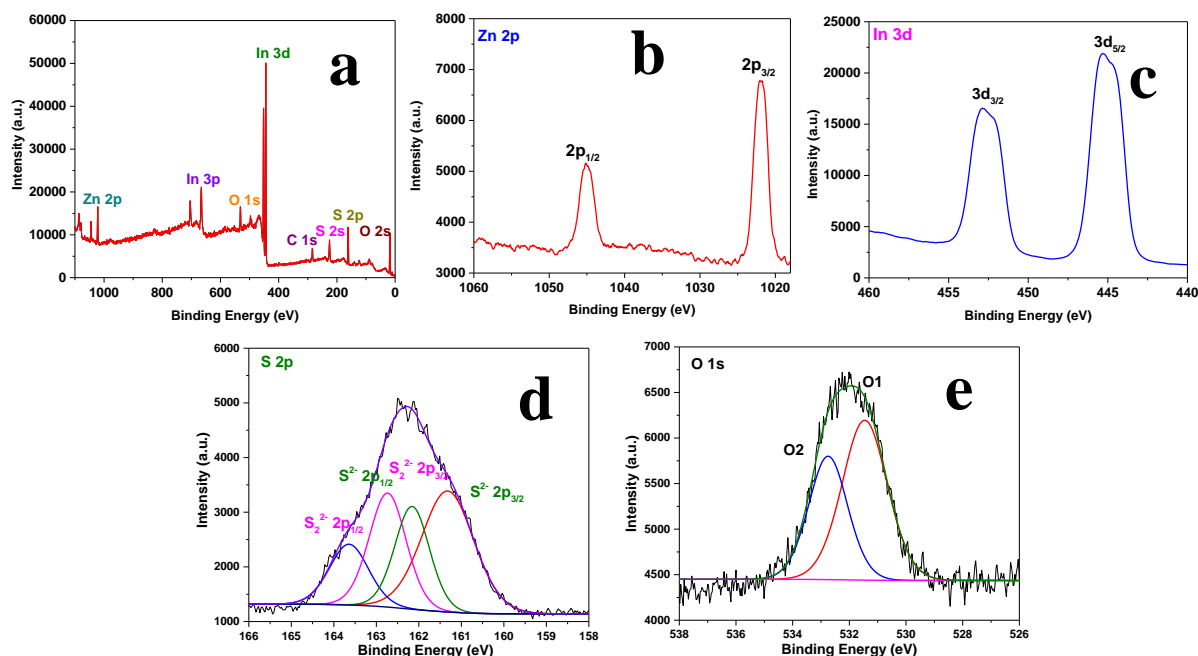
Figure 5.4: XPS spectra of $ZnIn_{2.2}S_y$-5 (a) survey spectrum, high resolution XPS spectrum of (b) Zn 2p, (c) In 3d, (d) S 2p, (e) O 1s, respectively.

Figure 5.4c shows the high resolution XPS spectra of indium. It shows two peaks centered at 445.33 eV and 452.84 eV which are due to In $3d_{5/2}$ and In $3d_{3/2}$, respectively of In^{3+}. **Figure 5.4d** is exhibiting high-resolution deconvoluted XPS spectrum of S 2p. It shows four peaks located which are indexed due to S $2p_{3/2}$ and S $2p_{1/2}$ states of S^{2-} and S_2^{2-}, respectively. **Figure 5.4e** shows

the deconvoluted XPS spectrum of O 1s and the peaks are assigned as O1 and O2 in the spectrum. The obtained peak assigned at 531.4 eV is due to defects, under-coordinated lattice oxygen on the surface. Another peak at 532.7 eV is indexed due to the physisorbed/chemisorbed water at or near the surface $ZnIn_{2.2}S_y$-5. Deconvoluted XPS spectrum of O1s clearly indicates that the ratio of O1:O2 is ~1.5:1. It can be claimed from XPS analysis that with calcination, the presence of under-coordinated oxygen significantly increases in $ZnIn_{2.2}S_y$. So, XPS analysis confirms the successful incorporation of O as a dopant in $ZnIn_{2.2}S_y$ without having any impurity.[23,32]

5.3.1.3 FESEM and EDS Analysis

FESEM images demonstrate the surface morphology of all the synthesized materials. FESEM images of $ZnIn_{2.2}S_y$-0 shows the initialization of typical growth of 2D sheet-like structure (**Figure 5.5a, b**). Here, observed 2D sheets are not very uniformly grown on FTO. FESEM images of $ZnIn_{2.2}S_y$-5 are shown in **Figure 5.5c, d**. Low magnification image indicates the formation of uniform vertical grown thin nanosheets on FTO.
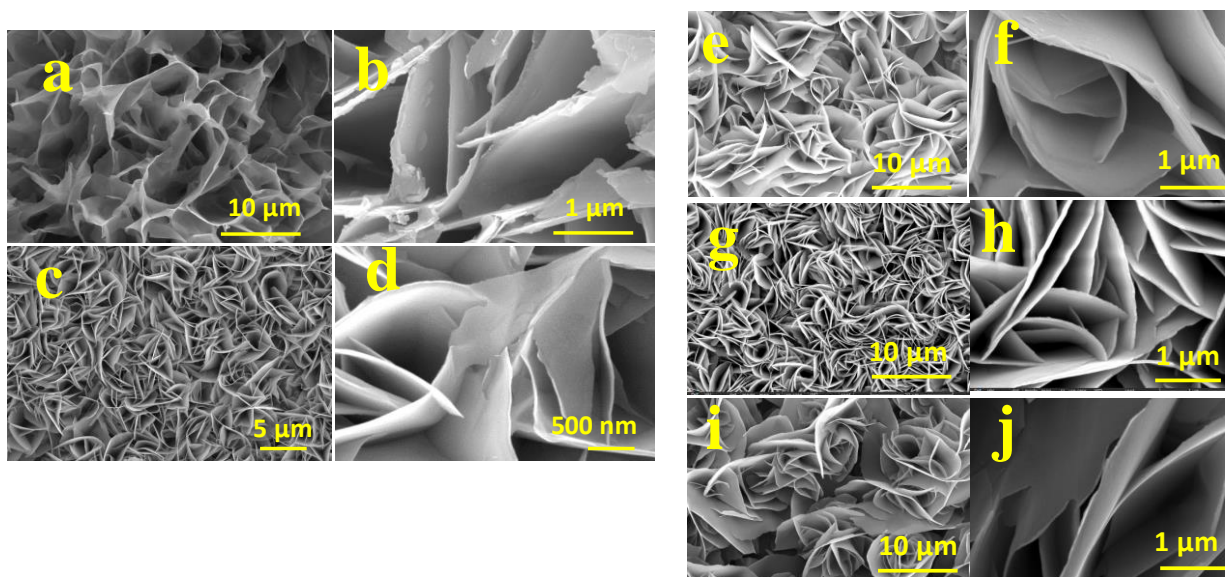
Figure 5.5: FESEM images of (a, b) $ZnIn_{2.2}S_y$-0, (c, d) $ZnIn_{2.2}S_y$, (e, f) $ZnIn_{1.6}S_y$, (g,h) $ZnIn_2S_y$, (i,j) $ZnIn_3S_y$ at low and high magnifications, respectively.

From the high magnification image, it is clearly observed that $ZnIn_{2.2}S_y$ nanosheets are interconnected to each other leading to an observable cavity inside which can facilitate the penetration of electrolyte inside the material. High magnification FESEM image also indicates very sharp and clear edges of 2D sheets which are quite similar to the $ZnIn_2S_y$. FESEM images of $ZnIn_xS_y$ (x= 1.6, 2, and 3) are shown in **Figure 5.5e-j**. All the developed $ZnIn_xS_y$ show the vertical growth of thin 2D sheets on FTO. It is also observed that in the case of $ZnIn_{1.6}S_y$ and $ZnIn_3S_y$, the edges of the developed 2D sheets are a bit wavy compared to $ZnIn_2S_y$ and $ZnIn_{2.2}S_y$. It results in the flowery nature of $ZnIn_{1.6}S_y$ and $ZnIn_3S_y$. $ZnIn_{2.2}S_y$ shows thinnest nanosheets compared to other developed $ZnIn_xS_y$.

To know the composition of the as-prepared samples, elemental analysis is carried out with the help of energy dispersive analysis. EDS analysis indicates the presence of 'Zn', 'In' and 'S' as elements which are present very uniformly throughout the material (**Figure 5.6a**). EDS mapping and spectra of $ZnIn_xS_y$ (x= 1.6, 2, 2.2 and 3) confirm the presence of Zn, In, S, O. Incorporation of 'O' as an element in all the developed material is confirmed with the help of EDS analysis. (**Figure 5.6b-e**).
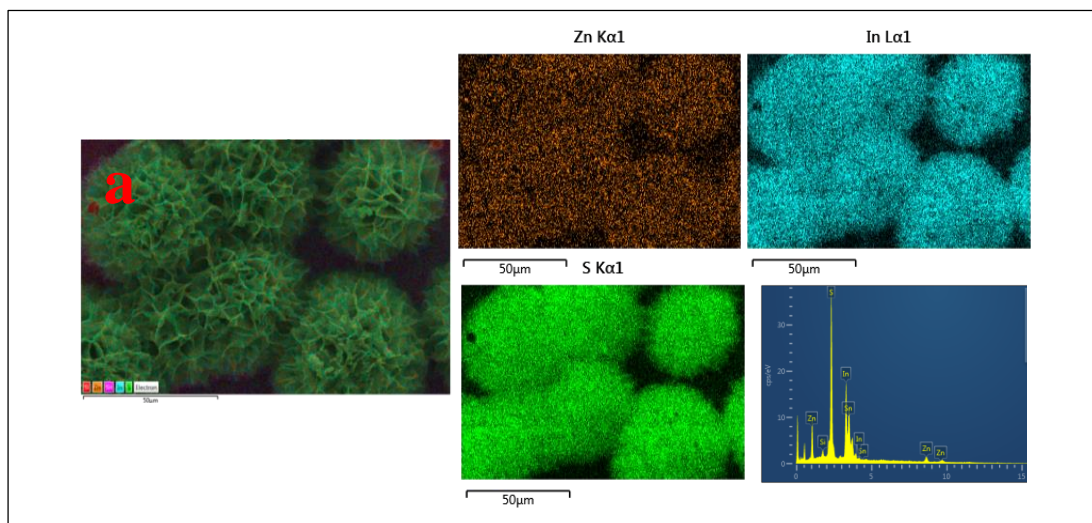
Figure 5.6: (a) EDS analysis of $ZnIn_{2.2}S_y$-0 nanosheets on FTO which shows the uniform distribution of 'Zn', 'In' and 'S'.
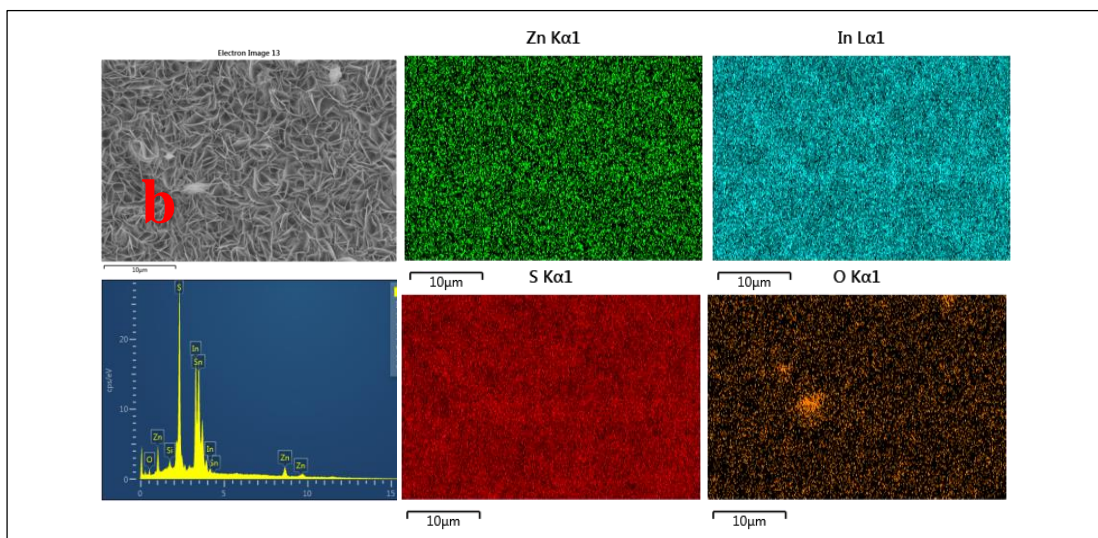
Figure 5.6: (b) EDS analysis of $ZnIn_{1.6}S_y$ nanosheets on FTO which shows the uniform distribution of 'Zn', 'In', 'S' and 'O'.
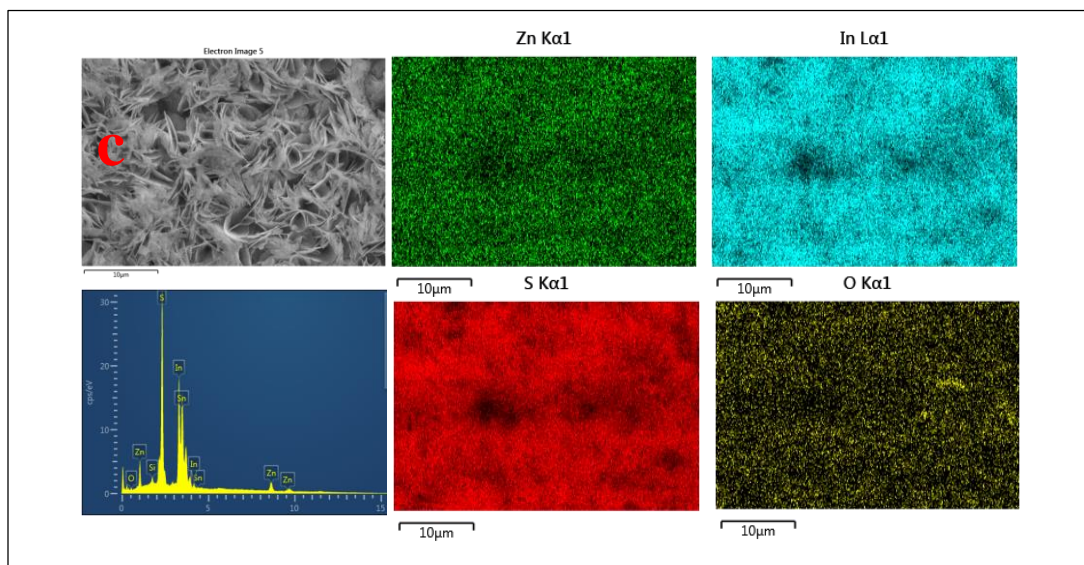
Figure 5.6: (c) EDS analysis of $ZnIn_2S_y$ nanosheets on FTO which shows the uniform distribution of 'Zn', 'In', 'S' and 'O'.
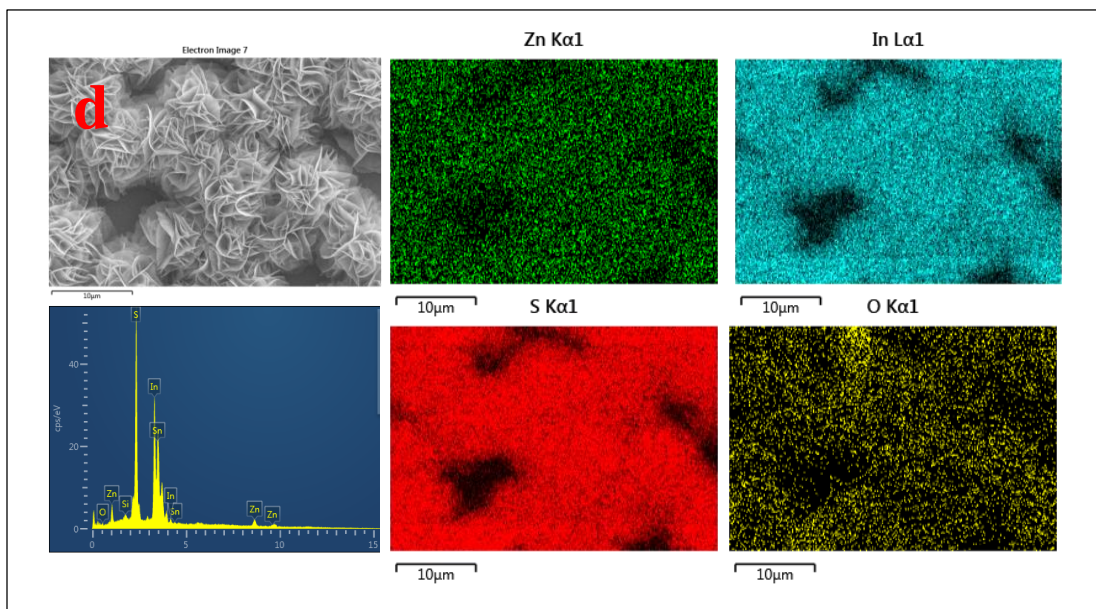
Figure 5.6: (d) EDS analysis of $ZnIn_{2.2}S_y$ nanosheets on FTO which shows the uniform distribution of 'Zn', 'In', 'S' and 'O'.
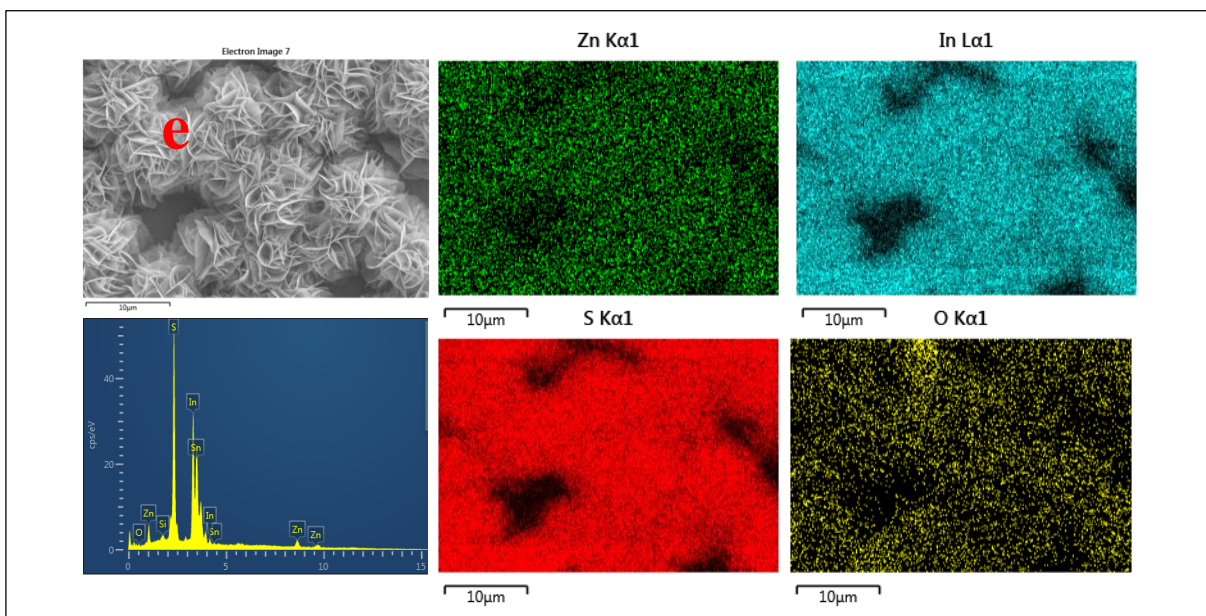
Figure 5.6: (e) EDS analysis of $ZnIn_3S_y$ nanosheets on FTO which shows the uniform distribution of 'Zn', 'In', 'S' and 'O'.

5.3.1.4 Optical Property

The optical absorbance of the synthesized $ZnIn_xS_y$ (x= 1.6, 2, 2.2, and 3) are determined with the help of UV-visible absorption spectroscopy. UV-vis absorption spectra of $ZnIn_xS_y$-0 shows insignificant absorbance in the visible region. Whereas, $ZnIn_xS_y$ calcined at 200 °C for 5 hours shows enhanced absorbance in the visible region, and the observed spectra are shown in **Figure 5.7a**. Calcination leads to uniform growth of vertically oriented sheets of $ZnIn_xS_y$ (x= 1.6, 2, 2.2, and 3). Vertically oriented 2D sheets lead to multiple reflection and scattering of light inside the material, which increases the light and matter interaction leading to enhanced light absorption by the material. The influence of annealing times on the absorbance of visible light is further judged by $ZnIn_{2.2}S_y$-3, 4, 5, 8, and 10. It is observed that the $ZnIn_{2.2}S_y$-5 shows high light absorbance as well as shifts of absorbance edge in the visible region compared to others (**Figure 5.7b**). The sharp absorption edge is due to the band gap transition, not due to the transition from impurity level to conduction band of $ZnIn_xS_y$.[33] In the case of $ZnIn_{2.2}S_y$-5 the absorption edge is stepped more, and slightly shifts in longer wavelength which indicates the $ZnIn_{2.2}S_y$-5 have higher absorbance, and presumably due to the vertically grown thin sheet having sharp edges.
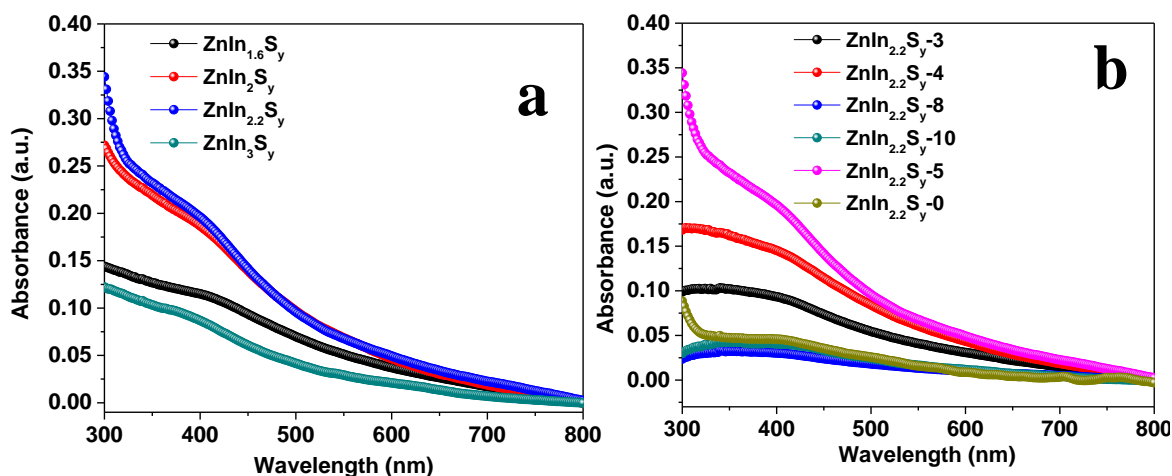
Figure 5.7: UV-visible spectra of (a) $ZnIn_xS_y$ (x=1.6, 2, 2.2, and 3), (b) $ZnIn_{2.2}S_y$-0, 3, 4, 5, 8, and 10.

From FESEM analysis, it is very clear that the edges of vertically grown sheets of $ZnIn_{2.2}S_y$ and $ZnIn_2S_y$ are very sharp whereas, in the case of $ZnIn_{1.6}S_y$ and $ZnIn_3S_y$, edges are curvy. Vertically oriented 2D sheets lead to multiple reflection and scattering of light inside the material, which

increases the light and matter interaction leading to enhanced light absorbance. Whereas, in the case of $ZnIn_{1.6}S_y$ and $ZnIn_3S_y$, comparatively the edges of vertically grown 2D sheets are curvy. It leads to less light and matter interaction because less amount of light can penetrate inside the material and some part will be reflected out. So, with the help of UV-visible absorbance spectroscopy, it is confirmed that vertically grown thin sheets allow more light to penetrate inside the materials and have more light harvesting efficiency than curvy sheets.

5.3.2 Photoelectrochemical Activity

5.3.2.1 Linear Sweep Voltammetry

The PEC performances of the as-synthesized $ZnIn_xS_y$ (x = 1.6, 2, 2.2, 3) and $ZnIn_{2.2}S_y$-0, 3, 4, 5, 8, 10 are checked with the help of linear sweep voltammetry (LSV) techniques and i~t amperometric technique in the presence of continuous and chopped illumination condition. PEC activity of synthesized photoanodes is studied using three electrode system, where Ag/AgCl as a reference electrode, Pt wire as a counter, and sample deposited FTO (fluorine-doped tin oxide coated glass) as a working electrode, respectively and 0.5 Na_2SO_3 is used as an electrolyte. With the application of potential under irradiation of light of 100 mW/cm^2, photocurrent density changes are determined. $ZnIn_{2.2}S_y$-0 shows photoactivity and it can generate a photocurrent density of 0.287 mA/cm^2 under application of '0.7767' V vs. RHE. Vertically grown 'O' incorporated $ZnIn_xS_y$ (x= 1.6, 2, 2.2, and 3) nanosheets are synthesized via hydrothermal method followed by calcination in the air. PEC activity of $ZnIn_xS_y$ (x= 1.6, 2, 2.2, and 3) is determined, and all the electrodes show photoactivity. It is observed that after calcination, photocurrent density increases successively. The less observed photocurrent density in the case of $ZnIn_{2.2}S_y$-0 is due to the lack in crystallinity as well as the absence of 'O' dopant. Another probability is that it may be due to the effect of morphology. The FESEM image of $ZnIn_{2.2}S_y$-0 shows the growth of non-uniform 2D sheets on FTO which are not very active to absorb adequate visible light. The cumulative effect of all factors results in lowering the photoactivity of the material. Whereas, all the synthesized $ZnIn_xS_y$ (x= 1.6, 2, 2.2 and 3) have more surface-active and exposed atoms that helps to improve the ability of light harvesting and at the same time, ease of charge transportation. Vertically grown interconnected thin sheets allow to penetrate inside more electrolyte so that the photogenerated charge carriers can quickly react with the electrolyte. Comparative LSV curves of the as obtained photoanodes of $ZnIn_xS_y$ (x = 1.6, 2, 2.2, and 3) are shown in **Figure 5.8a**.
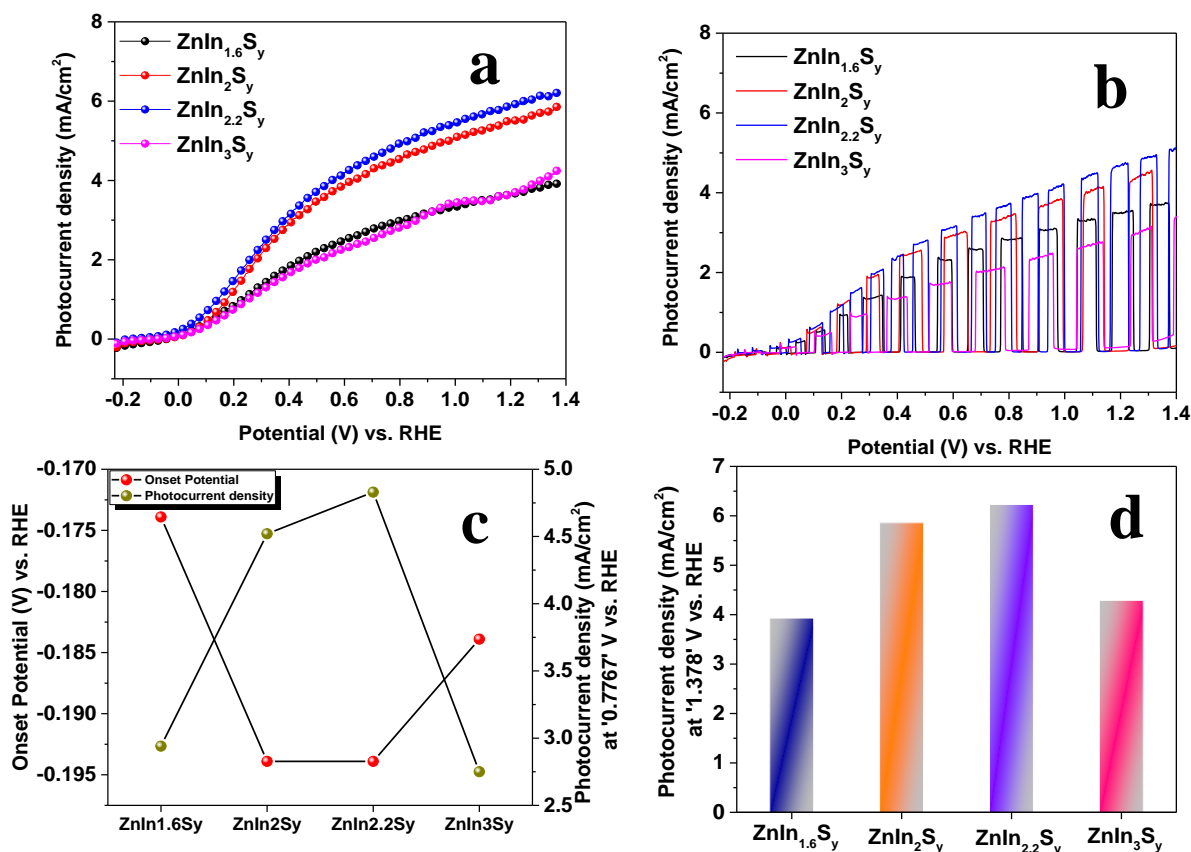
Figure 5.8: LSV plot of $ZnIn_xS_y$ (x=1.6, 2, 2.2, and 3) under (a) continuous illumination and (b) chopped illumination, (c) observed plot of photocurrent density at '0.7767' V vs. RHE and onset potentials with respect to $ZnIn_xS_y$ (x=1.6, 2, 2.2, and 3), (d) plot of comparative photocurrent density at '1.378' V vs. RHE with respect to $ZnIn_xS_y$ (x=1.6, 2, 2.2, and 3).

The transient photoactivity of $ZnIn_xS_y$ (x = 1.6, 2, 2.2, and 3) is shown in **Figure 5.8b** under chopped illumination condition, which shows the switch off-on behavior with the light of all the electrodes. All the $ZnIn_xS_y$ (x = 1.6, 2, 2.2, and 3) show very negligible dark current. Onset potential of $ZnIn_{1.6}S_y$ is -0.173 V vs. RHE which shifts cathodically to -0.193 V vs. RHE for $ZnIn_{2.2}S_y$ and $ZnIn_2S_y$. The further anodic shift in the onset potential is observed in the case of $ZnIn_3S_y$ (-0.183 V vs. RHE). $ZnIn_{2.2}S_y$ thin sheets show the highest photocurrent density 4.83 mA/cm^2, 6.23 mA/cm^2 at '0.7767' and '1.378' V vs. RHE, respectively. However, $ZnIn_{1.6}S_y$, $ZnIn_2S_y$, and $ZnIn_3S_y$ can generate the photocurrent density 2.94, 4.52, and 2.75 mA/cm^2, respectively at under application of '0.7767' V vs. RHE, and 3.93, 5.86 and 4.29 mA/cm^2 at '1.378'

V vs. RHE. Comparative plots of observed onset potential and the photocurrent density at '0.7767' V vs. RHE is shown in **Figure 5.8c** and the plot of photocurrent density obtained at '1.378' V vs. RHE is shown in **Figure 5.8d**.
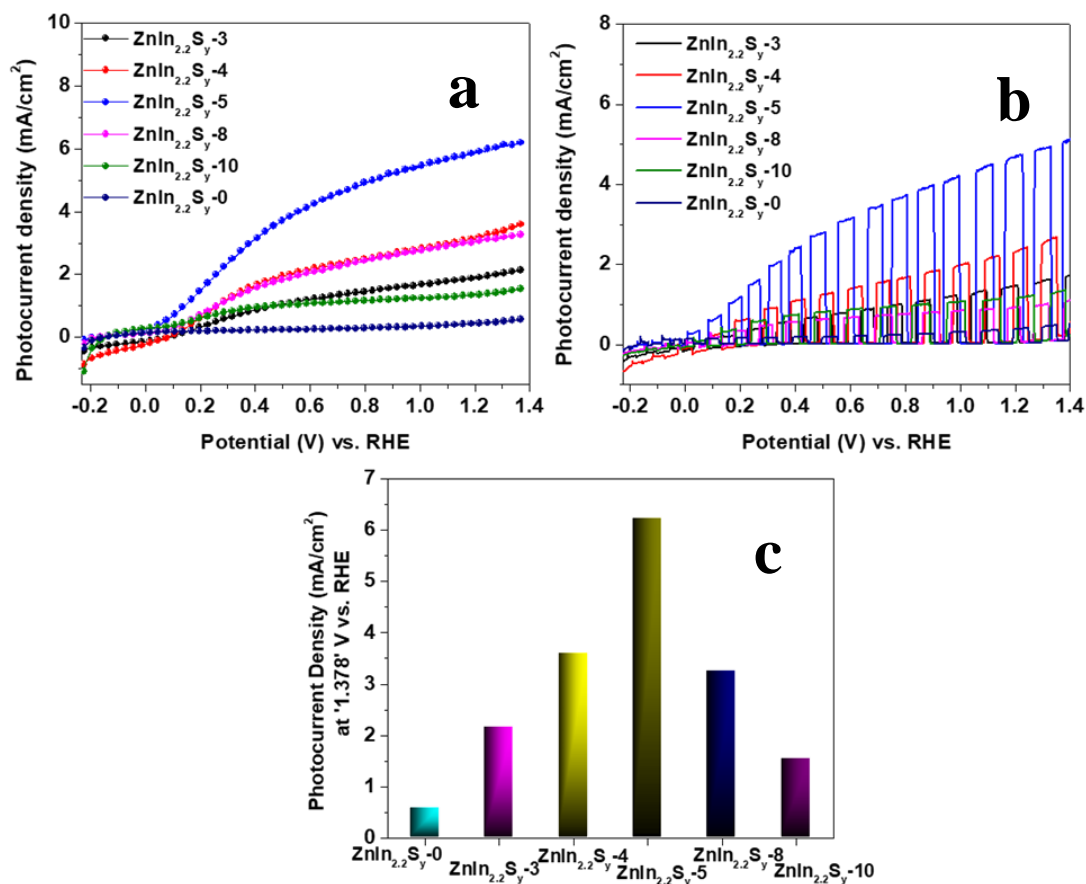
Figure 5.9: LSV plot of $ZnIn_{2.2}S_y$-0, 3, 4, 5, 8, 10 (a) continuous illumination (b) chopped illumination, and (c) current density at '1.378' V vs. RHE with respect to $ZnIn_{2.2}S_y$-0, 3, 4, 5, 8, 10.

Highest obtained photocurrent density of $ZnIn_{2.2}S_y$ may be assumed due to the effect of morphology. With the help of FESEM imaging, it is already observed that in the case of $ZnIn_{1.6}S_y$ and $ZnIn_3S_y$, the edges of the developed 2D sheets are a bit wavy compared to $ZnIn_2S_y$ and $ZnIn_{2.2}S_y$. It results in the flowery nature of $ZnIn_{1.6}S_y$ and $ZnIn_3S_y$. However, $ZnIn_{2.2}S_y$ indicates sharp and clear edges of 2D sheets which are quite similar to the $ZnIn_2S_y$. It may be presumed that vertically grown interconnected thin nanosheets with sharp edges allow multiple reflection and

scattering, which leads to more light and matter interaction resulting in enhanced visible light absorbance. Enhanced visible light absorbance of $ZnIn_{2.2}S_y$ is already observed from the UV-visible spectroscopy. $ZnIn_{2.2}S_y$ bears the thinnest nanosheets morphology compared to other developed $ZnIn_xS_y$, which can facilitate the penetration of electrolyte inside the material with the ease of charge transportation.

To know the optimum condition of calcination, $ZnIn_{2.2}S_y$ is calcined at 200 °C for different time intervals such as 3, 4, 5, 8, and 10 hours. $ZnIn_{2.2}S_y$-3 shows the improved PEC activity. With an increase in the calcination time, the PEC activity of $ZnIn_{2.2}S_y$ is increased, and the maximum photocurrent density is obtained in the case of $ZnIn_{2.2}S_y$-5. Further, increase in the calcination time leads to a decrease in the photocurrent density.

In the case of $ZnIn_{2.2}S_y$-0 the photocurrent density is observed 0.287 mA/cm^2 at '0.7767' V vs. RHE, and in the case of $ZnIn_{2.2}S_y$-3, 4, 5, 8, and 10 the photocurrent density increases 5.0, 8.6, 16.82, 8.39, 4.04-folds, respectively (**Figure 5.9a**). So, it can be assumed that, after calcination of 5 h, crystallinity reaches maximum without having any impurity of In_2S_3 and In_2O_3. While in the case of high calcination time (8 h, 10 h) along with 'O' doping, In_2O_3 is also growing with $ZnIn_{2.2}S_y$, which leads to reduced PEC performance of the photoanodes. The switch on-off behavior with light for all the photoanodes ($ZnIn_{2.2}S_y$-3, 4, 5, 8, and 10) is shown in **Figure 5.9b**. All the photoelectrodes show negligible dark current. The comparative plot of the obtained photocurrent density at '1.378' V vs. RHE for all the electrodes is shown in **Figure 5.9c**.

5.4.3.2 Photostability and Stability of Photoanode

The photoelectrochemical stability of the $ZnIn_xS_y$ (x = 1.6, 2, 2.2, and 3) are checked up to 90 seconds under applied potential '0.7767' V vs. RHE and shown in **Figure 5.10a**. At the same time, photoelectrochemical stability of $ZnIn_{2.2}S_y$-5 is determined under an applied potential of '0.7767' V vs. RHE up to 1000 seconds under continuous and chopped illumination of 100 mW/cm^2 (**Figure 5.10b, c**). The $ZnIn_{2.2}S_y$-5 remains stable and can generate the unaltered photocurrent density for 1000 seconds.
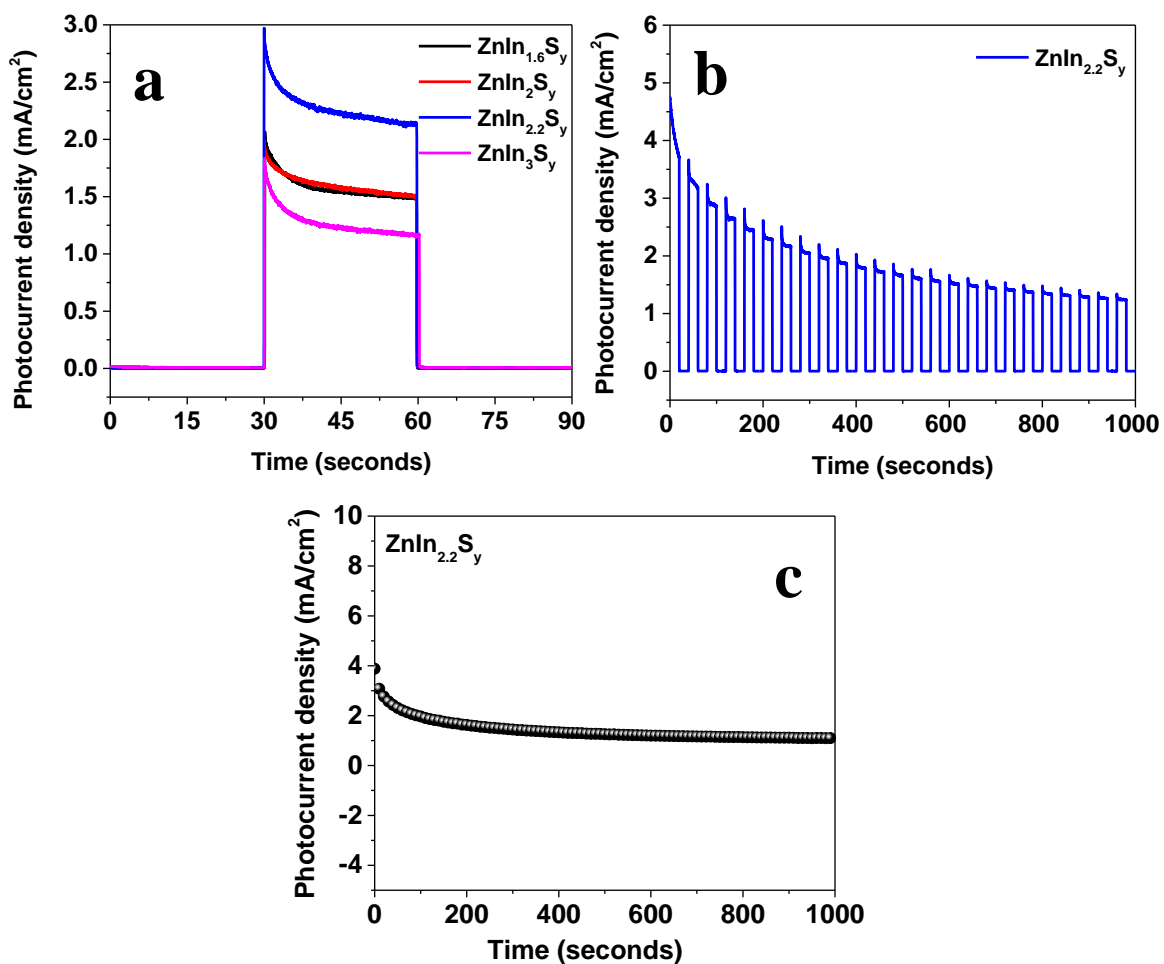
Figure 5.10: (a) i-t plot of $ZnIn_xS_y$ (x=1.6, 2, 2.2, and 3) for 90 seconds in chronoamperometry study, (b, c) plot of photostability of $ZnIn_{2.2}S_y$ checked at potential of '0.7767' V vs. RHE for 1000 seconds under chopped and continuous illumination, respectively.

The morphological and structural robustness are determined with the help of FESEM and XRD analysis after PEC water-splitting and it is observed that $ZnIn_{2.2}S_y$-5 can retain its morphology as well as there is no structural change in $ZnIn_{2.2}S_y$-5 (**Figure 5.11a-c**).
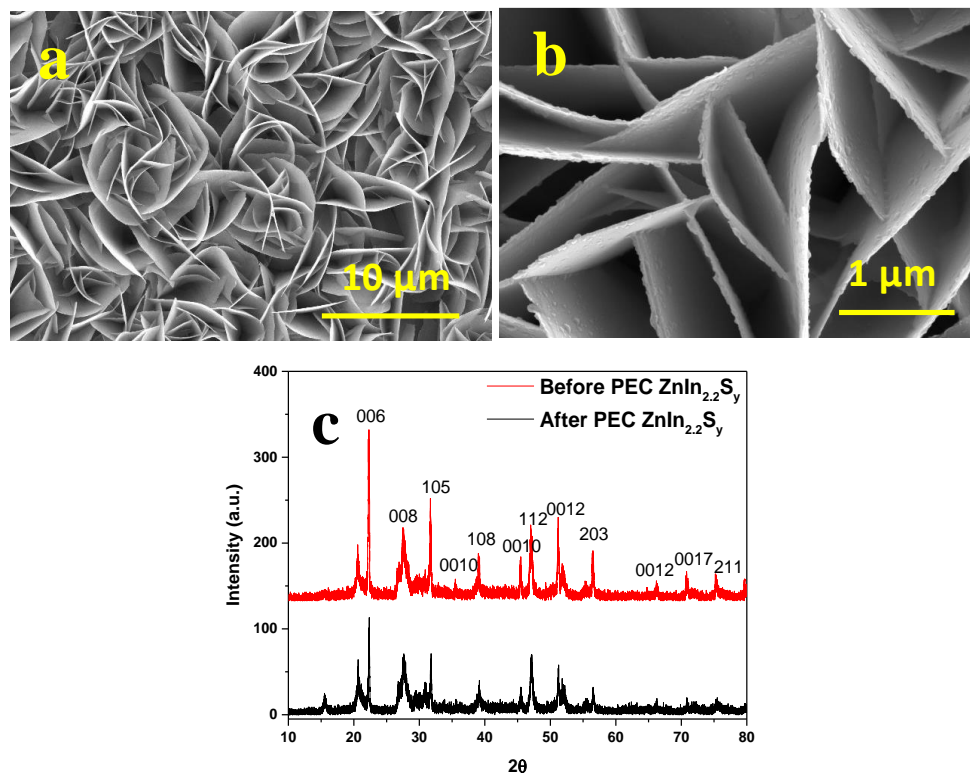
Figure 5.11: (a, b) FESEM images and (c) XRD pattern of ZnIn$_{2.2}$S$_y$ after checking photostability in PEC water-splitting reaction.

5.4.3.3 Mott-Schottky Analysis, Impedance Spectra, and Photoconversion Efficiencies of the developed photoanodes

To understand the superiority of the synthesized ZnIn$_{2.2}$S$_y$, the electronic properties, and carrier concentration were calculated for all the developed electrodes based on Mott-Schottky plot, which are shown in **Figure 5.12a**. The observed data dictates the positive slopes of all synthesized ZnIn$_x$S$_y$ (x = 1.6, 2, 2.2, and 3) indicating the n-type nature of ZnIn$_x$S$_y$. The carrier density and flat band potential is determined with the help of the following equation: [34,35]

$$1/C^2 = (2/e\varepsilon\varepsilon_0 N_d A^2) \ [(V-V_{FB}-kT/e)]$$

Where C is the specific capacitance, N$_d$ is the carrier density, e is the electron charge, ε_0 is the electric permittivity of vacuum, ε is the dielectric constant of the semiconductor, V$_{FB}$ is the flat band potential, A is the area of the sample, T is the temperature, and k is the Boltzmann constant. The slope of ZnIn$_{2.2}$S$_y$ is lower than other ZnIn$_x$S$_y$ (x = 1.6, 2, and 3) which depicts the highest carrier density. It supports the observed highest performance of ZnIn$_{2.2}$S$_y$ in PEC water-splitting.

The calculated carrier density of $ZnIn_{2.2}S_y$ is 8.82×10^{21} cm^{-3}. $ZnIn_xS_y$ (x = 1.6, 2, and 3) show the carrier densities 3.8, 1.37, and 3.4-fold lower than that of $ZnIn_{2.2}S_y$. The flat band potential for $ZnIn_xS_y$ (x= 1.6, 2, 2.2, and 3) is calculated from the extrapolation in the Mott-Schottky plot. The observed flat potential for $ZnIn_{2.2}S_y$ is -0.23 V vs. RHE, for $ZnIn_{1.6}S_y$ it is -0.031 V, for $ZnIn_2S_y$ it is -0.11 V, and for $ZnIn_3S_y$ it is -0.006 V vs. RHE, respectively. Most negative shift is observed in the case of $ZnIn_{2.2}S_y$. The negative shift of the flat band potential is associated with the accelerated interfacial charge transfer of the photoanode which suggests the faster charge transfer for water oxidation. The higher carrier density enables $ZnIn_{2.2}S_y$ to generate higher photocurrent density in PEC water-splitting.
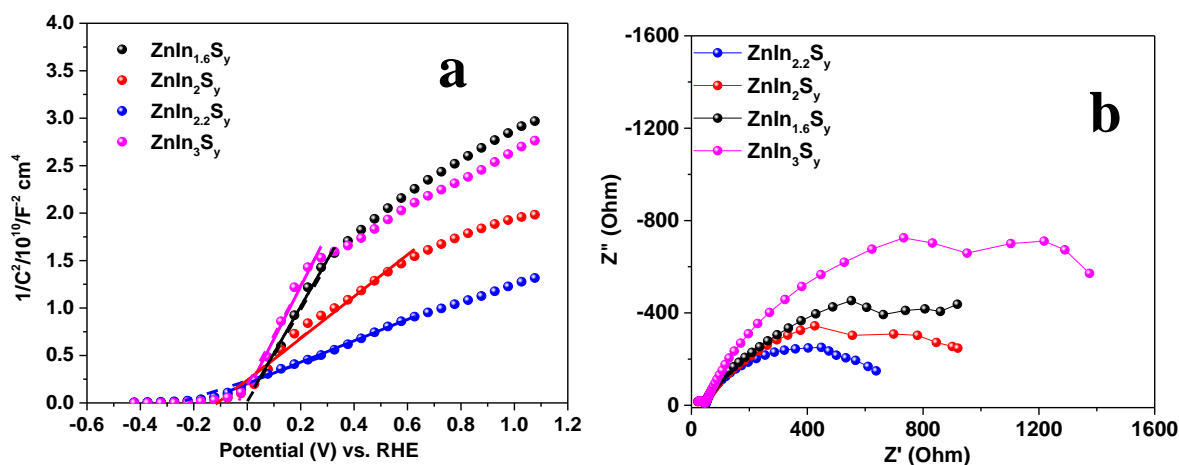
Figure 5.12: (a) Mott-Schottky plots and (b) PEIS spectra of $ZnIn_xS_y$ (x=1.6, 2, 2.2, and 3).

The superior photoelectrochemical activity of thin sheets of $ZnIn_{2.2}S_y$ in comparison of other $ZnIn_xS_y$ (x = 1.6, 2, and 3) is determined with the help of impedance spectra by measuring the charge carrier ability under the applied potential of '0.7767' V vs. RHE upon illumination of 100 mW/cm^2 light. All the $ZnIn_xS_y$ (x = 1.6, 2, 2.2, and 3) show the distinct semicircles. The observed radius of the semicircle of the Nyquist plots indicates the charge transfer resistance. For $ZnIn_{2.2}S_y$ charge transfer resistance is lower than the others, which signifies the higher charge transportation for $ZnIn_{2.2}S_y$. It may be due to the formation of such vertically grown, thin sheets and optimum doping of oxygen. The lowest R_{CT} of $ZnIn_{2.2}S_y$ is enabled for the ease of charge transportation, which indicates the highest conductivity, and it supports the higher number of

charge carriers in $ZnIn_{2.2}S_y$. This PEIS observation supports the PEC activity of $ZnIn_{2.2}S_y$ (**Figure 5.12b**).

Further, to determine quantitatively the photoactivity of the synthesized $ZnIn_xS_y$ (x = 1.6, 2, 2.2, and 3) the photo conversion efficiency (η) is calculated with the help of the J-V curve and shown in **Figure 5.13a, b**. The following equation is used for the calculation of photoconversion efficiency.[36-37]

$$\eta = [J\ (1.23\text{-}V_{RHE})/P_{in}]\ \%$$

Where J is the observed photocurrent density, V_{RHE} is the applied potential with respect to reversible hydrogen electrodes, and P_{in} is the incident light intensity on the electrode. The plot of photoconversion efficiency (η) vs. applied potential shows that η considerable changes with the amount variation of indium content and the maximum efficiency is observed in the case of $ZnIn_{2.2}S_y$ which is about 2.744% at potential 0.507 V vs. RHE. Photoconversion efficiency of $ZnIn_{1.6}S_y$, $ZnIn_2S_y$, $ZnIn_3S_y$ are 1.615, 2.524, and 1.485% at 0.507, 0.497, and 0.494 V vs. RHE, respectively.
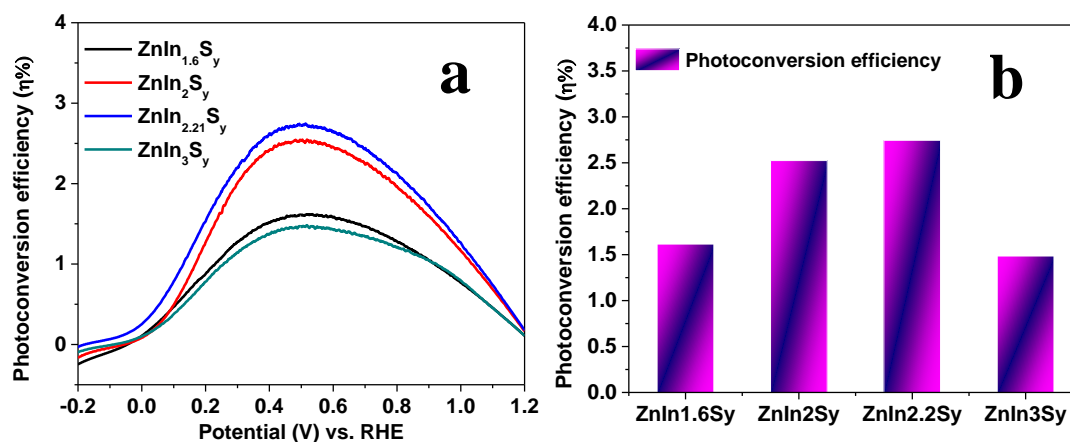
Figure 5.13: (a, b) Plot of photoconversion efficiency values of various $ZnIn_xS_y$ (x=1.6, 2, 2.2, and 3).

With increase in the indium in $ZnIn_xS_y$, the photoconversion efficiency increases and reaches a maximum in the case of $ZnIn_{2.2}S_y$. Photoconversion efficiency (η) further decreases with again increasing the amount of indium in the case of $ZnIn_3S_y$. Enhanced conversion efficiency in the case of $ZnIn_{2.2}S_y$ thin sheets may be due to the more visible light absorption efficiency and at the same time due to efficient charge collection and transportation to electrolyte nanosheets.

The observed photoactivity in the presence of visible light towards PEC water-splitting of $ZnIn_xS_y$ (x= 1.6, 2, 2.2, 3) is described above. It is observed that photocurrent density increases rapidly with the value of x from 1.6 to 2.2 and further decreases when the x is higher than 2.2. The observed PEC activity of $ZnIn_xS_y$ is influenced with the indium content following the order $ZnIn_{2.2}S_y > ZnIn_2S_y > Zn_{1.6}S_y > ZnIn_3S_y$. To analyze the reason for the PEC activity, the correlation between the photoactivity and the photoelectrodes are analyzed. The optimum catalyst obtained is $ZnIn_{2.2}S_y$; it has the vertically grown 2D sheets with very sharp edges which allow more light-matter interaction leading to high light absorbance. Similarly, $ZnIn_{2.2}S_y$ has the maximum carrier density.

5.4.3.4 Band Alignment of the Developed Photoanodes
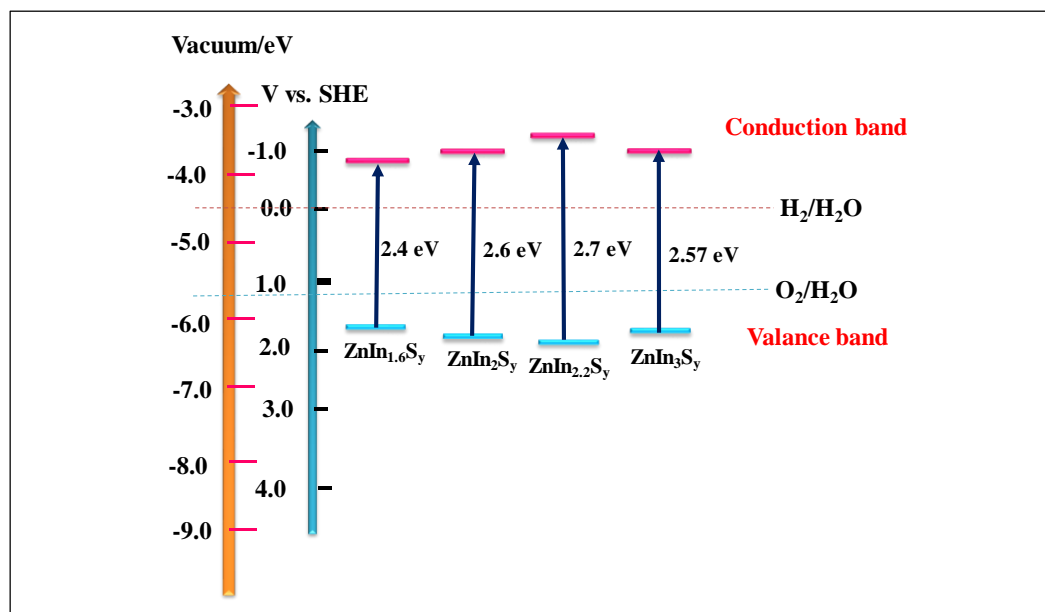
Scheme 5.2: Schematic representation of the band alignments for $ZnIn_xS_y$ (x=1.6, 2, 2.2, and 3).

The observed photoactivity can be explained with the help of the band alignment of the developed materials. From the UV-visible absorbance spectra, the band gap of all the developed materials can be determined, and the values are 2.4, 2.6, 2.7, and 2.6 eV for $ZnIn_xS_y$ (x= 1.6, 2, 2.2, and 3), respectively. Band energy alignment can be determined using the formula: $E_{CB} = -X + ½ E_g$; $E_{VB} = E_{CB}-E_g$, where X is the electronegativity of the semiconductor, E_g is the band gap, E_{VB} and E_{CB} are the valence band and conduction band edge potential. Electronegativity of $ZnIn_xS_y$ is reported

as 4.894 eV.[32] From the calculation; it is clear that an increase in the indium in $ZnIn_xS_y$ from 1.6 to 2.2, valence band energy shifts more negatively (**Scheme 5.2**). The more negative shift of valence band energy of a semiconductor leads to easiness for the oxidation of H_2O to O_2. Conduction band and valence band edge of $ZnIn_{2.2}S_y$ is -3.544 eV and -6.244 eV. Higher the valence band energy leads to the higher oxidizing ability of the semiconductor, i.e. $ZnIn_{2.2}S_y$. Whereas, in the case of $ZnIn_3S_y$, further valence band energy decreases and the PEC activity decreases. All the above-mentioned calculations indicate that the most efficient photoelectrode is $ZnIn_{2.2}S_y$.

5.4 Comparative Study

A comparative study of the photocurrent density for the developed $ZnIn_{2.2}S_y$ is shown in **Table 5.1**. In this present study, the photocurrent density of $ZnIn_{2.2}S_y$ is comparable with the existing literature reports.

Table 5.1 Comparative PEC performance data of $ZnIn_{2.2}S_y$ as photoanode with the existing literature.

S. N.	Photoanodes	Photocurrent density	electrolyte	Required potential	References
1.	$ZnIn_2S_4$ nanosheets	0.5 mA/cm^2	0.25 M Na_2SO_3 and 0.35 M Na_2S	1.4 V vs. RHE	38
2.	$ZnIn_2S_4$ nanostructured	0.04 mA/cm^2	0.2 M Na_2SO_4	0.9 V vs. Ag/AgCl	39
3.	ZnO NAs/RGO/$ZnIn_2S_4$	2.2 mA/cm^2	1 M Na_2SO_4	1.5 V vs. Ag/AgCl	40
4.	$ZnIn_{2.2}Sy$ nanosheets	4.29 mA/cm^2	0.5 M Na_2SO_3	1.4 V vs. RHE	**This study**

5.5 Conclusion

In summary, a facile hydrothermal approach is developed to synthesize the $ZnIn_xS_y$ (1.6, 2, 2.2, and 3) thin sheets following the air treatment (calcination) and systematically applied for PEC water-splitting. The air treatment enables the oxygen doping in $ZnIn_xS_y$ thin sheets. The calcination temperature and amount of indium content may affect the band structure, morphology, and visible light absorbance, which is helpful in the enhancement of PEC activity of $ZnIn_xS_y$. The optimum photoanode $ZnIn_{2.2}S_y$-5 h shows the highest photocurrent density of 4.83 mA/cm^2 at '0.7767' V vs. RHE, which is higher than the other synthesized photoanodes and $ZnIn_{2.2}S_y$-0. It shows the maximum photoconversion efficiency (η) 2.744% at applied potential 0.504 V vs. RHE as well as the higher carrier density 7.886×10^{21} cm^{-3} which is 2.37, 1.77, and 3.69-fold than $ZnIn_{1.6}S_y$, $ZnIn_2S_y$, and $ZnIn_3S_y$, respectively. The 'O' doped $ZnIn_{2.2}S_y$-5 have comparatively vertically grown interconnected thin sheets containing more active and exposed surface atoms and can absorb more visible light than the others, which is responsible for better charge transportation and reduces the electron-hole recombination and enhances the PEC performance.

5.5 References

1. Chen, X.; Shen, S.; Guo, L.; Mao, S. S. Semiconductor-Based Photocatalytic Hydrogen Generation. *Chem. Rev*., **2010**, *110*, 6503-6570.

2. Li, P.; Chen, X.; He, H.; Zhou, X.; Zhou, Y.; Zhigang, Z. Polyhedral 30-Faceted BiVO$_4$ Microcrystals Predominantly Enclosed by High-Index Planes Promoting Photocatalytic Water-Splitting Activity. *Adv. Mater.*, **2018**, *30*, 1703119-1703123.

3. He, W.; Wang, R.; Zhou, C.; Yang, J.; Li, F.; Xiang, X. Controlling the Structure and Photoelectrochemical Performance of BiVO$_4$ Photoanodes Prepared from Electrodeposited Bismuth Precursors: Effect of Zinc Ions as Directing Agent. *Ind. Eng. Chem. Res*., **2015**, *54*, 10723-10730.

4. Zhang, X.; Wang, R.; Li, F.; An, Z.; Pu, M.; Xiang, X. Enhancing Photoelectrochemical Water Oxidation Efficiency of BiVO$_4$ Photoanodes by a Hybrid Structure of Layered Double Hydroxide and Graphene. *Ind. Eng. Chem. Res*., **2017**, *56*, 10711-10719.

5. Tang, Y.; Wang, R.; Yang, Y.; Yan, D.; Xiang, X. Highly Enhanced Photoelectrochemical Water Oxidation Efficiency Based on Triadic Quantum Dot/Layered Double Hydroxide/BiVO$_4$ Photoanodes. *ACS Appl. Mater. Interfaces* **2016**, *8*, 19446-19455.

6. He, W.; Wang, R.; Zhang, L.; Zhu, J.; Xiang, X.; Li, F. Enhanced photoelectrochemical water oxidation on a BiVO$_4$ photoanode modified with multifunctional layered double hydroxide nanowalls. *J. Mater. Chem. A* **2015**, *3*, 17977-17982.

7. Wang, R.; Luo, L.; Zhu, X.; Yan, Y.; Zhang, B.; Xiang, X.; He, J. Plasmon-Enhanced Layered Double Hydroxide Composite BiVO$_4$ Photoanodes: Layering-Dependent Modulation of the Water-Oxidation Reaction. *ACS Appl. Energy Mater*., **2018**, *1*, 3577-3586.

8. Li, C.; Luo, Z.; Wang, T.; Gong, J. Surface, Bulk, and Interface: Rational Design of Hematite Architecture toward Efficient Photo-Electrochemical Water Splitting. *Adv. Mater.*, **2018**, *30*, 1707502-1707524.

9. Wang, C.; Long, X.; Wei, S.; Wang, T.; Li, F.; Gao, L.; Hu, Y.; Li, S.; Jin, J. Conformally Coupling CoAl-Layered Double Hydroxides on Fluorine-Doped Hematite: Surface and Bulk Co-Modification for Enhanced Photoelectrochemical Water Oxidation. *ACS Appl. Mater. Interfaces* **2019**, *11*, 29799-29806.

10. Li, F.; Li, J.; Gao, L.; Hu, Y.; Long, X.; Wei, S.; Wang, C.; Jin, J.; Ma, J. Construction of an efficient hole migration pathway on hematite for efficient photoelectrochemical water oxidation. *J. Mater. Chem. A* **2018**, *6*, 23478-23485.

11. Zhou, Y.; Zhang, L.; Lin, L.; Wygant, B. R.; Liu, Y.; Zhu, Y.; Zheng, Y.; Mullins, B. C.; Zhao, Y.; Zhang, X.; Yu, G. Highly Efficient Photoelectrochemical Water Splitting from Hierarchical $WO_3/BiVO_4$ Nanoporous Sphere Arrays. *Nano Lett*., **2017**, *17*, 8012-8017.

12. Zhang, A-Y.; Wang, W-Y.; Chen, J-J.; Liu, C.; Li, Q-X.; Zhang, X.; Li, W-W.; Sia, Y.; Yu, H-Q. Epitaxial facet junctions on TiO_2 single crystals for efficient photocatalytic water splitting. *Energy Environ. Sci.,* **2018**, *11*, 1444-1448.

13. He, W.; Yang, Y.; Wang, L.; Yang, J.; Xiang, X.; Yan, D.; Li, F. Photoelectrochemical Water Oxidation Efficiency of a Core/Shell Array Photoanode Enhanced by a Dual Suppression Strategy. *ChemSusChem* **2015**, *8*, 1568-1576.

14. Long, J.; Wang, W.; Fu, S.; Liu, L. Hierarchical architectures of wrinkle-like $ZnFe_2O_4$ nanosheet-enwrapped ZnO nanotube arrays for remarkably photoelectrochemical water splitting to produce hydrogen. *J Colloid Interface Sci.*, **2019**, *536*, 408-413.

15. Zhou, M.; Lou, X. W.; Xie, Y. Two-Dimensional Nanosheets for Photoelectrochemical Water Splitting: Possibilities and Opportunities. *Nano Today* **2013**, *8*, 598-618.

16. Romeo, N.; Dallaturca, A.; Braglia, R.; Sberveglieri, G. Charge Storage in $ZnIn_2S_4$ Single Crystals. *Appl. Phys. Lett*., **1973**, *22*, 21-22.

17. Wang, S.; Guan, B. Y.; Lou, X. W. D. Construction of $ZnIn_2S_4$-In_2O_3 Hierarchical Tubular Heterostructures for Efficient CO_2 Photoreduction. *J. Am. Chem. Soc.*, **2018**, *140*, 5037-5040.

18. Ding, Y.; Wei, D.; He, R.; Yuan, R.; Xie, T.; Li, Z. Rational Design of Z-Scheme PtS-$ZnIn_2S_4$/WO_3-MnO_2 for Overall Photo-catalytic Water Splitting Under Visible Light. *Appl Catal B-Enviorn.*, **2019**, *258*, 117948.

19. Lei, Z.; You, W.; Liu, M.; Zhou, G.; Takata, T.; Hara, M.; Domen, K.; Li, C. Photocatalytic Water Reduction under Visible Light on a Novel $ZnIn_2S_4$ Catalyst Synthesized by Hydrothermal Method. *Chem. Commun*., **2003**, 2142-2143.

20. Shi, R.; Ye, H. F.; Liang, F.; Wang, Z.; Li, K.; Weng, Y.; Lin, Z.; Fu, W. F.; Che, C. M.; Chen, Y. Interstitial P-Doped CdS with Long-Lived Photogenerated Electrons for Photocatalytic Water Splitting without Sacrificial Agents. *Adv. Mater.,* **2018**, *30*, 1705941-1705946.

21. Zheng, J.; Lyu, Y.; Wang, R.; Xie, C.; Zhou, H.; Jiang, S. P.; Wang, S. Crystalline TiO_2 protective layer with graded oxygen defects for efficient and stable silicon based photocathode. *Nat. Commun*., **2018**, *9*, 3572-3581.

22. Liu, G.; Wang, L.; Yang, H. G.; Cheng, H. M.; Lu, G. Q. Titania-based photocatalysts-crystal growth, doping and heterostructuring. *J. Mater. Chem.*, **2010**, *20*, 831-843.

23. Tian, F.; Zhu, R.; Song, K.; Ouyang, F.; Cao, G. The effects of amount of La on the photocatalytic performance of $ZnIn_2S_4$ for hydrogen generation under visible light. *Int. J. Hydrog. Energy* **2015**, *40*, 2141-2148.

24. Yang, W.; Zhang, L.; Xie, J.; Zhang, X.; Liu, Q.; Yao, T.; Wei, S.; Zhang, Q.; Xie, Y. Enhanced Photoexcited Carrier Separation in Oxygen-Doped $ZnIn_2S_4$ Nanosheets for Hydrogen Evolution. *Angew. Chem. Int. Ed*., **2016**, *55*, 6716-6720.

25. Chaudhari, N. S.; Warule, S. S.; Kale, B. B. Architecture of rose and hollow marigold-like $ZnIn_2S_4$ flowers: structural, optical and photocatalytic study. *RSC Adv*., **2014**, *4*, 12182-12187.

26. Xu, R.; Li, H.; Zhang, W.; Yang, Z.; Liu, G.; Xu, Z.; Shao, H.; Qiao, G. The fabrication of In_2O_3/In_2S_3/Ag nanocubes for efficient photoelectrochemical water splitting. *Phys. Chem. Chem. Phys*., **2016**, *18*, 2710-2717.

27. Gantassi, A.; Essaidi, H.; Hamed, Z. B.; Gherouel, D.; Boubaker, K.; Colantoni, A.; Monarca, D.; Kouki, F.; Amlouk, M.; Manoubi, T. Growth and characterization of single phase $AgInS_2$ crystals for energy conversion application through β-In_2S_3 by thermal evaporation. *J. Cryst. Growth* **2015**, *413*, 51-60.

28. Shen, S.; Guo, P.; Zhao, L.; Du, Y.; Guo, L. Insights into photoluminescence property and photocatalytic activity of cubic and rhombohedral $ZnIn_2S_4$. *J. Solid State Chem*., **2011**, *184***, 2250-2256.

29. Shen, S.; Zhao, L.; Guan, X.; Guo, L. Improving visible-light photocatalytic activity for hydrogen evolution over $ZnIn_2S_4$: A case study of alkaline-earth metal doping. *J. Phys. Chem. Solids* **2012**, *73*, 79-83.

30. Umeshbabu, E.; Rao, G. R. $NiCo_2O_4$ hexagonal nanoplates anchored on reduced graphene oxide sheets with enhanced electrocatalytic activity and stability for methanol and water oxidation. *Electrochim. Acta* **2016**, *213*, 717-729.

31. Mahala, C.; Basu, M. Nanosheets of $NiCo_2O_4$/NiO as Efficient and Stable Electrocatalyst for Oxygen Evolution Reaction. *ACS Omega* **2017**, *2*, 7559-7567.

32. Liu, Q.; Lu, H.; Shi, Z.; Wu, F.; Guo, J.; Deng, K.; Li, L. 2D $ZnIn_2S_4$ Nanosheet/1D TiO_2 Nanorod Heterostructure Arrays for Improved Photoelectrochemical Water Splitting. *ACS Appl. Mater. Interfaces* **2014**, *6*, 17200-17207.

33. Song, K.; Zhu, R.; Tian, F.; Cao, G.; Ouyang, F. Effects of indium contents on photocatalytic performance of $ZnIn_2S_4$ for hydrogen evolution under visible light. *J. Solid State Chem.*, **2015**, *232*, 138-143.

34. Sharma, M. D.; Mahala, C.; Basu, M. Shape-Controlled Hematite: An Efficient Photoanode for Photoelectrochemical Water Splitting. *Ind. Eng. Chem. Res.*, **2019**, *58*, 7200-7208.

35. Wang, J.; Chen, Y.; Zhou, W.; Tian, G.; Xiao, Y.; Fu, H.; Fu, H. Cubic quantum dot/hexagonal microsphere $ZnIn_2S_4$ heterophase junctions for exceptional visible-light-driven photocatalytic H_2 evolution. *J. Mater. Chem. A* **2017**, *5*, 8451-8460.

36. Mahala, C.; Sharma, M. D.; Basu, M. ZnO@CdS heterostructures: an efficient photoanode for photoelectrochemical water splitting. *New J. Chem.*, **2019**, *43*, 7001-7010.

37. Han, J.; Liu, Z.; Guo, K.; Wang, B.; Zhang, X.; Hong, T. High-efficiency photoelectrochemical electrodes based on $ZnIn_2S_4$ sensitized ZnO nanotube arrays. *Appl Catal B-Enviorn.*, **2015**, *163*, 179-188.

38. Zhou, M.; Liu, Z.; Song, Q.; Li, X.; Chen, B.; Liu, Z. Hybrid 0D/2D edamame shaped $ZnIn_2S_4$ photoanode modified by Co-Pi and Pt for charge management towards efficient photoelectrochemical water splitting. *Appl. Catal. B: Environ.*, **2019**, *244*, 188-196.

39. Fan, B.; Chen, Z.; Liu, Q.; Zhang, Z.; Fang, X. One-pot hydrothermal synthesis of Ni-doped $ZnIn_2S_4$ nanostructured film photoelectrodes with enhanced photoelectrochemical performance. *Appl. Surf. Sci.*, **2016**, *370*, 252-259.

40. Bai, Z.; Yan, X.; Kang, Z.; Hu, Y.; Zhang, X.; Zhang, Y. Photoelectrochemical performance enhancement of ZnO photoanodes from $ZnIn_2S_4$ nanosheets coating. *Nano Energy* **2015**, *14*, 392-400.

Chapter 6

Vertically Grown Cd-ZnIn$_{2.2}$S$_y$ Nanosheets for Photoelectrochemical Water Splitting
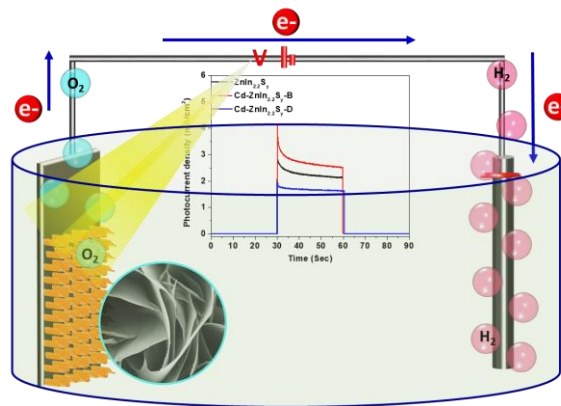
- *In this chapter nanosheets of Cd-ZnIn$_{2.2}$S$_y$ are developed via a simple hydrothermal technique followed by cation-exchange method.*

- *The developed nanosheets of Cd-ZnIn$_{2.2}$S$_y$ is used as photoanode for photoelectrochemical water-splitting and Cd-ZnIn$_{2.2}$S$_y$ shows enhanced photoelectrochemical activity compared to ZnIn$_{2.2}$S$_y$ photoanode.*

Abstract

To attain a sustainable energy source, in the present study, a visible light active semiconductor, $ZnIn_{2.2}S_y$ is developed initially and surface engineering is carried out to grow $Cd-ZnIn_{2.2}S_y$ following a multi-step method. A hydrothermal technique is developed for the synthesis of vertically grown 2D nanosheets of visible light active photoanode, $ZnIn_{2.2}S_y$. Further, the cation exchange method is followed to synthesize $Cd-ZnIn_{2.2}S_y$ nanosheets for photoanodic application in PEC water-splitting reaction. In PEC water-splitting, vertically grown 2D nanosheets of $Cd-ZnIn_{2.2}S_y$ shows improved photoactivity compared to bare $ZnIn_{2.2}S_y$ by virtue of surface engineering. The vertically grown 2D-nanosheets efficiently absorb visible light through multiple reflection and scattering which results in more light and matter interaction. The optimized $Cd-ZnIn_{2.2}S_y$ nanosheets can generate a photocurrent density of 5.85 mA/cm^2 at an applied potential '0.78' V vs. RHE under back illumination. The photoconversion efficiency ($\eta\%$) legitimizes the superiority of $Cd-ZnIn_{2.2}S_y$ nanosheets. $\eta\%$ is ~ 3.10 at 0.53 V vs. RHE for $Cd-ZnIn_{2.2}S_y$ whereas, in the case of $ZnIn_{2.2}S_y$ it is only 2.74% at 0.51 V vs. RHE. After the development of $Cd-ZnIn_{2.2}S_y$, carrier density enhances nearly 4 times than that of $ZnIn_{2.2}S_y$. $Cd-ZnIn_{2.2}S_y$ avails higher carrier density, faster charge carrier transportation, and a wide space charge layer. The widening of the space charge layer is confirmed from the calculation of flat band potential. Both $ZnIn_{2.2}S_y$ and $Cd-ZnIn_{2.2}S_y$ nanosheets show excellent stability under continuous back illumination for 1h.

6.1 Introduction

Visible light active semiconductors receive the most attention in PEC water-splitting for maximum utilization of solar energy. Having immense versatile utility, visible light active semiconductors suffer majorly due to photocorrosion. The progress in PEC water-splitting is very slothful and the key point is that it is hard to get an efficient semiconductor that can absorb visible light, efficiently separate the charge carriers and carry out the surface reaction. However, to date, a large number of photoelectrodes are already developed but till now not a single electrode can fulfill the aforementioned criteria. To develop efficient photoelectrodes, different strategies have been undertaken such as surface modification, morphology control, surface passivation, co-catalyst decoration, plasmonic nanoparticle decoration, interface engineering (heterojunction), etc.[1] Among them, morphology controlling and interface engineering drag our attention for the development of efficient photoanodes for PEC water-splitting reaction. Earlier, it is observed that vertically grown 2D thin nanosheets play a crucial role in the enhancement of photoactivity in PEC water-splitting reaction.[2] Vertically grown 2D thin-sheets show enhanced light absorbance through multiple light reflection and scattering inside the material resulting in more light and matter interaction. At the same time these thin sheets decouple the direction of light absorbance as well as minority carrier diffusion, which enhances the carrier lifetime.[3] So, the enhanced light absorbance as well as, short carrier diffusion length cumulatively helps to enrich the activity in PEC water-splitting. In addition, the vertically grown 2D nanosheets are attributed to a larger number of uncoordinated surface-active atoms that facilitate the interfacial reaction.[4] Moreover, these interconnected 2D-nanosheets allow more electrolyte to penetrate inside the materials. To improve the PEC activity of 2D nanosheets heterojunction development is an effective tool.[5] Surface or interface engineering of photoanodes can develop efficient active sites, increases the surface-active atoms, as well as helps to tune the band gap of the semiconductor which are highly helpful in the charge carrier mobility and charge carrier collection.[6] At the same time the heterointerface helps to increase the charge carrier density, photoconversion efficiency, and diminution of the resistance of photoanode which contributes to enhance the PEC performance.[7]

These basic strategies motivate for the development of the efficient visible light active semiconductor (photoanode and photocathode) materials for PEC water-splitting. Among all the developed visible light active semiconductors, recently $ZnIn_2S_4$, a ternary metal chalcogenide, is getting explored in PEC water-splitting although the photoactivity is unveiled previously. $ZnIn_2S_4$

obtains much attention as a photoanode due to its many-fold advantages such as visible light activity, moderate band gap, and stability. In this context, in 2003, Li *et al*. synthesized nanoparticles of $ZnIn_2S_4$ and reported the photoactivity of $ZnIn_2S_4$, which was the beginning.[8] Further, Xie *et al*. modified the surface of $ZnIn_2S_4$ nanosheets by incorporating oxygen to enhance the PEC performance. Oxygen incorporation creates the active sites for photogenerated charge carriers which facilitate the charge separation and remarkably increase the carrier density and PEC activity of $ZnIn_2S_4$.[9] Recently, our group tuned the band gap of $ZnIn_2S_4$ by varying the Zn: In ratio, at the same time 'O' incorporation via air calcination to increase the active sites in the $ZnIn_2S_4$. The 'O' doped $ZnIn_{2.2}S_y$ can generate maximum photoconversion efficiency 2.74%.[10] Liu *et al*. synthesized the 2D/1D heterostructure of Cu-Zn-In-S/TiO_2 with a favorable energy band, which increased the surface area and accelerated the charge transfer. The heterostructure passivated with the coating of ZnS significantly suppressed the interfacial recombination.[11]

In our earlier report, it was observed that when the Zn:In ratio was 1:2.2, high photoconversion efficiency was obtained. Photoactivity of $ZnIn_{2.2}S_y$ nanosheets is further aimed to enhance through surface engineering by partial replacement of 'Zn^{2+}' by 'Cd^{2+}' ions. For that, Cd-$ZnIn_{2.2}S_y$ nanosheets are synthesized via multi-step methodology. Initially, 2D nanosheets of $ZnIn_{2.2}S_y$ are synthesized applying a hydrothermal technique. After that oxygen incorporation is carried out through low-temperature air calcination. In the third step, Cd-$ZnIn_{2.2}S_y$ is synthesized via ion exchange methodology. The synthesized materials are characterized with the help of different physical techniques. The PEC activity of $ZnIn_{2.2}S_y$ and Cd-$ZnIn_{2.2}S_y$ are determined in continuous and chopped illumination conditions. The maximum photocurrent density of 9.41 mA/cm^2 at an applied potential '1.6' V vs. RHE is achieved for Cd-$ZnIn_{2.2}S_y$, which is ~ 1.33-fold higher than $ZnIn_{2.2}S_y$. The photoconversion efficiency ~3.10% is achieved for Cd-$ZnIn_{2.2}S_y$ at potential 0.53 V vs. RHE. Higher carrier density and low charge transfer resistance of Cd-$ZnIn_{2.2}S_y$ support the superior activity in PEC water-splitting. The developed photoanodes Cd-$ZnIn_{2.2}S_y$ and $ZnIn_{2.2}S_y$ nanosheets can generate unaltered photocurrent density for 1 h.

6.2 Experimental Section

6.2.1 Synthesis of $ZnIn_{2.2}S_y$: $ZnIn_{2.2}S_y$ nanosheets were synthesized following the similar procedure reported earlier by our group.[10] The sample decorated FTO is characterized and kept for synthesizing Cd-$ZnIn_{2.2}S_y$.

6.2.2 Synthesis of Cd-ZnIn$_{2.2}$S$_y$: Cd-ZnIn$_{2.2}$S$_y$ were synthesized following cation-exchange method. Initially 10 mL of CdCl$_2$ (0.1M) was prepared, then ZnIn$_{2.2}$S$_y$@FTO were dipped into this solution for different time intervals such as 30 minutes, 1, 2, and 3 h at room temperature (**Scheme 6.1**) for cation exchange. After that, the sample deposited FTO were washed thoroughly and dried in air and named as Cd- ZnIn$_{2.2}$S$_y$-A, -B, -C, and -D throughout the MS.

6.2.3 Direct Synthesis of CdZnIn$_{2.2}$S$_y$: CdZnIn$_{2.2}$S$_y$ was aimed to synthesize from direct hydrothermal method. Firstly, CdCl$_2$ and ZnCl$_2$ were taken as 'Cd' and 'Zn' precursor and the molar ratio was 1.74:1. At the same time 0.599 mmol of thiourea and 0.397 mmol of InCl$_3$ were taken in 15 mL of DI water. A cleaned FTO was dipped into the reaction vessel. The reaction was kept into the hydrothermal container at 160 ℃ for 6 h. After the hydrothermal reaction the developed compound was rinsed with DI water, dried, and calcined in air at 200 ℃ for 5 h. The synthesized material is kept for further study.
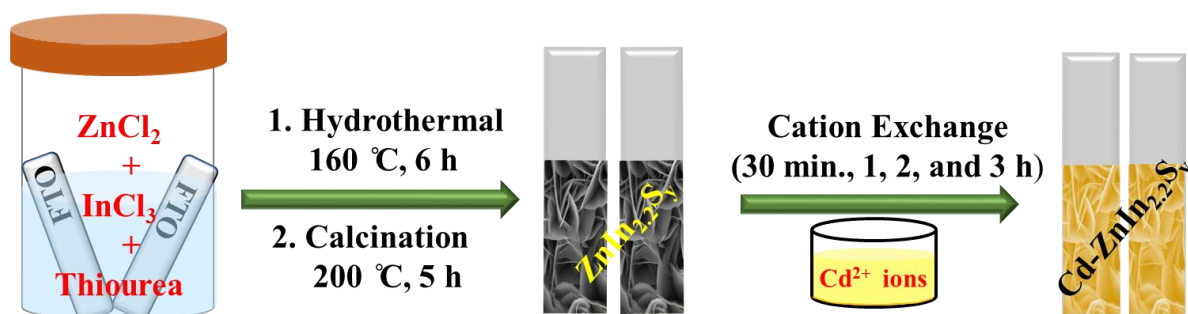
Scheme 6.1: Schematic representation for the development of vertically grown thin nanosheets of Cd-ZnIn$_{2.2}$S$_y$ using hydrothermal technique followed by cation exchange method.

6.3 The Formation mechanism of Cd-ZnIn$_{2.2}$S$_y$

ZnIn$_{2.2}$S$_y$ has a hexagonal crystal structure. In this crystal structure, 'Zn^{2+}' and partial 'In^{3+}' are coordinated tetrahedrally by four 'S^{2-}' neighboring atoms; whereas the rest of 'In^{3+}' are octahedrally coordinated with neighboring six 'S^{2-}' atoms. So, when ZnIn$_{2.2}$S$_y$ undergoes a cation exchange reaction with 'Cd^{2+}', there is a most probable ion exchange of 'Zn^{2+}' than 'In^{3+}'. The chemical state of 'In^{3+}' is more stable in ZnIn$_{2.2}$S$_y$ and less likely to be substituted with 'Cd^{2+}'. Other factors for favorable exchange of 'Zn^{2+}' with 'Cd^{2+}'are the size factor and the diffusion of

the metal ion. The sizes of 'Zn^{2+}', 'Cd^{2+}', and 'In^{3+}' are 74 pm, 94 pm, and 95 pm, respectively.[12] So, the 'Zn^{2+}' will come out from the crystal lattice instead of large-sized cation 'In^{3+}'. Diffusion coefficients of 'Zn^{2+}', 'Cd^{2+}', and 'In^{3+}' are 7.03×10^{-10}, 7.19×10^{-10}, and 4.93×10^{-10} m^{2}s^{-1}, which is favorable for the incorporation of 'Cd^{2+}' by 'Zn^{2+}' in the ZnIn$_{2.2}$S$_y$. Above all, according to the HSAB principle the hard-hard and soft-soft interactions are stronger than hard-soft interaction. So, the interaction of 'Cd^{2+}' with 'S^{2-}' is more favorable than 'Zn^{2+}' and 'S^{2-}', and 'In^{3+}' and 'S^{2-}'. There are few many reports in the literature for such kind of cation/anion exchange reactions for the synthesis of hierarchal heterostructures, which generally occur in the heterogeneous condition.[13-16]

6.4 Result and Discussion

The characterization and application of developed ZnIn$_{2.2}$S$_y$ and Cd-ZnIn$_{2.2}$S$_y$ photoanode are discussed in the below sections.

6.4.1 Characterization

6.4.1.1 XRD and Raman Analysis

To know the crystallinity and the phase purity, X-ray diffraction (XRD) analysis is carried out. All the planes (006), (008), (105), (112), (0012), (203), and (211) are corresponding to the hexagonal crystal phase of ZnIn$_{2.2}$S$_y$ (JCPDS No.- 72-0773) and shown in **Figure 6.1a**.[17] After the exchange of 'Zn^{2+}' in ZnIn$_{2.2}$S$_y$ with 'Cd^{2+}', the peaks of (006) and (008) planes are shifted at a lower angle (**Figure 6.2b**). The peak shifting at a lower angle indicates the incorporation of strain in ZnIn$_{2.2}$S$_y$ crystal after the exchange of 'Zn^{2+}' with 'Cd^{2+}'. No additional peak due to any side product or impurity is observed. So, from XRD analysis it can be claimed that cadmium is incorporated in the ZnIn$_{2.2}$S$_y$ matrix through the cation exchange method at room temperature. Purity and phase of the aimed CdZnIn$_{2.2}$S$_y$ from directly synthesized methodology is also checked with the help of XRD analysis (**Figure 6.1c**). The synthesized material is the mixture of CdIn$_2$S$_4$, ZnIn$_2$S$_4$, and CdS instead of CdZnIn$_{2.2}$S$_y$ and assigned as CdIS/ZIS/CdS throughout the MS.

Further, the crystallinity and synthesis of material are corroborated with the help of Raman analysis (**Figure 6.1d, e**). The Raman spectra of ZnIn$_{2.2}$S$_y$ shows four prominent peaks. The peak at 123 cm^{-1} signifies the hexagonal layered structure of ZnIn$_{2.2}$S$_y$. Along with this, the peaks at 217 and 245 cm^{-1} are assigned to the F$_{1u}$ (TO$_1$) and LO$_1$ (longitudinal optical mode) modes of ZnIn$_{2.2}$S$_y$. The weak signals of Raman peak at 302 and 358 cm^{-1} are due to the transverse optical mode (TO$_2$)

and second harmonic longitudinal mode (LO_2) of $ZnIn_{2.2}S_y$, which confirms the formation of $ZnIn_{2.2}S_y$ via our synthesis protocol.[18,19] After the successful incorporation of 'Cd^{2+}' in $ZnIn_{2.2}S_y$, all the peaks have become broader than the bare $ZnIn_{2.2}S_y$. At the same time, the peaks are slightly getting shifted at the lower wavenumber.
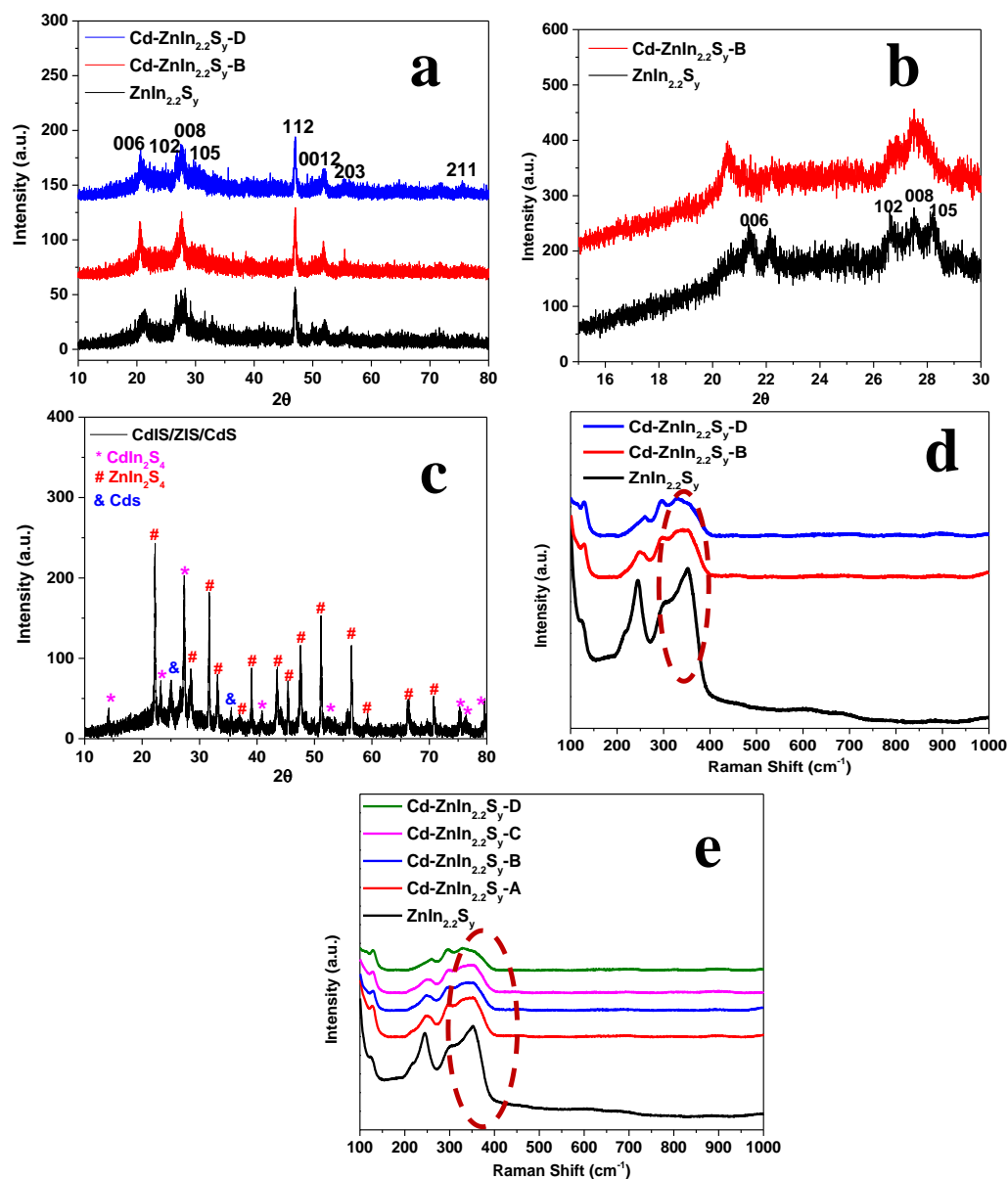
Figure 6.1: PXRD pattern at different scan rates (a) fast scan rate (2θ/ min), (b) slow scan rate (0.5θ/ min) of $ZnIn_{2.2}S_y$, Cd-$ZnIn_{2.2}S_y$-B, and –D, (c) PXRD of CdIS/ZIS/CdS, (d) Raman spectra of $ZnIn_{2.2}S_y$, Cd-$ZnIn_{2.2}S_y$-B, and Cd-$ZnIn_{2.2}S_y$-D, and (e) Raman spectra of $ZnIn_{2.2}S_y$, Cd-$ZnIn_{2.2}S_y$-A, -B, -C, and -D.

The peak broadening depicts a decrease in crystallinity due to the non-stoichiometric cation ratio in $ZnIn_{2.2}S_y$ nanosheets after the ion exchange process, while that the blue shifting may happen due to the incorporation of 'Cd^{2+}' in the $ZnIn_{2.2}S_y$ matrix. Raman analysis indicates that following our developed protocol, pure phase $Cd-ZnIn_{2.2}S_y$ has been successfully synthesized.

6.4.1.2 Optical Property

For the application in the PEC water-splitting, the optical absorbance plays a significant role. The optical absorbance of the synthesized materials is determined with the help of UV-visible absorbance spectroscopy and shown in **Figure 6.2a, b**. $ZnIn_{2.2}S_y$ shows the optical absorbance in visible region ~400-500 nm with band gap of 2.70 eV.[20, 21] After the partial exchange of 'Zn^{2+}' by 'Cd^{2+}' in the $ZnIn_{2.2}S_y$ nanosheets, optical absorbance enhances with negligible shift in the band edge. However, $Cd-ZnIn_{2.2}S_y$-B shows an enhanced optical absorbance compared to bare $ZnIn_{2.2}S_y$. The optical activities of $Cd-ZnIn_{2.2}S_y$-C and D are nearly similar to the bare $ZnIn_{2.2}S_y$. So, the enhanced optical absorbance may be because of the optimum exchange of 'Zn^{2+}' by 'Cd^{2+}' in $ZnIn_{2.2}S_y$.
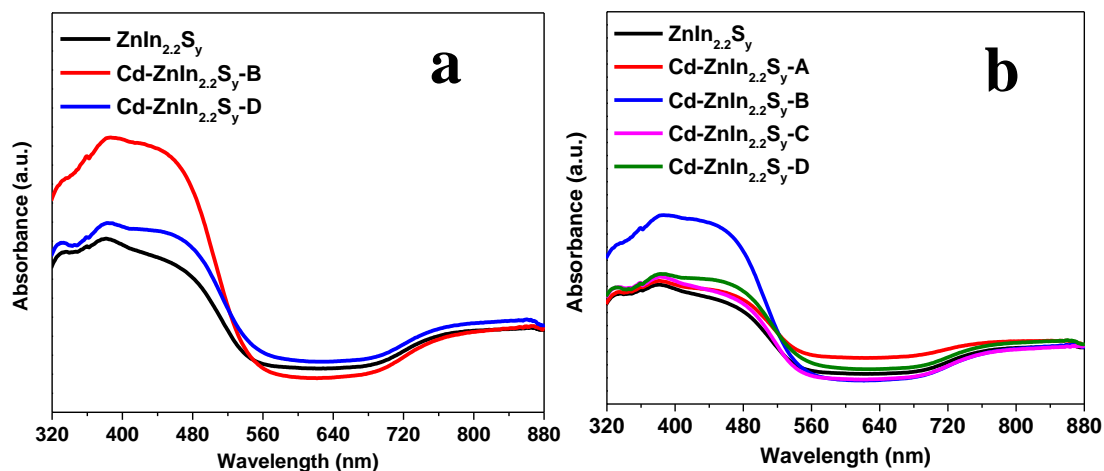
Figure 6.2: UV-visible spectra of (a) $ZnIn_{2.2}S_y$, $Cd-ZnIn_{2.2}S_y$-B, and $Cd-ZnIn_{2.2}S_y$-D, (b) $ZnIn_{2.2}S_y$, $Cd-ZnIn_{2.2}S_y$-A, -B, -C, and -D.

6.4.1.3 FESEM Analysis

To know the typical morphology of the synthesized materials, FESEM (field emission electron microscope) analysis is carried out. From FESEM analysis, vertically grown and interconnected

2D nanosheets of $ZnIn_{2.2}S_y$ are observed (**Figure 6.3a, b**). These vertically grown sheets can absorb more light through multiple light reflection and scattering and at the same time, the cavity generated through the arrangement of these nanosheets assist easy penetration of the electrolyte into the materials. The $Cd-ZnIn_{2.2}S_y$-A and $Cd-ZnIn_{2.2}S_y$-B also have interconnected 2D nanosheets with a rough surface, which indicates the surface exchange reaction of 'Zn^{2+}' with 'Cd^{2+}' in $ZnIn_{2.2}S_y$ nanosheets (**Figure 6.3c-f**).
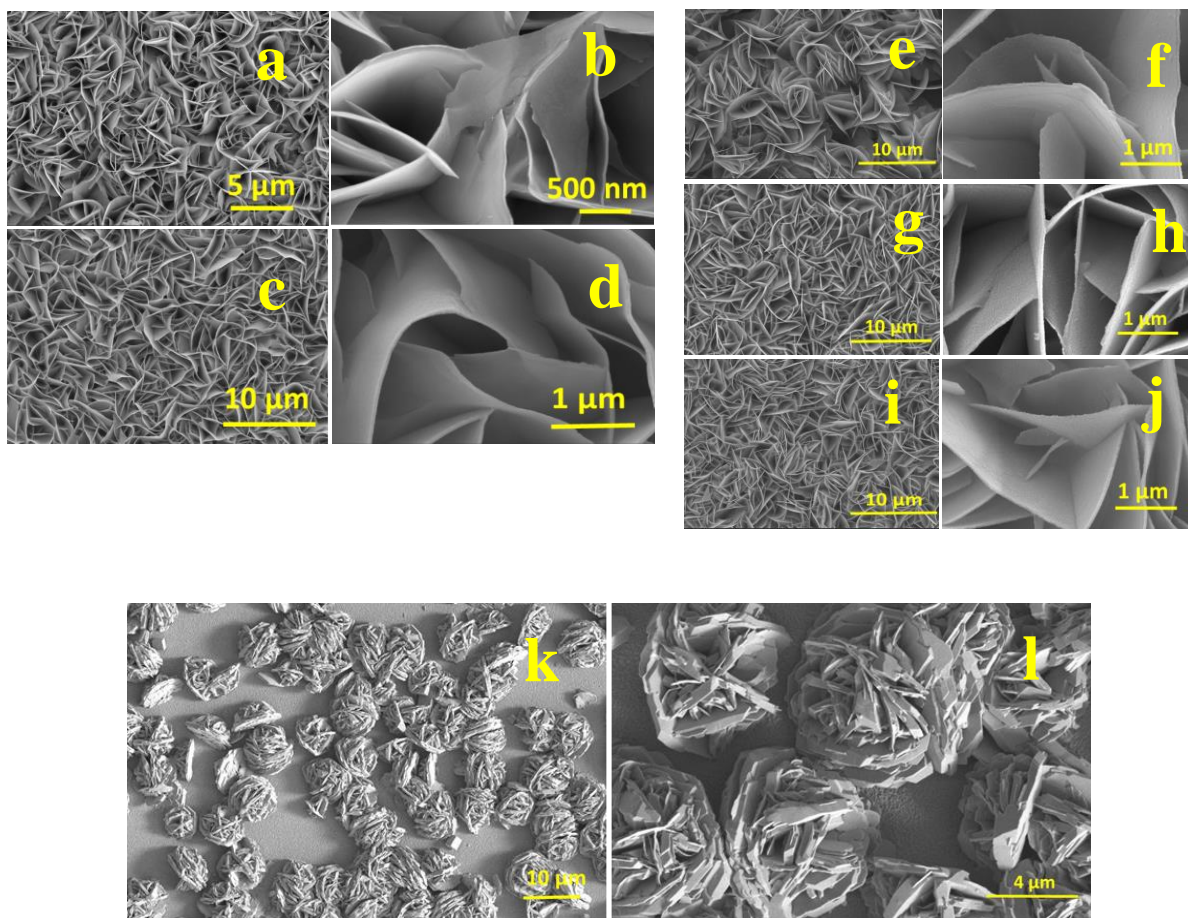
Figure 6.3: FESEM images of (a, b) $ZnIn_{2.2}S_y$ nanosheets (c, d) $Cd-ZnIn_{2.2}S_y$-B nanosheets (e-j) $Cd-ZnIn_{2.2}S_y$-A, -C, and -D nanosheets, (k, l) CdIS/ZIS/CdS at low and high magnification, respectively.

Due to such cation exchange reaction, vertically grown 2D nanosheets of $Cd-ZnIn_{2.2}S_y$ are obtained which can retain the morphology after the cation exchange. In the case of $Cd-ZnIn_{2.2}S_y$-C and $Cd-ZnIn_{2.2}S_y$-D, the surface of the vertically grown nanosheets become rougher due to the

sufficient surface exchange of 'Zn^{2+}' (**Figure 6.3g-j**). CdIS/ZIS/CdS shows very thick nanosheets which are arranged to develop a flower like morphology (**Figure 6.3k, l**).

6.4.1.4 EDS and ICP-OES Analysis

To confirm the elements and elemental composition the EDS analysis of ZnIn$_{2.2}$S$_y$ and Cd-ZnIn$_{2.2}$S$_y$-A to -D is performed and shown in **Figure 6.4a-e**. The EDS analysis shows the uniform distribution of 'Cd', 'Zn', 'In', 'S', and 'O' in the Cd-ZnIn$_{2.2}$S$_y$-A, -B, -C, and -D materials. While in the case of ZnIn$_{2.2}$S$_y$, 'Zn', 'In', 'S', and 'O' elements are thoroughly present.
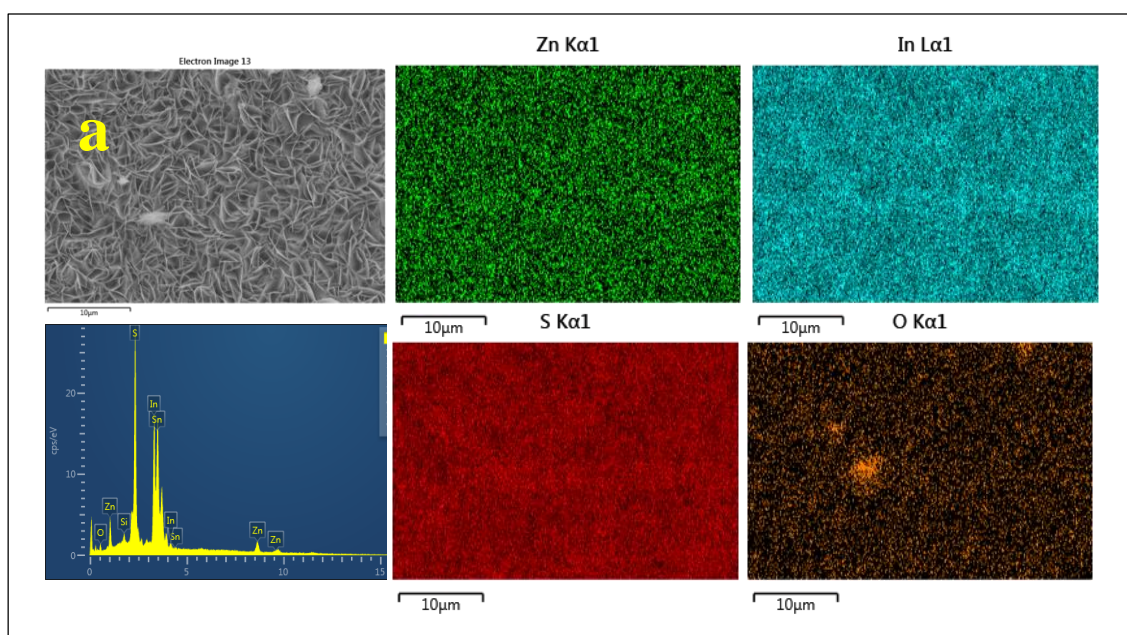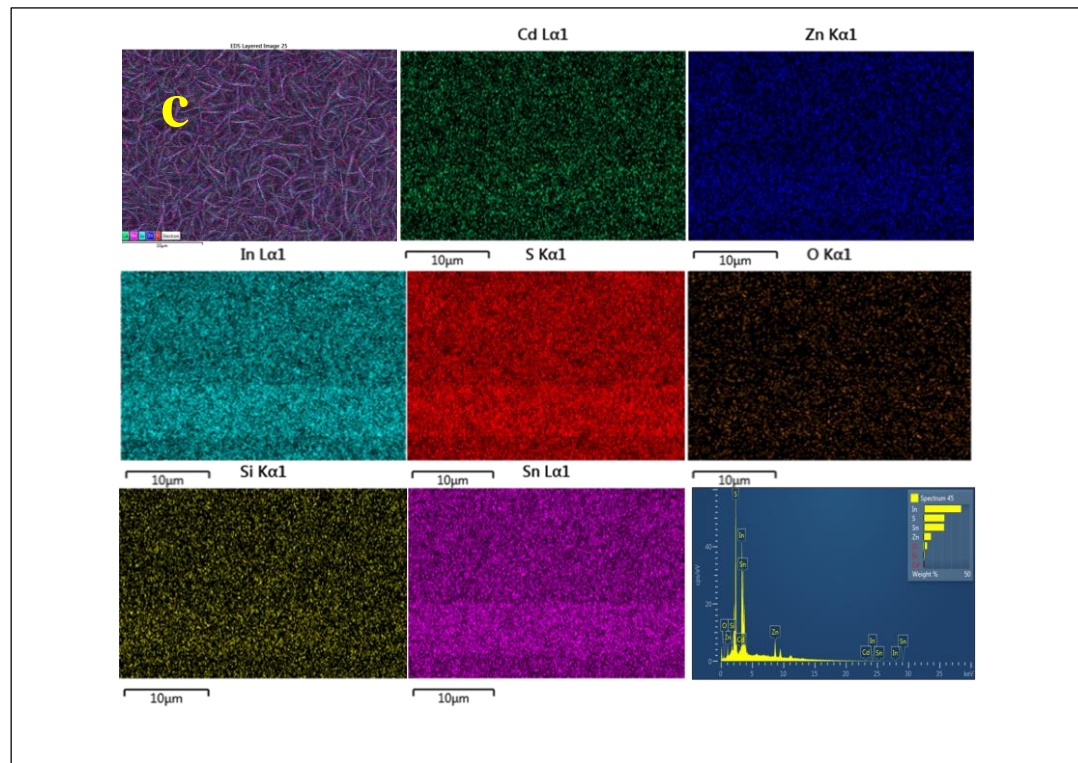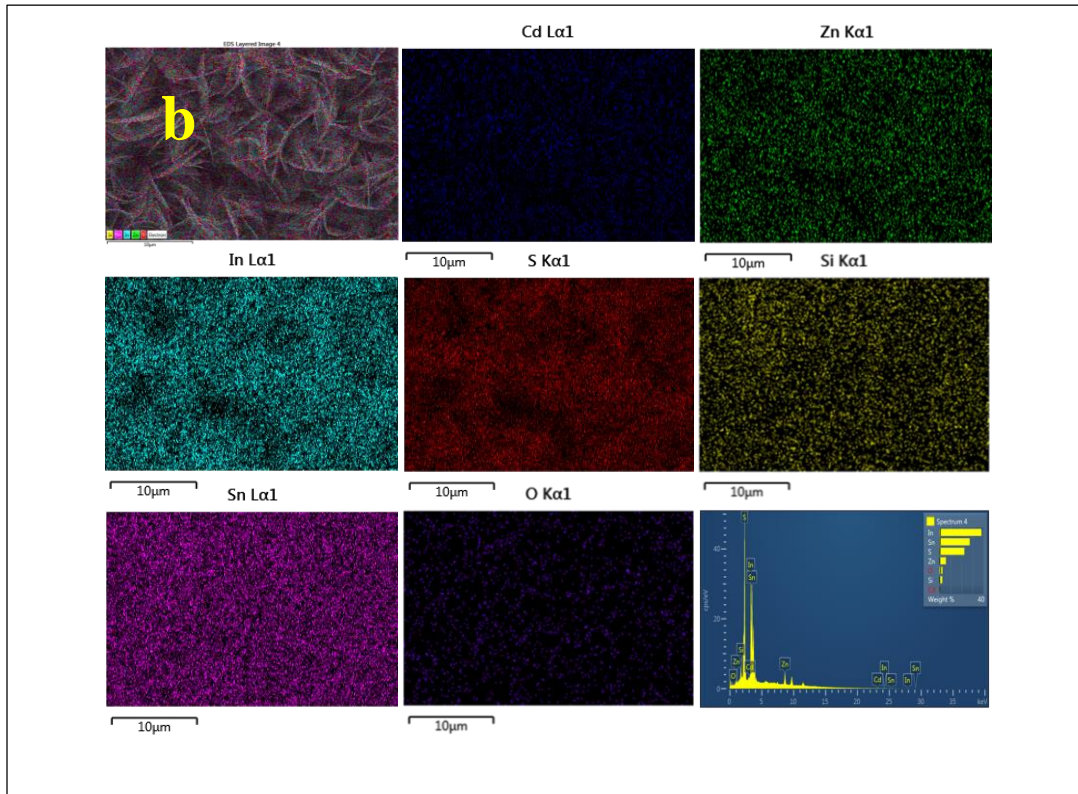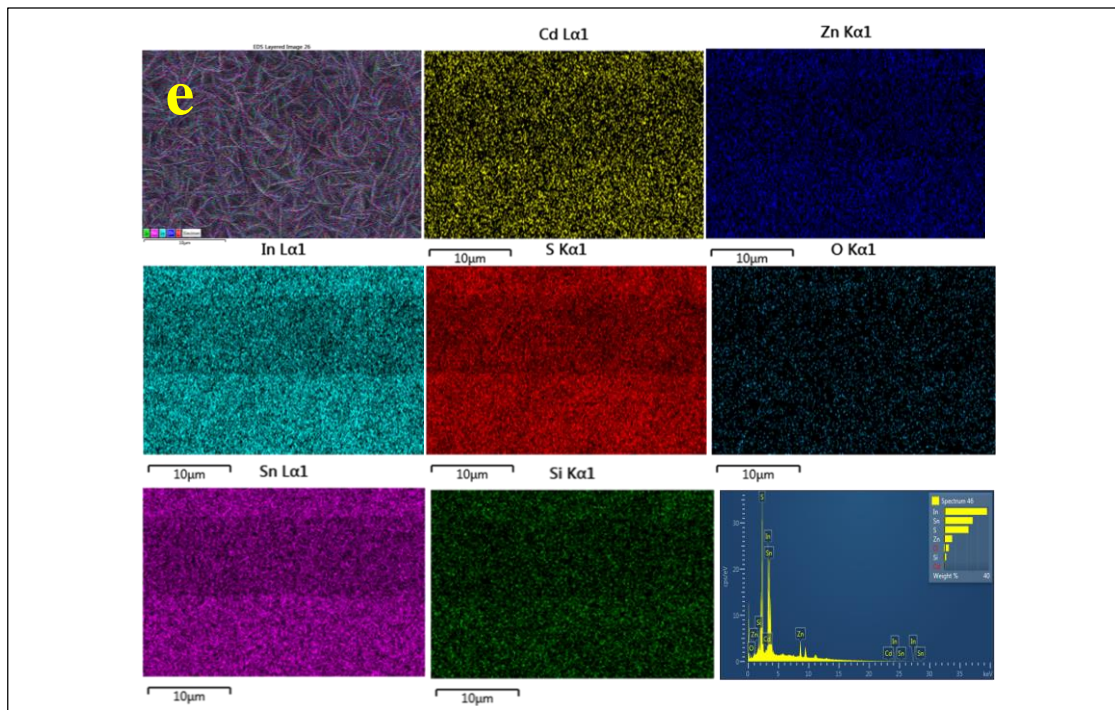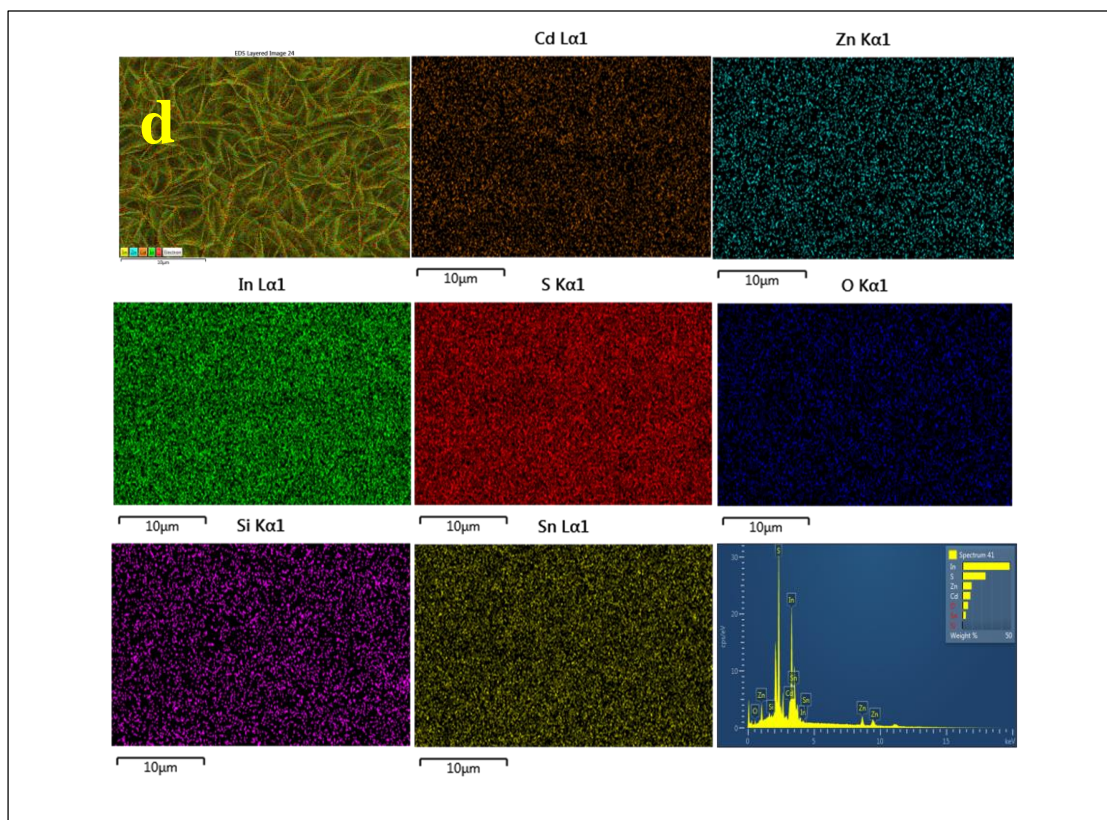
Figure 6.4: EDS analysis of (a) $ZnIn_{2.2}S_y$, (b) $Cd-ZnIn_{2.2}S_y$-A, (c) $Cd-ZnIn_{2.2}S_y$-B, (d) $Cd-ZnIn_{2.2}S_y$-C, and (e) $Cd-ZnIn_{2.2}S_y$-D.

To understand whether the heterostructure is getting formed in between $CdIn_{2.2}S_y$ and $ZnIn_{2.2}S_y$ or surface engineering is taking place through the partial ion exchange process by 'Cd^{2+}', EDS analysis is carried out on the single nanosheet. In the case of $Cd-ZnIn_{2.2}S_y-B$, the Zn: Cd ratio is ~1:1.73 on the edge points as well as ~1:1.78 on the core part of the nanosheets and shown in **Figure 6.5a**. On the other hand, the ratio of Zn: Cd increases ~1:6 in the case of $Cd-ZnIn_{2.2}S_y-D$ throughout (edges as well as core part) the nanosheet (**Figure 6.5b**). So, from the observation, it is clear that the ratio of Zn: Cd remains the same throughout the single nanosheet even when the 'Cd^{2+}' exchange is high. It depicts the formation of $Cd-ZnIn_{2.2}S_y$ nanosheets via the partial exchange of 'Zn^{2+}' by 'Cd^{2+}' ion not the formation of heterostructure.
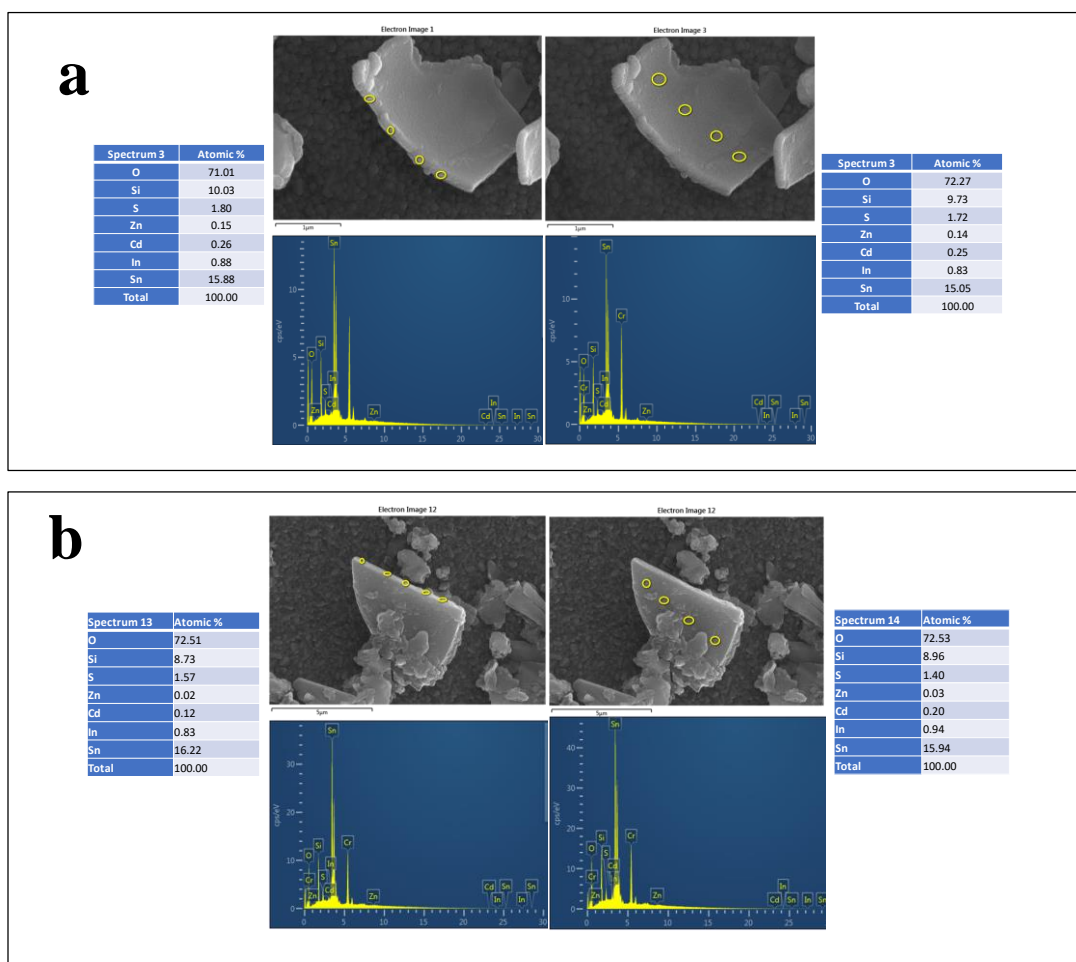
Figure 6.5: EDS point mapping of $Cd-ZnIn_{2.2}S_y-B$ and -D (a) at the edge of the nanosheets, and (b) at the center of the nanosheets, respectively.

ICP-OES analysis is carried out for Cd-ZnIn$_{2.2}$S$_y$-B and Cd-ZnIn$_{2.2}$S$_y$-D to know exact amount of 'Zn^{2+}' and 'Cd^{2+}' in Cd-ZnIn$_{2.2}$S$_y$. **Table 6.1** indicates the ratio of 'Zn^{2+}' and 'Cd^{2+}' is ~1:1.74 for Cd-ZnIn$_{2.2}$S$_y$-B and ~1:3.76 for Cd-ZnIn$_{2.2}$S$_y$-D. The ICP-OES analysis indicates the partial exchange of 'Zn^{2+}' with 'Cd^{2+}'. The ICP-OES analysis data is well accordance with the EDS analysis.

Table 6.1: ICP-OES results for Cd-ZnIn$_{2.2}$S$_y$ photoanodes showing the ratio of Cd:Zn.

Synthesized Material	Cd (Atomic %)	Zn (Atomic %)	Cd:Zn ratio
Cd-ZnIn$_{2.2}$S$_y$-B	0.0136	0.0078	1.74:1
Cd-ZnIn$_{2.2}$S$_y$-D	0.0226	0.006	3.76:1

6.4.1.5 TEM, HRTEM, and SAED Analysis

To further confirm the morphology, crystallinity, and formation of Cd-ZnIn$_{2.2}$S$_y$ nanosheets transmission electron microscopy (TEM) analysis have been carried out. **Figure 6.6a** TEM image of Cd-ZnIn$_{2.2}$S$_y$ nanosheets display that the after partial replacement of 'Zn^{2+}' via 'Cd^{2+}' thin sheet-like morphology of the ZnIn$_{2.2}$S$_y$ retains. The high resolution-TEM image shows the lattice spacing of Cd-ZnIn$_{2.2}$S$_y$ ~0.34 nm which is corresponding to (008) plane (**Figure 6.6b**). While the d-spacing of ZnIn$_{2.2}$Sy (~0.32 nm) is confirmed from the XRD data.[22] The d-spacing of Cd-ZnIn$_{2.2}$S$_y$ is in accordance with the XRD analysis.
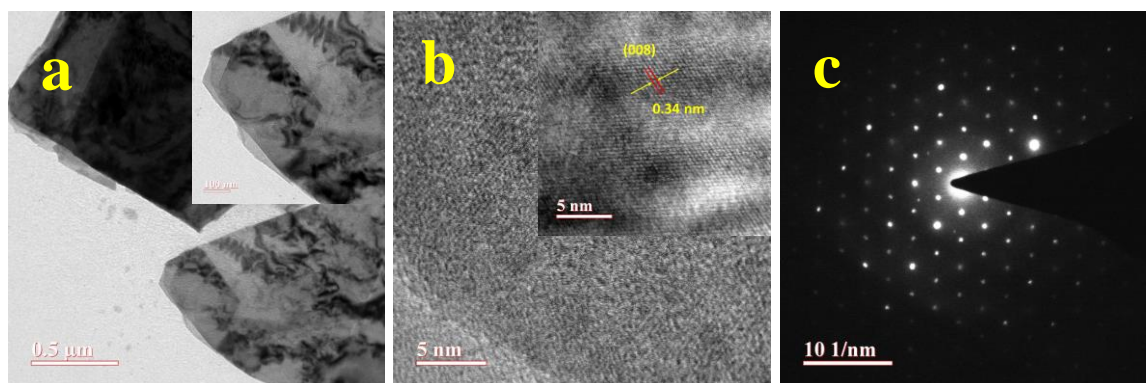
Figure 6.6: (a) TEM image, (b) HRTEM image, and (c) SAED pattern of Cd-ZnIn$_{2.2}$S$_y$-B.

The selected area electron diffraction (SAED) pattern shows the distinct array of the well-defined ring, which is demonstrating the polycrystalline nature of Cd-ZnIn$_{2.2}$S$_y$ nanosheets (**Figure 6.6c**).

6.4.2 Photoelectrochemical Activity

6.4.2.1 Linear Sweep Voltametry

To investigate the photoelectrochemical activity of the developed photoanodes, three- electrode system is used. The Ag/AgCl electrode, Pt wire, and the sample decorated electrode are used as a reference, counter, and the working electrode in 0.5 M Na$_2$SO$_3$ and 3.5wt% NaCl which are used as an electrolyte for PEC measurement. The potential vs. photocurrent plots are obtained with the help of a linear sweep voltammetry technique (LSV) under both continuous and chopped illumination. The photostability of the developed materials is checked with the help of the chronoamperometry technique. The developed ZnIn$_{2.2}$S$_y$ nanosheets can produce 4.83 mA/cm^2 of photocurrent density at an applied potential of '0.78' V vs. RHE, at the same time it can generate 7.05 mA/cm^2 of photocurrent density at the applied potential of '1.6' V vs. RHE. The PEC activity of Cd-ZnIn$_{2.2}$S$_y$-A to D is determined to know the effect of 'Cd^{2+}' exchange in ZnIn$_{2.2}$S$_y$ nanosheets. The photocurrent density increases gradually with the increase in the 'Cd^{2+}' in ZnIn$_{2.2}$S$_y$ nanosheets and the optimum condition is reached in the case of Cd-ZnIn$_{2.2}$S$_y$-B. The observed photocurrent density can be arranged in an order like: Cd-ZnIn$_{2.2}$S$_y$-B>Cd-ZnIn$_{2.2}$S$_y$-A>ZnIn$_{2.2}$S$_y$~Cd-ZnIn$_{2.2}$S$_y$-C>Cd-ZnIn$_{2.2}$S$_y$-D. The developed Cd-ZnIn$_{2.2}$S$_y$-B generates 5.85, and 9.41 mA/cm^2 photocurrent densities under applied potentials of '0.78' and '1.6' V vs. RHE, respectively. The enhancement in photocurrent density can be presumed due to the enhanced visible light absorbance and quick photoinduced charge generation and separation due to the introduction of 'Cd^{2+}' in ZnIn$_{2.2}$S$_y$. It is presumed that the incorporation of 'Cd^{2+}' in place of 'Zn^{2+}' promotes facile charge transportation and further suppress the charge carrier recombination. Meanwhile, the enhanced visible light absorbance resulting from the multiple reflections and scattering of light inside the vertically grown thin sheets plays an important role to increase the PEC activity of the developed material. The photoactivity further decreases in the case of Cd-ZnIn$_{2.2}$S$_y$-C and to Cd-ZnIn$_{2.2}$S$_y$-D, which can produce ~7.82 and ~7.28 mA/cm^2 photocurrent density at an applied potential of '1.6' V vs. RHE. The comparative LSV plots are shown in **Figure**

6.7a, b. All the developed photoanodes show negligible dark current and switch on-off behavior with light (**Figure 6.7c, d**).
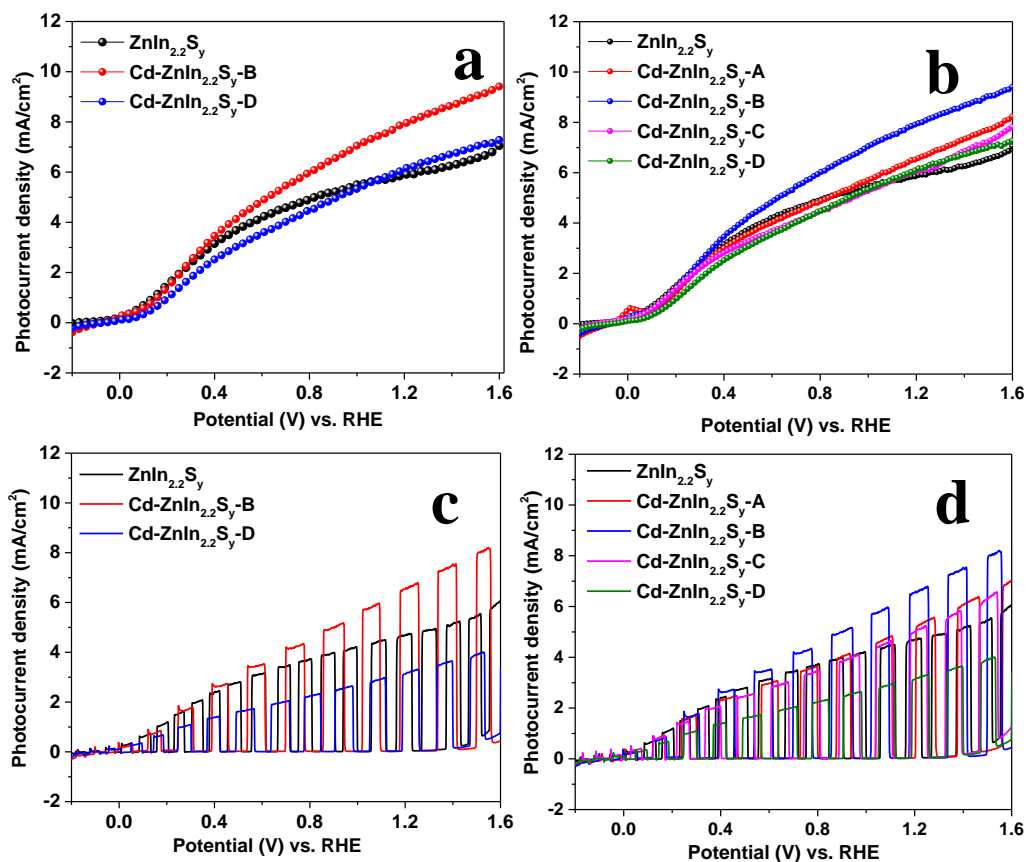
Figure 6.7: LSV plots of (a) $ZnIn_{2.2}S_y$, $Cd-ZnIn_{2.2}S_y$-B, -D (b) $ZnIn_{2.2}S_y$, $Cd-ZnIn_{2.2}S_y$-A, -B, -C, and -D under continuous illumination, (c) $ZnIn_{2.2}S_y$, $Cd-ZnIn_{2.2}S_y$-B, -D, and (d) $ZnIn_{2.2}S_y$, $Cd-ZnIn_{2.2}S_y$-A, -B, -C, and -D under chopped illumination, respectively.

Enhanced 'Cd^{2+}' ion-exchange in $ZnIn_{2.2}S_y$ further decreases the photoabsorbance (**Figure 6.2a, b**). The reason for a diminution in photocurrent density may be attributed to the lowering in optical absorbance and charge carrier migration. On the other hand, CdIS/ZIS/CdS can generate maximum photocurrent density 3.31 mA/cm^2 at an applied potential of '1.6' V vs. RHE which is ~2.48-fold lower than $Cd-ZnIn_{2.2}S_y$-B (**Figure 6.8a, b**). To widen the applicability of the synthesized photoanode $Cd-ZnIn_{2.2}S_y$-B PEC activity is also determined in 3.5% NaCl solution. The photoanode can function efficiently in the corrosive environment (**Figure 6.8c-d**).
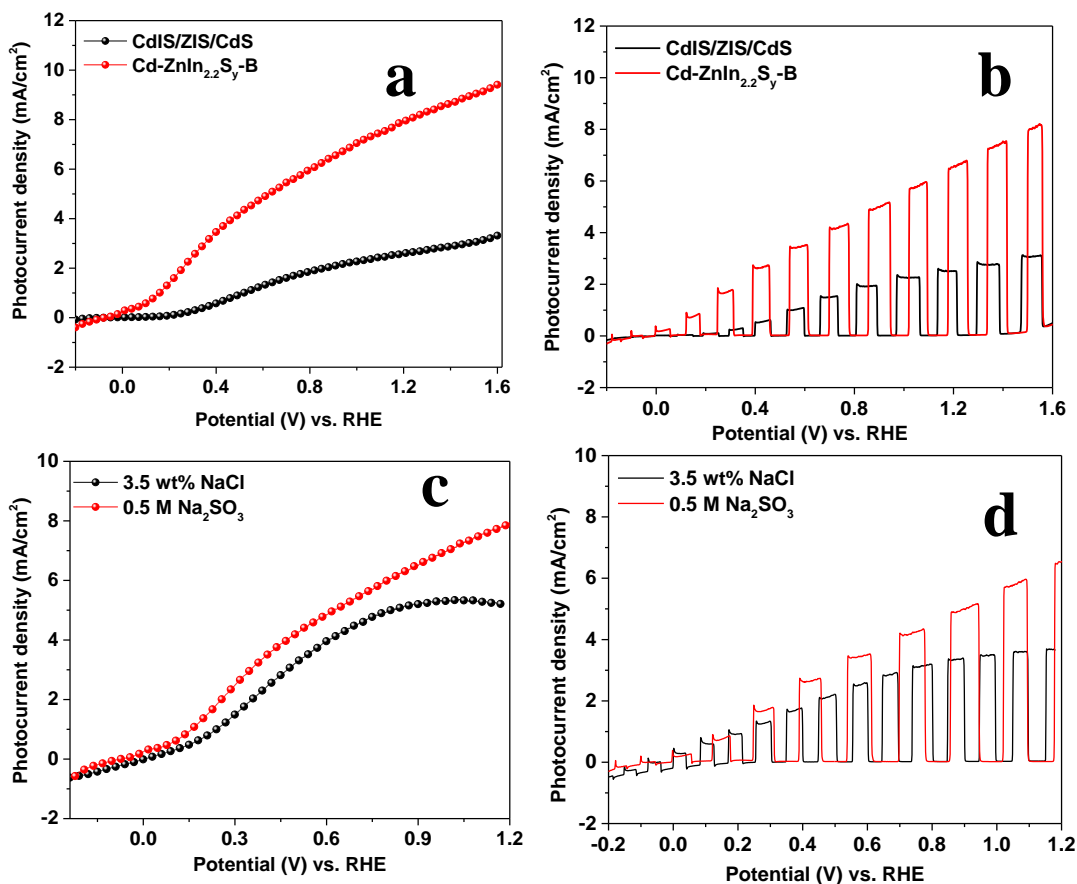
Figure 6.8: LSV plots of (a) Cd-ZnIn$_{2.2}$S$_y$ -B and CdIS/ZIS/CdS in 0.5 M Na$_2$SO$_3$ under (a) continuous, and (b) chopped illumination condition. Linear-sweep voltammograms of Cd-ZnIn$_{2.2}$S$_y$-B in 3.5 wt% NaCl (c) under continuous, (d) chopped illumination, respectively.

6.4.2.2 Photostability and Stability of Photoanode

The photostability of developed photoanodes (ZnIn$_{2.2}$S$_y$, Cd-ZnIn$_{2.2}$S$_y$-B, and -D) is checked at potential '0.78' V vs. RHE for the 90 seconds in 0.5 M Na$_2$SO$_3$. (**Figure 6.9a**). **Figure 6.9b** shows the comparative photostability of Cd-ZnIn$_{2.2}$S$_y$-B in 0.5 M Na$_2$SO$_3$ and 3.5wt% NaCl. The long term stabilities of ZnIn$_{2.2}$S$_y$ and Cd-ZnIn$_{2.2}$S$_y$-B nanosheets are checked up to 1h at potential '0.28' V vs. RHE by using the chronoamperometry technique (**Figure 6.9c**). From the observed result, it is clear that sufficient enhancement in stability is introduced after incorporation of 'Cd^{2+}' in ZnIn$_{2.2}$S$_y$.
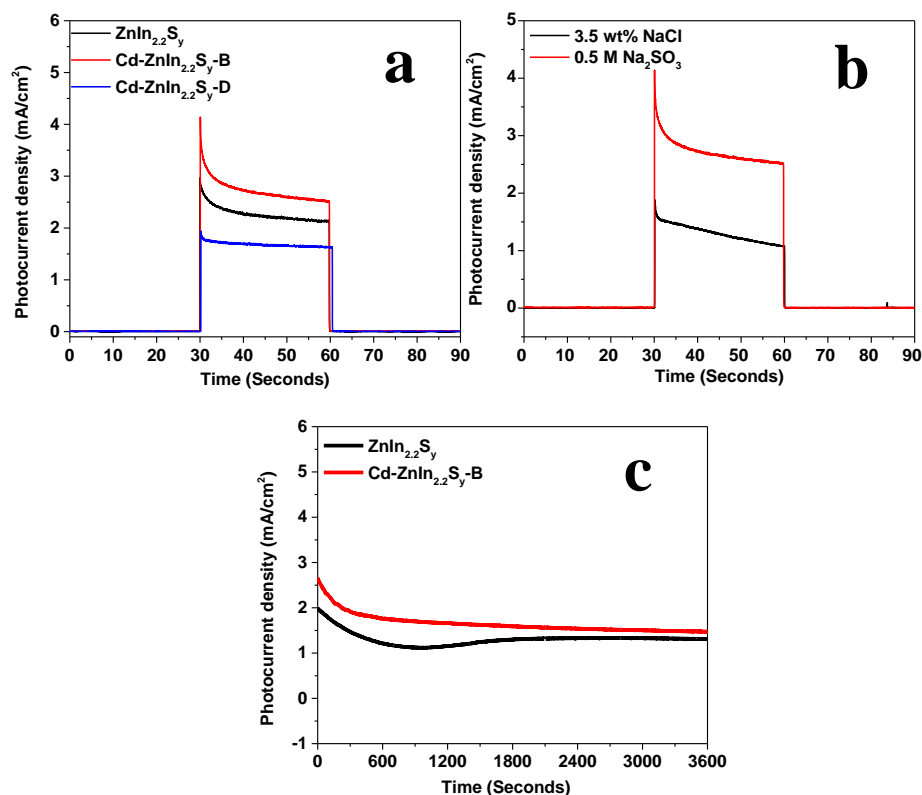
Figure 6.9: i-t plot of (a) $ZnIn_{2.2}S_y$, $Cd-ZnIn_{2.2}S_y$-B, -D at a fixed potential of '0.78' V vs. RHE for 90 seconds, (b) $Cd-ZnIn_{2.2}S_y$-B in 3.5 wt% NaCl and 0.5 M Na_2SO_3 in chronoamperometry study, (c) plot of photostability of $ZnIn_{2.2}S_y$, $Cd-ZnIn_{2.2}S_y$-B, at a fixed potential of '0.28' V vs. RHE for 1h under continuous back illumination.

The morphological robustness is determined with the help of FESEM analysis of Cd-$ZnIn_{2.2}S_y$-B after long term stability and it is observed that $Cd-ZnIn_{2.2}S_y$-B can retain its morphology (**Figure 6.10a, b**).
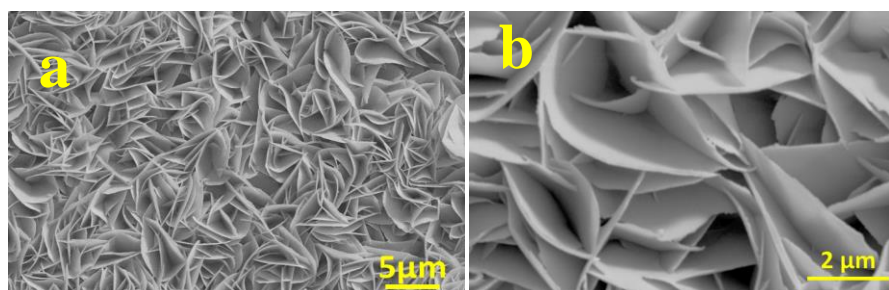
Figure 6.10: FESEM images of (a, b) $Cd-ZnIn_{2.2}S_y$-B after 1h photostability testin 0.5 M Na_2SO_3.

6.4.2.3 Determination of Carrier Density through Mott-Schottky Plot, Photoconversion Efficiencies, and Charge Carrier Transportation Ability from Impedance Spectra

Further, to evaluate the electronic properties and carrier concentration of the materials the Mott-Schottky analysis is carried out. As shown in **Figure 6.11a**, the negative slope indicates the n-type nature of $ZnIn_{2.2}S_y$ and Cd-$ZnIn_{2.2}S_y$ nanosheets. Meanwhile, the lower slope depicts the higher carrier concentrations in the Cd-$ZnIn_{2.2}S_y$ nanosheets. The carrier densities and flat band potentials are calculated by using the following equation:[23,24]

$$1/C^2 = (2/e\varepsilon\varepsilon_0 N_d A^2) [(V-V_{FB}-kT/e)]\ldots\ldots\ldots1$$

where C = specific capacitance, N_d = carrier density, e = electron charge, ε_0 = electric permittivity of vacuum, ε = dielectric constant of the semiconductor, V_{FB} = flat band potential, A = area of the sample, T = temperature, and k = Boltzmann constant. The slope of Cd-$ZnIn_{2.2}S_y$-B is 0.4197×10^{10} which is smaller than the Cd-$ZnIn_{2.2}S_y$-D, and bare $ZnIn_{2.2}S_y$ (4.90×10^{10} and 1.68×10^{10}). Calculated carrier densities are 1.80×10^{21}, 6.14×10^{20}, and 7.16×10^{21} for bare $ZnIn_{2.2}S_y$, Cd-$ZnIn_{2.2}S_y$-D, and Cd-$ZnIn_{2.2}S_y$-B, respectively. The flat band potential is calculated by the extrapolation in the Mott-Schottky plot and for $ZnIn_{2.2}S_y$ it is -0.07 V vs. RHE and -0.79 V and -0.41 V vs. RHE for Cd-$ZnIn_{2.2}S_y$-B and Cd-$ZnIn_{2.2}S_y$-D, respectively. The negative shift of flat band potential indicates the broadening of the space charge region. As a result, there is a decrease in recombination due to the accelerated charge-carrier transportation at the electrode-electrolyte interface in PEC water oxidation. The higher carrier density and observed the most negative flat band potential of Cd-$ZnIn_{2.2}S_y$-B indicates the efficient PEC activity.

To understand the effect of incorporation of 'Cd^{2+}' in $ZnIn_{2.2}S_y$, photoconversion efficiency (applied bias photocurrent conversion efficiency, η) is calculated with the help of the observed J-V curve. The following equation is used for the calculation of η:[25,26]

$$\eta = [J (1.23-V_{RHE})/P_{in}]\%\ldots\ldots\ldots\ldots2$$

Where J = observed photocurrent density, V_{RHE} = applied potential with respect to reversible hydrogen electrode, and P_{in} = incident light intensity on the electrode. The photoconversion efficiency vs. applied potential plot shows that the photoconversion efficiency changes with the exchange of 'Zn^{2+}' with 'Cd^{2+}'. In our previous report, it was observed that the photoconversion

efficiency of $ZnIn_{2.2}S_y$ is ~2.74% at an applied potential of 0.51 V vs. RHE.[10] Whereas, Cd-$ZnIn_{2.2}Sy$-B shows the maximum photoconversion efficiency of ~3.10% at an applied potential of 0.53 V vs. RHE. The enhancement in photoconversion efficiency signifies that the photogenerated charge carriers reach the electrode-electrolyte interface to react efficiently with electrolyte prior to the charge-carrier recombination. Facile charge transportation becomes feasible after the optimum exchange of 'Zn^{2+}' with 'Cd^{2+}'. The comparative photoconversion efficiency of all the developed materials is shown in **Figure 6.11b, c**.
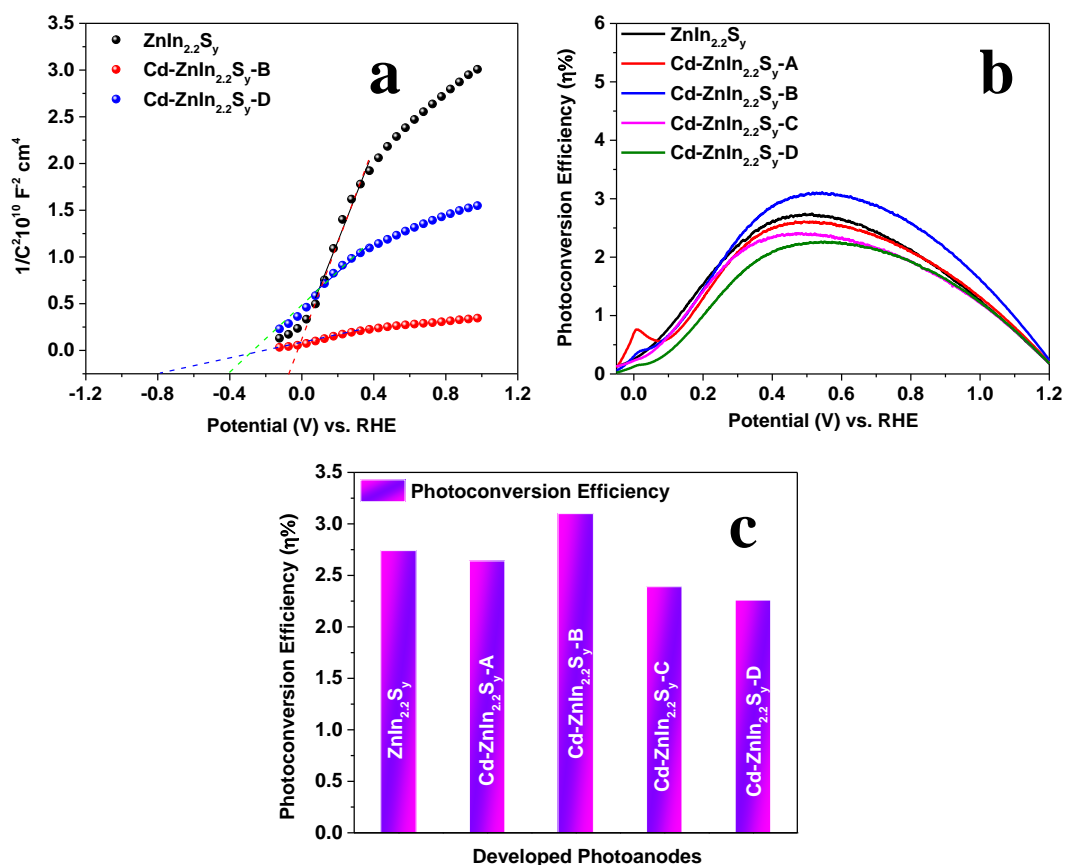
Figure 6.11: (a) Mott-Schottky plots of $ZnIn_{2.2}S_y$, Cd-$ZnIn_{2.2}S_y$-B, and Cd-$ZnIn_{2.2}S_y$-D, (b, c) plots of photoconversion efficiency of $ZnIn_{2.2}S_y$ and Cd-$ZnIn_{2.2}S_y$-A to -D.

The efficient interfacial charge transportation in Cd-$ZnIn_{2.2}S_y$ is evaluated with the help of electrochemical impedance spectra under illumination condition. The arc of a semicircle of EIS plot signifies the charge transportation of photogenerated charge carriers. The Cd-$ZnIn_{2.2}S_y$-B shows a smaller semicircle than the Cd-$ZnIn_{2.2}S_y$-D, and bare $ZnIn_{2.2}S_y$. The lower charge transfers

resistance (R_{CT}) indicates the faster charge transportation through interfacial charge separation because of Cd-$ZnIn_{2.2}S_y$ development. At the same time, R_{CT} value decreases due to the effective charge transportation through the interface of Cd-$ZnIn_{2.2}S_y$-B and electrolyte. The comparative EIS plot of the developed photoanodes is shown in **Figure 6.12a**. CdIS/ZIS/CdS shows higher charge transfer resistance than Cd-$ZnIn_{2.2}S_y$-B (**Figure 6.12b**).
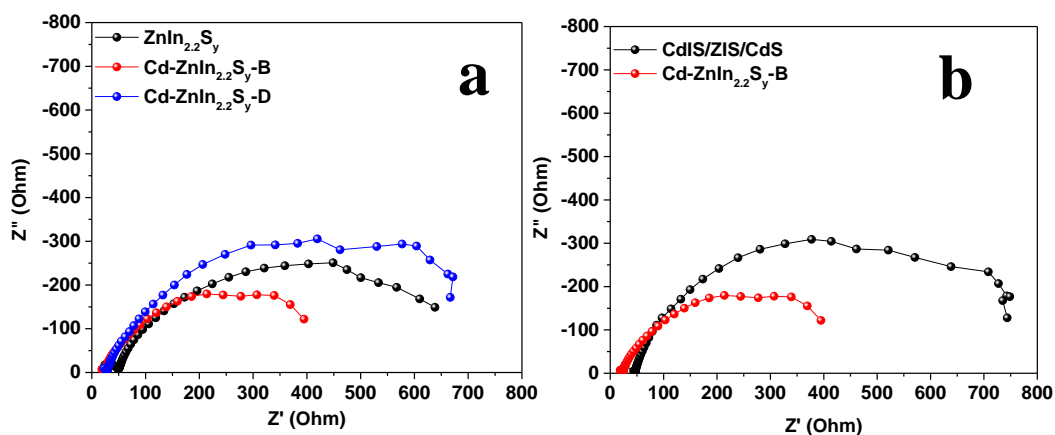
Figure 6.12: (a) Comparative EIS plot of (a) $ZnIn_{2.2}S_y$, Cd-$ZnIn_{2.2}S_y$-B, -D, (b) CdIS/ZIS/CdS and Cd-$ZnIn_{2.2}S_y$-B.

6.5 Comparative Study

The observed PEC performace of the Cd-$ZnIn_{2.2}S_y$ indicates the higher PEC activity than the $ZnIn_{2.2}S_y$ nanosheets. The observed PEC activity of Cd-$ZnIn_{2.2}S_y$-B in our present study is comparable with the similar kind of existing literature (**Table 6.2**).

Table 6.2: Comparative data of PEC activity of Cd-ZnIn$_{2.2}$S$_y$ with the reported data in literature.

S.N.	Photoanodes	Photocurrent density	Electrolyte	References
1	ZnS/Cu-Zn-In-S/TiO$_2$	0.81 mA/cm^2 at 0.8 V vs. RHE	0.35 M Na$_2$SO$_3$ and 0.24 M Na$_2$S	24
2	Cu$_2$In$_2$ZnS$_5$	2.0 mA/cm^2 at 0.82 V vs. NHE	0.25 M Na$_2$SO$_3$ and 0.35 M Na$_2$S	27
3	ZnIn$_2$S$_4$/CuInS$_2$	8 μA/cm^2 at 0.24 V vs. RHE	0.5 M Na$_2$SO$_4$	28
4	Cu-ZnIn$_2$S$_4$	3.8 μA/cm^2	0.5 M Na$_2$SO$_4$	29
5	Cd-ZnIn$_{2.2}$S$_y$-B	9.41 mA/cm^2	0.5 M Na$_2$SO$_3$	**This work**

6.6 Conclusion

In this study, an efficient photoanode for PEC water-splitting is developed. Nanosheets of ZnIn$_{2.2}$S$_y$ are vertically grown through hydrothermal technique, which is previously reported by our group. Further, Cd-ZnIn$_{2.2}$S$_y$ is synthesized via a simple and effective ion exchange strategy. The optimized Cd-ZnIn$_{2.2}$S$_y$-B nanosheets can generate ~5.85 mA/cm^2 photocurrent density at an applied potential of '0.78' V vs. RHE, which is higher than ZnIn$_{2.2}$S$_y$ nanosheets. Furthermore, the increase in optical absorbance, enhanced charge carrier density, facile charge-carrier separation, and transportation promote the photoactivity of Cd-ZnIn$_{2.2}$S$_y$-B nanosheets compared to ZnIn$_{2.2}$S$_y$, resulting in enhanced photoconversion efficiency of Cd-ZnIn$_{2.2}$S$_y$-B. Cd-ZnIn$_{2.2}$S$_y$-B photoanode is very stable and it can generate unaltered photocurrent density up to 1h. The developed protocol can be applied to other photoanodes to improve their PEC performance via tuning the exchange of cation, increasing light-harvesting capability, accelerated charge transfer efficiency, reduced interface recombination, and increase the charge transfer ability of the photoanode. The incorporation of hetero-ion opens up a new avenue in the field of PEC water-splitting.

6.7 References

1. Chen, H. M.; Chen, C. K.; Liu, R-S.; Zhang, L.; Zhang, J.; Wilkinson, D. P.; Nano-architecture and material designs for water splitting photoelectrodes. *Chem. Soc. Rev*., **2012**, *41*, 5654-5671.

2. Sharma, M. D.; Mahala, C.; Basu, M. Shape-Controlled Hematite: An Efficient Photoanode for Photoelectrochemical Water Splitting. *Ind. Eng. Chem. Res*., **2019**, *58*, 7200-7208.

3. Zhou, M.; Lou, X. W. (D.); Xie, Y. Two-dimensional nanosheets for photoelectrochemical water splitting: Possibilities and opportunities. *Nano Today* **2013**, *8*, 598-618.

4. Zuoa, G.; Wang, Y.; Teo, W. L.; Xie, A.; Guo, Y.; Dai, Y.; Zhou, W.; Jana, D.; Xian, Q.; Dong, W.; Zhao, Y. Enhanced photocatalytic water oxidation by hierarchical 2D-Bi_2MoO_6@2DMXene Schottky junction nanohybrid. *Chem. Eng. J.*, **2020**, *403*, 126328-126336.

5. Kang, Z.; Si, H.; Zhang, S.; Wu, J.; Sun, Y.; Liao, Q.; Zhang, Z.; Zhang, Y. Interface Engineering for Modulation of Charge Carrier Behavior in ZnO Photoelectrochemical Water Splitting. *Adv. Funct. Mater*., **2019**, *29*, 808032-1808050.

6. Li, H.; Shang, J.; Zhu, H.; Yang, Z.; Ai, Z.; Zhang, L. Oxygen Vacancy Structure Associated Photocatalytic Water Oxidation of BiOCl. *ACS Catal*., **2016**, *6*, 8276-8285.

7. Kuang, Y.; Yamada, T.; Domen, K. Surface and Interface Engineering for Photoelectrochemical Water Oxidation. *Joule* **2017**, *1*, 290-305.

8. Lei, Z.; You, W.; Liu, M.; Zhou, G.; Takata, T.; Hara, M.; Domen, K.; Li, C. Photocatalytic Water Reduction under Visible Light on a Novel $ZnIn_2S_4$ Catalyst Synthesized by Hydrothermal Method. *Chem. Commun*., **2003**, 2142-2143.

9. Yang, W.; Zhang, L.; Xie, J.; Zhang, X.; Liu, Q.; Yao, T.; Wei, S.; Zhang, Q.; Xie, Y. Enhanced Photoexcited Carrier Separation in Oxygen-Doped $ZnIn_2S_4$ Nanosheets for Hydrogen Evolution. *Angew. Chem., Int. Ed*., **2016**, *55*, 6716-6720.

10. Sharma, M. D.; Mahala, C.; Basu, M. Band gap tuning to improve the photoanodic activity of $ZnIn_xS_y$ for photoelectrochemical water oxidation. *Catal. Sci. Technol*., **2019**, *9*, 6769-6781.

11. Liu, Q.; Cao, F.; Wu, F.; Chen, S.; Xiong, J.; Li, L. Partial Ion Exchange Derived 2D Cu−Zn−In−S Nanosheets as Sensitizers of 1D TiO_2 Nanorods for Boosting Solar Water Splitting. *ACS Appl. Mater. Interfaces* **2016**, *8*, 26235-26243.

12. Liu, J.; Chen, G.; Sun, J. Ag_2S-Modified $ZnIn_2S_4$ Nanosheets for Photocatalytic H_2 Generation. *ACS Appl. Nano Mater.*, **2020**, *3*, 11017-11024.

13. Basu, M.; Sinha, A. K.; Pradhan, M.; Sarkar, S.; Govind, Pal, T. CuO Barrier Limited Corrosion of Solid Cu_2O Leading to Preferential Transport of Cu(I) Ion for Hollow Cu_7S_4 Cube Formation. *J. Phys. Chem. C* **2011**, *115*, 12275-12282.

14. Mu, L.; Wang, F.; Sadtler, B.; Loomis, R. A.; Buhro, W. E. Influence of the Nanoscale Kirkendall Effect on the Morphology of Copper Indium Disulfide Nanoplatelets Synthesized by Ion Exchange. *ACS Nano* **2015**, *9*, 7419-7428.

15. Stam, W. V.; Bladt, E.; Rabouw, F. T.; Bals, S.; Donega, C. D. M. Near-Infrared Emitting $CuInSe_2$/$CuInS_2$ Dot Core/Rod Shell Heteronanorods by Sequential Cation Exchange. *ACS Nano* **2015**, *9*, 11430-11438.

16. Naushad, M.; Khan, M. R.; Bhande, S. S.; Shaikh, S. F.; Alfadul, S. M.; Shinde, P. V.; Mane, R. S. High current density cation-exchanged SnO_2-CdSe/ZnSe and SnO_2-CdSe/SnSe quantum-dot photoelectrochemical cells. *New J. Chem.*, **2018**, *42*, 9028-9036.

17. Chaudhari, N. S.; Warule, S. S.; Kale, B. B. Architecture of rose and hollow marigold-like $ZnIn_2S_4$ flowers: structural, optical and photocatalytic study. *RSC Adv.*, **2014**, *4*, 12182-12187.

18. Shen, S.; Guo, P.; Zhao, L.; Du, Y.; Guo, L. Insights into photoluminescence property and photocatalytic activity of cubic and rhombohedral $ZnIn_2S_4$. *J. Solid State Chem.*, **2011**, *184*, 2250-2256.

19. Shen, S.; Zhao, L.; Guan, X.; Guo, L. Improving visible light photocatalytic activity for hydrogen evolution over $ZnIn_2S_4$: A case study of alkaline-earth metal doping. *J. Phys. Chem. Solids*, **2012**, *73*, 79-83.

20. Pan, X.; Shang, C.; Chen, Z.; Jin, M.; Zhang, Y.; Zhang, Z.; Wang, X.; Zhou, G. Enhanced Photocatalytic H_2 Evolution over $ZnIn_2S_4$ Flower-Like Microspheres Doped with Black Phosphorus Quantum Dots. *Nanomaterials* **2019**, *9*, 1266-1278.

21. Xu, S.; Dai, J.; Yang, J.; You, J.; Hao, J. Facile Synthesis of Novel $CaIn_2S_4$/$ZnIn_2S_4$ Composites with Efficient Performance for Photocatalytic Reduction of Cr(VI) under Simulated Sunlight Irradiation. *Nanomaterials* **2018**, *8*, 472-488.

22. Zhang, Z.; Liu, K.; Feng, Z.; Bao, Y.; Dong, B. Hierarchical Sheet-on-Sheet $ZnIn_2S_4$/g-C_3N_4 Heterostructure with Highly Efficient Photocatalytic H_2 production Based on Photoinduced Interfacial Charge Transfer. *Sci. Rep.*, **2016**, *6*, 19221-19230.

23. Liu, Q.; Lu, H.; Shi, Z.; Wu, F.; Guo, J.; Deng, K.; Li. L. 2D $ZnIn_2S_4$ Nanosheet/1D TiO_2 Nanorod Heterostructure Arrays for Improved Photoelectrochemical Water Splitting. *ACS Appl. Mater. Interfaces* **2014**, *6*, 17200-17207.

24. Liu, Q.; Wu, F.; Cao, F.; Chen, L.; Xie, X.; Wang, W.; Tian, W.; Li, L. A multi junction of $ZnIn_2S_4$ nanosheet/TiO_2 film/Si nanowire for significant performance enhancement of water splitting. *Nano Res*., **2015**, *8*, 3524-3534.

25. Mahala, C.; Sharma, M. D.; Basu, M. Near-Field and Far-Field Plasmonic Effects of Gold Nanoparticles Decorated on ZnO Nanosheets for Enhanced Solar Water Splitting. *ACS Appl. Nano Mater*., **2020**, *3*, 1153-1165.

26. Han, J.; Liu, Z.; Guo, K.; Wang, B.; Zhang, X.; Hong, T. High-efficiency photoelectrochemical electrodes based on $ZnIn_2S_4$ sensitized ZnO nanotube arrays, *Appl. Catal. B-Environ*., **2015**, *163*, 179-188.

27. Hong, T.; Liu, Z.; Zhang, J.; Li, G.; Liu, J.; Zhang, X.; Lin, S. Flower-like $Cu_2In_2ZnS_5$ Nanosheets: A Novel Promising Photoelectrode for Water Splitting. *ChemCatChem* **2016**, *8*, 1288-1292.

28. Guo, X.; Peng, Y.; Liu, G.; Xie, G.; Guo, Y.; Zhang, Y.; Yu, J. An Efficient $ZnIn_2S_4$@$CuInS_2$ Core-Shell p-n Heterojunction to Boost Visible-Light Photocatalytic Hydrogen Evolution. *J. Phys. Chem. C* **2020**, *124*, 5934-5943.

29. Wang, P.; Shen, Z.; Xia, Y.; Wang, H.; Zheng, L.; Xi, W.; Zhan, S. Atomic Insights for Optimum and Excess Doping in Photocatalysis: A Case Study of Few-Layer $Cu-ZnIn_2S_4$. *Adv. Funct. Mater*., **2019,** *29*, 1807013-1807021.

Surface Modified Vertically Grown 2D Thin Nanosheets of CdIn$_{2.2}$S$_y$: Photoanode for Photoelectrochemical Water-splitting Reaction
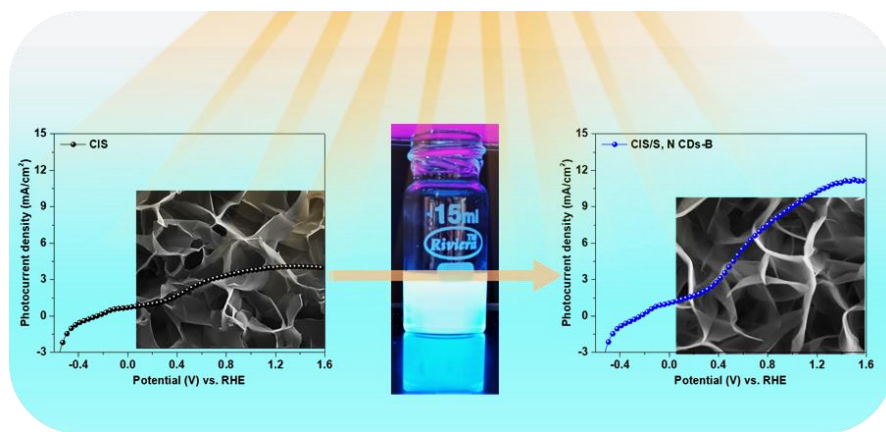
- In this chapter CdIn$_{2.2}$S$_y$/ S, N-CDs heterostructure is developed via a simple hydrothermal technique followed by dip-coating method.

- The decoration of S, N-CDs on CdIn$_{2.2}$S$_y$ thin sheets leads the enhancement in PEC activity.

- The observed enhancement in PEC activity is due to increase in light absorption and improved photogenerated charge carrier separation efficiency.

Abstract

Looking at the theoretical efficiency and the solar spectrum, the visible light active semiconductors are the most suitable candidate. Herein, CdIn$_{2.2}$S$_y$ (CIS), a visible light active semiconductor, is explored as a photoanode for PEC water-splitting. The thin nanosheets of CIS are grown vertically through the hydrothermal method. These can proficiently absorb visible light through multiple reflections and scattering of light inside the material and enhance the light-matter interaction. The interconnected thin nanosheets are enabled to react efficiently with electrolytes. As a result, the developed CIS thin nanosheets can produce ~2.73 mA/cm^2 photocurrent density at an applied potential of '0.6' V vs. RHE, and maximum photocurrent density of 3.97 mA/cm^2 is achieved at '1.6' V vs. RHE under continuous back illumination. On the other hand, CIS can attain maximum photoconversion efficiency ~1.72% at '0.60' V vs. RHE. Further, to improve the efficiency and stability, 'S' and 'N' co-doped C-dot (S, N-CDs) are adorned on the surface of the CIS photoanode. The 'S' and 'N' co-doped C-dot and CIS form the type-II heterostructure which further boosts the charge separation and transportation rate of photogenerated charge carriers. The transient decay time becomes longer in the case of heterostructure compare to bare CIS. The developed heterostructure can generate 5.99 mA/cm^2 and 11.2 mA/cm^2 photocurrent densities at applied potentials of '0.6' V and '1.6' V vs. RHE, respectively. At the same time, the heterostructure CIS/S, N-CDs-B can achieve the ~2.08-fold higher photoconversion efficiency compare to bare CIS nanosheets and stable up to 1500 seconds under continuous back illumination. This work provides an approach to design an efficient and stable photoanode for PEC water-splitting.

7.1 Introduction

A practical PEC water-splitting reaction required a class of material that can utilize a large portion of the sunlight efficiently. The visible light active materials absorb the important range of sunlight because it contains 46% visible light and only 4% UV light.[1] According to the aforementioned discussion, the electron-hole recombination rate needs to be reduced to improve the STH efficiency in PEC water-splitting. So, to increase the efficiency of a semiconductor a careful design is required to tune the bulk and surface properties. Keeping all the things in mind, in search of an efficient photoelectrode, especially photoanode in PEC water-splitting reaction, $CdIn_2S_4$ is explored here with the hope that it may fulfill the above-mentioned criteria. The $CdIn_2S_4$ is a visible light semiconductor with a bandgap of ~2.4 eV.[2,3] Owing to the appropriate band gap it is getting utilized in different fields such as photocatalytic water-splitting, organic dye degradation, CO_2 photoreduction, and PEC water-splitting.[4-6] Here, initially, morphology is controlled to have optimum activity of $CdIn_{2.2}S_y$. In our earlier reports, it is already established that vertically grown 2D nanosheets are more photoactive compared to other nanostructures.[7,8] It is because, vertically grown 2D nanosheets can absorb more light and can increase the light-matter interaction inside the material, at the same time providing a more exposed electrode-electrolyte interface, which helps to boost the PEC performance of the material. Thin nanosheets allow electrolytes to penetrate easily and due to the shortened path length of the minority carriers, the minority carrier can promptly reach the interface to oxidize water.

However, while dealing with metal sulfide besides the high photoabsorbance ability of visible light active metal sulfide, one important issue is the photocorrosion which lowers its acceptability due to the reduced photostability. During the PEC process, interfacial redox reaction if sluggish, h^+ favors to oxidize the S^{2-} to S (0) present in the semiconductor and undergo the self photocorrosion. Growing attention is getting concentrated on the increase in the stability of the metal sulfides. In this regard, Xu *et al.* reported the double-side interfacial engineering for $CdIn_2S_4$ photoanode to improve the efficiency towards for PEC water-splitting reaction. Both sides of $CdIn_2S_4$ photoanode were modified by TiO_2 (underlayer), which serves as electron transporter through back contact, and NiO (overlayer) as a p-type semiconductor, which forms a p-n heterojunction with $CdIn_2S_4$, making a built-in electric field to ease of charge transportation.[9] Meng *et al.* reported $CdIn_2S_4/In_2S_3$ bulk-heterojunction photoanode to increase the charge separation efficiency and decorated ultrathin amorphous SnO_2 to improve the surface oxygen

reaction kinetics.[10] Liang *et al.* decorated the CQDs on the surface of hydrogenated TiO_2 for trapping the photoinduced electrons and to increase the solar light-harvesting efficiency. The $CQDs/H-TiO_2$ can generate ~6.0-fold higher photocurrent density than pristine TiO_2 with high stability.[11] Our group decorated the 'C' dot on the surface of ZnO nanosheets to develop a type-II heterostructure. The designed heterostructure of 'ZnO/C' dots display a nearly 2 times higher photocurrent density than bare ZnO, at the same time 'C' dot helps to improve the surface kinetics by increasing the charge separation and transportation.[12] Recently, Zhou *et al.* reported the heterostructure of $CQDs/FeOOH/BiVO_4$ photoanode to the charge separation efficiency in bulk and surface, and to enhance the photostability of the $BiVO_4$. The heterojunction of FeOOH on the surface of $BiVO_4$ increases the surface charge separation efficiency and decreases the overpotential of $BiVO_4$ for PEC water-splitting. While the decoration of CQDs decreases the bulk recombination of charge carriers and increases the charge separation and transportation ability of $BiVO_4$. The co-modification of $BiVO_4$ with CQDs and FeOOH increases the PEC activity as well as photostability. The heterostructure of $CQDs/FeOOH/BiVO_4$ is stable up to 2 h and after the decoration of CQDs, $BiVO_4$ can generate ~10.7-fold and $FeOOH/BiVO_4$ can generate ~2.98-fold higher photocurrent density.[13] So, it is observed that there is enough scope to increase the stability as well as the efficiency of $CdIn_{2.2}S_y$. Here, to improve the PEC performance, the surface of vertically grown 2D thin nanosheets of $CdIn_{2.2}S_y$ is decorated with the S, N-CDs. The S, N-CDs increase charge-carrier separation and transportation, extend the band edge in the visible region, and show the resistance towards the photocorrosion of the material.

Herein, a facile hydrothermal method is developed to grow vertically thin, interconnected nanosheets of $CdIn_{2.2}S_y$ on the fluorine-doped tin oxide coated glass (FTO) surface. Further to develop a heterostructure of $CdIn_{2.2}S_y$/S, N-CDs, S, N-CDs have been synthesized via microwave technique. The developed heterostructure of $CdIn_2S_4$/ S, N-CDs, and bare counterparts are characterized with different physical techniques and the optical property is checked with the help of UV-visible spectroscopy. The PEC activity of all the characterized materials is demonstrated in 0.5 M Na_2SO_4. The role of vertically grown thin nanosheets and S, N-CDs are clearly defined and the PEC mechanism of a heterostructure of $CdIn_{2.2}S_y$/ S, N-CDs are specifically discussed.

7.2 Experimental Section

7.2.1 Method 1: Synthesis of CdIn$_{2.2}$S$_y$ thin nanosheets: CdIn$_{2.2}$S$_y$ thin nanosheets were synthesized on FTO via hydrothermal technique followed by calcination in air. Initially, FTO was cleaned through a multi-step method that is described in our earlier reports.[12] For the synthesis of vertically grown thin nanosheets of CdIn$_{2.2}$S$_y$, 0.179 mmol of CdCl$_2$, 0.397 mmol of InCl$_3$, 0.599 mmol of L-cysteine are dissolved in 15 mL Milli-Q water. The cleaned FTO was kept in the hydrothermal container and the prepared solution was poured into it. The reaction was kept in the autoclave for 16 h at 180 ℃. After the natural cooling of the reaction, the sample deposited FTO was washed 2-3 times with Mill-Q water and ethanol, respectively. The sample decorated FTO was kept for the air calcination at 200 ℃ for 5 h. Synthesized CdIn$_{2.2}$S$_y$@FTO were further used for the characterization and the study of PEC water-splitting. The synthesized CdIn$_{2.2}$S$_4$ is named CIS in the MS.

Method 2: Synthesis of CdIn$_{2.2}$S$_y$ Nanoballs: CdIn$_{2.2}$S$_y$ nanoballs were synthesized on FTO by following the hydrothermal method followed by air calcination. For the synthesis of CdIn$_{2.2}$S$_y$ nano balls, thioacetamide was taken as 'S' precursor. 0.599 mmol of Thioacetamide, 0.179 mmol of CdCl$_2$, 0.397 mmol of InCl$_3$ are dissolved in 15 mL Milli-Q water. The cleaned FTO was kept in the hydrothermal container and the prepared solution was poured into it. The reaction was kept in the autoclave for 16 h at 180 ℃. After the natural cooling of the reaction, the sample deposited FTO was washed 2-3 times with Mill-Q water and ethanol, respectively. The sample decorated FTO was kept for the air calcination at 200 ℃ for 5 h. Synthesized CdIn$_{2.2}$S$_y$@FTO were further used for the characterization and the study of PEC water-splitting. The developed CdIn$_{2.2}$S$_y$ nanoballs are named CIS nanoballs throughout the MS.

7.2.2 Synthesis of S, N-CDs: The S, N-CDs were synthesized via microwave technique followed by centrifugation. 0.19 g citric acid, 0.11 g L-cysteine, and 0.30 g of β-cyclodextrin were dissolved in 15 mL of Milli-Q water and sonicated thoroughly. The whole solution was transferred into the microwave G30 glass vial and the reaction was carried out for 3 min at 180 ℃ in the microwave (300 W). A clear, stable brown color solution was obtained without any precipitation.

7.2.3 Synthesis of bare C dot and N-CDs: The bare C dots were synthesized via the above-mentioned method by using only 0.19 g citric acid and 0.30 g of β-cyclodextrin and denoted as CDs. In the case of N-CDs urea is used as an 'N' source along with citric acid and β-cyclodextrin and denoted as N-CDs in the MS.

7.2.4 Development of CdIn$_{2.2}$S$_y$/S, N-CDs heterostructure: To decorate the S, N-CDs on the synthesized CIS thin nanosheets dip-coating method was explored (**Scheme 7.1**). Initially, a dilute solution of S, N-CDs was prepared using S, N -CDs, and Milli-Q water in a 1:9 ratio (volume). The CIS@FTO was dipped into the S, N-CDs solution for different time intervals like 5, 10, and 15 min to vary the deposition amount of S, N-CDs on the surface of CIS thin nanosheets. The CIS/S, N-CDs photoelectrodes are named as CIS/S, N-CDs-A, -B, and -C throughout the MS.
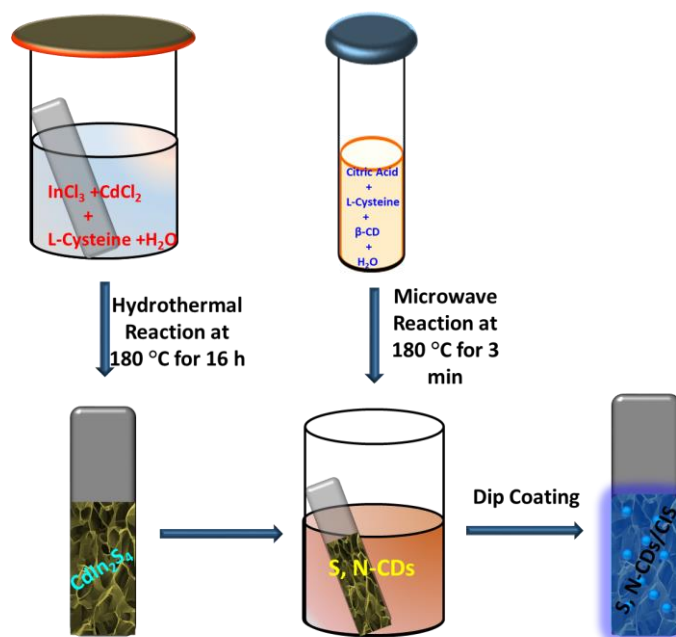
Scheme 7.1: Schematic representation for synthesis of CIS, S, N-CDs, and heterostructure of CIS/S, N-CDs.

Table 7.1: The calculated decoration amount of S, N-CDs on CIS surface

S. No.	Developed Photoanodes	Decoration amount of S, N-CDs
1.	CIS/S, N-CDs-A	19.10%
2.	CIS/S, N-CDs-B	32.07%
3.	CIS/S, N-CDs-C	45.86%

The amount of S, N-CDs on CIS surfaces is calculated in the case of CIS/S, N-CDs-A, -B, and -C from the direct weighing method, and the data is given in **Table 7.1**.

7.3 Result and Discussion

The characterization and application of devloped CIS and CIS/S, N-CDs heterostructures are discussed in the following sections.

7.3.1 Characterization

7.3.1.1 Optical Property

The optical activity of both the semiconductor and the sensitizer play important role in the application in PEC water-splitting reaction. The light absorption profile of CIS, bare CDs, N-CDs, S, N-CDs, and the heterostructure is investigated with the assistance of UV-visible absorbance spectroscopy. The N-CDs and S, N-CDs show the optical absorptivity in the UV region with the absorbance maxima at wavelength 280 nm corresponding to π -π^* transition and at 339 nm indicates the n-π^* transition with an extended tail to the visible region. The absorbance band due to n-π^* transition is absent in the case of bare CDs. The observed result is in accordance with the existing literature.[14,15] After the incorporation of 'S' and 'N' in the CDs framework the optical absorbance is significantly improved than bare CDs and N-CDs, at the same time the absorption band edge shifted towards the visible region. The S, N-CDs show higher optical activity than the bare CDs and N-CDs (**Figure 7.1a**). On the other hand, CIS shows a broad absorbance band in the visible region with the extended tail. The vertically grown thin nanosheets of CIS help to absorb more visible light through multiple reflection and scattering of light inside the material and it increases the light-matter interaction.
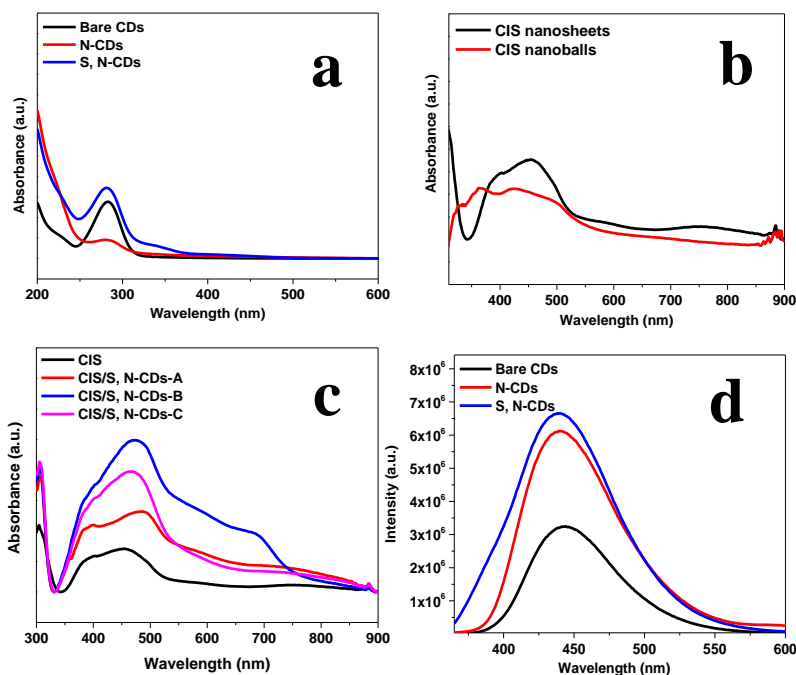
Figure 7.1: UV-visible spectra of (a) CIS and heterostructure of CIS/S, N-CDs-A, -B, and -C, (b) bare CDs, N-CDs, and S, N-CDs, (c) comparative UV-visible spectra of CIS nanosheets and CIS nanoballs, and (d) photoluminescence (PL) spectra of bare CDs, N-CDs, and S, N-CDs.

To confirm this phenomenon, the optical activity of 3D-nanoballs of CIS is determined and compared with thin nanosheets of CIS. **Figure 7.1b** indicates that thin nanosheets of CIS are more efficient to absorb visible light than the CIS nanoballs. The S, N-CDs enable to absorb more light than bare CDs and N-CDs, so preferably S, N-CDs decorated on the surface of CIS to extend the absorption in the broad-spectrum region. The S, N-CDs act as an optical antenna and the optimum decoration of S, N-CDs enhances the light absorption of CIS. The absorption band of CIS is extended in visible to near IR range from CIS/S, N-CDs-A to CIS/S, N-CDs-B which further shifts to lower wavelength in the case of CIS/S, N-CDs-C. The excess amount of S, N-CDs aggregates on the CIS surface due to which light absorption further decreases (**Figure 7.1c**). The PL spectrum of bare CDs shows a broadband at 440 nm. The PL intensity is enhanced after doping of 'S' and 'N' in the CDs framework (**Figure 7.1d**). Cyclic voltammetry (CV) analysis is carried out to determine the conduction band (E_{CB}) and valence band (E_{VB}) edge position of CIS and S, N-CDs (**Figure 7.2a, b**).[16] The calculated E_{CB} and E_{VB} positions are -3.64 eV and -6.10 eV for CIS and -

3.73 eV and -6.06 eV for S, N-CDs, respectively. The obtained band gap values for CIS and S, N-CDs are 2.46 eV and 2.27 eV, respectively, which is confirmed with the help of the Tauc plot (**Figure 7.2c, d**).
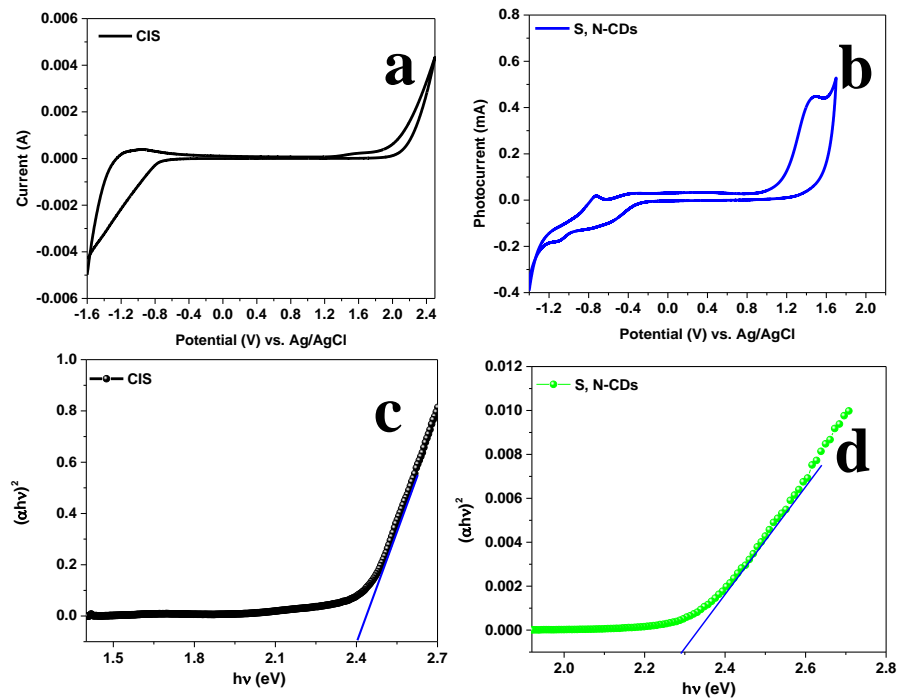
Figure 7.2: (a, b) Cyclic voltammogram, (c, d) Tauc plot of CIS and S, N-CDs, respectively.

The synthesized S, N-CDs show blue emission under UV excitation at 365 nm which is brighter than the bare CDs and N-CDs (**Figure 7.3a, b**).
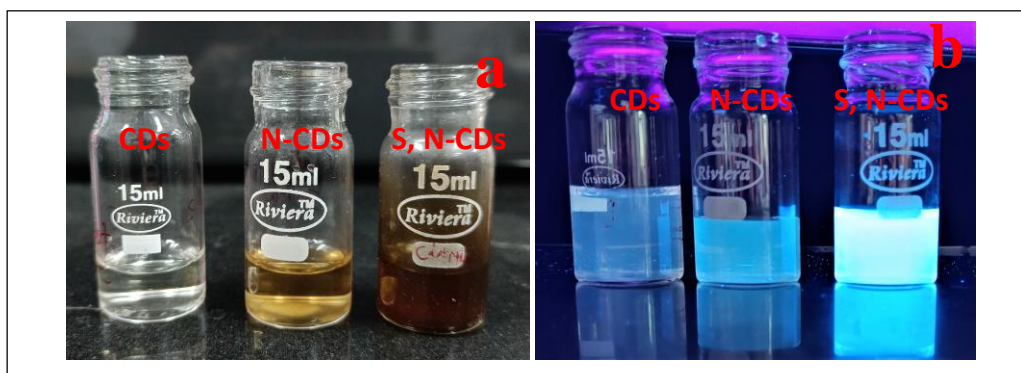
Figure 7.3: (a) Day light images of CDs, N-CDs, and S, N-CDs, (b) Images of CDs, N-CDs, and S, N-CDs, under UV light (at wavelength-365 nm).

7.3.1.2 XRD and Raman Analysis

With the help of XRD analysis, phase, crystal structure, purity, and crystallinity of the synthesized heterostructure and the counterparts are determined. XRD pattern of S, N-CDs is shown in **Figure 7.4a**. It demonstrates that S, N-CDs show a broad hump at 20.29º, which reflects the less crystallinity of carbon. The developed S, N-CDs shows the shift at a lower 2θ value in the XRD pattern compared to existing literature reports of CDs, which signifies the successful incorporation of strain in CDs after incorporation of 'S' and 'N' as the dopant.[12] Observed XRD patterns for the heterostructure and bare CIS are shown in **Figure 7.4b**. All the observed peaks indicate the synthesis of pure phase CIS nanostructure with the cubic crystal structure.[17,18]
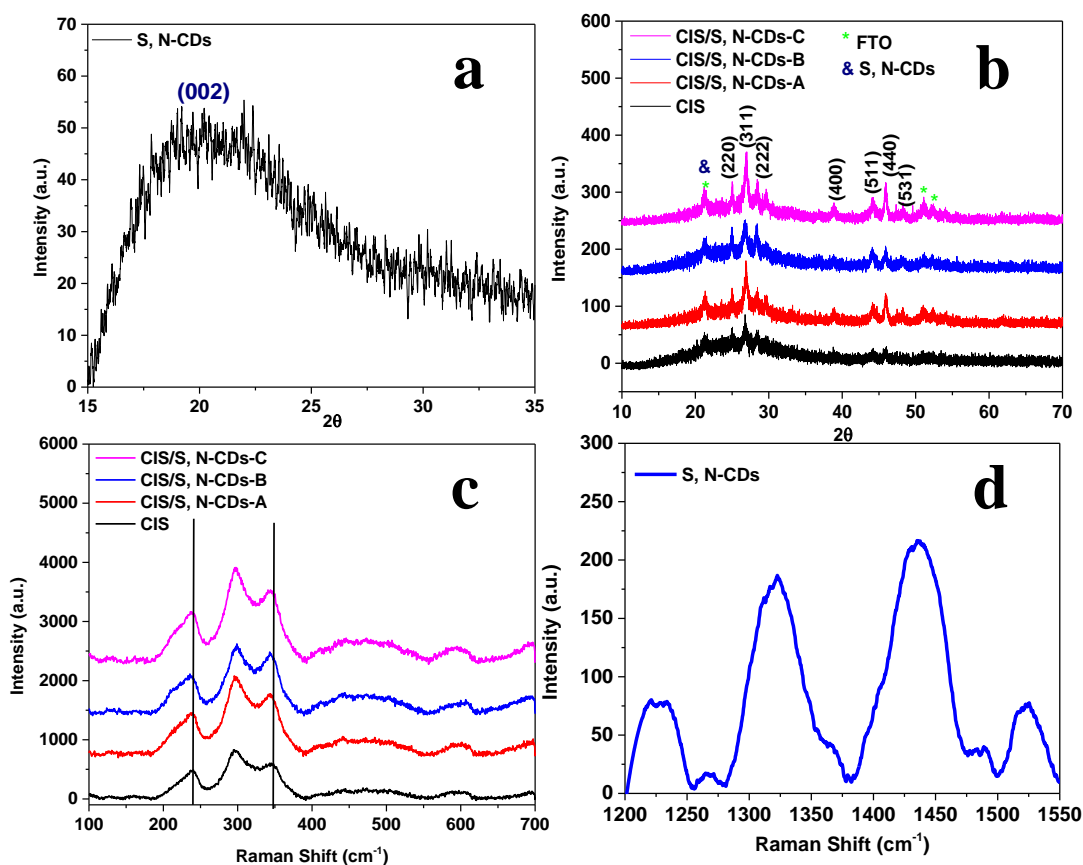
Figure 7.4: XRD of (a) CIS and CIS/S, N-CDs-A, -B, and -C, (b) S, N-CDs, Raman spectra of (c) CIS and heterostructure of CIS/S, N-CDs-A, -B, and -C, and (d) S, N-CDs.

Along with the peak of CIS, there are some other peaks at 21.26º, 36.80º, 38.83º, and 52.34º which are indexed for the FTO.[19] As the developed CIS layer is very thin, XRD analysis detects the presence of the beneath the layer of FTO. The obtained XRD pattern of CIS/S, N-CDs does

not show any clear peak for the S, N-CDs, which is presumably either due to the amorphous nature or very low loading of S, N-CDs or nearly the same peak position of FTO and S, N-CDs.

The crystallinity and purity of the CIS, S, N-CDs, and the heterostructure are further confirmed with the help of Raman analysis. The sharp peak at 298 cm^{-1} is endorsed the cubic structure of CIS. Peaks at 238 cm^{-1} and 347 cm^{-1} are due to the longitudinal optical modes (LO$_1$ and LO$_2$, respectively) of the CIS. A broad peak located at 602 cm^{-1} signifies the 2T$_2$g mode of CIS.[20, 21] After the decoration of S, N-CDs the peak of LO$_1$, LO$_2$, and 2T$_2$g modes are shifted at lower wavenumber which confirms the interaction between CIS and S, N-CDs, and formation of CIS and S, N-CDs heterostructure (**Figure 7.4c**). The Raman spectra of S, N-CDs notably have four peaks at 1225, 1322, 1436, and 1524 cm^{-1} due to the vibration in the β-C$_3$N$_4$ structure lattice and signifies that the CDs have β-C$_3$N$_4$ like structure (**Figure 7.4d**).[22]

7.3.1.3 FTIR Analysis

Following our developed methodology, clear dispersion of CDs is obtained which indicates the successful stabilization of the CDs in the solution. To ensure the surface functional group Fourier transform infrared (FTIR) analysis is carried out. A broad vibration band at ~3100-3400 cm^{-1} is due to the stretching vibration of O-H/N-H bonds, which signifies the hydroxyl and amino group on the surface of S, N-CDs. The peaks located between 2100-2400 cm^{-1} are attributed to the C-N and S-H groups. Peak observed at 1630 cm^{-1} corresponds to the stretching frequency of $\upsilon_{C=O}$/$\upsilon_{C=N}$/N-H in the -CONH$_2$ group.
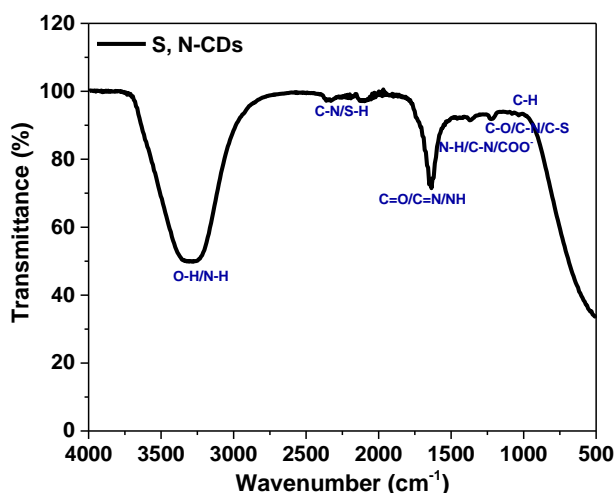
Figure 7.5: FTIR spectra of S, N-CDs.

The peaks at 1374 and 1217 cm^{-1} are assigned for the N-H / C-N/ COO$^-$ and C-O/C-N/CS-band, respectively. A less intense peak is observed between 900-1100 cm^{-1} due to the C-H bond. The FTIR results confirm that the 'S' and 'N' are successfully doped in the CDs (**Figure 7.5a**). The observed result is in well-accordance with the reported literature.[23-25]

7.3.1.4 FESEM and EDS Analysis

To determine the surface morphology of the developed materials field emission scanning electron microscope (FESEM) analysis is executed. The CIS is composed of vertically grown interconnected thin nanosheets (**Figure 7.6a, b**). The thin nanosheets are interconnected in such a way that it creates a cavity inside. The vertical and interconnected arrangement of thin nanosheets of CIS helps to increase the light absorption resulting in more light-matter interaction.
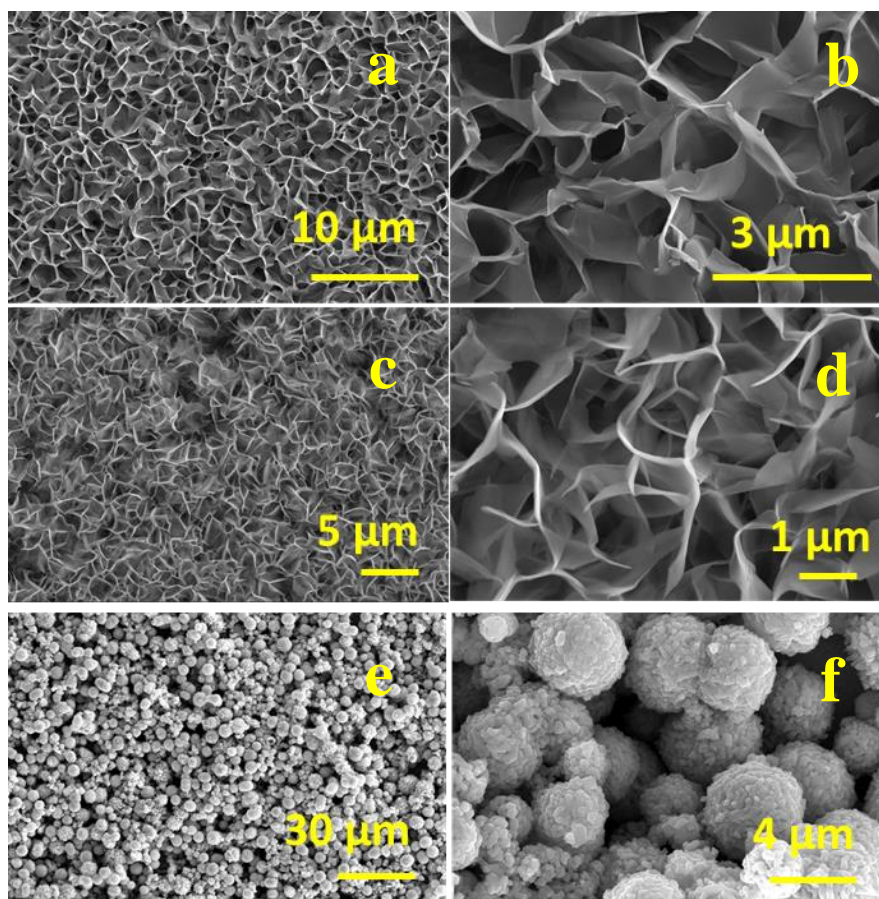
Figure 7.6: FESEM images of (a, b) CIS, (c, d) Heterostructure of CIS/S, N-CDs-B, (e, f) CIS nanoballs at low and high magnifications, respectively.

The cavity formation enhances the penetration of electrolytes inside the material. It results in an increased electrode-electrolyte interface which may be beneficial for PEC reaction. To know the effect of adornment of S, N-CDs on the surface of CIS thin nanosheets, FESEM imaging of heterostructure of CIS/ S, N-CDs-B is carried out (**Figure 7.6c, d**). After the decoration of S, N-CD the morphology remains intact. The decoration of S, N-CDs is hard to locate on the surface of CIS thin nanosheets probably due to the very small size of S, N-CDs. CIS synthesized from method 2 shows the 3D- nanoball-like morphology through FESEM analysis (Figure 7.6e, f).

The elemental composition of the heterostructure (CIS/S, N-CDs-B) and bare CIS is determined by performing EDS mapping analysis. CIS thin nanosheets consist of Cd, In, S, Si, and Sn throughout the material. On the other hand, the heterostructure has 'C', 'N', 'S' along with 'Cd', 'In', 'S', 'Si', and 'Sn' throughout the material (**Figure 7.7 and 7.8**). The perceived result designates the formation of the heterostructure.
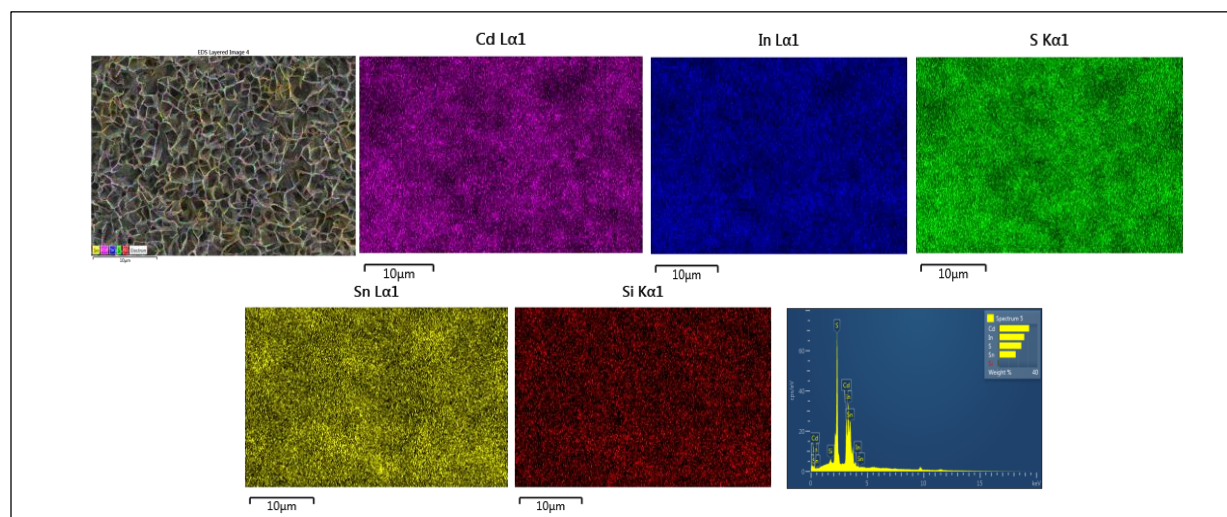
Figure 7.7: EDS analysis of CIS thin sheets on FTO which shows the uniform distribution of 'Cd', 'In' and 'S'.
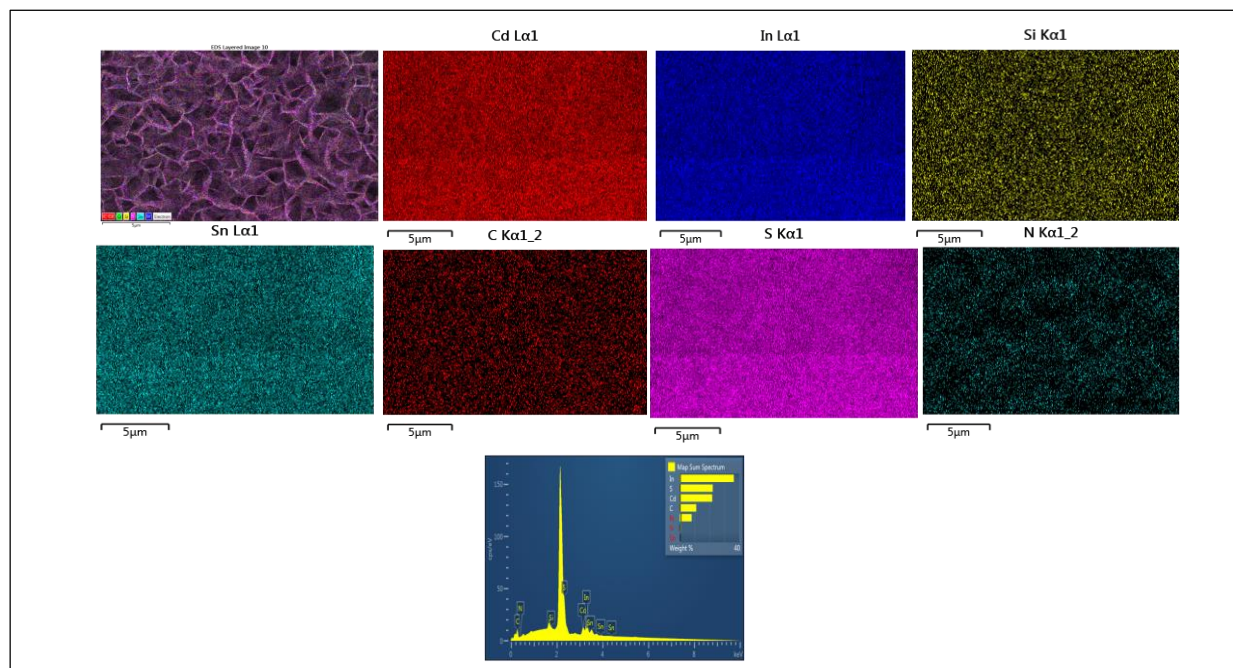
Figure 7.8: EDS analysis of CIS/S, N-CDs-B thin sheets on FTO which shows the uniform distribution of 'Cd', 'In', 'S' and 'N' and 'C'.

7.3.1.5 TEM, HRTEM, and SAED Analysis

Further, the TEM and HRTEM analysis is carried out to know the size and lattice spacing of synthesized S, N-CDs. **Figure 7.9a, b** shows the TEM and HRTEM image of S, N-CDs which indicates the crystalline nature of the C-dots as clear lattice fringes are observed. The distance between two lattice spacing is 0.372 nm, which corresponds to the basal plane spacing. It is worth noting that the spacing of the basal plane of developed S, N-CDs is larger than the basal plane of bulk graphite (0.335 nm)[26] which is due to the incorporation of 'S' and 'N' in the lattice of CDs and it confirms the synthesis of graphitic like S, N-CDs.[27] The size of synthesized S, N-CDs is in the range of ~3-5 nm. The SAED pattern further supports the less crystalline nature of S, N-CDs (**Figure 7.9c**). The decoration of S, N-CDs on the surface of CIS thin nanosheets is confirmed from the TEM analysis (**Figure 7.9d**). **Figure 7.9e** displays the HRTEM image of CIS and the calculated lattice spacing is 0.34 nm corresponding to the (311) crystal plane. The SAED pattern shows the crystalline nature of developed CIS/S, N-CDs-B heterostructure **Figure 7.9f**.
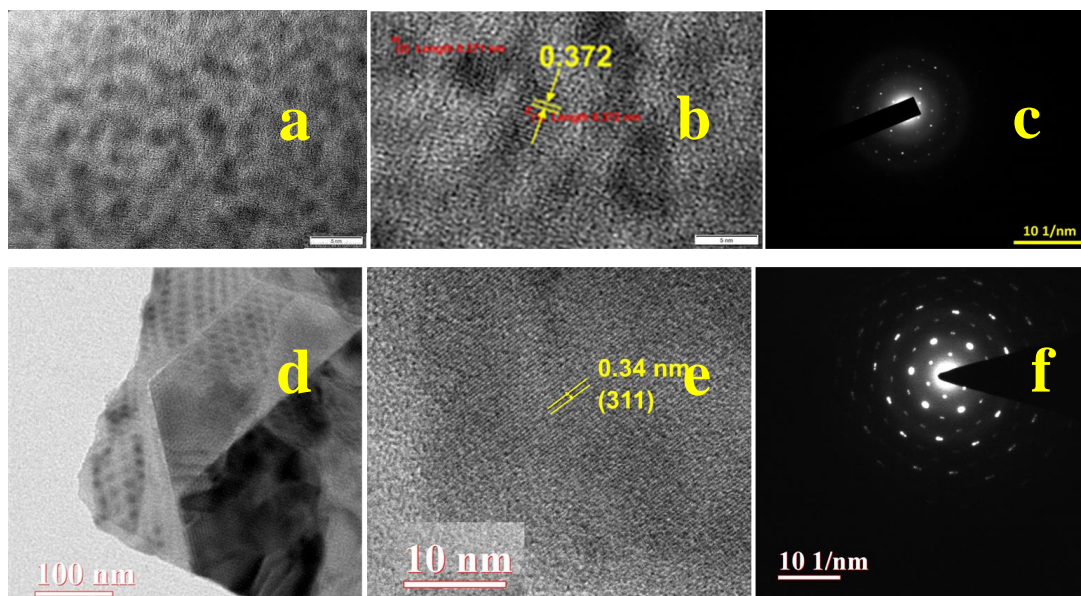
Figure 7.9: HRTEM images of (a, b) S, N-CDs, (C) SAED pattern of S, N-CDs, (d) TEM image of CIS/S, N-CDs-B, (e) HRTEM image of CIS, and (f) SAED pattern of of CIS/S, N-CDs-B.

7.3.1.5 Zeta Potential Measurement

The type of interaction between S, N-CDs and CIS nanosheets is determined with the help of Zeta potential measurement. It indicates that CIS nanosheets posses the positive charge on the surface, whereas the negative charge presents on the surface of S, N-CDs. The presence of opposite charge on the surface reveals the electrostatic interaction between S, N-CDs and CIS nanosheets (**Figure 7.10**).
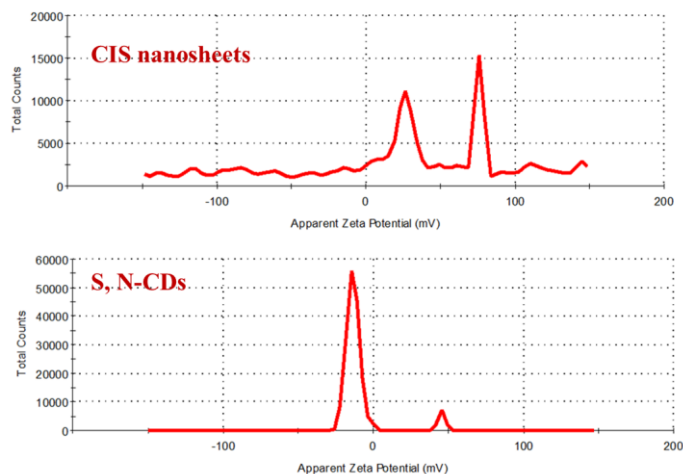
Figure 7.10: Zeta potential values of CIS nanosheets and S, N-CDs.

7.3.2 Photoelectrochemical Activity

7.3.2.1 Linear Sweep Voltametry

The photoelectrochemical (PEC) performance of all the synthesized heterostructures and bare CIS is determined with the help of the linear sweep voltammetry (LSV) technique under back irradiation of light (100 mW/cm^2). The PEC study is carried out applying a three-electrode system, where Ag/AgCl Pt wire, and sample deposited FTO acted as a reference, counter, and working electrode in 0.5 M Na$_2$SO$_4$, respectively. The stabilities of the synthesized photoanodes are checked with the assistance of chronoamperometry techniques. All the PEC measurement data are recorded with respect to Ag/AgCl electrode and reported in RHE. The developed CIS thin nanosheets have efficiently taken part in PEC water-splitting reaction and can generate ~2.73 mA/cm^2 photocurrent density at an applied potential of '0.6' V vs. RHE and maximum photocurrent density of 3.97 mA/cm^2 can be generated at 1.6 V vs. RHE under continuous back illumination. In the literature, it is discussed that in the case of metal sulfides, the photogenerated charge carriers are inefficient to readily come to the electrode surface to react with electrolytes and oxidize itself during the PEC reaction. At the same time, the charge carrier recombination that takes place within a very short time (10 ns) is the main issue for the semiconductor material.[28] So, to overcome the mentioned issues, S, N-CDs are decorated on the surface of CIS thin nanosheets.
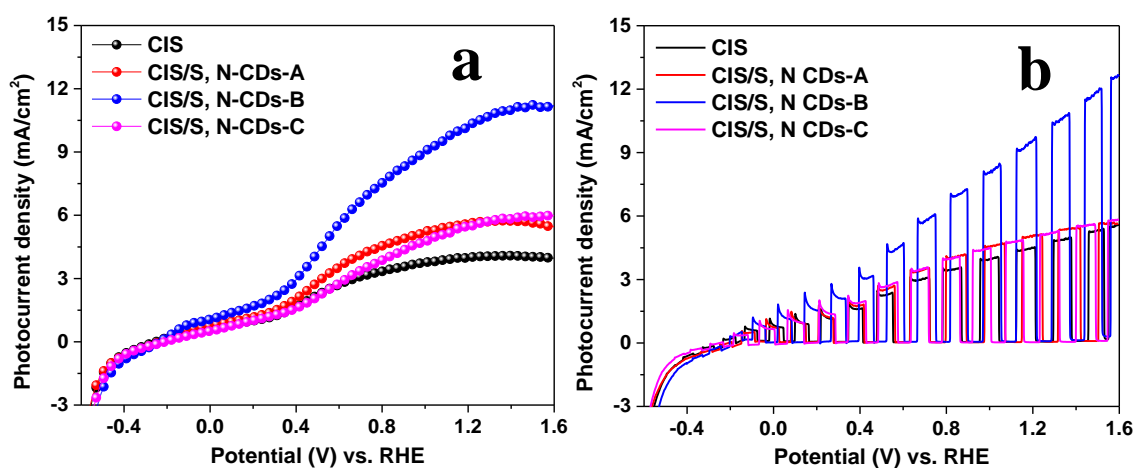
Figure 7.11: LSV curves of CIS and heterostructure of CIS/S, N-CDs-A, -B, and -C (a) Continuous illumination, (b) Chopped illumination.

From the experimental data, it is observed that the PEC activity of CIS thin nanosheets is improved after the decoration of S, N-CDs. The CIS/S, N-CDs-A can generate the photocurrent density ~3.58 mA/cm^2, and 5.44 mA/cm^2 at applied potentials of '0.6' V and '1.6' V vs. RHE, respectively. The photocurrent density reaches the maximum when the dipping time is enhanced from 5 min to 10 min and the developed heterostructure CIS/S, N-CDs-B can generate 5.99 mA/cm^2 and 11.2 mA/cm^2 photocurrent densities at '0.6' V and '1.6' V vs. RHE, respectively. The generated maximum photocurrent density is ~ 2.8-fold higher than that of bare CIS thin nanosheets. Further, increasing the loading amount of S, N-CDs on CIS by increasing the time from 10 min to 15 min does not lead to any further enhancement in PEC activity. In the case of CIS/S, N-CDs-C the photocurrent density decreases and it is near to the bare CIS thin nanosheets. When the decoration of S, N-CDs is excess then it aggregates on the surface of CIS, and due to which light absorption is further decreased and aggregated S, N-CDs can act as recombination center which results in decrease in photocurrent density of CIS/S, N-CDs-C. Under both applied potentials '0.6' V and '1.6' V vs. RHE, the CIS/S, N-CDs-C can generate only 2.74 mA/cm^2 and 5.99 mA/cm^2 photocurrent densities, respectively. The comparative LSV plots of all the photoanodes under continuous illumination are shown in **Figure 7.11a**.The transient photoactivity of the developed photoanodes are determined under chopped illumination conditions and it is perceived that all the photoelectrodes can show switch off and on behavior under chopped illumination (**Figure 7.11b**). To further investigate the above observation, the electrochemical active surface area (ECSA) is calculated for the developed photoanodes with the help of CV analysis (**Figure 7.12a-e**). CIS/S, N-CDs-A and CIS/S, N-CDs-B show ~1.4 fold and 2.75 fold enhanced ECSA values than bare CIS. On the other hand, ECSA value decreases in the case of CIS/S, N-CDs-C compared to bare CIS which reveals the excess decoration of S, N-CDs. The over deposited S, N-CDs act as recombination centers that block the electrochemically active sites (Table 7.2).
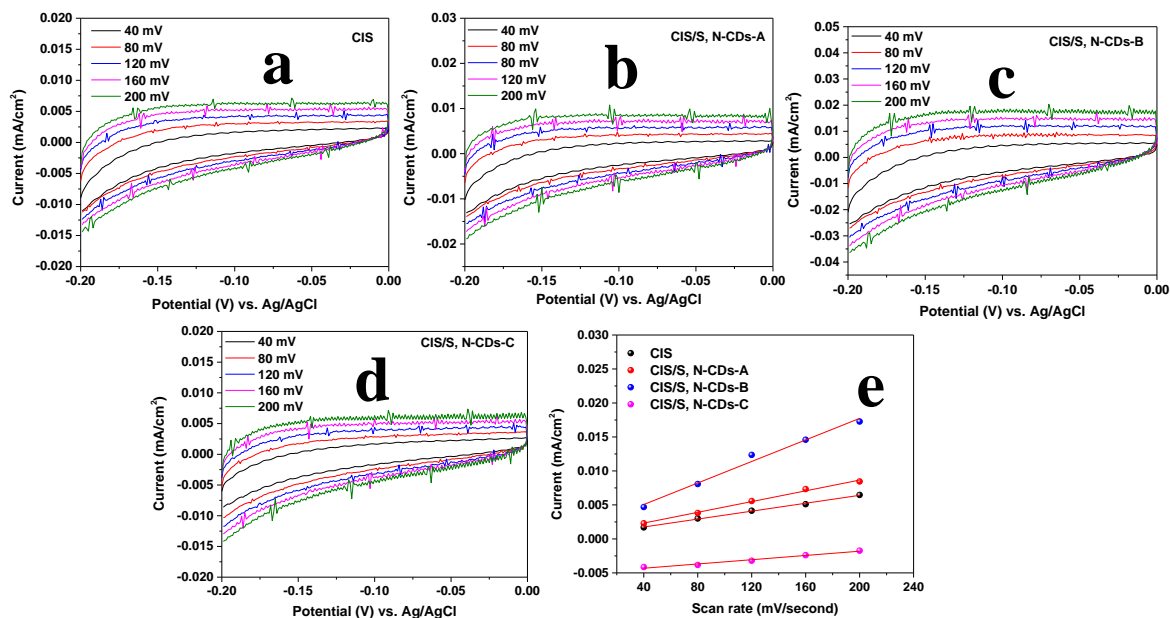
Figure 7.12: CV curves of (a) CIS, (b) CIS/S, N-CDs-A, (c) CIS/S, N-CDs-B, (d) CIS/S, N-CDs-C, and (e) comparative plot of Cdl values for CIS, CIS/S, N-CDs-A, -B, and -C.

Table 7.2: Comparative electrochemically active surface area values of the developed photoanodes.

S. N.	Developed Photoanode	ECSA (cm^2)
1.	CIS	0.048
2.	CIS/S, N-CDs-A	0.066
3.	CIS/S, N-CDs-B	0.132
4.	CIS/S, N-CDs-C	0.0261

7.3.2.2 Transient Decay Time (τ)

Under chopped illumination, the chronoamperometry study of CIS and heterostructures is carried out for 90 seconds at '0.6' V vs. RHE to understand the behavior of the charge-carrier under light off-on conditions (**Figure 7.10a**). In this case, photocurrent decay is observed. It is because when the photoanode illuminates continuously more charge carriers generate. As the water oxidation process is sluggish the photogenerated holes are accumulated on the working electrodes. Consequently, decay in photocurrent is observed during the light on/off cycle at a fixed potential.
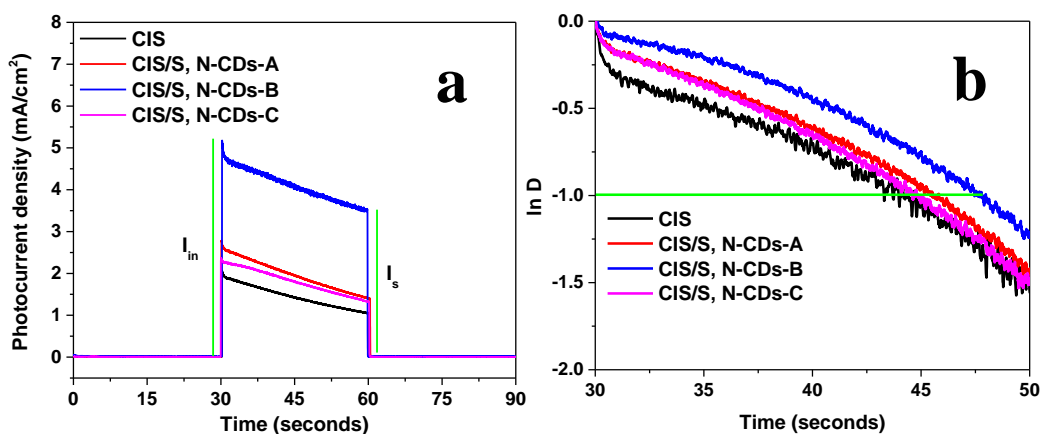
Figure 7.13: (a) Chronoamperometry technique for developed photoandes 90 seconds at 0.6 V vs. RHE, (b) Transient decay time plot for CIS and CIS/S, N-CDs-A, -B, and -C.

From **Figure 7.13a** the transient decay time (τ) is calculated for heterostructures and CIS by using the following equation:[29, 30]

$$D = (I_t - I_s)/(I_{in} - I_s)$$

where I_t, I_s, and I_{in} denote the photocurrent at time t, the current at steady state, and the current of the anodic spike, respectively. The transient decay time (τ) is defined as the time at which ln D = -1. **Figure 7.13b** shows that after adornment of S, N-CDs on the surface of CIS transient decay time becomes longer than that of CIS thin nanosheets. It is observed that the CIS/S, N-CDs-B have a longer transient decay time than other developed photoanodes. The result confirmed that heterostructure suppresses the recombination at the interface by transporting holes to the electrolyte.

7.3.2.3 Photostability and Durability of Photoanodes

The photostability of CIS and CIS/S, N-CDs-B is also determined under continuous illumination up to 1500 seconds at an applied potential of '0.4' V vs. RHE, and the comparative data is given in **Figure 7.14a**. At the same potential, the photostability of CIS/S, N-CDs–B is examined for 1 h under continuous illumination. It is observed that CIS/S, N-CDs–B losses ~50% photocurrent density after 1 h (**Figure 7.14b**). The FESEM analysis confirms that the morphology of CIS/S, N-CDs-B is also a bit affected during long-term PEC reaction conditions (**Figure 7.14c**).
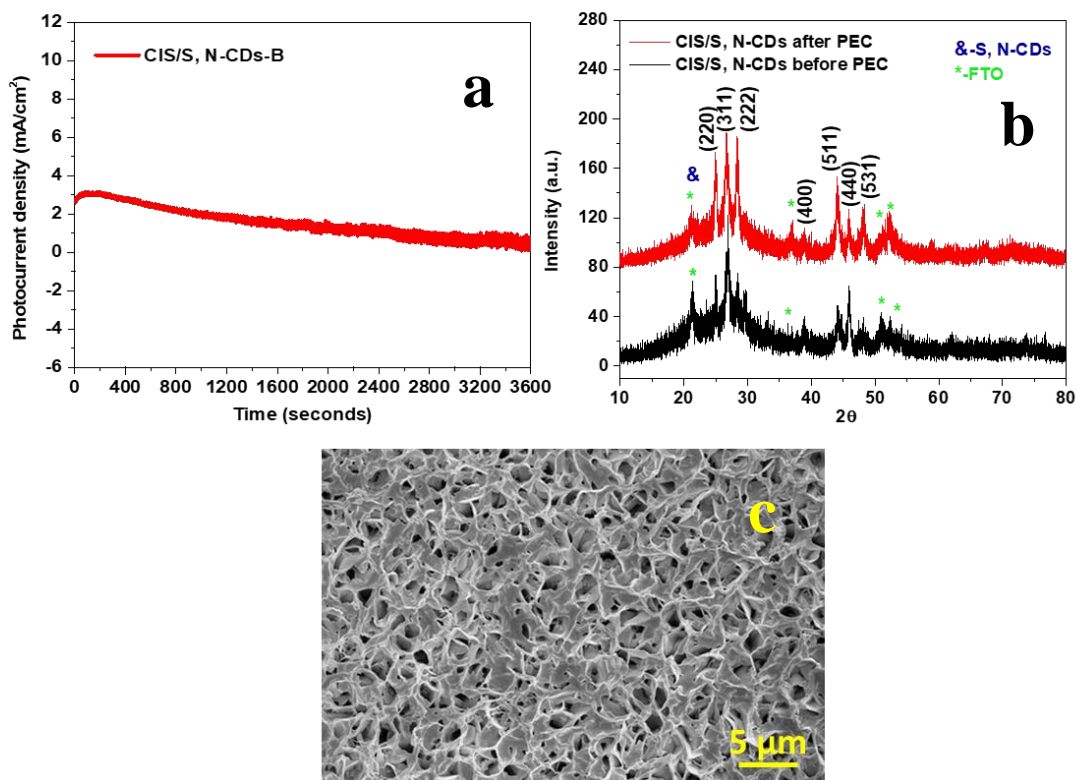
Figure 7.14: i-t plots of (a) CIS and CIS/S, N-CDs-B for 1500 seconds, (b) for CIS/S, N-CDs-B for 1 h under continuous illumination at 0.4 V vs. RHE in chronoamperometry study, (c) FESEM image of CIS/S, N-CDs-B after 1 h photostability test under continuous illumination.

7.3.2.4 Mechanism of Charge carrier Separation through Type-II Band Alignment

The observed enhancement in the PEC activity is yet to understand. With the help of different techniques, the reason for such enhancement is determined whether it is due to the higher charge carrier separation, or charge carrier transportation. Importantly, from the band edge alignment, it is observed that CIS and S, N-CDs develop type-II heterostructure which promotes the charge carrier separation by changing the distribution of charge-carrier density.
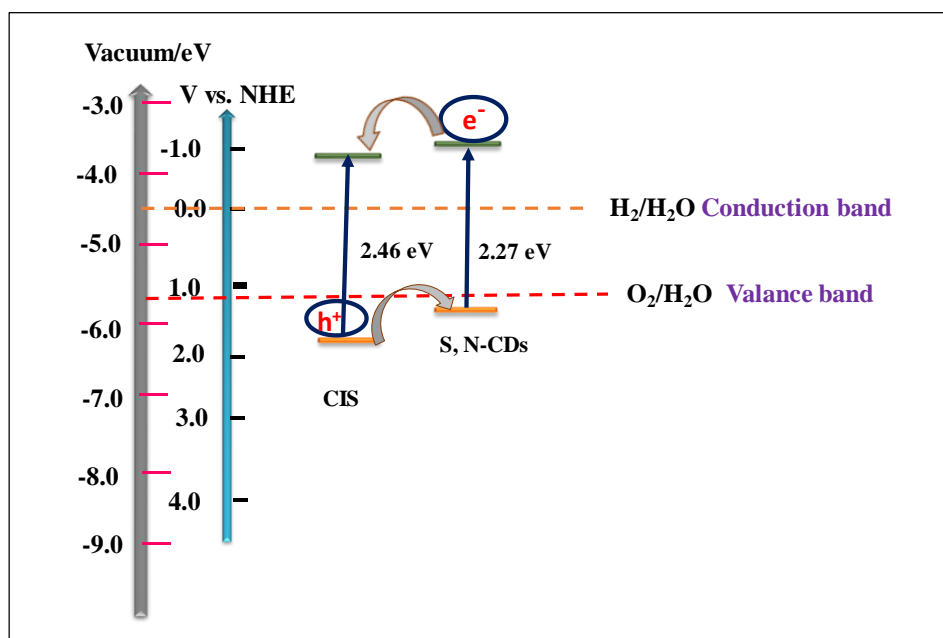
Scheme 7.2: Schematic presentation of type -II heterostructure of CIS and S, N-CDs.

The conduction band (E_{CB}) and valence band (E_{VB}) edge position of CIS and S, N-CDs are determined from the CV analysis (**Figure 7.2a, b**).[16] The calculated E_{CB} and E_{VB} positions are -3.64 eV and -6.10 eV for CIS and -3.73 eV and -6.06 eV for S, N-CDs, respectively. The obtained band gap values for CIS and S, N-CDs are 2.46 eV and 2.27 eV, respectively. The Type-II band alignment favors the photogenerated hole relocate from the VB of CIS to S, N-CDs, and the photogenerated electrons transfer from the CB of S, N-CDs to CIS. The transfer of photogenerated charge carriers in opposite direction helps to diminish the charge-carrier recombination rate (**Scheme 7.2**).

7.3.2.1 Charge Carrier Separation and Injection Efficiencies

Further to investigate the benefits of heterostructure formation, charge-carrier separation ($\eta_{sep}\%$) and charge carrier injection efficiencies (η_{inj}) of CIS/S, N-CDs-B, and bare CIS are calculated using a mixture of solutions as an electrolyte. In which 0.5 M Na_2SO_4 and methanol as a hole scavenger.[31,32] The photocurrent density obtained from the PEC water-splitting depends on the following factor:

$$J_{PEC} = J_{abs} \times \eta_{sep} \times \eta_{inj}$$

where J_{abs} denotes the maximum photocurrent density when all the photons are completely converting into current (J_{abs}). The surface recombination of charge carriers can largely suppress the without persuading the charge separation in the bulk electrode (i.e., $\eta_{inj} = 100\%$) by injection of the hole as the electrolyte. Therefore, η_{inj} and η_{sep} can be determined as follows:[33-35]

$$\eta_{inj} = J_{H2O}/ J_{hole\ scavenger}, \text{ and } \eta_{sep} = J_{hole\ scavenger}/J_{abs}$$

where J_{H2O}= observed photocurrent density in H_2O, $J_{hole\ scavenger}$ = photocurrent density in the presence of hole scavenger, respectively. Based on these equations, the heterostructure of CIS/S, N-CDs-B shows ~1.93-fold higher photocurrent density or ~1.93-fold higher charge separation efficiency compared to bare CIS at an applied potential of 1.23 V vs. RHE. On the other hand, the calculated charge injection efficiencies are 73.13% and 54.89% for CIS/S, N-CDs-B, and bare CIS, respectively. Thus, the improved charge-carrier separation and charge injection efficiency signify the better charge separation and transportation in the heterostructure than the bare CIS (**Figure 7.15a**).
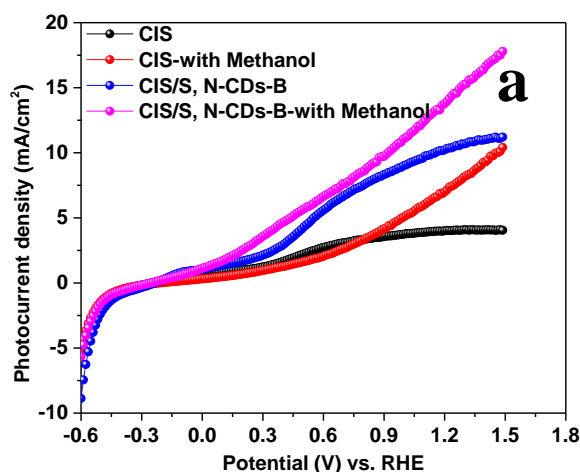
Figure 7.15: (a) LSV plots for CIS and CIS/S, N-CDs-B with and without methanol as a hole scavenger.

7.3.2.5 Calculation of Photoconversion Efficiencies of Developed Photoanodes

Further, to quantitatively evaluate the improved photoactivity after the decoration of S, N-CDs on CIS thin nanosheets, applied-bias-to-photon conversion efficiency ($\eta\%$) is deliberated with the help of obtained J-V plot and the following equation is used:[36-37]

$$\eta = [J (1.23-V_{RHE})/P_{in}] \%$$

where J is denoting photocurrent density, V_{RHE} = applied potential with respect to RHE, and P_{in} = incident light intensity.
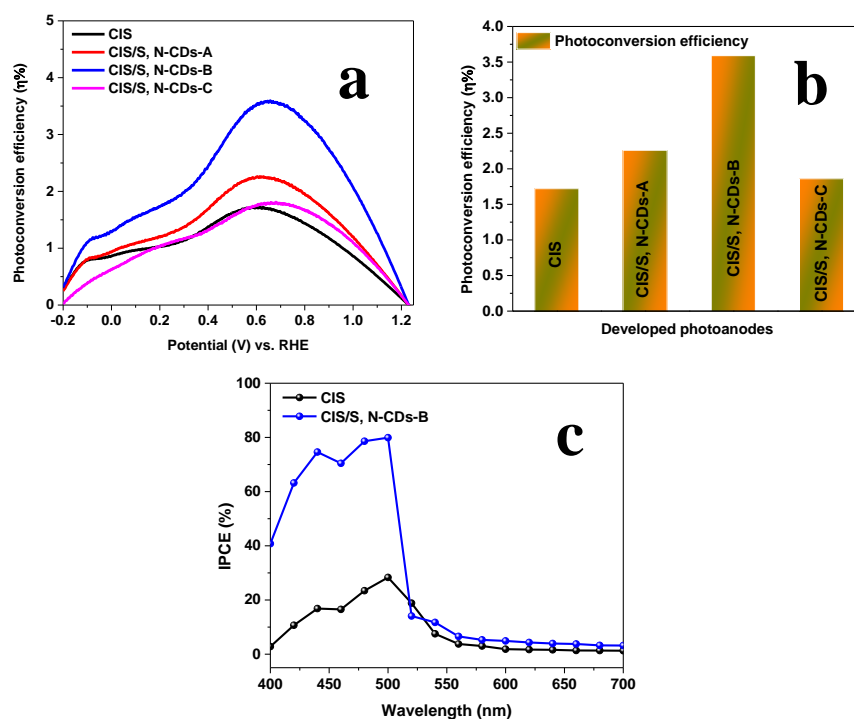
Figure 7.16: (a, b) ABPE of CIS, CIS/S, N-CDs-A, -B, and -C, (c) IPCE of CIS CIS/S, N-CDs-B.

After the decoration of S, N-CDs on CIS, the photoconversion efficiency enhances, and maximum η% is attained in the case of CIS/S, N-CDs-B, and the obtained data is shown in **Figure 7.16a, b**. The heterostructure CIS/S, N-CDs-B can attain the maximum η% of ~3.59% at an applied potential of '0.65' V vs. RHE which is ~2.08-fold higher than bare CIS nanosheets (1.72% at '0.60' V vs. RHE). Whereas, at the potential of '0.61' and '0.66' V vs. RHE, CIS/S, N-CDs-A and -C can achieve η% 2.26 and 1.86, respectively. The maximum photoconversion efficiency of the heterostructure signifies the maximum light absorption, more carrier density in the heterostructure, simultaneously, higher charge-carrier separation and transportation. To further gain visibility about the quantum efficiency, the incident photon to current conversion efficiency (%IPCE) is calculated by determining the power of the incident beam of light at every specified wavelength, using the following equation.[36]

$$IPCE\ (\%) = (1240/\lambda) \times (I_{ph}/P_{in}) \times 100$$

Here, λ is the wavelength (nm) of the incident light, I_{Ph} represents the photocurrent in mA/cm^2 and P_{in} is the power of the incident beam in mW/cm^2. IPCE defines the ratio of 'effective photons' that generate electron-hole pairs in the semiconductor and the 'incident photons' of the monochromatic light. The maximum IPCE value is obtained at ~79.81% for the CIS/S, N-CDs-B which is ~2.84 fold higher than the bare CIS (28.13%) (**Figure 7.16c**). In the region of 450-500 nm, the enhancement in IPCE is achieved mainly due to the improved light-harvesting ability after the decoration of S, N-CDs.

7.3.2.6 Determination of Charge Transfer Resistance through EIS Spectra

To gain a clear insight on the charge transfer kinetics of the different synthesized CDs, CIS, and heterostructure at the electrode/electrolyte interface electrochemical impedance (EIS) study is carried out under the light illumination at an applied potential of '1.5' V and '0.6' V vs. RHE, respectively. The charge transfer resistance of S, N-CDs is compared with N-CDs and bare CDs and it is observed that after co-doping of CDs by 'S' and 'N' the charge transfer resistance decreases.
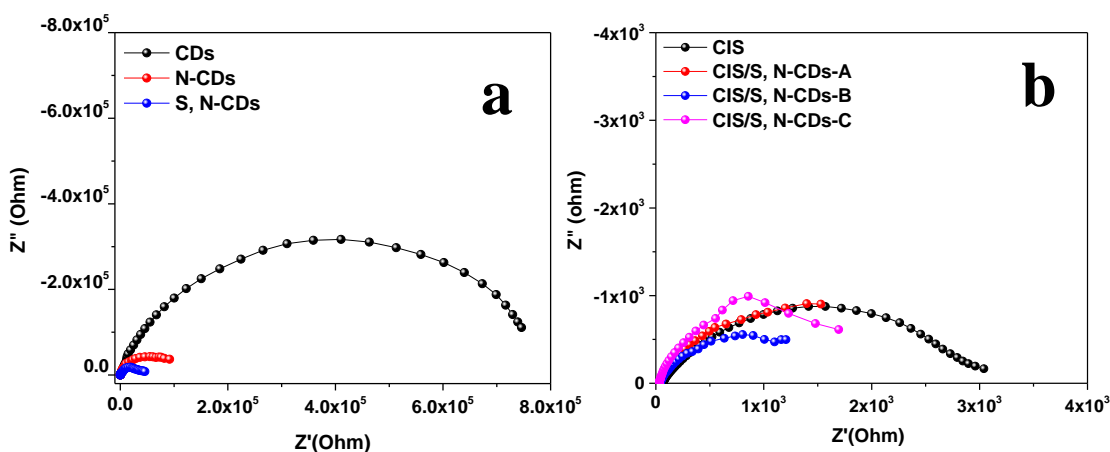
Figure 7.17: (a) EIS plot of bare CDs, N-CDs, and S, N-CDs, and (b) EIS plot of CIS and heterostructure of CIS/S, N-CDs-A, -B, and -C.

The S, N-CDs have the higher charge transferability and because of that, it is chosen as the sensitizer for the preferential decoration on the surface of CIS to increase the efficiency (**Figure 7.17a**). The PEIS plot indicates the given order for the radius of semicircles: CIS > CIS/S, N-CDs-

C > CIS/S, N-CDs-A > CIS/S, N-CDs-B (**Figure 7.17b**). The smallest radius of CIS/S, N-CDs -B implies faster charge transportation and lower interfacial charge transfer resistance (R_{CT}). The formation of type II heterostructure helps to have effective charge carrier separation as well as transportation at the electrode/electrolyte interface.

7.3.2.7 Calculation of Carrier Density of Developed Photoanodes

The electronic property and the carrier density of the heterostructure CIS/S, N-CDs-B, and bare CIS are determined with the help of Mott-Schottky (M-S plot) analysis and shown in (**Figure 7.18a**). The n-type nature of the developed photoanodes; CIS and heterostructure is confirmed from the positive slope of the M-S plot. The carrier density and flat band potential are calculated by using the following equation:[37,38]

$$1/C_s^2 = (2/e\varepsilon\varepsilon_0 N_d A^2) \ [(V-V_{FB}-kT/e)]$$

Where C_s = specific capacitance, ε_0 = electric permittivity of vacuum, e = electron charge, ε = the dielectric constant of the semiconductor, V_{FB} = flat band potential, N_d= carrier density, T = temperature, A= area of the sample, and k = Boltzmann constant. The calculated carrier density of the heterostructure (3.5×10^{21} cm^{-3}) is ~3-fold higher than bare CIS thin nanosheets (1.04×10^{21} cm^{-3}). The higher carrier density indicates the efficacy of the heterostructure in the PEC water-splitting reaction.
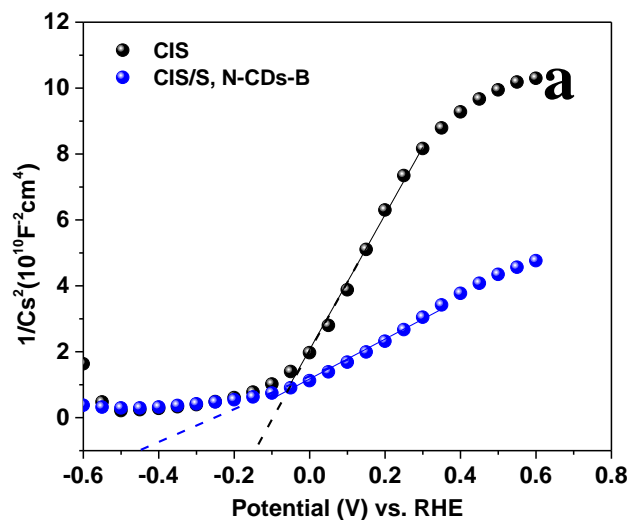
Figure 7.18: Mott-Schottky plot of (a) CIS and heterostructure of CIS/S, N-CDs-B.

Flat band potential (V_{FB}) can be calculated by the extrapolation of the M-S plot. It is one of the salient physical parameters to study the degree of band bending of semiconductor materials. The obtained flat band potential of CIS/S, N-CDs is -0.44 V vs. RHE, which is more negative than bare CIS thin nanosheets (-0.13 V vs. RHE). The more negative flat band potential signifies the greater degree of band bending resulting in higher charge transportation of charge carriers for the water oxidation reaction, at the same time the negative flat band potential indicates the widening of the space charge layer. It is presumed that the efficacy of the heterostructure is devised due to the enhanced ability of charge separation and transportation after the decoration of the S, N-CDs.

7.4 Comparative Study

The observed PEC performance of CIS/S, N-CDs heterostructure is better than bare CIS nanosheets and it is quite high with the existing literature (**Table 7.3**).

Table 7.3: Comparative PEC activity data of CIS/S, N-CDs heterostructure with the reported existing data in literature.

S.N.	Photoanodes	Electrolyte	Photocurrent density	References
1.	NGQDs/ZnO NT	0.1 M Na_2SO_4	3.4 mA/cm^2 at potential of 1.0 V vs. Ag/AgCl	39
2.	H:ZnO/CdS/CQDs	0.25 M Na_2S and 0.35 M Na_2SO_3	10 mA/cm^2 at potential of 1.0 V vs. SCE	40
3.	N-GQDs/ZnO NW	0.5 M Na_2SO_4	0.61 mA/cm^2 at potential of 1.0 V vs. Ag/AgCl	41
4.	ZnO@CDs	0.1 M Na_2SO_4	1.6 mA/cm^2 at potential of 1.8 V vs. RHE	42
5.	BiVO$_4$-N/C CoPOM	0.5 M phosphate buffer solution	3.30 mA/cm^2 at potential of 1.23 V vs. RHE	43
6.	S,N-GQD/Ag-ZnO NRs	0.1 M Na_2SO_4	2.60 mA/cm^2 at potential of 1 V vs. Ag/AgCl	44
7.	ZnO nanotubes@N-CDs@ZIF-8	0.5 M Na_2SO_4	0.45 mA/cm^2 at potential of 0.5 V vs. Ag/AgCl	45
8.	ZnO/C dots	0.5 M Na_2SO_4	2.05 mA/cm^2 at potential of 0.6 V vs. Ag/AgCl	12
9.	ZnO-S, N-CDs@NF	1 M KOH	0.28 mA/cm^2 at potential of 0.9 V vs. Ag/AgCl	46
10.	CIS/S,N-CDs	0.5 M Na_2SO_4	11.2 mA/cm^2 at potential of 1.6 V vs. RHE	In this study

7.5 Conclusion

In this study, an efficient photoanode CIS/S, N-CDs is developed following a chemical method for the application in PEC water-splitting reaction. FESEM analysis indicates the synthesis of interconnected, vertically grown thin nanosheets of CIS. These vertically grown thin nanosheets of CIS can attain a maximum photocurrent density of 3.97 mA/cm^2 at '1.6' V vs. RHE under continuous back illumination. The thin nanosheets of CIS have increased visible light absorption which is attained through multiple reflections and scattering of light inside the material resulting in more light-matter interaction. The heterostructure of CIS/S, N-CDs exhibits improved photoactivity and produces ~2.8-fold higher photocurrent density than the bare CIS. The increased PEC performance is due to the decoration of S, N-CDs. The S, N-CDs acts as optical antennas that boost the optical property of CIS. Simultaneously, S, N-CDs, and CIS form the type-II heterostructure. The formation of type-II heterostructure enables to increase in the separation of photogenerated charge carriers. The transient decay time becomes longer in the case of a heterostructure of CIS/S, N-CDs than the bare CIS. On the other hand, the more negative flat band potential of CIS/S, N-CDs than the bare CIS indicates the widening of space charge layers which signifies the high rate of charge carrier transport in the heterostructure. At the same time, adornment of the S, N-CDs on the surface of CIS decreases the R_{CT} value which further assists in the enhancement of the charge transfer kinetics and stability of the heterostructure under continuous back illumination. This study provides a sustainable avenue to produce clean energy as the future fuel.

7.6 References

1. Yang, Y.; Niu, S.; Han, D.; Liu, T.; Wang, G.; Li, Y. Progress in Developing Metal Oxide Nanomaterials for Photoelectrochemical Water-splitting. *Adv. Energy Mater.*, **2017**, *7,* 1700555 (1-26).

2. Song, J-P.; Yin, P-F.; Mao, J.; Qiao, S-Z.; Du, X-W. Catalytically active and chemically inert $CdIn_2S_4$ coating on a CdS photoanode for efficient and stable water-splitting. *Nanoscale* **2017**, *9*, 6296-6301.

3. Wang, Y.; Chen, C.; Tian, W.; Xu, W.; Li, L. Designing $WO_3/CdIn_2S_4$ type-II heterojunction with both efficient light absorption and charge separation for enhanced photoelectrochemical water-splitting. *Nanotechnology* **2019**, *30*, 495402 (1-10).

4. Xue, C.; An, H.; Yan, X.; Li, J.; Yang, B.; Wei, J.; Yang, G. Spatial charge separation and transfer in ultrathin $CdIn_2S_4/rGO$ nanosheet arrays decorated by ZnS quantum dots for efficient visible-light-driven hydrogen evolution. *Nano Energy* **2017**, *39*, 513-523.

5. Ding, S.; Liu, X.; Shi, Y.; Liu, Y.; Zhou, T.; Guo, Z.; Hu, J. Generalized Synthesis of Ternary Sulfide Hollow Structures with Enhanced Photocatalytic Performance for Degradation and Hydrogen Evolution. *ACS Appl. Mater. Interfaces* **2018**, *10,* 17911-17922.

6. Wang, S.; Guan, B. Y.; Lu, Y.; Lou, X. W(D). Formation of Hierarchical In_2S_3-$CdIn_2S_4$ Heterostructured Nanotubes for Efficient and Stable Visible Light CO_2 Reduction. *J. Am. Chem. Soc.*, **2017**, *139*, 17305-17308.

7. Sharma, M. D.; Mahala, C.; Basu, M. Shape-Controlled Hematite: An Efficient Photoanode for Photoelectrochemical Water-splitting. *Ind. Eng. Chem. Res.*, **2019**, *58*, 7200-7208.

8. Sharma, M. D.; Mahala, C.; Basu, M. Band gap tuning to improve the photoanodic activity of $ZnIn_xS_y$ for photoelectrochemical water oxidation. *Catal. Sci. Technol.*, **2019**, *9*, 6769-6781.

9. Xu, W.; Tian, W.; Meng, L.; Cao, F.; Li, L. Ion Sputtering-Assisted Double-Side Interfacial Engineering for $CdIn_2S_4$ Photoanode toward Improved Photoelectrochemical Water-splitting. *Adv. Mater. Interfaces* **2020**, *7*, 1901947 (1-9).

10. Meng, L.; Wang, M.; Sun, H.; Tian, W.; Xiao, C.; Wu, S.; Cao, F.; Li, L. Designing a Transparent $CdIn_2S_4/In_2S_3$ Bulk-Heterojunction Photoanode Integrated with a Perovskite Solar Cell for Unbiased Water-splitting. *Adv. Mater.*, **2020**, *32*, 2002893 (1-7).

11. Liang, Z.; Hou, H.; Fang, Z.; Gao, F.; Wang, L.; Chen, D.; Yang, W. Hydrogenated TiO_2 Nanorod Arrays Decorated with Carbon Quantum Dots Toward Efficient Photoelectrochemical Water-splitting. *ACS Appl. Mater. Interfaces*, 2019, **11**, 19167-19175.

12. Mahala, C.; Sharma, M. D.; Basu, M. Type-II Heterostructure of ZnO and Carbon Dots Demonstrates Enhanced Photoanodic Performance in Photoelectrochemical Water-splitting. *Inorg. Chem.*, **2020**, *59*, 6988-6999.

13. Ye, K-H.; Wang, Z.; Gu, J.; Xiao, S.; Yuan, Y.; Zhu, Y.; Zhang, Y.; Mai, W.; Yang, S. Carbon quantum dots as a visible light sensitizer to significantly increase the solar water-splitting performance of bismuth vanadate photoanodes. *Energy Environ. Sci.*, **2017**, *10*, 772-779.

14. Dong, Y.; Pang, H.; Yang, H. B.; Guo, C.; Shao, J.; Chi, Y.; Li, C. M.; Yu, T. Carbon-Based Dots Co-doped with Nitrogen and Sulfur for High Quantum Yield and Excitation-Independent Emission. *Angew. Chem. Int. Ed.*, **2013**, *52*, 1-6.

15. Zhu, S.; Meng, Q.; Wang, L.; Zhang, J.; Song, Y.; Jin, H.; Zhang, K.; Sun, H.; Wang, H.; Yang, B. Highly Photoluminescent Carbon Dots for Multicolor Patterning, Sensors, and Bioimaging. *Angew. Chem. Int. Ed.*, **2013**, *52*, 3953-3959.

16. Barman, M. K.; Mitra, P.; Bera, R.; Das, S.; Pramanik, A.; Parta, A. An efficient charge separation and photocurrent generation in the carbon dot-zinc oxide nanoparticle composite. *Nanoscale*, **2017**, *9*, 6791-6799.

17. Jiang, Y.; Peng, Z.; Wu, F.; Xiao, Y.; Jing, X.; Wang, L.; Liu, Z.; Zhang, J.; Liu, Y.; Ni, L. A novel 3D/2D $CdIn_2S_4$ nano-octahedron/ZnO nanosheet heterostructure: facile synthesis, synergistic effect and enhanced tetracycline hydrochloride photodegradation mechanism. *Dalton Trans.*, **2018**, *47*, 8724-8737.

18. Apte, S. K.; Garaje, S. N.; Bolade, R. D.; Ambekar, J. D.; Kulkarni, M. V.; Naik, S. D.; Gosavi, S. W.; Baeg, J. O.; Kale, B. B. Hierarchical nanostructures of $CdIn_2S_4$ via hydrothermal and microwave methods: efficient solar-light-driven photocatalysts. *J. Mater. Chem.*, **2010**, *20*, 6095-6102.

19. Velanganni, S.; Pravinraj, S.; Immanuel, P.; Thiruneelakandan, R. Nanostructure CdS/ZnO heterojunction configuration for photocatalytic degradation of Methylene blue. *Phys. Rev. B Condens. Matter,* **2018**, *534*, 56-62.

20. Naik, S. D.; Apte, S. K.; Garaje, S. N.; Sethi, Y. A.; Shinde, M. D.; Arbuj, S. A.; Kale, B. B.; Sonawane, R. S. Facile template free approach for the large-scale solid phase synthesis of nanocrystalline XIn_2S_4 (X = Cd/Zn) and its photocatalytic performance for H_2 evolution. *New J. Chem.*, **2020**, *44*, 9634-9646.

21. Unger, W. K.; Famworth, B.; Irwin, J.C. Raman and Infrared Spectra of $CdIn_2S_4$ and $ZnIn_2S_4$. *Solid State Commun.*, **1978**, *25*, 913-915.

22. Sciortino, L.; Sciortino, A.; Popescu, R.; Schneider, R.; Gerthsen, D.; Agnello, S.; Cannas, M.; Messina, F. Tailoring the Emission Color of Carbon Dots through Nitrogen-Induced Changes of Their Crystalline Structure. *J. Phys. Chem. C* 2018, *122*, 19897-19903.

23. Qu, D.; Zheng, M.; Du, P.; Zhou, Y.; Zhang, L.; Li, D.; Tan, H.; Zhao, Z.; Xied, Z.; Sun, Z. Highly luminescent S, N co-doped graphene quantum dots with broad visible absorption bands for visible light photocatalysts. *Nanoscale* **2013**, *5*, 12272-12277.

24. Sun, D.; Ban, R.; Zhang, P-H.; Wu, G-H.; Zhang, J-R.; Zhu, J-J. Hair fiber as a precursor for synthesizing of sulfur- and nitrogen-co-doped carbon dots with tunable luminescence properties. *Carbon* **2013**, *64*, 424-434.

25. Miao, X.; Yan, X.; Qu, D.; Li, D.; Tao, F.; Sun, Z. Green Preparation of S and N Co-Doped Carbon Dots from Water Chestnut and Onion as Well as Their Use as an Off-On Fluorescent Probe for the Quantification and Imaging of Coenzyme A. *ACS Sustainable Chem. Eng.*, **2017**, *5*, 4992-5000.

26. Li, F.; Li, Y.; Yang, X.; Han, X.; Jiao, Y.; Wei, T.; Yang, D.; Xu, H.; Nie, G. Highly Fluorescent Chiral N-S-Doped Carbon Dots from Cysteine:Affecting Cellular Energy Metabolism. *Angew. Chem. Int. Ed.*, **2018**, *57*, 2377-2382.

27. Tang, L.; Ji, R.; Li, X.; Bai, G.; Liu, C. P.; Hao, J.; Lin, J.; Jiang, H.; Teng, K. S.; Yang, Z.; Lau, S. P. Deep Ultraviolet to Near-Infrared Emission and Photoresponse in Layered N-Doped Graphene Quantum Dots. *ACS Nano* **2014**, *8*, 6312-6320.

28. Li, J.; Wu, N. Semiconductor-based photocatalysts and photoelectrochemical cells for solar fuel generation: a review. *Catal. Sci. Technol.*, **2015**, *5*, 1360-1384.

29. Gao, L.; Li, F.; Hu, H.; Long, X.; Xu, N.; Hu, Y.; Wei, S.; Wang, C.; Ma, J.; Jin, J. Dual Modification of a $BiVO_4$ Photoanode for Enhanced Photoelectrochemical Performance. *ChemSusChem*, **2018**, *11*, 2502-2509.

30. Tafalla, D.; Salvador, P.; Benito, R. M. Kinetic Approach to the Photocurrent Transients in Water Photoelectrolysis at n-TiO$_2$ Electrodes II. Analysis of the Photocurrent-Time Dependence. *J. Electrochem. Soc.*, **1990**, *137*, 1810-1815.

31. Pendlebury, S. R.; Barroso, M.; Cowan, A. J.; Sivula, K.; Tang, J.; Gratzel, M.; Klug, D.; Durrant, J. R. Dynamics of photogenerated holes in nanocrystalline α-Fe$_2$O$_3$ electrodes for water oxidation probed by transient absorption spectroscopy. *Chem. Commun.*, **2011**, *47*, 716-718.

32. Mesa, C. A.; Kafizas, A.; Francàs, L.; Pendlebury, S. R.; Pastor, E.; Ma, Y.; Formal, F. L.; Mayer, M. T.; Grätzel, M.; Durrant, J. R. Kinetics of Photoelectrochemical Oxidation of Methanol on Hematite Photoanodes. *J. Am. Chem. Soc.*, **2017**, *139*, 11537-11543. Hou, J.; Cao, S.; Sun, Y.; Wu, Y.; Liang, F.; Lin, Z.; Sun, L. Atomically Thin Mesoporous In$_2$O$_{3-x}$/In$_2$S$_3$ Lateral Heterostructures Enabling Robust Broadband-Light Photo-Electrochemical Water-splitting. *Adv. Energy Mater.*, **2017**, *8*, 1701114 (1-9).

33. Sharma, M. D.; Mahala, C.; Basu, M. Photoelectrochemical Water-splitting by In$_2$S$_3$/In$_2$O$_3$ Composite Nanopyramids. *ACS Appl. Nano Mater.*, **2020**, *3*, 11638-11649.

34. Moir, J. W.; Sackville, E. V.; Hintermair, U.; Ozin, G. A. Kinetics versus Charge Separation: Improving the Activity of Stoichiometric and Non-Stoichiometric Hematite Photoanodes Using a Molecular Iridium Water Oxidation Catalyst. *J. Phys. Chem. C* **2016**, *120*, 12999-13012.

35. Varghese, O. K.; Grimes, C. A. Appropriate strategies for determining the photoconversion efficiency of water photoelectrolysis cells: A review with examples using titania nanotube array photoanodes. *Sol. Energy Mater Sol. Cells* **2008**, *92*, 374-384.

36. Xu, X-T.; Pan, L.; Zhang, X.; Wang, L.; Zou, J-J. Rational Design and Construction of Cocatalysts for Semiconductor-Based Photo-Electrochemical Oxygen Evolution: A Comprehensive Review. *Adv. Sci.*, **2018**, *6*, 1801505 (1-35).

37. Hajra, P.; Shyamal, S.; Mandal, H.; Fageria, P.; Pande, S.; Bhattacharya, C. Photocatalytic activity of Bi$_2$O$_3$ Nanocrystalline Semiconductordeveloped via Chemical-bath Synthesis. *Electrochim. Acta* **2014**, *123*, 494-500.

38. Hankin, A.; B-Lora, F. E., Alexander, J. C.; Regoutz, A.; Kelsall, G. H. Flat band potential determination: avoiding the pitfalls. *J. Mater. Chem. A* **2019**, *7*, 26162-26176.

39. Majumder, T.; Dhar, S.; Chakraborty, P.; Debnath, K.; Mondal, S. P. Advantages of ZnO nanotaper photoanodes in photoelectrochemical cells and graphene quantum dot sensitized solar cell applications. *J. Electroanal. Chem.*, **2018**, *813*, 92-101.

40. Vuong, N. M.; Reynolds, J. L.; Conte, E.; Lee, Y-I. H:ZnO Nanorod-Based Photoanode Sensitized by CdS and Carbon Quantum Dots for Photoelectrochemical Water Splitting. *J. Phys. Chem. C* **2015**, *119*, 24323-24331

41. Zeng, Z.; Xiao, F-X.; Gui, X.; Wang, R.; Liu, B.; Tan, T. T. Y. Layer-by-layer assembly of nitrogen-doped graphene quantum dots monolayer decorated one-dimensional semiconductor nanoarchitectures for solar-driven water splitting. *J. Mater. Chem. A* **2016**, *4*, 16383-16393.

42. Xu, X.; Bao, Z.; Tang, W.; Wu, H.; Pan, J.; Hu, J.; Zeng, H. Surface states engineering carbon dots as multi-band light active sensitizers for ZnO nanowire array photoanode to boost solar water splitting. *Carbon* **2017**, *121*, 201-208.

43. Fan, K.; Chen, H.; He, B.; Yu, J. Cobalt polyoxometalate on N-doped carbon layer to boost photoelectrochemical water oxidation of $BiVO_4$. *Chem. Eng. J.*, **2020**, *392*, 123744 (1-10).

44. Majumder, T.; Dhar, S.; Debnath, K.; Mondal, S. P. Role of S, N co-doped Graphene Quantum Dots as a Green Photosensitizer with Ag-doped ZnO Nanorods for Improved Electrochemical Solar Energy Conversion. *Mater. Res. Bull*., **2017**, *93*, 214-222.

45. Han, H.; Karlicky, F.; Pitchaimuthu, S.; Shin, S. H. R.; Chen, A. Highly Ordered N-Doped Carbon Dots Photosensitizer on Metal-Organic Framework-Decorated ZnO Nanotubes for Improved Photoelectrochemical Water Splitting. *Small* **2019**, *15*, 1902771 (1-7).

46. Gadisa, B. T.; Baye, A. F.; Ntiamoah, R.; Kim, H. ZnO@Ni foam photoelectrode modified with heteroatom doped graphitic carbon for enhanced photoelectrochemical water splitting under solar light. *Int. J. Hydrog. Energy* **2021**, *46*, 2075-2085.

Chapter 8

Summary, Conclusion, and Future Scope of Study

- This chapter summarizes the work carried out in this thesis by highlighting the prominent attributes of the work.
- The future avenue of the work that can be carried out using this thesis are also comprised.

Summary

The summary of the thesis work is given in **Table 8.1**. In context of photostability the developed $ZnIn_{2.2}S_y$ and Cd-$ZnIn_{2.2}S_y$ are the most stable photoanodes. Whereas, CIS/S, N-CDs has higher photoconvesrion efficiency compared to other developed photoanodes.

Table 8.1: Comparative PEC activity data of the developed In_2S_3 based photoanode

Photoanodes	Photoconversion efficiency ($\eta\%$)	Carrier Density (N_d) (cm^{-3})	Stability
In_2S_3	0.043%	2.27×10^{20}	----------------
In_2S_3/In_2O_3	0.55%	7.39×10^{20}	Checked up till 1 hour (3.5 wt% NaCl)
In_2S_3/S-C_3N_4-dots	0.88%	5.70×10^{18}	Checked up till 2700 seconds (3.5 wt% NaCl)
$ZnIn_{2.2}S_y$	2.74%	6.40×10^{21}	Checked up till 1 hour (0.5 M Na_2SO_4)
Cd-$ZnIn_{2.2}S_y$	3.10%	7.16×10^{21}	Checked up till 1 hour (0.5 M Na_2SO_4)
CIS/S, N-CDs	3.59%	3.5×10^{21}	Checked up till 1500 seconds (0.5 M Na_2SO_4)

Conclusion

The introduction of the thesis gives an insight into nanoscience and nanotechnology. It presents a brief literature overview about the nanomaterials, their synthesis method, and their application in various emerging fields. This chapter provides a detailed discussion of the different pathways for solar water-splitting. This chapter also delivers an overview of semiconductor fundamentals, key features of a photoelectrode, and various strategies for the enhancing efficiency of a

photoelectrode. Chapter two demonstrates the synthesis methodology, calculation methods, chemicals, and instrumentation techniques that are used to carry out thesis work. Chapter three to seven describes the developed In_2S_3 based photoanodes for the water-splitting. To increase the to increase the PEC activity of In_2S_3, $ZnIn_2S_4$, and $CdIn_2S_4$, different strategies have been undertaken such as morphology controlling, type-II heterostructure formation, decoration of carbon-based materials, and ion exchange, etc. The developed faceted vertically grown In_2S_3/In_2O_3 nanocomposite absorb more visible light compared to nanobrick of In_2S_3 with the same mass loading on the surface of fluorine doped tin coated glass. In_2S_3/In_2O_3 nanocomposite traps more light through multiple reflection and scattering of light inside the material which increase the light-matter interaction. In_2S_3/In_2O_3 heterostructure helps to increase in charge carrier density and widening in the space charge layer. The widening in space charge layer improves the charge carrier separation in the In_2S_3/In_2O_3. The S-C_3N_4-dots decorated vertically grown In_2S_3 nanosheets can work in 3.5 wt% NaCl which indicates that the developed In_2S_3/S-C_3N_4-dots heterostructre could be used for practical application. The S-C_3N_4-dots act as an optical antenna and increase the optical absorbance of the In_2S_3 nanosheets. At the same time, type-II band alignment of S-C_3N_4 dots and In_2S_3 increases the lifetime of photogenerated charge carriers and diminish the charge-carrier recombination at the electrode/electrolyte interface. Morphology and bandgap of the $ZnIn_xS_y$ are tuned by controlling the indium content (x = 1.6, 2, 2.2, and 3) with respect to zinc and calcination time. The $ZnIn_{2.2}S_y$ has the optimum and appropriate amount of indium content and oxygen doping. The $ZnIn_{2.2}S_y$ has vertically grown 2D nanosheets with sharp edges and interconnected with each other. The proper arrangement of nanosheets in $ZnIn_{2.2}S_y$ enhances the light-matter interaction through multiple reflection and scattering of light inside the nanosheets. The negative valence band energy of $ZnIn_{2.2}S_y$ facile the water oxidation reaction. The photostability of $ZnIn_{2.2}S_y$ is checked under back continuous illumination for 1 h and it is stable. The charge-carrier density of $ZnIn_{2.2}S_y$ is enhanced through the cation exchange of 'Zn^{2+}' with 'Cd^{2+}'. At the same time, the widening in the space charge layer occurs due to the cation exchange which enhances the PEC activity, photoconvesrion efficiency, and photostability of developed Cd- $ZnIn_{2.2}S_y$. The vertically grown 2D thinsheets of $CdIn_{2.2}S_y$ (CIS) are able to trap the more solar light due to the multiple reflection and scattering of light inside the material which enhances the light-matter interaction. Furthermore, to increase the optical absorbance and charge transferability 'S' and 'N' co-doped C dots are used as a sensitizer on vertically grown 2D nanosheets of $CdIn_{2.2}S_y$ for

enhanced PEC water-splitting performance. The $CdIn_{2.2}S_y/S$, N-CDs exhibits better PEC performance compared to $CdIn_{2.2}S_y$ due to the increase in light absorption and charge carrier separation, and transfer efficiency. But the developed In_2S_3/In_2O_3 and $CdIn_{2.2}S_y/S$, N-CDs suffers from the stability issue in 0.5 M Na_2SO_4 under continuous back illumination. So, to improve the photostability some strategies can be explored in future.

Future Scope of Research Work

1. Morphology tuning is the effective way to increase the light absorption, charge carrier generation and collection efficiency. By tuning the thickness of the nanostructures bandgap can be tuned.

2. Synthesis of metal-free carbon-based dots from natural sources can be used as "sensitizers" on semiconductor surface because they have low-cost and non-toxic nature than conventional semiconductor QDs. Carbon based dots exhibit high optical absorbance, wavelength-dependent PL property, and resistant to photo-corrosion. Heterostructuring of semiconductor with carbon based materials and with another semiconductor is proficient route to increase the charge-carrier separation and transfer efficiency.

3. Cation exchange is an efficient strategy to regulate the carrier density and width of space charge layer of semiconductor to suppress the charge recombination. This strategy also helps to increase the active sites of the semiconductor which leads to increase in conductivity, catalytic property, and photostability of the semiconductor materials.

4. The efficient electrocatalysts for hydrogen and oxygen evolution reactions are developed. The developed electrocatalyst can be used as co-catalysts by coupling with photoanode/photocathode for PEC water-splitting to accelerates the reaction kinetics and photostability.

5. The junction between photoanode and photocathode (p-n junction) can developed to form the tandem cell which can efficiently use to improve the charge separation efficiency and Solar-to-hydrogen efficiency.

Appendices

List of Publications [A-1]

1. ****Sharma, M. D.;** Basu, M. Nanosheets of In_2S_3/ S-C_3N_4-Dots for Solar Water-Splitting in Saline Water. *Langmuir* **2022** (Just Accepted)

2. ****Sharma, M. D.;** Basu, M. Surface Modified Vertically Grown 2D Thin Nanosheets of $CdIn_{2.2}S_y$: Photoanode for Photoelectrochemical Water-splitting Reaction. *ACS Appl. Nano Mater.*, **2022**, *5*, 7811-7821.

3. ****Sharma, M. D.;** Mahala, C.; Basu, M. Vertically Grown Cd-$ZnIn_{2.2}S_y$ Nanosheets for Photoelectrochemical Water Splitting. *ACS Applied Nano Materials* **2021**, *4*, 3013-3021.

4. **Sharma, M. D.;** Mahala, C.; Basu, M. Doping of MoS_2 by "Cu" and "V": An Efficient Strategy for the Enhancement of Hydrogen Evolution Activity. *Langmuir* 2021, 37, 4847-4858.

5. ****Sharma, M. D.;** Mahala, C.; Basu, M. Photoelectrochemical Water Splitting by In_2S_3/In_2O_3 Composite Nanopyramids. *ACS Applied Nano Materials* **2020***, 3,* 11638-11649**.**

6. **Sharma, M. D.;** Mahala, C.; Basu, M. 2D Thin Sheet Heterostructures of MoS_2 on $MoSe_2$ as Efficient Electrocatalyst for Hydrogen Evolution Reaction in Wide pH Range. *Inorganic Chemistry* **2020**, *59*, 4377-4388.

7. **Sharma, M. D.;** Mahala, C.; Basu, M. Sensitization of vertically grown ZnO 2D thin sheets by MoS_x for efficient charge separation process towards photoelectrochemical water splitting reaction. *International Journal of Hydrogen Energy* **2020**, *45*, 12272-12282.

8. ****Sharma, M. D.;** Mahala, C.; Basu, M. Band gap tuning to improve the photoanodic activity of $ZnIn_xS_y$ for photoelectrochemical water oxidation. *Catalysis Science & Technology*, **2019**, *9*, 6769-6781.

9. **Sharma, M. D.;** Mahala, C.; Basu, M. Shape-Controlled hematite: an efficient photoanode for photoelectrochemical water splitting. *Industrial & Engineering Chemistry Research* **2019**, *58*, 7200-7208.

10. **Sharma, M. D.;** Mahala, C.; Basu, M. AgPd alloy nanoparticles decorated MoS_2 2D nanosheets: efficient hydrogen evolution catalyst in wide pH condition. *ChemistrySelect* **2019**, *4*, 378-386.

11. **Sharma, M. D.;** Mahala, C.; Basu, M. Nanosheets of $MoSe_2$@M (M= Pd and Rh) function as widespread pH tolerable hydrogen evolution catalyst. *Journal of colloid and interface science* **2019**, *534*, 131-141.

12. Rathore D.; **Sharma M. D.;** Sharma, A.; Basu, M.; Pande S. Aggregates of Ni/Ni(OH)$_2$/NiOOH Nanoworms on Carbon Cloth for Electrocatalytic Hydrogen Evolution. *Langmuir* **2020**, *36*, 14019-14030.

13. Mahala, C.; **Sharma, M. D.;** Basu, M. Type-II Heterostructure of ZnO and Carbon Dots Demonstrates Enhanced Photoanodic Performance in Photoelectrochemical Water Splitting. *Inorganic Chemistry* 2020, *59*, 6988-6999.

14. Mahala, C.; **Sharma, M. D.;** Basu, M. ZnO Nanosheets Decorated with Graphite-Like Carbon Nitride Quantum Dots as Photoanodes in Photoelectrochemical Water Splitting. *ACS Applied Nano Materials* 2020, *3*, 1999-2007.

15. Mahala, C.; **Sharma, M. D.;** Basu, M. Near-Field and Far-Field Plasmonic Effects of Gold Nanoparticles Decorated on ZnO Nanosheets for Enhanced Solar Water Splitting. *ACS Applied Nano Materials*, 2020, *3*, 1153-1165.

16. Mahala, C.; **Sharma, M. D.;** Basu, M. Fe-Doped Nickel Hydroxide/Nickel Oxyhydroxide Function as an Efficient Catalyst for the Oxygen Evolution Reaction. *ChemElectroChem* 2019, *6*, 3488-3498.

17. Mahala, C.; **Sharma, M. D.;** Basu, M. A core@ shell hollow heterostructure of Co$_3$O$_4$ and Co$_3$S$_4$: an efficient oxygen evolution catalyst. *New Journal of Chemistry* 2019, *43*, 15768-15776.

18. Mahala, C.; Sharma, R.; **Sharma, M. D.;** Pande, S. Development of Copper Cobalt Sulfide with Cu:Co Ratio Variation on Carbon Cloth as an Efficient Electrode Material for the Oxygen Evolution Reaction. *ChemElectroChem* 2019, *6*, 5301-5312.

19. Mahala, C.; **Sharma, M. D.;** Basu, M. ZnO@CdS heterostructures: an efficient photoanode for photoelectrochemical water splitting. *New Journal of Chemistry* 2019, *43*, 7001-7010.

20. Mahala, C.; **Sharma, M. D.;** Basu, M. 2D nanostructures of CoFe$_2$O$_4$ and NiFe$_2$O$_4$: efficient oxygen evolution catalyst. *Electrochimica Acta* 2018, *273*, 462-473.

Book Chapter:

1. **Sharma, M. D.;** Basu, M. Fundamentals of Semiconductor Photoelectrochemistry. Book Name: Photoelectrochemical Generation of Fuels, ISBN: 9781003211761, CRC Press.

**Incorporated in the Thesis

List of Poster Presented in Conferences [A-2]

1. **Sharma, M. D.**, International Conference "Nano and Functional Materials: Interface between Science and Engineering" (NFM), 16-18 November 2017, BITS Pilani, Pilani-Campus.

2. **Sharma, M. D.**, International Conference on "Electrochemistry in Advanced Materials, Corrosion and Radiopharmaceuticals" (CEAMCR), 15-17 February 2018, DAE Convention Centre, Anushaktinagar, Mumbai.

3. **Sharma, M. D.**, International Conference on "Frontiers at the Chemistry-Allied Sciences Interaface" (FCASI) 21-22 December 2018, University of Rajasthan, Jaipur, Rajasthan (**Best Poster Award**).

4. **Sharma, M. D.**, "Symposium on Carbon Nanomaterial Electronics" (SCNE), 8-9 November 2019, BITS-Pilani, Pilani Campus (**Best Poster Award**).

5. **Sharma, M. D.**, "Electrochemistry in Industry, Health, and Enviornment" (EIHE), 21-25 January 2020, DAE Convention Centre, Anushaktinagar, Mumbai (**Best Poster Award**).
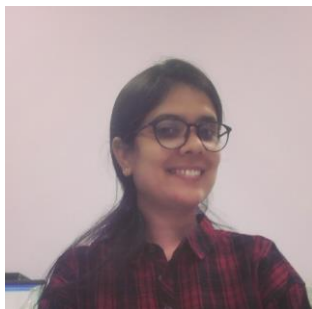
Name: Mamta Devi Sharma

Born at Sikar, Rajasthan, India

Bachelor of Science in Chemistry, Zoology, and Botany from University of Rajasthan, Rajasthan, India in 2011.

Master in Science from University of Rajasthan, Rajasthan (India) in 2014 with the specialization in Organic Chemistry.

Permanent Address:

Mamta Devi Sharma
Village-Mundru
Teh. –Shrimadhopur
District-Sikar
Pin-332712
Rajasthan, India
Email: mamtadevisharma1991@gmail.com

Brief Biography of the Supervisor [A-4]

Dr. MRINMOYEE BASU
Assistant Professor, Department of Chemistry,
BITS Pilani, Pilani Campus, Rajasthan, 333031
Email: mbasupande@gmail.com,
mrinmoyee.basu@pilani.bits-pilani.ac.in

Dr. Mrinmoyee Basu is the Assistant Professor in the Department of Chemistry, BITS-Pilani, Pilani-Campus. Previously, she has worked as DST-Inspire faculty in the Department of Chemistry, Birla Institute of Technology & Science, Pilani from November 2015-October 2020. Dr. Basu did her Ph. D. in Nanoscience and Nanotechnology from IIT-Kharagpur. During her Ph. D. she worked on the synthesis of hierarchical metal chalcogenide nanostructure and their application in catalysis and photocatalysis. She also worked as a research associate at IIT-Delhi where she had developed different type-II semiconductor materials for the application in photocatalysis. Dr. Basu was a postdoctoral fellow at National Taiwan University where she worked on photoelectrochemical solar water splitting. She is presently working on the development of stable and efficient photoelectrodes for photoelectrochemical water splitting. She has handled projects from DST, SERB, and BITS agencies, and her one student defended their thesis successfully in the field of electrocatalysis and photoelectrochemical water-splitting.

Brief Biography of the Co-Supervisor [A-5]

Dr. SUROJIT PANDE
Associate Professor, Department of Chemistry,
BITS Pilani, Pilani Campus, Rajasthan, 333031
Email: surojitpande@gmail.com,
spande@pilani.bits-pilani.ac.in

Dr. Pande did his M.Sc. in Inorganic Chemistry, Kalyani University, Kalyani, West Bengal, and Ph. D. from the Indian Institute of Technology, Kharagpur. During his Ph. D., he worked on metal and metal oxide nanoparticles and their application in catalysis and surface-enhanced Raman spectroscopy. He worked on the application of metal and metal oxide nanoparticles in catalysis, analytical and environmental chemistry, and surface enhances Raman scattering (SERS) studies. Before joining BITS in March 2012, Dr. Pande was a postdoctoral fellow in the Richard M. Crooks research group at The University of Texas at Austin, Texas (USA), with research interests in homogeneous catalysis using dendrimer-encapsulated nanoparticles. He was experienced in the spectroscopic study of the sixth and fourth generation of hydroxy-terminated poly(amidoamine) (PAMAM) dendrimer. Dr. Pande has joined BITS Pilani as an Assistant Professor in March 2012. Since then he has developed various mono- and bi-metallic, oxide, sulfide, and vertically grown heterostructure nanomaterials for catalysis, photocatalysis, and electrocatalysis reactions. He has handled projects from DST, UGC, and BITS agencies and his three students defended their thesis successfully in the field of catalysis, electrocatalysis, photocatalysis, and photoelectrochemical water-splitting.